Nonlinear optical phenomena within the discontinuous Galerkin time-domain framework

Dissertation

zur Erlangung des akademischen Grades

doctor rerum naturalium

(Dr. rer. nat.)

im Fach Physik

Spezialisierung: Theoretische Physik

eingereicht an der

Mathematisch-Naturwissenschaftlichen Fakultät

der Humboldt-Universität zu Berlin

von

M.Sc. Dan-Nha Huynh

Präsidentin der Humboldt-Universität zu Berlin

Prof. Dr. Sabine Kunst

Dekan der Mathematisch-Naturwissenschaftlichen Fakultät

Prof. Dr. Elmar Kulke

Gutachter/innen:

1. Prof. Dr. Kurt Busch
2. Prof. Dr. Alejandro Saenz
3. Stephen K. Gray, Ph.D.

Tag der mündlichen Prüfung: 19. Juli 2018

Ich erkläre, dass ich die Dissertation selbständig und nur unter Verwendung der von mir gemäß §7 Abs. 3 der Promotionsordnung der Mathematisch-Naturwissenschaftlichen Fakultät, veröffentlicht im Amtlichen Mitteilungsblatt der Humboldt-Universität zu Berlin Nr. 126/2014 am 18.11.2014 angegebenen Hilfsmittel angefertigt habe.

Weiterhin erkläre ich, dass ich mich nicht bereits anderwärts um einen Doktorgrad im Promotionsfach Physik beworben habe beziehungsweise einen entsprechenden Doktorgrad besitze.

Ich habe Kenntnis der dem Promotionsverfahren zugrunde liegenden Promotionsordnung der Mathematisch-Naturwissenschaftlichen Fakultät, veröffentlicht im Amtlichen Mitteilungsblatt der Humboldt-Universität zu Berlin Nr. 126/2014 am 18.11.2014.

Berlin, den 5. September 2018

Mathematisch-Naturwissenschaftliche Fakultät
Institut für Physik

Nonlinear optical phenomena within the discontinuous Galerkin time-domain framework

A study on plasmonic and Raman-active materials

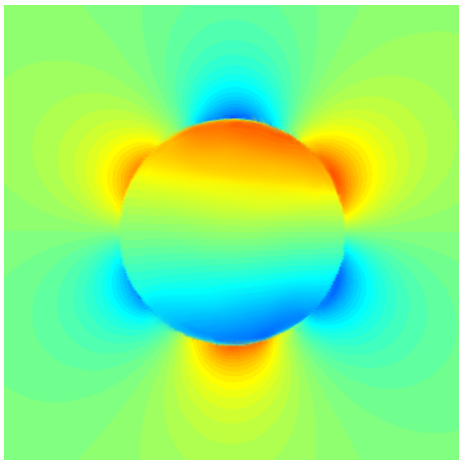

Ph.D. thesis
by Dan-Nha Huynh

Supervisor: Prof. Dr. Kurt Busch

To my parents

"All things are difficult before they are easy."

–Dr. Thomas Fuller, 1732

Abstract

This thesis is concerned with the theoretical description of nonlinear optical phenomena with regards to the (numerical) discontinuous Galerkin time-domain (DGTD) method. It deals with two different material models: the hydrodynamic model for metals and the model for Raman-active dielectrics. In the first part, we review the hydrodynamic model for metals, where we apply a perturbative approach to the model. We use this approach to calculate the second-order nonlinear optical effects of second-harmonic generation and sum-frequency generation using the DGTD method. In this context, we will see how to optimize the second-order response of plasmonic nanoantennas by applying a deliberate tuning scheme for the optical excitations as well as by choosing an intelligent nanoantenna design. In the second part, we examine the material model for Raman-active dielectrics. In particular, we see how to derive the third-order nonlinear response by which one can describe the process of stimulated Raman scattering. We show how to incorporate this third-order response into the DGTD scheme yielding a novel set of auxiliary differential equations. Finally, we demonstrate the workings of the modified numerical scheme.

Zusammenfassung

Nichtlineare optische Phänomene im Rahmen des unstetigen Galerkin-Zeitraumverfahrens

Diese Arbeit befasst sich mit der theoretischen Beschreibung nichtlinearer optischer Phänomene in Hinblick auf das (numerische) unstetige Galerkin-Zeitraumverfahren. Insbesondere werden zwei Materialmodelle behandelt: das hydrodynamische Modell für Metalle und das Modell für Raman-aktive Materialien. Im ersten Teil der Arbeit wird das hydordynamische Modell für Metalle unter Verwendung eines störungstheoretischen Ansatzes behandelt. Insbesondere wird dieser Ansatz genutzt, um die nichtlinearen optischen Effekte, Erzeugung zweiter Harmonischer und Summenfrequenzerzeugung, mit Hilfe des unstetigen Galerkin-Verfahrens zu studieren. In diesem Zusammenhang wird demonstriert, wie das optische Signal zweiter Ordnung von Nanoantennen optimiert werden kann. Hierzu wird ein hier erarbeitetes Schema für die Abstimmung des eingestrahten Lichtes angewandt. Zudem führt eine intelligente Wahl des Antennendesigns zu einem optimierten Signal. Im zweiten Teil dieser Arbeit wird das Modell für Raman-aktive Dielektrika behandelt. Genauer wird die nichtlineare Antwort dritter Ordnung für stimulierte Raman-Streuung hergeleitet. Diese wird dazu genutzt, um ein System aus Hilfsdifferentialgleichungen für das unstetige Galerkin-Verfahren zu konstruieren. Die Ergebnisse des erweiterten numerischen Verfahrens werden im Anschluss gezeigt und diskutiert.

Preface

Since the beginning of mankind light has always fascinated human beings. Accordingly, the scientific field of optics dates back to the ancient Egyptian empire [1]. About in the sixth century B.C. the Greeks discovered that the propagation of light can be described mathematically. Centuries later starting from the renaissance, more efforts towards the mathematical characterization of light were made. In 1864, the Scottish physicist and mathematician J. C. Maxwell first realized that light is an electromagnetic wave [2]. He captured his discovery in a set of equations known today as Maxwell's equations [3]. These equations form the basis of any modern physical description of optical phenomena.

One of the first descriptions of nonlinear optical phenomena was given by Raman [4, 5]. He discovered that the illumination of molecules mostly leads to the elastic scattering of light. However, a small fraction of light is scattered in-elastically. This nonlinear effect is known today as Raman scattering. Raman was awarded with the Nobel prize in 1930 for his research on molecular light scattering [6]. The phenomenon of Raman scattering can be classified as a resonant nonlinear optical effect. In addition to this category, there is also the class of non-resonant optical phenomena.

One type of non-resonant optical effects is the second-harmonic generation (SHG) of light, which takes place at sufficiently high field intensities comparable with the atomic field strength. Its discovery was only possible after the development of the first working laser by Maiman in 1960 [7]. Only one year later Franken et al. were able to observe SHG at crystalline glass for the first time [8]. In their 1961 research they sent the light of a ruby laser at a wavelength of 694 nm through a quartz crystal. The spectrometer showed not only a signal at 694 nm but also a small spot at 347 nm corresponding to a signal of double the frequency of the initial light beam. This result was published in Physical Review Letters [8]. Unfortunately, the original SHG signal recorded with photographic paper was removed by the editor (see fig. 1), as it was mistaken for a dirt spot [9]. The field of nonlinear optics has gained special interest in the plasmonic community after it was discovered by Brown et al. that SHG could also be observed in silver films [10], where the effective nonlinear optical response was increased by plasmonic effects [11]. More recently, the interest has shifted towards nonlinear plasmonic structures in the nanometer regime. The reason for this is the ability to tailor the nonlinear optical response through the resonances of each nano building block [12].

This thesis is dedicated to the theoretical description of both resonant and non-resonant optical

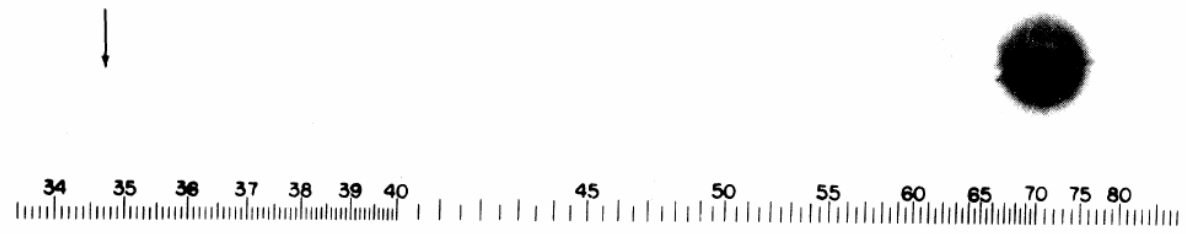

Figure 1: Image from the famous 1961 paper entitled "Generation of Optics Harmonics" by Franken et al. [8]. The second-harmonic spot originally at the position indicated by the arrow was erroneously removed by the editor

phenomena. More specifically, I am going to model nonlinear metallic nano-structures as well as Raman-active dielectrics. Because nonlinear problems are in most cases not solvable purely analytically, I employ a numerical method, known as the discontinuous Galerkin time-domain (DGTD) method [13, 14]. It is best described as a finite element method [15] in time domain, which gives maximal flexibility in calculating the optical response of arbitrarily shaped nanostructures. Within my research group (AG theoretische Optik & Photonik, head of group Prof. Dr. Busch) a DGTD code (SWG 2.2) was developed, with which Maxwell's equations are solved along with an appropriate set of material equations. Within this thesis I elaborate which model equations are well-suited to describe the desired nonlinear optical response and what adjustments need to be made to incorporate them into the numerical framework. During my research I have extended the preexisting code by the corresponding material models. The thesis itself covers two main topics, which are related to these extensions.

As a first topic, I consider the so-called hydrodynamic material model for conduction electrons, with which I describe plasmonic nanostructures. Previous works on the hydrodynamic model have proven to be successful in this field [16–19]. Moreover, there have been extensive studies by Moeferdt and Prohm within my own research group [20, 21]. Based on their works, I introduce a new approach, namely a perturbative approach, to the hydrodynamic model [H1]. We will see that this offers some interesting results, which are unique to my approach.

The second topic covers the modelling Raman-active dielectrics. Though some work in this regard has been done within the finite difference time-domain method by Groojian et al. and Varin [22], I have not seen a three-dimensional implementation for the DGTD method, yet. So far, I have only found the fairly recent publication by the applied mathematicians Bokil et al. [23], where the Raman scattering is treated in a one-dimensional DGTD framework.

The common ground on both of these topics is the perturbative treatment of the electromagnetic fields within the DGTD method, which allows a clean distinction between linear and nonlinear optical effects.

Outline

I dedicate chapter 1 to the basic concepts of linear optics, including the fundamentals of classical electrodynamics. I further take a brief look at light-matter interaction in the limit of classical electromagnetic fields.

Proceeding from the considerations on linear optics, I present some essentials to nonlinear optics in chapter 2, which form the theoretical basis of later discussions. In particular, I explain the concepts of wave mixing and Raman scattering.

In chapter 3 I outline the numerical DGTD method used in this thesis. It is based on the work of Hesthaven and Warburton [24], who adjusted the general DGTD scheme to solve Maxwell's equations. We will see that one key element of the scheme is the concept of the numerical flux. Accordingly, I show how to derive this numerical flux as it is needed to incorporate material models into the DGTD scheme correctly. Furthermore, a few modification need to be made with regards to nonlinear problems.

In chapter 4 I examine the hydrodynamic material model for plasmonic nanostructures. In particular, I first review the hydrodynamic model in terms of the Landau-Silin theory of Fermi liquids [25]. I then proceed to introduce the perturbative approach to the model and discuss the needed adjustment for the DGTD method subsequently. Lastly, I use the modified DGTD code to calculate the second-order nonlinear response from plasmonic structures. More specifically, I study the wave-mixing phenomena of SHG and sum-frequency generation (SFG) from silver nanoantennas. In this context, I show how to optimize the efficiency of the nonlinear response.

In chapter 5 I deal with Raman-active dielectrics. For this, I derive the corresponding nonlinear response at optical frequencies based on the work of Hellwarth [26]. The resulting material equations are then modified to fit the framework of the DGTD method. We will see that in this case a set of auxiliary differential equations needs to be implemented. Finally, I demonstrate the workings of the material model in combination with the DGTD scheme.

Contents

CHAPTER 1

General remarks on light-matter interaction

In this chapter we present some fundamental statements on classical electrodynamics and light-matter interaction. We equip the reader with the necessary tools to understand the formalisms and considerations on the optical phenomena in this thesis. Besides we give the reader the chance to become acquainted with the notation and conventions used in this thesis. As many of the topics within this chapter can be found in standard textbooks the reader might skip this chapter to read about the nonlinear optical phenomena presented within this thesis straightaway.

In section 1.1 we focus on classical electrodynamics. In particular, we introduce Maxwell's equations, both their microscopic and their macroscopic form, in section 1.1.1 as they are the foundation to the description of optical phenomena. In section 1.1.2 we present the electromagnetic boundary conditions at interfaces between two different materials, which are associated to Maxwell's equations. Under the consideration of these boundary conditions we show how to calculate the scattering and absorption cross section from the electromagnetic fields for a setup with a single scatterer excited by an external light source. Going forward we use the resulting cross section formulas to create the nonlinear spectra of the nonlinear materials presented in this thesis. In section 1.1.4 we comment on the electromagnetic potentials and gauges that are commonly applied to the electromagnetic potentials. In this context we show a special gauge, the Barron-Gray gauge, in section 1.2, which enables us to describe the light-matter interaction in the limit of a classical homogeneous electromagnetic field in a simple way. This light-matter interaction description will proof useful in our depiction of Raman-active materials in chapter 5, notably, as the assumptions made within section 1.2 are coherent with the assumptions made in section 5.1.1.

1.1 Classical electrodynamics

Our goal is to describe optical phenomena in a classical manner. In particular, we view the occuring electromagnetic fields as classical. Therefore, we present some elements of classical electrodynamics that are fundamental to our description of the optical effects shown in this thesis.

1.1.1 Maxwell's equations

In 1864 J.C. Maxwell published a paper on "A Dynamical Theory of the Electromagnetic Field" [2] giving the fundamental mathematical description of light as an electromagnetic phenomenon. The outcome of this description is known today as *Maxwell's equations*. The modern form of Maxwell's equations was derived by Heaviside in 1893 [27]. Herein, he introduced symbolic vector calculus to achieve an elegant, more lucid form of Maxwell's equations, which can be found in most standard textbooks on electrodynamics like [28–31].

Maxwell's equations describe the behaviour of the electromagnetic light field passing through a medium. We first state Maxwell's equations for a very simple medium - individual microscopic charges with charge surrounded by vacuum. The individual charges can be described by the microscopic charge density ϱ_{mic} and the current density $\mathbf{j}_{\mathrm{mic}}$. Maxwell's equations now relate the electric field $\mathbf{e}(\mathbf{r},t)$ and the magnetic field $\mathbf{b}(\mathbf{r},t)$ to each other and, notably, to the charge density $\varrho_{\mathrm{mic}}(\mathbf{r},t)$ and the current density $\mathbf{j}_{\mathrm{mic}}(\mathbf{r},t)$ by

$$\nabla \cdot \mathbf{e}(\mathbf{r},t) = \frac{1}{\varepsilon_0}\,\varrho_{\mathrm{mic}}(\mathbf{r},t) \tag{1.1}$$

$$\nabla \cdot \mathbf{b}(\mathbf{r},t) = 0 \tag{1.2}$$

$$\nabla \times \mathbf{e}(\mathbf{r},t) = -\partial_t\,\mathbf{b}(\mathbf{r},t) \tag{1.3}$$

$$\nabla \times \mathbf{b}(\mathbf{r},t) = \mu_0\,\mathbf{j}_{\mathrm{mic}}(\mathbf{r},t) + \mu_0\,\varepsilon_0\,\partial_t\,\mathbf{e}(\mathbf{r},t). \tag{1.4}$$

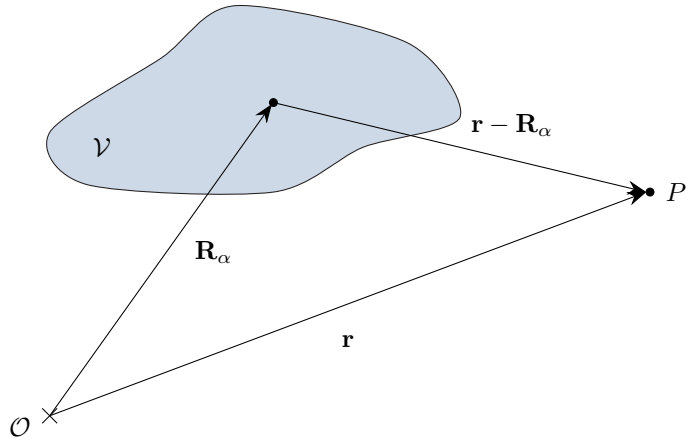

Figure 1.1: Schematic depiction of a finite charge distribution in a volume $\mathcal{V}$, where the individual charge positions are represented by the vector $\mathbf{R}_\alpha$. The electric and magnetic field are measured at point P.

(1.1) to (1.4) are referred to as microscopic Maxwell equations and are valid universally. Nevertheless, they are often not practical because the microscopic charge density and the current density are commonly unknown and not even accessible experimentally, as every (macroscopic) measurement only provides mean values over space and time. Usual media contain a huge number of particles ($\sim 10^{23}$ particles per 1 cm^3). Hence, it makes sense to describe a medium by its macroscopic, i.e. time- and space-averaged, charge density $\varrho(\mathbf{r}, t)$ and current density $\mathbf{J}(\mathbf{r}, t)$. One can consider these quantities as a result of a phenomenological averaging process of the microscopic charge density and the current density, respectively. For example, one can take the average over all individual charge positions $\mathbf{R}_\alpha$

$$\varrho(\mathbf{r}, t) = \frac{1}{v(\mathbf{r})} \int\limits_{v(\mathbf{r})} \mathrm{d}^3 R_\alpha \; \varrho_{\mathrm{mic}}\left(\mathbf{R}_\alpha, t\right) \tag{1.5a}$$

$$\mathbf{B}(\mathbf{r}, t) = \frac{1}{v(\mathbf{r})} \int\limits_{v(\mathbf{r})} \mathrm{d}^3 R_\alpha \; \mathbf{j}_{\mathrm{mic}}\left(\mathbf{R}_\alpha, t\right) \tag{1.5b}$$

within a microscopically large, but macroscopically small spherical volume $v(\mathbf{r})$ with center point $\mathbf{r}$ to obtain the macroscopic value (see fig. 1.1), if the medium is sufficiently dense. Both, the macroscopic charge density and the current density are then measured by a test charge at the position $\mathbf{r}$. One is then interested in the macroscopic electric and magnetic field, which underly the same phenomenological averaging process as in (1.5a) and (1.5b)

$$\mathbf{E}(\mathbf{r}, t) = \frac{1}{v(\mathbf{r})} \int\limits_{v(\mathbf{r})} \mathrm{d}^3 R_\alpha \; \mathbf{e}\left(\mathbf{R}_\alpha, t\right) \tag{1.6a}$$

$$\mathbf{B}(\mathbf{r}, t) = \frac{1}{v(\mathbf{r})} \int\limits_{v(\mathbf{r})} \mathrm{d}^3 R_\alpha \; \mathbf{b}\left(\mathbf{R}_\alpha, t\right) \tag{1.6b}$$

The macroscopic equivalent to (1.1) to (1.4) then reads[1]

Maxwell's equations

$$\nabla \cdot \mathbf{E}(\mathbf{r}, t) = \frac{1}{\varepsilon_0} \varrho(\mathbf{r}, t) \tag{1.7}$$

$$\nabla \cdot \mathbf{B}(\mathbf{r}, t) = 0 \tag{1.8}$$

$$\nabla \times \mathbf{E}(\mathbf{r}, t) = -\partial_t \mathbf{B}(\mathbf{r}, t) \tag{1.9}$$

$$\nabla \times \mathbf{B}(\mathbf{r}, t) = \mu_0 \, \mathbf{J}(\mathbf{r}, t) + \mu_0 \, \varepsilon_0 \, \partial_t \mathbf{E}(\mathbf{r}, t). \tag{1.10}$$

[1] We have, therein assumed that the phenomenological averaging commutes with the spatial gradient and the time derivative, respectively

We refer to this set of equations as Maxwell's equations with macroscopic fields or simply Maxwell's equations. We will see later in sections 1.2 and 5.1.1 that classical phenomena are well described by the macroscopic field quantities. In particular, if the wavelength of the electromagnetic field is much larger than any atomic separation length ($\sim 1\,\text{Å}$) within the medium, the electric field as well as the magnetic field can be viewed as homogeneous across any atomic distance and it suffices to describe the electromagnetic field classically according to (1.7) to (1.10). The macroscopic Maxwell equations express the behaviour of light passing a medium. Yet, to formulate the whole problem one also needs to model the mediums response to the electromagnetic field. This is done by constructing a set of material equations. One possible way is to give a set of partial differential equations for the charge and current density under the premise that the charges are preserved within a close system. Thus, the *continuity equation*

$$\partial_t \, \varrho(\mathbf{r}, t) + \nabla \cdot \mathbf{J}(\mathbf{r}, t) = \mathbf{0} \tag{1.11}$$

needs to be fulfilled at all times. One example for this is given in section 4.1 for the hydrodynamic model. Another way of incorporating material properties is by introducing two auxiliary fields, the *electric polarization* $\mathbf{P}$ and the *magnetic polarization* $\mathbf{M}$. The electric polarization is caused by a displacement of charges within the material due to the electric field. Hence, the electric polarization and the electric field are related to each other by the *electric response function* $\underline{\boldsymbol{\chi}}$. For linear, non-dispersive materials the relation is simply given by

$$\mathbf{P}(\mathbf{r}, t) = \varepsilon_0 \, \underline{\boldsymbol{\chi}}(\mathbf{r}) \cdot \mathbf{E}(\mathbf{r}, t). \tag{1.12}$$

We will get to know a more complex relation between the polarization and the electric field for nonlinear, dispersive materials within the nonlinear response theory in section 2.1. In contrast, the magnetic polarization is caused by ring currents due to presence of a magnetic field. Thereby, the magnetic polarization is related to the magnetic field via the *magnetic response function*[2] $\underline{\boldsymbol{\chi}}_\text{m}$. For linear, non-dispersive materials the relation simply reads

$$\mathbf{M}(\mathbf{r}, t) = \mu_0 \, \underline{\boldsymbol{\chi}}_\text{m}(\mathbf{r}) \cdot \mathbf{B}(\mathbf{r}, t) \tag{1.13}$$

In order to introduce the electric and magnetic polarization into Maxwell's equations (1.7) to (1.10) one distinguishes between bound and free excess charges within the medium. If we denote the bound charge density by ϱ_bound and the free charge density by ϱ_free, one can express the total charge density by their sum

$$\varrho(\mathbf{r}, t) = \varrho_\text{bound}(\mathbf{r}, t) + \varrho_\text{free}(\mathbf{r}, t). \tag{1.14}$$

[2] Throughout this thesis we will only consider electromagnetic fields with frequencies in the optical regime (400–700 THz, [32]). In natural materials the magnetic response diminishes at frequencies lower than a few Gigahertz [30, 33]. Hence, we will not observe any magnetic effects as the magnetic response of conventional materials is too slow to follow the fastly oscillation magnetic field. Accordingly, no ring currents are formed and we can neglect the magnetic polarization $\mathbf{M} \approx 0$ in following chapters.

Accordingly, the current density can be split into a contribution originating from the bound charges $\mathbf{J}_{\text{bound}}$ and one originating from the free excess charges $\mathbf{J}_{\text{free}}$, which resutls in

$$\mathbf{J}(\mathbf{r},t) = \mathbf{J}_{\text{bound}}(\mathbf{r},t) + \mathbf{J}_{\text{free}}(\mathbf{r},t) \tag{1.15}$$

for the total current density. One then relates the bound charge and current density to the electric and magnetic polarization: The bound current density has a contribution that is caused by the temporal change in electric polarization

$$\mathbf{J}_{\text{P}}(\mathbf{r},t) = \partial_t \mathbf{P}(\mathbf{r},t) \tag{1.16}$$

and another contribution that stems from the formation of ring currents due to the magnetic polarization

$$\mathbf{J}_{\text{M}}(\mathbf{r},t) = \nabla \times \mathbf{M}(\mathbf{r},t). \tag{1.17}$$

The total bound current density can then be expressed by the sum of the two contributions (1.16) and (1.17)

$$\mathbf{J}_{\text{bound}}(\mathbf{r},t) = \mathbf{J}_{\text{P}}(\mathbf{r},t) + \mathbf{J}_{\text{M}}(\mathbf{r},t) = \partial_t \mathbf{P}(\mathbf{r},t) + \nabla \times \mathbf{M}(\mathbf{r},t). \tag{1.18}$$

In addition, one can relate the polarization to the bound charge density by using the continuity equation (1.11) for the bound charges

$$\partial_t \varrho_{\text{bound}}(\mathbf{r},t) + \nabla \cdot \mathbf{J}_{\text{bound}}(\mathbf{r},t) = 0. \tag{1.19}$$

By inserting the bound charge density (1.18) into (1.19) one obtains that the bound charge density is solely evoked by the polarization

$$\varrho_{\text{bound}}(\mathbf{r},t) = -\nabla \cdot \mathbf{P}(\mathbf{r},t), \tag{1.20}$$

where we have used $\nabla \cdot (\nabla \times \mathbf{M}) = 0$. This is due to the fact that there are no magnetic charges, which is consistent with Maxwell's divergence equation for the magnetic field (1.8).

By inserting (1.15) into (1.10) while using the expression (1.18) yields a modified version of Maxwell's curl equation for the magnetic field

$$\nabla \times \left[\frac{1}{\mu_0} \mathbf{B}(\mathbf{r},t) - \mathbf{M}(\mathbf{r},t) \right] = \mathbf{J}_{\text{free}}(\mathbf{r},t) + \partial_t \left[\varepsilon_0 \mathbf{E}(\mathbf{r},t) + \mathbf{P}(\mathbf{r},t) \right], \tag{1.21}$$

where we have the electric and magnetic polarization instead of the bound current density. We refer to (1.21) as the free source Maxwell curl equation for the magnetic field[3]. In a similar manner the divergence equation for the electric field (1.7) can be modified. For this, we insert (1.14) into (1.7) and use (1.20), which yields the modified version of Maxwell's divergence

[3]Commonly, two additional auxiliary fields are introduced at this point, the magentic field strength

$$\mathbf{H}(\mathbf{r},t) = \frac{1}{\mu_0} \mathbf{B}(\mathbf{r},t) - \mathbf{M}(\mathbf{r},t) \tag{1.22}$$

equation for the electric field

$$\nabla \cdot \left[\varepsilon_0 \, \mathbf{E}(\mathbf{r}, t) + \mathbf{P}(\mathbf{r}, t)\right] = \varrho_{\text{free}}(\mathbf{r}, t) \tag{1.24}$$

after some rearrangement. We refer to (1.24) as the free source Maxwell divergence equation for the electric field. Because in the free source Maxwell equations (1.21) and (1.24) the medium's information is absorbed in the electric and magnetic polarization we now need to supplement the modified set of Maxwell's equations (1.8), (1.9), (1.21) and (1.24) with the material equations for the electric and magnetic polarization instead of the charge and current density. One example, where the material information is given in terms of the electric polarization, is the material model for non-magnetic Raman-active materials according to section 5.1.

1.1.2 Electromagnetic boundary conditions

Usually, we do not consider an infinitley extended material but rather a material confined within certain boundaries. For example, if we have a particle with a certain geometry sitting in a contrasting material, the problem is not fully described by Maxwell's equations (1.7) to (1.10) and a supplementary set of material equations. In addition, one needs boundary conditions, which determine the behaviour of the macroscopic fields at the interface between the particle and its surrounding. In the following we determine the boundary conditions for the electric and magnetic field at the interface between two different materials denoted by 1 and 2. Note, however, that in addition one needs to choose appropriate boundary conditions for the material quantities, e.g. the the charge and current density, which are specific to the material model at hand. This is done, for instance, for the hydrodynamic material model in section 4.4. We, first, focus on the boundary condition for the normal component of the electric and magnetic field, respectively. Therefore, we imagine a closed pillbox volume V at the interface with the basis area F along the tangential plane of the interface and height h (see fig. 1.2). To explore the behaviour of the normal component of the electric field we integrate Maxwell's divergence equation for the electric field (1.7) over the pillbox volume

$$\int_V \mathrm{d}^3 r \; \nabla \cdot \mathbf{E}(\mathbf{r}, t) = \frac{1}{\varepsilon_0} \int_V \mathrm{d}^3 r \; \varrho(\mathbf{r}, t). \tag{1.25}$$

In the limit of an infinitesimally small pillbox height ($h \to 0$) the integral on the r.h.s. of (1.25) is equivalent to the charge q_{surf} at the surface

$$\lim_{h \to 0} \int_V \mathrm{d}^3 r \; \varrho(\mathbf{r}, t) = q_{\text{surf}}. \tag{1.26}$$

---

and the dielectric displacement

$$\mathbf{D}(\mathbf{r}, t) = \varepsilon_0 \, \mathbf{E}(\mathbf{r}, t) + \mathbf{P}(\mathbf{r}, t), \tag{1.23}$$

which lead to a version of Maxwell's equations often referred to as Maxwell's equations in matter [28, 29]. We abstain from the introduction of these auxiliary fields as we want to describe the electromagnetic field by the electric field $\mathbf{E}$ and $\mathbf{B}$ instead.

We then calculate the l.h.s of (1.25) in the limit of $h \to 0$ by using Gauß's theorem [31]

$$\lim_{h\to 0} \int_V \mathrm{d}^3 r \; \nabla \cdot \mathbf{E}(\mathbf{r}, t) \overset{\text{Gauß's theorem}}{=} \lim_{h\to 0} \int_{\partial V} \mathrm{d}^2 r \; \breve{\mathbf{n}} \cdot \mathbf{E}(\mathbf{r}, t) = F \; \breve{\mathbf{n}} \cdot (\mathbf{E}_2 - \mathbf{E}_1) \tag{1.27}$$

where the face normal $\breve{\mathbf{n}}$ of the interface and the directional area $\mathbf{F}$ are given according to fig. 1.2. Furthermore, $\mathbf{E}_1$ denotes the limit of the electric field at the interface coming from material 1 and $\mathbf{E}_2$ denotes the limit of the electric field at the interface coming from material 2. Then from (1.26) and (1.27) it follows that the normal component of the electric field has a jump discontinuity across the interface of two different materials according to

$$\breve{\mathbf{n}} \cdot (\mathbf{E}_2 - \mathbf{E}_1) = \frac{q_{\text{surf}}}{\varepsilon_0 \, F}. \tag{1.28}$$

Following the same argumentation line as for the normal component of the electric field one finds the boundary condition for the normal component of the magnetic field. We, hence, integrate Maxwell's divergence equation of the magnetic field (1.8) over the pillbox volume V

$$\int_V \mathrm{d}^3 r \; \nabla \cdot \mathbf{B}(\mathbf{r}, t) = 0. \tag{1.29}$$

Using Gauß's theorem the l.h.s. of (1.29) becomes

$$\lim_{h\to 0} \int_V \nabla \cdot \mathbf{B}(\mathbf{r}, t) \overset{\text{Gauß's theorem}}{=} \lim_{h\to 0} \int_V \mathrm{d}^2 r \; \breve{\mathbf{n}} \cdot \mathbf{B}(\mathbf{r}, t) = F \; \breve{\mathbf{n}} \cdot (\mathbf{B}_2 - \mathbf{B}_1). \tag{1.30}$$

in the limit of $h \to 0$. Then from (1.29) and (1.30) it follows that due to the lack of magnetic charges the normal component of the magnetic field is continuous across the interface

$$\breve{\mathbf{n}} \cdot (\mathbf{B}_2 - \mathbf{B}_1) = 0. \tag{1.31}$$

So far, we have only discussed the boundary conditions for the normal component of the electric and magnetic field, respectively. To obtain the boundary conditions for the entire electric and magnetic field we, yet, need to determine the boundary conditions for the tangential

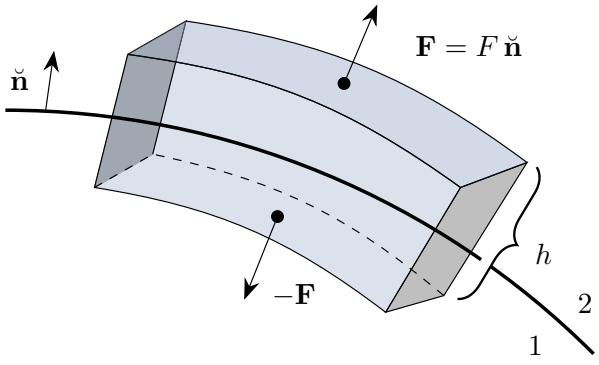

Figure 1.2: Depiction of an auxiliary volume to determine the boundary conditions for the normal component of the electric and the magnetic field at the interface of two different materials 1 and 2. Adapted from [31].

components. We, thus, imagine a two-dimensional box formed by the closed path $\mathbf{C} = \mathbf{s}_1 - \mathbf{h} + \mathbf{s}_2 + \mathbf{h}$ around an arbitrary point at the interface between material 1 and 2 (see fig. 1.3), where we require the path segments $\mathbf{s}_1$ and $\mathbf{s}_2$ to be in binormal direction with respect to the interface tangential $\breve{\mathbf{t}}$ and the interface normal $\breve{\mathbf{n}}$. Accordingly, $\mathbf{s}_1$ and $\mathbf{s}_2$ have the same lengths, yielding $\mathbf{s}_1 = -\mathbf{s}_2 \equiv s\,(\breve{\mathbf{t}} \times \breve{\mathbf{n}})$. Furthermore, the path $\mathbf{C}$ encloses the directional area $\mathbf{F}$, where the face normal of $\mathbf{F}$ is equivalent to the interface's tangential. We, therefore, have $\mathbf{F} \equiv F\,\breve{\mathbf{t}}$. We now integrate Maxwell's curl equation for the electric field (1.9) over the area F

$$\int_F \mathrm{d}\mathbf{f} \cdot [\nabla \times \mathbf{E}(\mathbf{r}, t)] = \int_F \mathrm{d}\mathbf{f} \cdot [\partial_t \mathbf{B}(\mathbf{r}, t)] \tag{1.32}$$

In the limit of an infinitesimally small box height ($h \to 0$) the integral on the r.h.s. of (1.32) vanishes identically

$$\lim_{h\to 0} \int_F \mathrm{d}\mathbf{f} \cdot [\partial_t \mathbf{B}(\mathbf{r}, t)] = 0 \tag{1.33}$$

as the partial derivative ($\partial_t\, \mathbf{B}$) is bounded at the interface. Using Stokes' theorem [31] we calculate the l.h.s. of (1.32) in the limit of $h \to 0$

$$\begin{aligned} \lim_{h\to 0} \int_F \mathrm{d}\mathbf{f} \cdot [\nabla \times \mathbf{E}(\mathbf{r}, t)] &\overset{\text{Stokes' theorem}}{=} \lim_{h\to 0} \int_C \mathrm{d}\mathbf{l} \cdot \mathbf{E}(\mathbf{r}, t) = \\ &= \mathbf{s}_1 \cdot \mathbf{E}_1 + \mathbf{s}_2 \cdot \mathbf{E}_2 = s\,(\breve{\mathbf{t}} \times \breve{\mathbf{n}}) \cdot (\mathbf{E}_2 - \mathbf{E}_1) = \\ &= s\,[\,\breve{\mathbf{n}} \times (\mathbf{E}_2 - \mathbf{E}_1)\,] \cdot \breve{\mathbf{t}}, \end{aligned} \tag{1.34}$$

where we have used the vector identity $(\mathbf{A} \times \mathbf{B}) \cdot \mathbf{C} = (\mathbf{B} \times \mathbf{C}) \cdot \mathbf{A}$ in the last line. From (1.33) and (1.34) it follows that the tangential component of the electric field is continuous across the interface, yieling

$$\breve{\mathbf{n}} \times (\mathbf{E}_2 - \mathbf{E}_1) = \mathbf{0}. \tag{1.35}$$

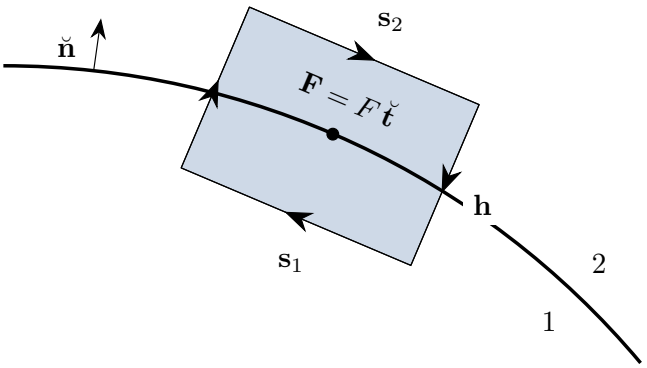

Figure 1.3: Depiction of an auxiliary area to determine the boundary conditions for the tangential components of the electric and magnetic field at the interface of two different materials 1 and 2. Adapted from [31].

In the same manner we construct the boundary condition for the tangential component of the magnetic field strength. By integrating (1.10) over the area A one finds

$$\int_A \mathrm{d}\mathbf{f} \cdot [\nabla \times \mathbf{B}(\mathbf{r},t)] = \mu_0 \int_A \mathrm{d}\mathbf{f} \cdot \mathbf{J}(\mathbf{r},t) + \mu_0\, \varepsilon_0 \int_A \mathrm{d}\mathbf{f} \cdot \partial_t\, \mathbf{E}(\mathbf{r},t). \tag{1.36}$$

Since the temporal derivative of the electric field ($\partial_t\, \mathbf{E}$) is bounded at the surface the second integral on the r.h.s. of (1.36) vanishes identically in the limit of $h \to 0$

$$\lim_{h\to 0} \int_A \mathrm{d}\mathbf{f} \cdot \partial_t\, \mathbf{E}(\mathbf{r},t) = 0. \tag{1.37}$$

Therefore, only the surface integral of the current density remains on the r.h.s. of (1.36). For $h \to 0$ this yields

$$\lim_{h\to 0} \int_A \mathrm{d}\mathbf{f} \cdot \mathbf{J}(\mathbf{r},t) = I_{\mathrm{surf}}, \tag{1.38}$$

where I_{surf} is the electric current at the interface. Finally, in the limit of $h \to 0$ the surface integral on the l.h.s. of (1.36) yields

$$\lim_{h\to 0} \int_A \mathrm{d}\mathbf{f} \cdot [\nabla \times \mathbf{B}(\mathbf{r},t)] \overset{\text{Stokes' theorem}}{=} \lim_{h\to 0} \int_C \mathrm{d}\mathbf{s} \cdot \mathbf{B}(\mathbf{r},t) = s\, [\breve{\mathbf{n}} \times (\mathbf{B}_2 - \mathbf{B}_1)] \cdot \breve{\mathbf{t}}. \tag{1.39}$$

Hence, combining (1.36) to (1.39) it follows that the tangential component of the magnetic field is discontinuous at the interface, where the jump discontinuity is determined by

$$\breve{\mathbf{n}} \times (\mathbf{B}_2 - \mathbf{B}_1) = \frac{\mu_0\, I_{\mathrm{surf}}}{s}\, \breve{\mathbf{t}}. \tag{1.40}$$

Note, that according to (1.21) for non-magnetic materials ($\mathbf{M} = \mathbf{0}$) the surface current can only stem from the free excess charges at the surface because $\lim_{h\to 0} \int_A \mathrm{d}\mathbf{f} \cdot \partial_t\, \mathbf{P} = \mathbf{0}$ as long as ($\partial_t\, \mathbf{P}$) is bounded at the interface. Thus, if there are no excess charges, the tangential component of the magnetic field is smooth at the interface between two different non-magnetic materials.

We summarize the boundary conditions for the electric and magnetic field at the interface of two different materials 1 and 2 by

Electromagnetic boundary conditions

$$\breve{\mathbf{n}} \cdot (\mathbf{E}_2 - \mathbf{E}_1) = \frac{q_{\mathrm{surf}}}{\varepsilon_0\, F} \tag{1.28}$$

$$\breve{\mathbf{n}} \cdot (\mathbf{B}_2 - \mathbf{B}_1) = 0 \tag{1.31}$$

$$\breve{\mathbf{n}} \times (\mathbf{E}_2 - \mathbf{E}_1) = \mathbf{0} \tag{1.35}$$

$$\breve{\mathbf{n}} \times (\mathbf{B}_2 - \mathbf{B}_1) = \frac{\mu_0\, I_{\mathrm{surf}}}{s}\, \breve{\mathbf{t}}. \tag{1.40}$$

1.1.3 Poynting's theorem and scattering cross section

Sometimes one is interested in the energy flow across a surface; in particular, if the goal is to determine the scattering or absorption cross section of a scattering setup (see fig. 1.4). In the following we calculate the energy flow based on the principle that energy shall be conserved in a closed system. For this we consider an arbitrary finite charge distribution $\varrho(\mathbf{r},t)$ within ai finite volume V. If the charge distribution is exposed to an electromagnetic field, then the electromagnetic *Lorentz force* acts on the charges [28–30]. The density of the Lorentz force is given by

$$\mathbf{f}(\mathbf{r},t) = \varrho(\mathbf{r},t)\left[\,\mathbf{E}(\mathbf{r},t) + \mathbf{v}(\mathbf{r},t)\times\mathbf{B}(\mathbf{r},t)\,\right], \tag{1.41}$$

where $\mathbf{v}(\mathbf{r},t)$ denotes the velocity field of each individual charge. Thus, the associated work density done on the charges by the Lorentz force along a differential path $\mathrm{d}\mathbf{s} = \mathbf{v}\,\mathrm{d}t$ is given by

$$\mathrm{d}u(\mathbf{r},t) = \mathbf{f}(\mathbf{r},t)\cdot\mathbf{v}(\mathbf{r},t)\,\mathrm{d}t. \tag{1.42}$$

The current density is related to the charge density and the charge velocity field by

$$\mathbf{J}(\mathbf{r},t) = \varrho(\mathbf{r},t)\,\mathbf{v}(\mathbf{r},t). \tag{1.43}$$

Therefore, using (1.41) and (1.43) the power density is calculated by

$$\partial_t\, u(\mathbf{r},t) = \mathbf{J}(\mathbf{r},t)\cdot\mathbf{E}(\mathbf{r},t), \tag{1.44}$$

where we have used $\mathbf{v}\cdot(\mathbf{v}\times\mathbf{B}) = 0$ in arriving at (1.44). The power density (1.44) is known as *Joule heating* and is caused merely by the charge displacement for non-magnetic materials. It is formed as the power of the electromagnetic field is converted into the kinetic energy of the charges within the volume V. This kinetic energy then results in particle collisions and, thus, heating. If we replace the current density in (1.44) using Maxwell's curl equation for the magnetic field (1.10), the electromagnetic power density can be expressed by

$$\partial_t\, u(\mathbf{r},t) \;=\; \frac{1}{\mu_0}\,\mathbf{E}(\mathbf{r},t)\cdot[\nabla\times\mathbf{B}(\mathbf{r},t)] - \varepsilon_0\,\mathbf{E}(\mathbf{r},t)\cdot\partial_t\,\mathbf{E}(\mathbf{r},t). \tag{1.45}$$

We then apply the identity

$$\begin{aligned}\mathbf{E}(\mathbf{r},t)\cdot[\nabla\times\mathbf{B}(\mathbf{r},t)] &= -\,\nabla\cdot[\,\mathbf{E}(\mathbf{r},t)\times\mathbf{B}(\mathbf{r},t)\,] + \mathbf{B}\cdot[\,\nabla\times\mathbf{E}(\mathbf{r},t)\,] = \\ &\overset{(1.9)}{=} -\,\nabla\cdot[\,\mathbf{E}(\mathbf{r},t)\times\mathbf{B}(\mathbf{r},t)\,] - \mathbf{B}(\mathbf{r},t)\cdot\partial_t\,\mathbf{B}(\mathbf{r},t)\end{aligned} \tag{1.46}$$

to (1.45), which yields

$$\partial_t\, u(\mathbf{r},t) = -\frac{1}{\mu_0}\,\nabla\cdot[\mathbf{E}(\mathbf{r},t)\times\mathbf{B}(\mathbf{r},t)] - \frac{1}{\mu_0}\,\mathbf{B}(\mathbf{r},t)\cdot\partial_t\,\mathbf{B}(\mathbf{r},t) - \varepsilon_0\,\mathbf{E}(\mathbf{r},t)\cdot\partial_t\,\mathbf{E}(\mathbf{r},t). \tag{1.47}$$

It is often useful to define

$$u_0(\mathbf{r},t) = \frac{1}{2}\left[\frac{1}{\mu_0}\,\mathbf{B}(\mathbf{r},t)\cdot\mathbf{B}(\mathbf{r},t) + \varepsilon_0\,\mathbf{E}(\mathbf{r},t)\cdot\mathbf{E}(\mathbf{r},t)\right], \tag{1.48}$$

which can be interpreted as the energy density in vacuum, and the *Poynting vector* [28] for non-magnetic materials

$$\mathbf{S}(\mathbf{r},t) = \frac{1}{\mu_0}\,\mathbf{E}(\mathbf{r},t)\times\mathbf{B}(\mathbf{r},t). \tag{1.49}$$

Then using the definitions (1.48) and (1.49) it follows that for non-magnetic materials the power density can be expressed by

Poynting's theorem

$$\partial_t\, u(\mathbf{r},t) = -\left[\nabla\cdot\mathbf{S}(\mathbf{r},t) + \partial_t\, u_0(\mathbf{r},t)\right]. \tag{1.50}$$

Equation (1.50) is known as Poynting's or work-energy theorem [28–31]. Its integral form is given by

$$\int_V \mathrm{d}^3r\;\partial_t\,\underbrace{\left[u(\mathbf{r},t)+u_0(\mathbf{r},t)\right]}_{\equiv u_{\mathrm{tot}}(\mathbf{r},t)} = -\int_V \mathrm{d}^3r\;\nabla\cdot\mathbf{S}(\mathbf{r},t), \tag{1.51}$$

where we have defined the total energy density of the electromagnetic field u_{tot}. The integral on the l.h.s. of (1.51) represents the electromagnetic power. We denote this power by $\mathcal{P}$. Using Gauß's theorem we can express the r.h.s. of (1.51) by

$$\mathcal{P} \equiv -\int_V \mathrm{d}^3r\;\nabla\cdot\mathbf{S}(\mathbf{r},t) \overset{\text{Gauß's theorem}}{=} -\int_{\partial V} \mathrm{d}^2r\;\breve{\mathbf{n}}(\mathbf{r})\cdot\mathbf{S}(\mathbf{r},t), \tag{1.52}$$

where $\breve{\mathbf{n}}$ denotes the volume's outward pointing surface normal (cf. fig. 1.4) and the sign is due to convention[4]. Hence, the energy per unit time, which flows through the surface ∂V, can be calculated by (1.52).

In the following we calculate the energy flux for a typical scattering setup consisting of an arbitrarily shaped particle denoted by index 1 surrounded by a non-absorbing, non-magnetic medium denoted by index 2. We now imagine a spherical surface ∂V within the non-absorbing medium enclosing the particle (see fig. 1.4). The system is exposed to an external electromagnetic field $(\mathbf{E}_{\mathrm{inc}},\mathbf{B}_{\mathrm{inc}})$, which penetrates the spherical volume and is then attenuated by the particle. This attenuation, known as *extinction* of the electromagnetic field, is caused by

[4] Because the normal of the volume's surface shall point towards the outside of the volume $\breve{\mathbf{n}}\cdot\mathbf{S}$ indicates energy leaving the volume and is, thus, chosen to be negative in our notation. In reverse for $-\breve{\mathbf{n}}\cdot\mathbf{S}$ energy is absorbed within the volume and is, hence, positive. Therefore, $\mathcal{P}>0$ indicates power absorbed within the volume.

scattering and absorption of electromagnetic energy. Because the surrounding medium is non-absorbing, energy can only be absorbed within the particle. Therefore, the absorbed energy rate according to (1.52) is merely related to the electromagnetic field within the particle $(\mathbf{E}_1, \mathbf{B}_1)$

$$\begin{aligned}\mathcal{P}_1 \equiv \mathcal{P}_{\text{abs}} &= -\int\limits_{\partial V} \mathrm{d}^2 r\ \breve{\mathbf{n}}(\mathbf{r}) \cdot \mathbf{S}_1(\mathbf{r},t) \overset{(1.49)}{=} -\frac{1}{\mu_0} \int\limits_{\partial V} \mathrm{d}^2 r\ \breve{\mathbf{n}}(\mathbf{r}) \cdot [\mathbf{E}_1(\mathbf{r},t) \times \mathbf{B}_1(\mathbf{r},t)] = \\ &= -\frac{1}{\mu_0} \int\limits_{\partial V} \mathrm{d}^2 r\ \mathbf{B}_1(\mathbf{r},t) \cdot [\,\breve{\mathbf{n}}(\mathbf{r}) \times \mathbf{E}_1(\mathbf{r},t)\,], \end{aligned} \tag{1.53}$$

where we have used the vector identity $\mathbf{A} \cdot (\mathbf{B} \times \mathbf{C}) = \mathbf{C} \cdot (\mathbf{A} \times \mathbf{B}) = \mathbf{B} \cdot (\mathbf{C} \times \mathbf{A})$ in the last line of (1.53). Because the tangential component of the electric field is continuous at the particle's surface according to (1.35), i.e. $\breve{\mathbf{n}} \times \mathbf{E}_1 = \breve{\mathbf{n}} \times \mathbf{E}_2$, we can express (1.53) by

$$\mathcal{P}_{\text{abs}} = -\frac{1}{\mu_0} \int\limits_{\partial V} \mathrm{d}^2 r\ \mathbf{B}_1(\mathbf{r},t) \cdot [\,\breve{\mathbf{n}}(\mathbf{r}) \times \mathbf{E}_2(\mathbf{r},t)\,]$$

Again applying the vector identity from above we obtain

$$\mathcal{P}_{\text{abs}} = -\frac{1}{\mu_0} \int\limits_{\partial V} \mathrm{d}^2 r\ \mathbf{E}_2(\mathbf{r},t) \cdot [\,\mathbf{B}_1(\mathbf{r},t) \times \breve{\mathbf{n}}(\mathbf{r})\,]$$

If we assume that there is no electric current due to excess charges at the particle's surface, then according to (1.40) the tangential component of the magnetic field is continuous at the interface between the particle and the surrounding medium, i.e. $\breve{\mathbf{n}} \times \mathbf{B}_1 = \breve{\mathbf{n}} \times \mathbf{B}_2$, yielding

$$\mathcal{P}_{\text{abs}} = -\frac{1}{\mu_0} \int\limits_{\partial V} \mathrm{d}^2 r\ \mathbf{E}_2(\mathbf{r},t) \cdot [\,\mathbf{B}_2(\mathbf{r},t) \times \breve{\mathbf{n}}(\mathbf{r})\,] =$$

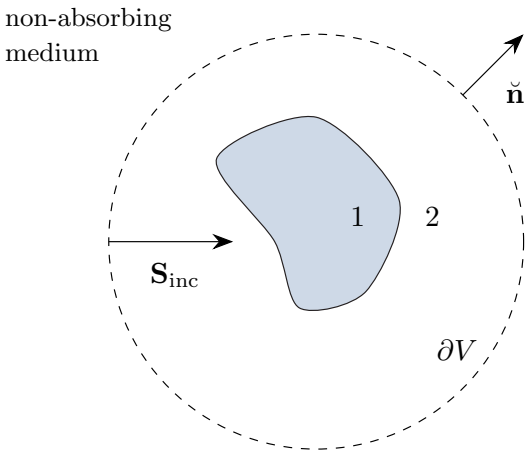

Figure 1.4: Scheme of a scattering setup: We consider a volume V enclosing a particle (blue) surrounded by a non-absorbing medium. The particle scatters the incoming electromagnetic field with Poynting flux $\mathbf{S} = \mathbf{S}(\mathbf{r},t)$. The scattered field leaves the volume through the surface ∂V, which is represented by its face normal $\breve{\mathbf{n}} = \breve{\mathbf{n}}(\mathbf{r})$.

$$= -\frac{1}{\mu_0} \int\limits_{\partial V} \mathrm{d}^2 r \; \breve{\mathbf{n}}(\mathbf{r}) \cdot [\, \mathbf{E}_2(\mathbf{r},t) \times \mathbf{B}_2(\mathbf{r},t) \,] = \mathcal{P}_2. \tag{1.54}$$

From (1.54) it follows that the power absorbed by the particle is equivalent to the power outside of the particle. We analyze this power a little further. The electromagnetic field contained in the surrounding medium is composed of the incident and the scattered field $(\mathbf{E}_2, \mathbf{H}_2) = (\mathbf{E}_{\mathrm{inc}} + \mathbf{E}_{\mathrm{scat}}, \mathbf{B}_{\mathrm{inc}} + \mathbf{B}_{\mathrm{scat}})$, which leads to the energy rate

$$\begin{aligned} \mathcal{P}_2 &= -\int\limits_{\partial V} \mathrm{d}^2 r \; \breve{\mathbf{n}}(\mathbf{r}) \cdot \mathbf{S}_2(\mathbf{r},t) = \\ &= -\int\limits_{\partial V} \mathrm{d}^2 r \; \breve{\mathbf{n}}(\mathbf{r}) \cdot [\, \mathbf{S}_{\mathrm{inc}}(\mathbf{r},t) + \mathbf{S}_{\mathrm{scat}}(\mathbf{r},t) + \mathbf{S}_{\mathrm{ext}}(\mathbf{r},t) \,] \end{aligned} \tag{1.55}$$

where we have defined the Poynting vector of the incident field

$$\mathbf{S}_{\mathrm{inc}}(\mathbf{r},t) = \frac{1}{\mu_0} \, \mathbf{E}_{\mathrm{inc}}(\mathbf{r},t) \times \mathbf{B}_{\mathrm{inc}}(\mathbf{r},t) \tag{1.56}$$

the scattered field

$$\mathbf{S}_{\mathrm{scat}}(\mathbf{r},t) = \frac{1}{\mu_0} \, \mathbf{E}_{\mathrm{scat}}(\mathbf{r},t) \times \mathbf{B}_{\mathrm{scat}}(\mathbf{r},t) \tag{1.57}$$

and the extinction

$$\mathbf{S}_{\mathrm{ext}}(\mathbf{r},t) = \frac{1}{\mu_0} \left[\mathbf{E}_{\mathrm{inc}}(\mathbf{r},t) \times \mathbf{B}_{\mathrm{scat}}(\mathbf{r},t) + \mathbf{E}_{\mathrm{scat}}(\mathbf{r},t) \times \mathbf{B}_{\mathrm{inc}}(\mathbf{r},t) \right]. \tag{1.58}$$

The extinction (1.58) mediates the coupling between the scattered and incident field. Accordingly, we define the energy rates

$$\mathcal{P}_{\mathrm{inc}} \equiv -\int\limits_{\partial V} \mathrm{d}^2 r \; \breve{\mathbf{n}}(\mathbf{r}) \cdot \mathbf{S}_{\mathrm{inc}}(\mathbf{r},t) \tag{1.59}$$

$$\mathcal{P}_{\mathrm{scat}} \equiv \int\limits_{\partial V} \mathrm{d}^2 r \; \breve{\mathbf{n}}(\mathbf{r}) \cdot \mathbf{S}_{\mathrm{scat}}(\mathbf{r},t) \tag{1.60}$$

$$\mathcal{P}_{\mathrm{ext}} \equiv -\int\limits_{\partial V} \mathrm{d}^2 r \; \breve{\mathbf{n}}(\mathbf{r}) \cdot \mathbf{S}_{\mathrm{ext}}(\mathbf{r},t) \tag{1.61}$$

where we have chosen the positive sign for the scattering energy rate to indicate scattering out of the sphere. It is worth mentioning that the energy rate of the incident wave $\mathcal{P}_{\mathrm{inc}}$ vanishes identically whenever the source is external to the considered volume. In this case we get

$$\mathcal{P}_{\mathrm{ext}} = \mathcal{P}_{\mathrm{abs}} + \mathcal{P}_{\mathrm{scat}} \tag{1.62}$$

from (1.54), (1.55), (1.60) and (1.61) One is often interested in how much of the electromagnetic energy is scattered or absorbed at a certain frequency. To this end we define the time-averaged Poynting vector

$$\boldsymbol{\sigma}(\omega) \equiv \left\langle \mathbf{S}_{\text{mono}}(\mathbf{r},t) \right\rangle_t = \lim_{\tau\to\infty} \frac{1}{\tau} \int_0^\tau \mathrm{d}t\; \mathbf{S}_{\text{mono}}(\mathbf{r},t) = \frac{1}{2\,\mu_0} \operatorname{Re}\left[\tilde{\mathbf{E}}_0(\mathbf{r},\omega) \times \tilde{\mathbf{B}}_0^*(\mathbf{r},\omega) \right] \tag{1.63}$$

of a *monochromatic wave*

$$\Big(\mathbf{E}(\mathbf{r},t),\, \mathbf{B}(\mathbf{r},t) \Big) = \Big(\tilde{\mathbf{E}}_0(\mathbf{r},\omega)\, \mathrm{e}^{-\mathrm{i}\omega t} + c.c.\,,\, \tilde{\mathbf{B}}_0(\mathbf{r},\omega)\, \mathrm{e}^{-\mathrm{i}\omega t} + c.c. \Big)\,. \tag{1.64}$$

Then the time-averaged power at a certain frequency is given by

$$\bar{\mathcal{P}}(\omega) = -\int_{\partial V} \mathrm{d}^2 r\; \breve{\mathbf{n}}(\mathbf{r}) \cdot \boldsymbol{\sigma}(\omega). \tag{1.65}$$

Because the resulting time-averaged power is still dependent on the amplitude of the incident wave, we normalize it with respect to the irradiance at each frequency $|\boldsymbol{\sigma}_{\text{inc}}(\omega)|$. As a result we obtain quantities, with which we can characterize the extinction, scattering or absorption properties of a material. These quantities are known as cross sections $C(\omega) = \frac{\bar{\mathcal{P}}(\omega)}{|\boldsymbol{\sigma}_{\text{inc}}(\omega)|}$. From (1.62) we get the balance equation of the cross sections

$$C_{\text{ext}}(\omega) = C_{\text{abs}}(\omega) + C_{\text{scat}}(\omega) \tag{1.66}$$

where we have introduced the *scattering cross section*

Scattering cross section

$$C_{\text{scat}} = \frac{\bar{\mathcal{P}}_{\text{scat}}(\omega)}{|\boldsymbol{\sigma}_{\text{inc}}(\omega)|} = \frac{1}{|\boldsymbol{\sigma}_{\text{inc}}(\omega)|} \int_{\partial V} \mathrm{d}^2 r\; \breve{\mathbf{n}}(\mathbf{r}) \cdot \boldsymbol{\sigma}_{\text{scat}}(\omega). \tag{1.67}$$

and the *absorption cross section*

Absorption cross section

$$C_{\text{abs}}(\omega) = \frac{\bar{\mathcal{P}}_{\text{abs}}(\omega)}{|\boldsymbol{\sigma}_{\text{inc}}(\omega)|} = -\frac{1}{|\boldsymbol{\sigma}_{\text{inc}}(\omega)|} \int_{\partial V} \mathrm{d}^2 r\; \breve{\mathbf{n}}(\mathbf{r}) \cdot \left[\, \boldsymbol{\sigma}_{\text{scat}}(\omega) + \boldsymbol{\sigma}_{\text{ext}}(\omega) \,\right], \tag{1.68}$$

which constitute the *extinction cross section* C_{ext}.

1.1.4 Electromagnetic potentials

In some cases it is more convenient to transform Maxwell's equations (1.7) to (1.10) in a way that the four first-order partial differential equations become a set of two second-order partial

differential equations. For this one introduces the so-called electromagnetic potentials, namely the scalar potential $\Phi(\mathbf{r},t)$ and the vector potential $\mathbf{A}(\mathbf{r},t)$, which relate to the electric and magnetic field. We, hence construct

$$\mathbf{B}(\mathbf{r},t) = \nabla \times \mathbf{A}(\mathbf{r},t) \tag{1.69}$$

so that Maxwell's divergence equation for the magnetic field (1.8) is fulfilled by definition. By inserting (1.69) into Maxwell's curl equation for the electric field (1.9) one arrives at the Ansatz

$$\mathbf{E}(\mathbf{r},t) = -\nabla\,\Phi(\mathbf{r},t) - \partial_t\,\mathbf{A}(\mathbf{r},t) \tag{1.70}$$

where the sign in front of the scalar potential is chosen due to convention. By inserting the expresseions (1.69) and (1.70) for the electric and magnetic field, respectively, into the Maxwell equations (1.7) and (1.10) one finds the second-order partial differential equations

$$\Delta\,\Phi(\mathbf{r},t) + \partial_t\,[\nabla\cdot\mathbf{A}(\mathbf{r},t)] = -\frac{1}{\varepsilon_0}\varrho(\mathbf{r},t) \tag{1.71}$$

and

$$\Big[\Delta\, - \varepsilon_0\,\mu_0\,\partial_t^2\,\Big]\mathbf{A}(\mathbf{r},t) - \nabla\Big[\nabla\cdot\mathbf{A}(\mathbf{r},t) + \varepsilon_0\,\mu_0\,\partial_t\,\Phi(\mathbf{r},t)\Big] = -\mu_0\,\mathbf{J}(\mathbf{r},t). \tag{1.72}$$

Note that the scalar and the vector potentials defined in (1.69) and (1.70) are not unique. Hence, we can transform the scalar potential by

$$\Phi'(\mathbf{r},t) = \Phi(\mathbf{r},t) - \partial_t\,\chi(\mathbf{r},t) \tag{1.73}$$

and the vector potential

$$\mathbf{A}'(\mathbf{r},t) = \mathbf{A}(\mathbf{r},t) + \nabla\,\chi(\mathbf{r},t) \tag{1.74}$$

where $\chi(\mathbf{r},t)$ is an arbitrary scalar field, leaving the electric field and magnetic field unchanged. Thus, the set of second-order parital differential equations (1.71) and (1.72) also remain unchanged by these transformations. The scalar potential χ is referred to as *gauge potential*. The particular choice of this gauge potential results in a specific gauge transformation. Two common gauge transformations are the *Coulomb gauge*, where χ is chosen in a way so that

$$\nabla\cdot\mathbf{A}(\mathbf{r},t) = 0. \tag{1.75}$$

can always be fulfilled, and the *Lorenz gauge*[5], where χ is chosen so that

$$\nabla\cdot\mathbf{A}(\mathbf{r},t) + \varepsilon_0\,\mu_0\,\partial_t\,\Phi(\mathbf{r},t) = 0. \tag{1.76}$$

[5]Note that the gauge is named after the Danish physicist and mathematician Ludvig Lorenz, whereas the name Lorentz condition stems from the fact that the Lorenz gauge is Lorentz invariant. The term Lorentz invariance is named after the Dutch physicist Hendrik Lorentz who developed the concept of Lorentz covariance.[34]

can always be fulfilled [31, 35]. For more information see appendix A.2.

Note that the previous considerations in this subsection can be generalized for the microscopic fields $\{\mathbf{e}, \mathbf{b}, \varrho_{\text{mic}}, \mathbf{j}_{\text{mic}}\}$ w.l.o.g., where we have the microscopic scalar potential $\phi(\mathbf{r}, t)$ and the macroscopic vector potential $\mathbf{a}(\mathbf{r}, t)$. We use the microscopic version of the representation of the electric and magnetic field by the scalar and vector potential (1.69) and (1.70) to introduce a new type of gauge fixing, the Barron-Gray gauge [36], in section 1.2. It will proof useful in terms of a perturbative description of light-matter interaction.

1.2 Semi-classical light-matter interaction

In the previous section section 1.1 we have considered light-matter interaction only in the limit of classical electrodynamics. In particular, the electromagnetic field is seen as classical. As we are going to examine the optical properties of nano-particles in this thesis we need to discuss under which circumstances a classical description of the electromagnetic field is justified. For this we again consider a microscopic finite charge distribution within a volume V, where the position of each charge q_α with mass m_α is denoted by $\mathbf{R}_\alpha$. We shall decompose these positions into a macroscopic position $\mathbf{r}$ at the center of mass of the finite charge distribution and a microscopic position $\mathbf{r}_\alpha$, which shall be representative of each charge (see fig. 1.5), i.e. $\mathbf{R}_\alpha = \mathbf{r} + \mathbf{r}_\alpha$. We assume that the changes of the macroscopic position $\mathbf{r}$ to take place on a much larger time scale than the ones of the individual positions $\mathbf{r}_\alpha$. Therefore, if we picture a microscopic time scale, the position $\mathbf{r}$ can be regarded as constant. When exposed to an external electromagnetic field the Lorentz force

$$\mathbf{F}(\mathbf{r}, t) = \sum_{\alpha=1}^{N} \mathbf{f}_\alpha(\mathbf{r} + \mathbf{r}_\alpha, t) = \sum_{\alpha=1}^{N} q_\alpha \left[\mathbf{e}(\mathbf{r} + \mathbf{r}_\alpha, t) + \dot{\mathbf{r}}_\alpha \times \mathbf{b}(\mathbf{r} + \mathbf{r}_\alpha, t)\right] \tag{1.77}$$

will act on the charges where the microscopic force $\mathbf{f}_\alpha$ acts on each of the N charges denoted by the index α. From the Lorentz force (1.77) one can derive the corresponding potential. Then from the potential and the kinetic energy of the charges one can calculates the quantum mechanical Hamiltonian yieling[6]

$$\hat{H} = \sum_{\alpha=1}^{N} \left\{ \frac{1}{2m_\alpha} \left[\hat{\mathbf{p}}_\alpha - q_\alpha \, \hat{\mathbf{a}}(\mathbf{r} + \hat{\mathbf{r}}_\alpha, t)\right]^2 + q_\alpha \, \hat{\phi}\,(\mathbf{r} + \hat{\mathbf{r}}_\alpha, t) \right\}. \tag{1.78}$$

Note that in the subspace of the individual charges the individual positions $\hat{\mathbf{r}}_\alpha$ as well as the their momentum $\hat{\mathbf{p}}_\alpha$ are operators as opposed to the macroscopic position $\mathbf{r}$. Accordingly, the microscopic scalar potential $\hat{\phi}$ and vector potential $\hat{\mathbf{a}}$ are also operators. The representation of the microscopic electric and magnetic field in terms the microscopic scalar and vector potential are given by

$$\hat{\mathbf{b}}(\mathbf{r} + \hat{\mathbf{r}}_\alpha, t) = \nabla_{\hat{\mathbf{r}}_\alpha} \times \hat{\mathbf{a}}(\mathbf{r} + \hat{\mathbf{r}}_\alpha, t) \tag{1.79}$$

[6] For the full derivation of the Hamiltonian (1.78) see appendix A.4 or [37].

and

$$\hat{\mathbf{e}}(\mathbf{r}+\hat{\mathbf{r}}_\alpha,t) = \nabla_{\hat{\mathbf{r}}_\alpha}\,\hat{\phi}\,(\mathbf{r}+\hat{\mathbf{r}}_\alpha,t) - \partial_t\,\hat{\mathbf{a}}(\mathbf{r}+\hat{\mathbf{r}}_\alpha,t) \tag{1.80}$$

in analogy to (1.69) and (1.70). We then separate the Hamiltonian (1.78) into free particle (kinetic) and light-matter interaction operators

$$\hat{H} = \sum_{\alpha=1}^{N}\left(\hat{H}_{0,\alpha} + \hat{V}_\alpha\right) \tag{1.81}$$

where we have defined the one-particle operator

$$\hat{H}_{0,\alpha} = \frac{\hat{\mathbf{p}}_\alpha^2}{2m_\alpha} \tag{1.82}$$

and the interaction operator

$$\begin{aligned}\hat{V}_\alpha(\mathbf{r}+\mathbf{r}_\alpha,t) = &-\frac{q_\alpha}{2m_\alpha}\left[\hat{\mathbf{p}}_\alpha\cdot\hat{\mathbf{a}}(\mathbf{r}+\hat{\mathbf{r}}_\alpha,t) + \hat{\mathbf{a}}(\mathbf{r}+\hat{\mathbf{r}}_\alpha,t)\cdot\hat{\mathbf{p}}_\alpha\right] + \\ &+\frac{q_\alpha^2}{2m_\alpha}\left[\hat{\mathbf{a}}(\mathbf{r}+\hat{\mathbf{r}}_\alpha,t)\right]^2 + q_\alpha\,\hat{\phi}\,(\mathbf{r}+\hat{\mathbf{r}}_\alpha,t).\end{aligned} \tag{1.83}$$

As an exact solution to the problem described by the full light-matter Hamiltonian (1.81) is often too complicated or even impossible to obtain we approximate the interaction operator (1.83) by a truncated Taylor series. Therefore, we need to find adequate approximations to the microscopic scalar and vector potential in (1.83). As a starting point we use the Taylor expansions of the microscopic electric and magnetic field

$$\begin{aligned}\hat{\mathbf{e}}(\mathbf{r}+\hat{\mathbf{r}}_\alpha,t) = \mathbf{e}(\mathbf{r},t) &+ \sum_{i=1}^{3}\hat{x}_{i,\alpha}\left[\frac{\partial}{\partial\hat{x}_{i,\alpha}}\,\hat{\mathbf{e}}(\mathbf{r}+\hat{\mathbf{r}}_\alpha,t)\right]_{\hat{\mathbf{r}}_\alpha=\mathbf{0}} + \\ &+\sum_{i,j=1}^{3}\hat{x}_{i,\alpha}\,\hat{x}_{j,\alpha}\left[\frac{\partial^2}{\partial\hat{x}_{i,\alpha}\partial\hat{x}_{j,\alpha}}\,\hat{\mathbf{e}}(\mathbf{r}+\hat{\mathbf{r}}_\alpha,t)\right]_{\hat{\mathbf{r}}_\alpha=\mathbf{0}} + \ldots\end{aligned} \tag{1.84}$$

$$\begin{aligned}\hat{\mathbf{b}}(\mathbf{r}+\hat{\mathbf{r}}_\alpha,t) = \mathbf{b}(\mathbf{r},t) &+ \sum_{i=1}^{3}\hat{x}_{i,\alpha}\left[\frac{\partial}{\partial\hat{x}_{i,\alpha}}\,\hat{\mathbf{b}}(\mathbf{r}+\hat{\mathbf{r}}_\alpha,t)\right]_{\hat{\mathbf{r}}_\alpha=\mathbf{0}} + \\ &+\sum_{i,j=1}^{3}\hat{x}_{i,\alpha}\,\hat{x}_{j,\alpha}\left[\frac{\partial^2}{\partial\hat{x}_{i,\alpha}\partial\hat{x}_{j,\alpha}}\,\hat{\mathbf{b}}(\mathbf{r}+\hat{\mathbf{r}}_\alpha,t)\right]_{\hat{\mathbf{r}}_\alpha=\mathbf{0}} + \ldots\end{aligned} \tag{1.85}$$

around the macroscopic position $\mathbf{r}$, respectively, where we require $\hat{\mathbf{r}}_\alpha \ll \mathbf{r}$. The Taylor expansions (1.84) and (1.85) are also referred to as *multipole expansions* [36, 38]. From (1.84)

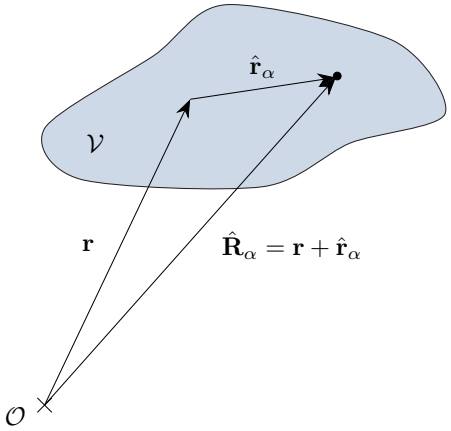

Figure 1.5: Schematic depiction of a finite charge distribution with volume $\mathcal{V}$, where the individual charge positions are represented by the vector $\hat{\mathbf{R}}_\alpha = \mathbf{r} + \hat{\mathbf{r}}_\alpha$. We assume the position $\mathbf{r}$ macroscopic compared to the microscopic position $\hat{\mathbf{r}}_\alpha$. Furthermore, we consider that the positions $\mathbf{r}$ vary on a much larger time scale than $\hat{\mathbf{r}}_\alpha$.

and (1.85) one constructs the scalar potential

$$\begin{aligned}\hat{\phi}\left(\mathbf{r}+\hat{\mathbf{r}}_\alpha,t\right) &= \phi\left(\mathbf{r},t\right) - \sum_{i=1}^{3} \hat{x}_{i,\alpha}\, e_i(\mathbf{r}+\hat{\mathbf{r}}_\alpha,t) - \frac{1}{2}\sum_{i,j=1}^{3} \hat{x}_{i,\alpha}\hat{x}_{j,\alpha}\left[\frac{\partial}{\partial \hat{x}_{j,\alpha}}\ \hat{e}_i(\mathbf{r}+\hat{\mathbf{r}}_\alpha,t)\right]_{\hat{\mathbf{r}}_\alpha=\mathbf{0}} - \\ &\quad - \frac{1}{6}\sum_{i,j,k=1}^{3} \hat{x}_{i,\alpha}\,\hat{x}_{j,\alpha}\,\hat{x}_{k,\alpha}\left[\frac{\partial^2}{\partial \hat{x}_{k,\alpha}\partial \hat{x}_{j,\alpha}}\ \hat{e}_i(\mathbf{r}+\hat{\mathbf{r}}_\alpha,t)\right]_{\hat{\mathbf{r}}_\alpha=\mathbf{0}} - \dots \\ &= \phi(\mathbf{r},t) - \sum_{n=0}^{\infty} \frac{1}{(n+1)!}\ \hat{\mathbf{r}}_\alpha\cdot(\hat{\mathbf{r}}_\alpha\cdot\nabla)^n\ \mathbf{e}(\mathbf{r},t)\end{aligned} \tag{1.86}$$

and the vector potential

$$\begin{aligned}\hat{\mathbf{a}}(\mathbf{r},t) &= \sum_{i,j,k=1}^{3} \epsilon_{ijk}\,\tilde{\mathbf{e}}_i \left\{\frac{1}{2}\,b_j(\mathbf{r},t) + \frac{1}{3}\sum_{l} \hat{x}_{l,\alpha}\left[\frac{\partial}{\partial \hat{x}_{l,\alpha}}\ \hat{b}_{j,\alpha}(\mathbf{r}+\hat{\mathbf{r}}_\alpha,t)\right]_{\hat{\mathbf{r}}_\alpha=\mathbf{0}} + \right. \\ &\quad \left. + \frac{1}{8}\sum_{l,m=1}^{3} \hat{x}_{l,\alpha}\,\hat{x}_{m,\alpha}\left[\frac{\partial^2}{\partial \hat{x}_{l,\alpha}\partial \hat{x}_{m,\alpha}}\,\hat{b}_{j,\alpha}(\mathbf{r}+\hat{\mathbf{r}}_\alpha,t)\right]_{\hat{\mathbf{r}}=\mathbf{0}} + \dots \right\} \hat{x}_{k,\alpha} \\ &= \sum_{n=0}^{\infty} \frac{1}{(2n+1)\cdot n!}\ \hat{\mathbf{r}}_\alpha\times(\hat{\mathbf{r}}_\alpha\cdot\nabla)^n\ \mathbf{b}(\mathbf{r},t)\end{aligned} \tag{1.87}$$

in accordance with (1.79) and (1.80). Note that the scalar potential (1.86) and the vector potential (1.87) neither fulfill the Coulomb gauge (1.75) nor the Lorentz gauge (1.76) but rather define an independent underlying gauge themselves. This gauge is known as the Barron-Gray gauge [36, 38]. By inserting the expression for the scalar potential (1.86) and the expression

for the vector potential (1.87) into (1.83) one obtains the light-matter interaction operator

$$\hat{V}_\alpha(\mathbf{r}+\hat{\mathbf{r}}_\alpha,t) = q_\alpha\,\phi(\mathbf{r},t) - q_\alpha\,\hat{\mathbf{r}}_\alpha\cdot\mathbf{e}(\mathbf{r},t) - \frac{q_\alpha}{2}\sum_{i,j=1}^{3}\hat{x}_{i,\alpha}\,\hat{x}_{j,\alpha}\,\left[\frac{\partial}{\partial\hat{x}_{j,\alpha}}\,e_i(\mathbf{r}+\hat{\mathbf{r}}_\alpha,t)\right]_{\hat{\mathbf{r}}_\alpha=\mathbf{0}} - \\ - \frac{q_\alpha}{2m_\alpha}\,\mathbf{b}(\mathbf{r},t)\,(\hat{\mathbf{r}}_\alpha\times\hat{\mathbf{p}}_\alpha) + \frac{q_\alpha^2}{8m_\alpha}\left[\mathbf{b}^2(\mathbf{r},t)\,\hat{\mathbf{r}}_\alpha^2 - \big(\mathbf{b}(\mathbf{r},t)\cdot\hat{\mathbf{r}}_\alpha\big)^2\right] + \dots \tag{1.88}$$

in the limit of $|\mathbf{r}| \gg |\hat{\mathbf{r}}_\alpha|$. As we are interested in photonic applications where the introduced optical field's wavelength (commonly 100 nm to 1 mm) is much larger than any microscopic length scale within the regarded nano-materials, i.e. any atomic distance ($\sim 1\,\text{Å}$), the electric and magnetic field can be seen as homogeneous throughout the material. Therefore, the microscopic electromagnetic fields $\mathbf{e}(\mathbf{r},t)$ and $\mathbf{b}(\mathbf{r},t)$ can be replaced by their macroscopic (classical) equivalents $\mathbf{E}(\mathbf{r},t)$ and $\mathbf{B}(\mathbf{r},t)$. Furthermore, we can truncate the series (1.88) after the first order. Hence, for a neutral material where $\phi(\mathbf{r},t)=0$ the light-matter interaction can modeled by the electric dipole interaction operator

Electric dipole interaction operator

$$\hat{V}_{\text{dipole}}(\mathbf{r},t) = -\hat{\mathbf{d}}\cdot\mathbf{E}(\mathbf{r},t) \tag{1.89}$$

where $\hat{\mathbf{d}}$ is defined as the electric dipole moment operator

$$\hat{\mathbf{d}} = \sum_{\alpha=1}^{N} q_\alpha\,\hat{\mathbf{r}}_\alpha. \tag{1.90}$$

and the electic field is purely classical for $|\hat{\mathbf{r}}_\alpha| \ll |\mathbf{r}|$.

CHAPTER 2

Nonlinear optics

So far, we have only considered linear materials, where the polarization is proportional to the electric field (cf. (1.12)). This relation no longer holds if the applied electromagnetic field is sufficiently strong. In this case the material's response becomes nonlinear and the polarization can be described by a power series of the electric field. Moreover, the electric field and the polarization are connected by a nonlinear response function. A useful tool in calculation this response function is the nonlinear response theory, which we present in section 2.1. The resulting nonlinear response function then possesses certain symmetry properties, which are discussed in section 2.2. One can then use the response function to describe nonlinear optical phenomena. Usually one distinguishes between two types of nonlinear optical effects; the resonant effects, which are related to a real energy transition within the material, and the non-resonant effects, which are not necessarily connected to a real energy transition. Optical phenomena that are in the latter category are wave-mixing effects. These are discussed in section 2.3.1 for second-order nonlinearities. An example for resonant phenomena is Raman scattering, which is introduced briefly in section 2.3.2. We will return later to the two nonlinear phenomena of wave-mixing and Raman scattering, respectively, when discussing nonlinear material models such as the hydrodynamic material model in chapter 4 and the Raman-active material model in chapter 5. In both cases, the result of the nonlinear response theory in section 2.1 (more specifically the nonlinear polarization) will proof useful.

2.1 Nonlinear response theory

A useful tool in describing nonlinear phenomena is given by the nonlinear response theory [39–41]. A very general form will be illustrated in the following. Suppose we have a generic Hamiltonian composed of an unperturbed time-independent Hamiltonian $\hat{H}_0$ and a time-dependent perturbation $\hat{V}(t)$, i.e.

$$\hat{H}(t) = \hat{H}_0 + \hat{V}(t), \tag{2.1}$$

where the perturbation operator is assumed to be of the form

$$\hat{V}(t) = -\int \mathrm{d}^3 r \; \hat{\mathbf{A}}(\mathbf{r}) \cdot \mathbf{a}(\mathbf{r}, t). \tag{2.2}$$

The minus sign in (2.2) is due to convention [42]. Furthermore, $\mathbf{a}(\mathbf{r}, t)$ is an external macroscopic field, which couples linearly to a position-dependent observable $\hat{\mathbf{A}}(\mathbf{r})$. The goal is now to obtain the response of the system due to the time-dependent perturbation, i.e. the expectation value of an arbitrary observable. For example, we want to determine the polarization of a material, which is caused by a time-dependent external electromagnetic field. There are several ways to calculate the expectation value [43–45]. We choose the density matrix formalism [45–47], where we perform our calculations in the interaction picture (Dirac representation) due to the nature of the given Hamiltonian (2.1). The density matrix's equation of motion (*von-Neumann equation*) in Dirac representation is given by

$$\mathrm{i}\hbar \partial_t \, \hat{\varrho}^{(\mathrm{D})}(t) = \left[\hat{V}^{(\mathrm{D})}(t), \hat{\varrho}^{(\mathrm{D})}(t) \right]_- , \tag{2.3}$$

where any arbitrary operator $\hat{\mathcal{O}}$ in Dirac representation is defined as

$$\hat{\mathcal{O}}^{(\mathrm{D})}(t) = \hat{U}_0^\dagger(t) \; \hat{\mathcal{O}} \; \hat{U}_0(t). \tag{2.4}$$

Thereby, $\hat{U}_0(t)$ denotes the time-evolution operator of the unperturbed system from a point in time $t_0 = 0$ to a later point in time t

$$\hat{U}_0(t) = \exp\left[-\frac{\mathrm{i}}{\hbar} \hat{H}_0 \, t \right]. \tag{2.5}$$

Accordingly, the interaction operator of (2.3) in Dirac representation can be expressed by

$$\hat{V}^{(\mathrm{D})}(t) = -\int \mathrm{d}^3 r \; \hat{\mathbf{A}}^{(\mathrm{D})}(\mathbf{r}, t) \cdot \mathbf{a}(\mathbf{r}, t). \tag{2.6}$$

If we assume that the external fields are not yet switched on at the initial time $t_i = -\infty$, i.e. $\mathbf{a}(\mathbf{r}, -\infty) = \mathbf{0}$, and suppose that the system is in thermal equilibrium at that time, we can write

the steady-state density operator as[1]

$$\hat{\varrho}_0 \equiv \hat{\varrho}(-\infty) = \frac{\mathrm{e}^{-\beta\hat{H}_0}}{\mathrm{Tr}\left\{\mathrm{e}^{-\beta\hat{H}_0}\right\}}, \tag{2.7}$$

where we have used $\beta = 1/(k_B T)$. Hence, (2.7) generates the Stefan-Boltzmann distribution [48]. By integrating and recursively inserting (2.3) under the initial condition (2.7) one obtains the *Dyson series*

$$\hat{\varrho}^{(\mathrm{D})}(t) = \hat{\varrho}_0 + \frac{1}{\mathrm{i}\hbar}\int_{-\infty}^{t} \mathrm{d}t_1 \left[\hat{V}^{(\mathrm{D})}(t_1), \hat{\varrho}_0\right]_- + \left(\frac{1}{\mathrm{i}\hbar}\right)^2 \int_{-\infty}^{t} \mathrm{d}t_1 \int_{-\infty}^{t_1} \mathrm{d}t_2 \left[\hat{V}^{(\mathrm{D})}(t_1), \left[\hat{V}^{(\mathrm{D})}(t_2), \hat{\varrho}_0\right]_-\right]_- + \dots \ . \tag{2.8}$$

The series converges as long as the perturbation is small, i.e. $\hat{V} \ll \hat{H}_0$. To give an estimate, the atomic electric field strength, i.e. the electric field at an atomic distance ($\sim 0.5\,\text{Å}$) to a proton, has a value of $E_{\mathrm{at}} \approx 5.14 \cdot 10^{11}\,\mathrm{V/m}$. This translates into a power density of about $\mathcal{P}_{\mathrm{at}} \approx 7.10 \cdot 10^{16}\,\mathrm{W/cm^2}$ of a plane wave traveling through free space. However, severe irreversible damage is done to most materials at power densities well below $10^{11}\,\mathrm{W/cm^2}$ [26]. Therefore, the applied external electric field needs to be much smaller than the atomic electric field and the perturbative treatment of is justified.

Using (2.8) one can now calculate the expectation value of an arbitrary observable $\hat{\mathbf{B}}(\mathbf{r}, t)$

$$\left\langle \hat{B}_i(\mathbf{r}, t) \right\rangle = \mathrm{Tr}\left\{\hat{B}_i^{(\mathrm{D})}(\mathbf{r}, t)\hat{\varrho}^{(\mathrm{D})}(t)\right\} = \tilde{B}_i^{(0)}(\mathbf{r}, t) + \sum_{n=1}^{\infty} \tilde{B}_i^{(n)}(\mathbf{r}, t), \tag{2.9}$$

for each vector component $i = \{1, 2, 3\}$. Thereby, the zeroth order expectation value is given by

$$\tilde{B}_i^{(0)}(\mathbf{r}, t) = \mathrm{Tr}\left\{\hat{B}_i(\mathbf{r}, t)\,\hat{\varrho}_0\right\}, \tag{2.10}$$

whereas the n-th order expectation value ($n > 0$) reads

$$\begin{aligned} \tilde{B}_i^{(n)}(\mathbf{r}, t) = \sum_{j_1=1}^{3}\sum_{j_2=1}^{3}\cdots\sum_{j_n=1}^{3} \int \mathrm{d}^3 r_1 \int \mathrm{d}^3 r_2 \ \dots \int \mathrm{d}^3 r_n \int \mathrm{d}t_1 \int \mathrm{d}t_2 \dots \int \mathrm{d}t_n \\ \mathcal{R}^{(n)}_{i,j_1,j_2,\dots,j_n}(\mathbf{r}, \mathbf{r}_1, \dots \mathbf{r}_n, t, t_1, t_2, \dots, t_n)\cdot \\ \cdot a_{j_1}(\mathbf{r}_1, t_1)\, a_{j_2}(\mathbf{r}_2, t_2) \dots a_{j_n}(\mathbf{r}_n, t_n). \end{aligned} \tag{2.11}$$

[1] For more information on the steady-state problem and its solution see appendix C.2.

We call the $(n+1)$-th rank tensor $\underline{\boldsymbol{\mathcal{R}}}^{(n)}(\mathbf{r},\mathbf{r}_1,\ldots,\mathbf{r}_n,t,t_1,\ldots,t_n)$ the n-th order response function to the perturbation $\hat{V}$, where its components are given by

$$\begin{aligned}
&\mathcal{R}^{(n)}_{i,j_1,j_2,\ldots,j_n}(\mathbf{r},\mathbf{r}_1,\ldots\mathbf{r}_n,t,t_1,\ldots,t_n) = \\
&\quad = \left(-\frac{1}{\mathrm{i}\hbar}\right)^n \mathrm{Tr}\left\{\hat{B}^{(\mathrm{D})}_i(\mathbf{r},t)\left[\hat{A}^{(\mathrm{D})}_{j_1}(\mathbf{r}_1,t_1),\ldots\left[\hat{A}^{(\mathrm{D})}_{j_n}(\mathbf{r}_n,t_n),\hat{\varrho}_0\right]_-\right]_-\right\}\cdot \\
&\qquad \cdot\Theta(t-t_1)\,\Theta(t_1-t_2)\,\ldots\,\Theta(t_{n-1}-t_n) = \\
&\overset{\text{see appendix B.1}}{=} \left(-\frac{1}{\mathrm{i}\hbar}\right)^n \mathrm{Tr}\left\{\left[\ldots\left[\hat{B}^{(D)}_i(\mathbf{r},t),\hat{A}^{(\mathrm{D})}_{j_1}(\mathbf{r}_1,t_1)\right]_-,\ldots,\hat{A}^{(\mathrm{D})}_{j_n}(\mathbf{r}_n,t_n)\right]_-\hat{\varrho}_0\right\}\cdot \\
&\qquad \cdot\Theta(t-t_1)\,\Theta(t_1-t_2)\,\ldots\,\Theta(t_{n-1}-t_n).
\end{aligned} \tag{2.12}$$

Note, that (2.12) contains the Heaviside step functions $\Theta(\bullet)$ in time to ensure causality in accordance with (2.8). In principle, the relation (2.11) can be used to describe any kind of matter, such as metals, dielectrics, fluids, plasmas, molecules, atoms, etc. . Based on (2.11) one realizes that a general material will exhibit spatially nonlocal properties, meaning the response will depend not only on the position $\mathbf{r}$ but also every neighbouring positions $\mathbf{r}_1,\mathbf{r}_2,\ldots$. In the following we will refer to this spatial non-locality simply as non-locality. If the material is considered as translationally invariant in space, the response function depends on the difference on the differences $\mathbf{r}-\mathbf{r}_1,\mathbf{r}-\mathbf{r}_2,\ldots$. In this case the material is said to be homogeneous in space. Similarly, the response function depends on the time differences $t-t_1,t-t_2,\ldots$ if a material exhibits only time-invariant properties, which is true in general for any physical properties. The material is said to be homogeneous in time.

We now apply the general approach (2.9) to (2.12) to calculate the polarization of a system as a response to an external electromagnetic field. The polarization of a non-magnetic material is defined as the average electric dipole moment density

$$\mathbf{P}(\mathbf{r},t) = \frac{1}{\mathcal{V}}\left\langle\hat{\mathbf{d}}\right\rangle(\mathbf{r},t) \tag{2.13}$$

where $\mathcal{V}$ denotes a unit volume and $\hat{\mathbf{d}}$ is the dipole operator as defined in (1.90). In most cases, the light-matter interaction is well-described by the electric dipole interaction operator (1.89) (for further information see section 5.1). Hence, we assign the interaction operator (1.89) to calculate the polarization, i.e. $\hat{V}(t)\to\hat{V}_{\mathrm{dipole}}(\mathbf{r},t)$. Accordingly, the polarization can be expressed by a power series of the electric field nonlinear polarization is expressed by

$$\mathbf{P}(\mathbf{r},t) = \mathbf{P}^{(0)} + \sum_{n=1}^{\infty}\mathbf{P}^{(n)}(\mathbf{r},t) = \mathbf{P}^{(0)} + \mathbf{P}^{(1)}(\mathbf{r},t) + \mathbf{P}^{(2)}(\mathbf{r},t) + \ldots\ , \tag{2.14}$$

where the zeroth order is given by

$$\mathbf{P}^{(0)} = \frac{1}{\mathcal{V}}\,\mathrm{Tr}\left\{\hat{\mathbf{d}}\,\hat{\varrho}_0\right\}. \tag{2.15}$$

Furthermore, the first and second order of this series, and their according response functions are given by[2]

$n = 1$:

$$P_i^{(1)}(\mathbf{r},t) = \varepsilon_0 \sum_{j=1}^{3} \int \mathrm{d}t'\; \mathcal{R}_{ij}^{(1)}(t-t')\, E_j(\mathbf{r},t') \tag{2.16}$$

$$\mathcal{R}_{ij}^{(1)}(t-t') = \left(-\frac{1}{\mathrm{i}\hbar\mathcal{V}}\right) \mathrm{Tr}\left\{\left[\hat{d}_i,\, \hat{d}_j{}^{(\mathrm{D})}(t'-t)\right]_- \hat{\varrho}_0\right\} \Theta(t-t') \tag{2.17}$$

$n = 2$:

$$P_i^{(2)}(\mathbf{r},t) = \varepsilon_0 \sum_{j,k=1}^{3} \int \mathrm{d}t' \int \mathrm{d}t''\; \mathcal{R}_{ijk}^{(2)}(t-t',t-t'')\, E_j(\mathbf{r},t')\, E_k(\mathbf{r},t'') \tag{2.18}$$

$$\begin{aligned}\mathcal{R}_{ijk}^{(2)}(t-t',t-t'') = \left(-\frac{1}{\hbar^2\mathcal{V}}\right) \mathrm{Tr}\left\{\left[\left[\hat{d}_i,\, \hat{d}_j{}^{(\mathrm{D})}(t'-t)\right]_-,\, \hat{d}_k{}^{(\mathrm{D})}(t''-t)\right]_- \hat{\varrho}_0\right\} \cdot \\ \cdot\, \Theta(t-t')\,\Theta(t'-t'').\end{aligned} \tag{2.19}$$

Note, that because the electric dipole moment operator does not depend on the macroscopic position $\mathbf{r}$ the resulting material response functions (2.17) and (2.19) do not depend on space either. Furthermore, the time dependence exhibited by these response function stems from the time evolution operators but not the dipole moment operator. Hence, the material response is, by construction, homogeneous in time with respect to the current time t.

2.2 Properties of the second-order response function in dipole approximation

It might be useful to give some properties of the nonlinear response function. For simplicity we demonstrate these properties by means of the second-order response function (2.19), which generates a second-order polarization. The properties shown below can be generalized to higher orders of nonlinearity without further ado [41].

We, first, consider symmetries, which are related either to the temporal or the frequency dispersion of the response function. To this end, we introduce our notation for the Fourier transform of an arbitrary time-dependent function $f(t)$

$$\tilde{f}(\omega) = \frac{1}{2\pi} \int \mathrm{d}t\; f(t)\, \mathrm{e}^{\mathrm{i}\omega t}, \tag{2.20}$$

where ω denotes the angular frequency. Then the back transform of (2.20) is given by

$$f(t) = \int \mathrm{d}\omega\, \tilde{f}(\omega)\, \mathrm{e}^{-\mathrm{i}\omega t}. \tag{2.21}$$

[2] Note, that we have used the general relation [43] $\left\langle A^{(D)}(t) B^{(D)}(t') \right\rangle = \left\langle A B^{(D)}(t'-t) \right\rangle = \left\langle A^{(D)}(t-t') B \right\rangle$ to arrive at (2.17) and (2.19).

Due to the response function's homogeneity in time (c.f. section 2.1) the temporal Fourier transform of the second-order polarization (2.18) yields

$$\tilde{P}_i^{(2)}(\mathbf{r},\omega) = \varepsilon_0 \sum_{j,k} \int \mathrm{d}\omega' \int \mathrm{d}\omega''\; \chi_{ijk}^{(2)}\Big(-\omega;\omega',\omega''\Big)\, \tilde{E}_j(\mathbf{r},\omega')\, \tilde{E}_k(\mathbf{r},\omega'') \tag{2.22}$$

according to (2.20), where we have introduced the second-order susceptibility[3]

$$\chi_{ijk}^{(2)}(-\omega;\omega',\omega'') = \delta[\omega-(\omega'+\omega'')] \int \mathrm{d}t' \int \mathrm{d}t''\; \mathcal{R}_{ijk}^{(2)}(t',t'')\, \mathrm{e}^{\mathrm{i}(\,\omega' t' + \omega'' t'')}. \tag{2.23}$$

A material which exhibits a response relation of the form (2.22) is said to be dispersive in frequency. Since both the polarization and the electric field are measurable quantities they are real. Thus, their Fourier amplitudes obey $\mathbf{P}(\mathbf{r},-\omega) = \mathbf{P}^*(\mathbf{r},\omega)$ and $\mathbf{E}(\mathbf{r},-\omega) = \mathbf{E}^*(\mathbf{r},\omega)$, respectively, where we demand the frequencies to be real. Hence, the response function ought to be real as well yielding

$$\chi_{ijk}^{(2)}(\omega;-\omega',-\omega'') = \Big[\chi_{ijk}^{(2)}(-\omega;\omega',\omega'')\Big]^*.$$

Of course, the reality of the response function is only one property. Additionally, the response function and its according susceptibility possess certain symmetries [41, 49, 50], some of which we present in the following.

Intrinsic permutation symmetry

One symmetry, which is valid independently of the specific material or the excitation, is the *intrinsic permutation symmetry* of the nonlinear response function

$$\mathcal{R}_{ijk}^{(2)}(t-t',t-t'') = \mathcal{R}_{ikj}^{(2)}(t-t'',t-t'). \tag{2.24}$$

One can proof this property by assuming that one can split the response function into a symmetric function $\mathcal{S}_{ijk}^{(2)}$ and an anti-symmetric function $\mathcal{A}_{ijk}^{(2)}$ leading to the ansatz

$$\mathcal{R}_{ijk}^{(2)}(t-t',t-t'') = \mathcal{S}_{ijk}^{(2)}(t-t',t-t'') + \mathcal{A}_{ijk}^{(2)}(t-t',t-t'') \tag{2.25}$$

where we postulate

$$\mathcal{S}_{ijk}^{(2)}(t-t',t-t'') = \quad \mathcal{S}_{ikj}^{(2)}(t-t'',t-t') \tag{2.26}$$

and

$$\mathcal{A}_{ijk}^{(2)}(t-t',t-t'') = -\mathcal{A}_{ikj}^{(2)}(t-t'',t-t'). \tag{2.27}$$

[3] The notation for the susceptibility is chosen according to P. Butcher and D. Cotter [49] and is commonly used in the field of nonlinear optics.

Hence, the polarization (2.18) can be separated into a symmetric and an anti-symmetric part

$$P_i^{(2)}(\mathbf{r},t) = P_{i,s}^{(2)}(\mathbf{r},t) + P_{i,as}^{(2)}(\mathbf{r},t). \tag{2.28}$$

Now we only consider the anti-symmetric part of the polarization, which according to (2.18) is given by

$$\begin{aligned}
P_{i,as}^{(2)}(\mathbf{r},t) =& \varepsilon_0 \sum_{j,k=1}^{3} \int \mathrm{d}t' \int \mathrm{d}t''\ \mathcal{A}_{ijk}^{(2)}(t-t',t-t'')\, E_j(\mathbf{r},t')\, E_k(\mathbf{r},t'') \\
=& \frac{\varepsilon_0}{2} \sum_{j,k=1}^{3} \int \mathrm{d}t' \int \mathrm{d}t''\ \Big[\mathcal{A}_{ijk}^{(2)}(t-t',t-t'')\, E_j(\mathbf{r},t')\, E_k(\mathbf{r},t'') \\
&+ \underbrace{\mathcal{A}_{OKs}^{(2)}(t-t',t-t'')}_{\overset{(2.27)}{=}-\mathcal{A}_{ijk}^{(2)}(t-t'',t-t')}\, E_k(\mathbf{r},t')\, E_j(\mathbf{r},t'')\Big] \\
=& \frac{\varepsilon_0}{2} \sum_{j,k=1}^{3} \int \mathrm{d}t' \int \mathrm{d}t''\ \mathcal{A}_{ijk}^{(2)}(t-t',t-t'')\ \Big[E_j(\mathbf{r},t')\, E_k(\mathbf{r},t'') - E_k(\mathbf{r},t'')\, E_j(\mathbf{r},t')\Big] = 0
\end{aligned}$$

Thus, the total polarization equals the the symmetric polarization $P_i^{(2)} = P_{i,s}^{(2)}$ and it follows that

$$\mathcal{R}_{ijk}^{(2)}(t-t',t-t'') = \mathcal{S}_{ijk}^{(2)}(t-t',t-t''),$$

i.e. the second-order response function possesses intrinsic permutation symmetry. Accordingly, the susceptibility $\chi_{ijk}^{(2)}(-\omega;\omega',\omega'')$ is invariant under the pairwise permutation of (j,ω') and (k,ω'') leading to 2! permutations.

Overall permutation symmetry

For a non-resonant excitation of a lossless nonlinear medium the second-order response function possesses *overall permutation symmetry*, meaning that all pairs (i,ω), (j,ω') and (k,ω'') can be interchanged simultaneously, which leads to 3! permutations. Specifically, we have

$$\begin{aligned}
\chi_{ijk}^{(2)}(-\omega;\omega',\omega'') &= \chi_{jki}^{(2)}(\omega';-\omega',\omega'') \\
&= \chi_{kji}^{(2)}(\omega'';\omega',-\omega).
\end{aligned} \tag{2.29}$$

If we consider the intrinsic permutation symmetry in addition to the overall permutation symmetry (2.29) we obtain a total of 6 possible permutations. Note that overall permutation symmetry only holds in the approximation of excitations that are far-off any energetic transition within the material, where the light-matter interaction is expressed by the dipole interaction (1.89). To proof the overall permutation symmetry for lossless nonlinear media with non-resonant excitations one needs to calculate the quantum-mechanical perturbative expression

for the second-order susceptibility including phenomenological damping. As the full derivation of the susceptibility goes beyond the scope of this chapter we would like to reference [49]. The reader should also take a look at section 5.1 to get an idea how such calculation is implemented for third-order susceptibilities.

Kleinman symmetry

Suppose the frequencies of the incoming fields are much lower than the smallest resonance frequency of the material. In this case the material responds almost instantaneously to the external field and the material can be regarded as lossless. Therefore, we assume that the susceptibility is nearly independent of the frequencies of the present field. As a consequence all Cartesian indices i, j, k of the susceptibility can be permuted independently of the frequencies, i.e.

$$\begin{aligned}\chi^{(2)}_{ijk}(-\omega;\omega',\omega'') &= \chi^{(2)}_{jki}(-\omega;\omega',\omega'') = \chi^{(2)}_{kij}(-\omega;\omega',\omega'') \\ &= \chi^{(2)}_{ikj}(-\omega;\omega',\omega'') = \chi^{(2)}_{jik}(-\omega;\omega',\omega'') \\ &= \chi^{(2)}_{kji}(-\omega;\omega',\omega'')\end{aligned} \tag{2.30}$$

resulting in 3! permutations. This kind of symmetry is known as *Kleinman symmetry* [49, 50]. We will use this symmetry later to derive the nonlinear response of Raman-active materials (see section 5.1 and appendix C.1).

Spatial symmetries

So far, we have only considered symmetries with respect to the time dependence of the response function or the frequency dependence of the susceptibility. In addition, a medium can also possess spatial symmetries due to the underlying structure of the material, which will reduce the response/susceptibility tensor to a minimal set of non-zero elements [41, 50]. In the special case of the spatially independent second-order response function (2.19), one can even state that the second-order response will vanish in an infinitely stretched material: Due to the lack of spatial dependence, the response tensor shall be invariant under inversion

$$\underline{\boldsymbol{\chi}}^{(2)}(t-t',t-t'') = \Gamma\,\underline{\boldsymbol{\chi}}^{(2)}(t-t',t-t'') \tag{2.31}$$

where we have the inversion operator

$$\Gamma = \begin{pmatrix} -1 & 0 & 0 \\ 0 & -1 & 0 \\ 0 & 0 & -1 \end{pmatrix}. \tag{2.32}$$

Then each component of the response tensor is given by

$$\chi^{(2)}_{ijk}(t-t',t-t'') = \sum_{a,b,c=1}^{3} \Gamma_{ia}\,\Gamma_{jb}\,\Gamma_{kc}\,\chi^{(2)}_{abc}(t-t',t-t'') = -\chi^{(2)}_{ijk}(t-t',t-t''). \tag{2.33}$$

This can only be true, if the overall second-order response tensor vanishes. In this case second-order nonlinear processes are suppressed. However, this only holds for bulk materials, where the response function either exhibits no spatial dependence at all or only depends on the absolute values $|\mathbf{r} - \mathbf{r}'|$ and $|\mathbf{r} - \mathbf{r}''|$, i.e. centrosymmetric materials. For small particles, where the system's surface plays a significant role, second-order nonlinear effects contribute significantly to the overall nonlinear response. Furthermore, in the case of a fluid, which – if unperturbed – can be seen as homogeneous and isotropic, the spatial symmetry of the material is heavily influenced by the external electromagnetic field[51]. Hence, the situation is not as simple as for a centrosymmetric material with a fixed crystalline structure. We will see in section 4.5 how the second-order signal looks like for a small hydrodynamic particle, where the system's response is not only nonlinear but also nonlocal.

2.3 Nonlinear optical phenomena

In general one can divide nonlinear optical phenomena into two classes, non-resonant (non-dissipative) and resonant (dissipative) effects. In the case of non-resonant processes the material is exposed to an optical field that is not able to mediate a real transition from one energy state of the medium to another. Therefore, there is no change of the net energy in the medium and the material is restored to its initial state when the process is completed [49]. Thus, non-resonant optical processes are non-dissipative and any energy transitions involved in these processes are purely virtual. Examples, for non-resonant optical processes are given by *wave-mixing phenomena* and the *optical Kerr effect* [41, 49]. We are going to discuss second-order wave-mixing phenomena, also known as *three-wave mixing*, in section 2.3.1 as it is of special interest for the design of nonlinear (plasmonic) nano-antennas with frequency ranges that might not be accessible by conventional (linear) antennas. We examine two special cases of three-wave mixing, the *second-harmonic generation* and the *sum-frequency generation*, in more detail and comment on how to tune the radiation of such nonlinear nano-antennas within the frame of a *hydrodynamic material model* in chapter 4.

In contrast, in the second class of nonlinear effects, the resonant phenomena, the energy flow between optical field and material will lead to a real energy transition within the medium. Hence, direct resonant transitions can only take place if the electromagnetic field has a frequency range that corresponds to the electronic transitions of the material at ultraviolet and visible frequencies ($\sim 10^{15}\,\mathrm{Hz}$) or the vibrational (nuclear) transitions at infrared frequencies ($\sim 10^{13}\,\mathrm{Hz}$)[4] [41]. Though we are not going to study any phenomena associated with direct resonant excitations in this thesis as we only use optical frequencies that are far from any material resonance. However, we examine an indirect resonant effect, known as *Raman scattering*. It occurs if the material is exposed to two optical fields where the difference in frequency of those two light beams matches a low frequency vibrational mode of the material. We discuss the effect of Raman scattering briefly in section 2.3.2 and in more detail in chapter 5.

[4] For isolated molecules and gases one would also account for rotational modes in the infrared-microwave range ($\sim 10^{11}\,\mathrm{Hz}$).

2.3.1 Three-wave mixing

In the following we discuss a second-order nonlinear phenomenon known as *three-wave mixing*. As mentioned before, it is a non-resonant, non-dissipative phenomenon as the material does not undergo a real net change of energy and all energy transitions are purely virtual. Therefore, the material will always return to its ground state (cf. fig. 2.1). More specifically, the effect of three-wave mixing is constituted of the four nonlinear phenomena, *sum-frequency generation* (SFG), *difference-frequency generation* (DFG), the *second-harmonic generation* (SHG), and *optical rectification* (OR)[41, 50]. We explain these four processes by the means of the second-order polarization amplitude.

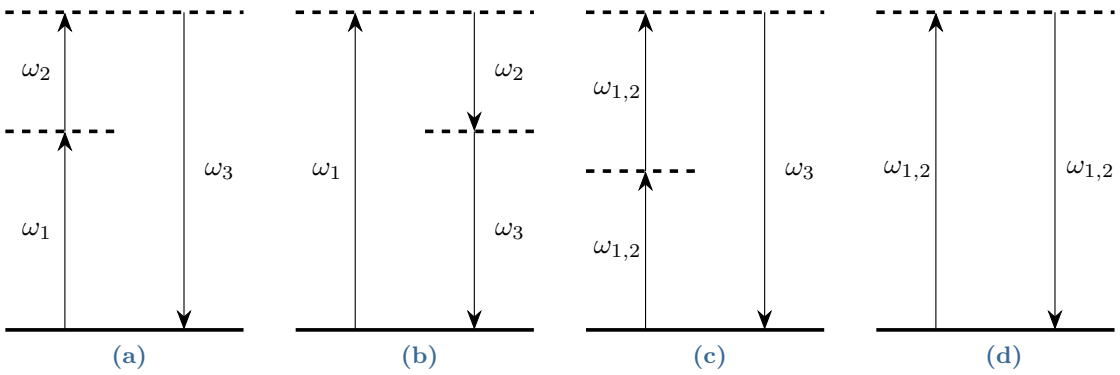

Figure 2.1: Energy level scheme for (a) sum-frequency generation (SFG), (b) difference-frequency generation (DFG), (c) second-harmonic generation (SHG) and (d) optical rectification (OR). The (real) ground state level is marked by a solid line, whereas virtual levels are depicted by dashed lines.

Imagine that the material is excited by two monochromatic electromagnetic fields with different frequencies ω_1 and ω_2, respectively, where $\omega_1 \neq \omega_2$. We call ω_1 and ω_2 the fundamental frequencies. Thus, the second-order polarization amplitude for two specific incoming frequencies, i.e. the discrete Fourier transform of (2.18), can be expressed by[5]

$$\tilde{P}_i^{(2)}(\mathbf{r},\omega) = \varepsilon_0 \sum_{j,k} \sum_{\omega'=-\omega_2}^{\omega_2} \sum_{\omega''=-\omega_2}^{\omega_2} \chi_{ijk}^{(2)}(-\omega;\omega',\omega'')\, \tilde{E}_j(\mathbf{r},\omega')\, \tilde{E}_k(\mathbf{r},\omega'') \tag{2.34}$$

where the sums over ω' and ω'' cover the discrete frequency region $\{-\omega_2, -\omega_1, \omega_1, \omega_2\}$. From (2.34) we extract the four aforementioned nonlinear processes (SFG, DFG, SHG, and OR): One

[5] For simplicity we have chosen a spatially independent expression of the nonlinear response function. As we only concentrate on frequency dependent effects in this section, the actual the material's actual spatial dependence is irrelevant.

of these processes is the second-order SFG, which is described by[6]

$$\tilde{P}_i^{(2)}(\mathbf{r},\omega_1+\omega_2) = 2\,\varepsilon_0 \sum_{j,k}\left[\chi_{ijk}^{(2)}\Big(-(\omega_1+\omega_2);\omega_1,\omega_2\Big)\,\tilde{E}_j(\mathbf{r},\omega_1)\,\tilde{E}_k(\mathbf{r},\omega_2)+\text{c.c.}\right]. \tag{2.35}$$

The SFG is depicted in the scheme fig. 2.1a. Here two incoming monochromatic electric fields at the fundamental frequencies, ω_1 and ω_2, respectively, excite the material virtually from its ground state. The system returns to its ground state by sending out a monochromatic electric field at the frequency $\omega_3 = \omega_1 + \omega_2$. As the process is purely virtual there is no energy dissipation.

Another process is the DFG illustrated in fig. 2.1b. For this we imagine that the incoming field with frequency ω_1 excites the material virtually, while the field of frequency ω_2 is present. We, furthermore, have $\omega_1 > \omega_2$. The material returns to its ground state by emitting two different fields, one at the difference frequency $\omega_3 = \omega_1 - \omega_2$ and one with the frequency ω_2. Since a field at the fundamental frequency ω_2 is already present, the two-photon process is stimulated and the fundamental field at frequency ω_2 is amplified. The nonlinear process of DFG is, therefore, also known as optical parametric amplification [50]. The polarization amplitude describing the DFG is given by

$$\tilde{P}_i^{(2)}(\mathbf{r},\omega_1-\omega_2) = 2\,\varepsilon_0 \sum_{j,k}\left[\chi_{ijk}^{(2)}\Big(-(\omega_1-\omega_2);\omega_1,-\omega_2\Big)\,\tilde{E}_j(\mathbf{r},\omega_1)\,\tilde{E}_k(\mathbf{r},-\omega_2)+\text{c.c.}\right]. \tag{2.36}$$

Furthermore, the incoming electric fields not only mix with each other – as seen in the SFG and the DFG – but also mix with themselves individually. If the fundamental fields at frequency ω_1 and ω_2, respectively, excite the material virtually in a way that the material emits two different monochromatic fields at double the fundamental frequencies, i.e. $2\omega_1$ and $2\omega_2$, when returning to its ground state, we speak of SHG. This process is depicted in fig. 2.1c. The corresponding two contributions to the total polarization amplitude (2.34) are given by

$$\tilde{P}_i^{(2)}(\mathbf{r},2\omega_1) = \varepsilon_0 \sum_{j,k}\left[\chi_{ijk}^{(2)}(-2\omega_1;\omega_1,\omega_1)\,\tilde{E}_j(\mathbf{r},\omega_1)\,\tilde{E}_k(\mathbf{r},\omega_1)+\text{c.c.}\right] \tag{2.37}$$

and

$$\tilde{P}_i^{(2)}(\mathbf{r},2\omega_2) = \varepsilon_0 \sum_{j,k}\left[\chi_{ijk}^{(2)}(-2\omega_2;\omega_2,\omega_2)\,\tilde{E}_j(\mathbf{r},\omega_2)\,\tilde{E}_k(\mathbf{r},\omega_2)+\text{c.c.}\right]. \tag{2.38}$$

The last possible second-order process is the OR, where the fundamental fields mix individually

[6] Note, that we have used the reality of the response function leading to $\tilde{\chi}_{ijk}^{(2)}\Big((\omega_1+\omega_2);-\omega_1,-\omega_2\Big) = \left[\tilde{\chi}_{ijk}^{(2)}\Big(-(\omega_1+\omega_2);\omega_1,\omega_2\Big)\right]^*$ (cf. section 2.2), which justifies the complex conjugate in (2.35). Furthermore, we have used the invariance of the susceptibility under the pairwise permutations of (j,ω_1) and (k,ω_2), which leads to the prefactor of 2 in (2.35). For further information regarding the symmetries of the second-order response function and susceptibility see section 2.2.

so that they produce a static polarization (zero frequency) across the material

$$\tilde{P}_i^{(2)}(\mathbf{r},0) = 2\,\varepsilon_0 \sum_{j,k} \Big[\chi_{ijk}^{(2)}(0;\omega_1,-\omega_1)\,\tilde{E}_j(\mathbf{r},\omega_1)\,\tilde{E}_k(\mathbf{r},-\omega_1) + \text{c.c.} + \\ + \chi_{ijk}^{(2)}(0;\omega_2,-\omega_2)\,\tilde{E}_j(\mathbf{r},\omega_2)\,\tilde{E}_k(\mathbf{r},-\omega_2) + \text{c.c.} \Big], \tag{2.39}$$

which leads to the occurrence of a direct current in the system. This process is depicted in fig. 2.1b.

2.3.2 Raman scattering

When light passes a material, it is either scattered elastically or inelastically. In the second case we speak of Raman scattering, named after his discoverer C. V. Raman [4]. The effect of *Raman scattering* is a resonant and, therefore, dissipative nonlinear optical process. This is in contrast to the nonlinear optical processes of wave-mixing presented in section 2.3.1, where any excitation mediated through the exchange in energy between optical field and material is seen as virtual. In Raman scattering, however, a low frequency vibrational mode[7] ($\sim 10^{13}\,\text{Hz}$) is excited through the external optical field, also referred to as pump field. Hence, the material undergoes a real energy level transition by using the energy flow between material and optical field while emitting radiation with a frequency that is shifted relative to the frequency of the incoming field. Moreover, Raman scattering is not only a dissipative but also a dispersive process because the nuclear response ($\sim 10^{-13}\,\text{s}$) of the material is much slower than the electronic response as well as any time scale given by the external optical field ($\sim 10^{-15}\,\text{s}$). The electronic response is, thus, seen as instantaneous in comparison to the (nuclear) Raman scattering response. One then has to account for retardation in the corresponding nuclear response function when describing Raman scattering analytically (cf. section 5.2).

Thereby, the aforementioned frequency shift between injected and emitted light corresponds to the energy gap between the initial and final vibrational state of the material. Though the state transition in the material is real, it is mediated by a virtual state transition. Therefore, we call Raman scattering an indirect resonant process. There are two conceivable scenarios: In the first one the material is in its vibrational ground state $|\text{g}\rangle$ (cf. fig. 2.2a). The material is excited by the optical pump field with energy $\hbar\omega$, where the energy of the optical field is much higher than any transition energy to an excited vibrational state and, in particular, as suggested by fig. 2.2a, much higher than the phonon energy $\hbar\omega_{\text{vib}}$ that is needed for the transition into the excited state $|\text{e}\rangle$. Hence, the material is excited virtually. As a small portion of this incident energy is taken up by the material for the transition from the vibrational ground state $|\text{g}\rangle$ to the excited vibrational state $|\text{e}\rangle$ the material emits radiation with the energy $\hbar(\omega - \omega_{\text{vib}})$. The emitted light has a smaller frequency compared to the frequency of the incoming pump light. In this case one says that the emitted light is *Stokes shifted* as compared to the incident light. In the second scenario the material is already in the excited vibrational state $|\text{e}\rangle$ (cf.

[7] In the case of condensed matter we mean the collective vibrational mode, i.e. the according phonon state.

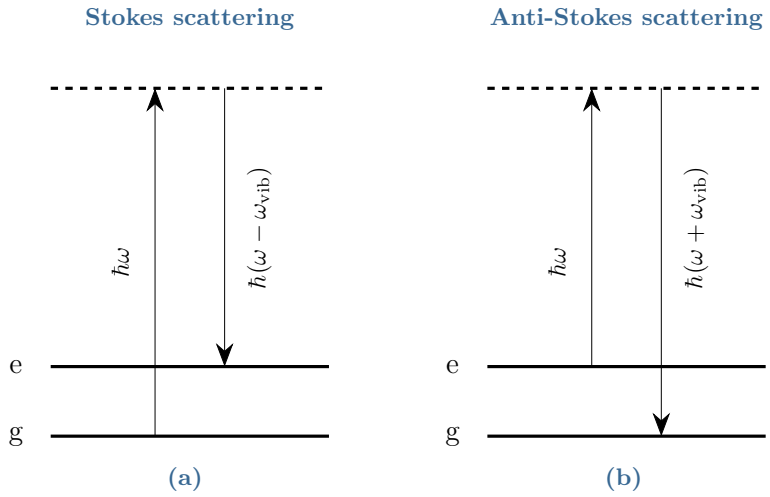

Figure 2.2: Energy schemes for (a) Stokes scattering and (b) Anti-Stokes scattering. Real energy levels of the system are marked by a solid line, while virtual energy levels are depicted by dashed lines.

fig. 2.2b) and the incident pump beam causes the material to relax into its ground state while emitting light with the energy $\hbar(\omega + \omega_{\text{vib}})$. Compared to the incoming light the emitted light has a higher, one says *Anti-Stokes shifted*, frequency. Usually Anti-Stokes scattering is less probable than Stokes scattering as the material already needs to be in an excited vibrational state at a given temperature for Anti-Stokes scattering to take place. In general the effect of Raman scattering we have described so far, which is more specifically known as *spontaneous Raman scattering*, is small compared to the elastic light scattering, which also occurs in the material simultaneously. To enhance the process of Raman scattering one can introduce a second light-beam at the shifted frequency $\omega \pm \omega_{\text{vib}}$ into the system. In this case the process is called *stimulated Raman scattering*. As we will see in section 5.2, stimulated Raman scattering is a third-order (nonlinear) process, which one can describe by an according polarization in Born-Oppenheimer approximation (cf. section 5.1).

CHAPTER 3

The discontinuous Galerkin time-domain method

In most cases an exact solution of Maxwell's equations along with an appropriate set of material equations (see section 1.1.1) is not possible. There are only few structures where an analytical solution can be found, e.g. infinitely stretched cylinders, spheres and ellipsoids. Hence, a numerical solution method might be practical for more complicated systems and is even inevitable when dealing with nonlinear problems (with the exception of few one-dimensional nonlinear problems [52]). A very common method to solve Maxwell's equations in the time domain one might come across is the finite-difference in time-domain (FDTD) method developed by Yee in 1966 [53]. There, the computational domain is discretized by a regular rectangular grid and differential operators are approximated by finite differences. Though this method is fairly easy to implement, it is not suitable for complex geometries that contain curved surfaces or interfaces due to the unadapted grid. In those cases, sufficiently high accuracies are very hard or even impossible to achieve due to artificial staircasing [54, 55]. Instead, we use a more intricate numerical scheme known as the discontinuous Galerkin time-domain (DGTD) method. It can be viewed as a finite element method [14, 56] in the time domain. Thus, the computational domain can be discretized in an unstructured way, i.e. the element size and shape is adapted to the specific structures within the computational domain, leading to a higher accuracy as compared to the FDTD method and avoiding the artificial staircasing effects.

We present the basic DGTD scheme in section 3.1. We will see that one central element of this DGTD method is the numerical flux. Hence, we elaborate further on how to construct a special numerical flux, the upwind flux, in section 3.2. It was shown by Hesthaven and Warburton [24] that a converging DGTD scheme can be derived for Maxwell's equations. Following [24], we will outline the application of the DGTD method to Maxwell's equation and show the corresponding numerical upwind flux in section 3.3. Afterwards, we discuss how to introduce external electromagnetic field sources and boundary conditions using the numerical upwind flux for Maxwell's equations in section 3.4. At last, we examine what issues might occur when dealing with nonlinear problems.

3.1 The discontinuous Galerkin time-domain scheme

In the following we describe how to derive a special semi-discrete explicit finite element scheme in time domain to solve equations in the form of conservation laws (3.1) and (3.21), the *discontinuous Galerkin time-domain* (DGTD) method. Therein, we follow the recipes given by Hesthaven and Warburton [14]. The idea is the following: The computational domain is discretized in space by an adaptive, irregular mesh, where the discretization element type, i.e. the overall shape, is arbitrary. On each of these elements a local solution scheme is applied. Afterwards, the global solution of the total compuational domain is constructed from the local solutions by introducing the so-called *numerical flux*, which is a key element of the overall numerical scheme.

We first study the one-dimensional case to explain the fundamental ideas of the scheme and then extend the resulting scheme to higher dimensions. Hence, consider the general scalar one-dimensional conservation law

$$\partial_t\, u(x,t) + \partial_x\, f(u) = s(x,t) \qquad x \in \Omega = [x_L, x_R] \tag{3.1}$$

where f denotes the flux of a conserved quantity u and s is a source or sink to this quantity. The problem's initial conditions are given by

$$u(x,0) = u_0(x). \tag{3.2}$$

Furthermore, we impose the inflow boundary conditions

$$\begin{aligned} u(x_L,t) &= g_L(t) \quad \text{for} \quad \partial_u f(u) \geq 0 \\ u(x_R,t) &= g_R(t) \quad \text{for} \quad \partial_u f(u) \leq 0. \end{aligned} \tag{3.3}$$

We now discretize the computational domain Ω by K non-overlapping, arbitrary, i.e. not necessarily equally sized, elements $D^k = [x_L^k, x_R^k]$ as illustrated by fig. 3.1. Accordingly, the global solution to the problem is approximated by a numerical solution, which shall be given by the direct sum of K numerical local solutions on each element denoted by index k

$$u(x,t) \approx u_h(x,t) = \bigoplus_{k=1}^{K} u_h^k(x,t). \tag{3.4}$$

Inserting this approximate solution into equation (3.1) will lead to a residual

$$R_h(x) = \partial_t\, u_h(x,t) + \partial_x\, f_h(u_h) - s(x,t). \tag{3.5}$$

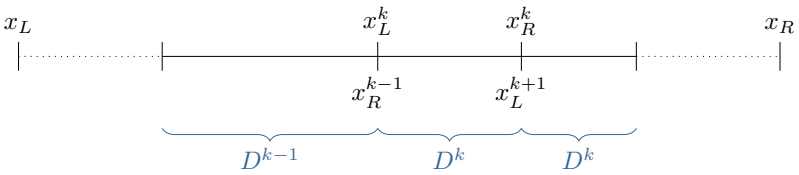

Figure 3.1: Arbitrary discretization of a one-dimensional computational domain

The residual vanishes if the numerical solution $u_h(x,t)$ is identical with the exact solution $u(x,t)$. We now introduce a set of local test function $\phi_h^k(x)$ defined on each element k, for which we require that the residual is orthogonal to each of these test functions locally

$$\int_{D^k} dx\ R_h(x)\phi_h^k(x) \stackrel{!}{=} 0, \qquad 1 \le k \le K. \tag{3.6}$$

By inserting (3.5) into (3.6) we get the weighted integral

$$\int_{D^k} \mathrm{d}x\ \left[\partial_t\, u_h^k(x,t) + \partial_x\, f_h^k(u_h^k) - s(x,t)\right]\ \phi_h^k(x) = 0. \tag{3.7}$$

By applying a spatial integration by parts to (3.7) we obtain the *weak form* of the conservation law

$$\begin{aligned}\int_{D^k} \mathrm{d}x\ \left(\frac{\partial u_h^k(x,t)}{\partial t}\,\phi_h^k(x) - f_h^k(u_h^k)\,\frac{\mathrm{d}\phi_h^k(x)}{\mathrm{d}x} - s(x,t)\phi_h^k(x)\right) &= -\left[f_h^k(u_h^k)\,\phi_h^k(x)\right]_{x_L^k}^{x_R^k} \\ &= -\int_{\partial D^k} \mathrm{d}x\ \breve{n}\cdot f_h^k(u_h^k)\,\phi_h^k(x)\end{aligned} \tag{3.8}$$

where the scalar $\breve{n}$ has the value $+1$ at the left interface and -1 at the right interface. Note, that expression (3.8) only holds locally. So far, we have neither imposed any boundary conditions on the approximate local solutions or the test functions at the interface between elements nor specified how to recover the global solution from the K local solutions. Therefore, the solution at an interface is, yet, multiply defined. As suggested in fig. 3.1 this can lead to a discontinuity in the global solution. Therefore, (3.8) does not produce a suitable scheme to find the global solution, yet. We, hence, need a method to approximate the solution at the interface, in which the multiple values are combined in a particular way. For now, we delay this problem to section 3.2 and replace the flux by the so-called *numerical flux* f_h^*, which shall solve the interface problem. One can say, that the numerical flux ensures the concrete exchange of information between the elements. Hence, the scheme including the numerical flux

$$\int_{D^k} \mathrm{d}x\ \left(\frac{\partial u_h^k(x,t)}{\partial t}\,\phi_h^k(x) - f_h^k(u_h^k)\,\frac{\mathrm{d}\phi_h^k(x)}{\mathrm{d}x} - s(x,t)\phi_h^k(x)\right) = -\int_{\partial D^k} \mathrm{d}x\ \breve{n}\cdot f_h^*\,\phi_h^k(x) \tag{3.9}$$

is semi-discrete as it also contains the information of neighboring elements. For (3.9) to be valid, we need to require that the test functions are smooth. To lift this constraint, we integrate (3.9) spatially once again leading to the *strong form*

$$\int_{D^k} \mathrm{d}x\ \left(\frac{\partial u_h^k(x,t)}{\partial t} + \frac{\partial f_h^k(u_h^k)}{\partial x} - s(x,t)\right)\ \phi_h^k(x) = \int_{\partial D^k} \mathrm{d}x\ \breve{n}\cdot\left(f_h^k(u_h^k) - f_h^*\right)\ \phi_h^k(x), \tag{3.10}$$

where we do not require any smoothness of $\phi_h^k(x)$.

Let us elaborate further on how to approximate the local solutions. We can express the

numerical local solutions by polynomials ψ_n of order N_p

$$u_h^k(x,t) = \sum_{n=1}^{N_\mathrm{p}+1} \tilde{u}_n^k(t)\,\psi_n(x). \tag{3.11}$$

The expansion (3.11) is known as modal representation. Alternatively, one can expand the numerical solution in terms of interpolating Lagrange polynomials

$$L_i^k(x) = \prod_{\substack{m=1\\m\neq i}}^{N} \frac{x - x_m}{x_i - x_m}, \qquad \text{where} \quad L_i^k(x_j) = \delta_{ij} \tag{3.12}$$

through $N = N_\mathrm{p} + 1$ nodal points x_i^k within the k-th element[1], yielding

$$u_h^k(x,t) = \sum_{i=1}^{N} u_h^k(x_i^k,t)\,L_i^k(x). \tag{3.13}$$

This approach is known as nodal representation. Both kinds of representations are equivalent. However, we choose the nodal representation as the expansion coefficients correspond to the physical field values at given points directly, which simplifies the interpretation of the computational results [57]. In the same manner, the local flux as well as the source can be expanded

$$f_h^k(x,t) = \sum_{i=1}^{N} f_h(x_i^k,t)\,L_i^k(x) \tag{3.14}$$

$$s_h^k(x,t) = \sum_{i=1}^{N} s(x_i^k,t)\,L_i^k(x). \tag{3.15}$$

Yet, we still need to choose our test functions. A very common choice is to use the same set of basis functions as for the expansion of the numerical solution, i.e. $\phi_h^k(x) = L_i^k(x)$. This is known as the Galerkin choice. In particular, if we define the mass matrix elements

$$\mathcal{M}_{ij}^k = \int_{D^k} \mathrm{d}x\; L_i^k(x) L_j^k(x), \tag{3.16}$$

the stiffness matrix elements

$$\mathcal{S}_{ij}^k = \int_{D^k} \mathrm{d}x\; L_i^k(x) \frac{\mathrm{d}L_j^k(x)}{\mathrm{d}x}, \tag{3.17}$$

[1] We do not comment on how these nodal points are chosen, e.g. Legendre-Gauß-Lobato quadrature nodes, as it would exceed the scope of this thesis. For more information, the reader is advised to take a look at [14, 57].

the face mass matrix elements

$$\begin{aligned}\mathcal{F}_{ij}^k &= \int_{\partial D^k} \mathrm{d}x\; L_i^k(x) L_j^k(x) \\ &= [f_h^k(x_R^k) - f_{h,R}^*]\, L_j^k(x_R^k) - [f_h^k(x_L^k) - f_{h,L}^*]\, L_j^k(x_L^k),\end{aligned} \tag{3.18}$$

and the column vectors $\vec{u}_h^k = [u_h^k(x_1^k, t), \ldots, u_h^k(x_N, t)]^{\mathrm{T}}$, $\vec{f}_h^k = [f_h^k(x_1^k), \ldots, f_h^k(x_N)]^{\mathrm{T}}$ and $\vec{s}_h^k = [s_h^k(x_1^k), \ldots, s_h^k(x_N)]^{\mathrm{T}}$, the scheme (3.10) becomes

$$\underline{\mathcal{M}}^k \left(\frac{\mathrm{d}\vec{u}_h^k}{\mathrm{d}t} - \vec{s}_h^k \right) + \underline{\mathcal{S}}^k\, \vec{f}_h^k = \underline{\mathcal{F}}^k\, \breve{n} \cdot \left(\vec{f}_h^k - \vec{f}_h^* \right). \tag{3.19}$$

Multiplying (3.19) with the inverse of the mass matrix yields the following time evolution scheme of the local solutions

$$\frac{\mathrm{d}\vec{u}_h^k}{\mathrm{d}t} = (\underline{\mathcal{M}}^k)^{-1} \left[\underline{\mathcal{F}}^k\, \breve{n} \cdot \left(\vec{f}_h^k - \vec{f}_h^* \right) - \underline{\mathcal{S}}^k\, \vec{f}_h^k \right] + \vec{s}_h^k. \tag{3.20}$$

Most commonly, the time-stepping in DGTD schemes like (3.20) is handled by explicit schemes like explicit *Runge-Kutta schemes* [24]. Specifically, we use a 14-stage fourth-order low-storage Runge-Kutta (LSRK) scheme [58] to accomplish the time-stepping. Unless, explicitly stated otherwise the initial value for the solution[2] shall be given by $\vec{u}_h^k(t=0) = \vec{0}$ for every element k.

One can readily extend the one-dimensional DGTD solution scheme (3.20) to d-dimensional (e.g. $d = 2, 3$) problems

$$\partial_t\, \mathbf{u}(\mathbf{r}, t) + \nabla \cdot \underline{\mathbf{f}}(\mathbf{u}) = \mathbf{s}(\mathbf{r}, t), \tag{3.21}$$

where the solution $\mathbf{u}$ and the source $\mathbf{s}$ are now a d-dimensional vectors and the flux is a $(d \times d)$-tensor composed of d vectors $\underline{\mathbf{f}} \equiv (\mathbf{f}^{(1)}, \ldots, \mathbf{f}^{(d)})$. Instead of the one-dimensional version (3.12) within the nodal scheme we then choose d-dimensional Lagrange polynomials[3] $L_i^k(\mathbf{r})$ as test functions and basis functions for the expansion of the numerical solution on each element k. Thereby, we have $L_i^k(\mathbf{r}_j) = \delta_{ij}$ for a given set of nodes within the element $\{\mathbf{r}_j\}$. Thus, the

[2] That goes, in particular, for the electric and magnetic field but also the current density, for which we will solve an appropriate set conservation laws (cf. sections 3.3 and 4.2).

[3] In general d-dimensional Lagrange polynomials of order N are given by

$$L_i(\mathbf{r}) = \sum_{l,m,n}^{l+m+n \leq N} a_{lmn}^{(i)}\, x_l\, y_m\, z_n.$$

where we have the Cartesian coordinates (x, y, z). The total number of nodes is given by $N = N_\mathrm{p} + 1$ in one dimension, $N = \frac{1}{2}(N_\mathrm{p}+1)(N_\mathrm{p}+2)$ in two and $N = \frac{1}{6}(N_\mathrm{p}+1)(N_\mathrm{p}+2)(N_\mathrm{p}+3)$ in three dimensions. The expansion coefficients a_{lmn} are computed using Koornwinder–Dubiner polynomials [24, 59], which solely depend on the node positions. Note, however, that in two and three dimensions the nodal points are no longer given by the Legendre-Gauß-Lobato [14] quadrature nodes but instead must be determined otherwise. Within the DGTD implementation created by our research group the nodal points that are calculated by the empirical Warp&Blend method [60].

nodal polynomial expansions of the solution, flux and source are expressed by

$$\mathbf{u}_h^k(\mathbf{r},t) = \sum_{i=1}^{N} \mathbf{u}_h^k(\mathbf{r}_i^k,t) L_i^k(\mathbf{r}) \tag{3.22}$$

$$\mathbf{f}_h^k(\mathbf{r},t) = \sum_{i=1}^{N} \mathbf{f}_h^k(\mathbf{r}_i^k,t) L_i^k(\mathbf{r}) \tag{3.23}$$

$$\mathbf{s}_h^k(\mathbf{r},t) = \sum_{i=1}^{N} \mathbf{s}_h^k(\mathbf{r}_i^k,t) L_i^k(\mathbf{r}) \tag{3.24}$$

Then the according mass matrix elements are given by

$$\mathcal{M}_{ij}^k = \int_{D^k} \mathrm{d}^d r \; L_i^k(\mathbf{r})\, L_j^k(\mathbf{r}) \tag{3.25}$$

where the mass matrix $\underline{\mathcal{M}}^k$ is a $(N \times N)$ on every element k. The stiffness matrix elements are then expressed by

$$\boldsymbol{\mathcal{S}}_{ij}^k = \int_{D^k} \mathrm{d}^d r \; L_i^k(\mathbf{r}) \left(\nabla L_j^k(\mathbf{r})\right) \tag{3.26}$$

for every element k. The stiffness matrix $\underline{\boldsymbol{\mathcal{S}}}^k$ is a $(N \times N \times d)$-matrix in the d-dimensional case. Furthermore, the face matrix $\underline{\mathcal{F}}^k$ is given by a $(N \times N)$-matrix, where the matrix elements read

$$\mathcal{F}_{ij}^k = \int_{\partial D^k} \mathrm{d}^{d-1} r \; L_i^k(\mathbf{r})\, L_j^k(\mathbf{r}) \tag{3.27}$$

Hence, in d dimensions the time evolution scheme[4] of the solution yields

$$\frac{\mathrm{d}\vec{\mathbf{u}}_h^k}{\mathrm{d}t} = (\underline{\boldsymbol{\mathcal{M}}}^k)^{-1} \left[\underline{\boldsymbol{\mathcal{F}}}^k \breve{\mathbf{n}} \cdot \left(\underline{\mathbf{f}}_h^k - \underline{\mathbf{f}}_h^* \right) - \underline{\boldsymbol{\mathcal{S}}}^k \cdot \underline{\mathbf{f}}_h^k \right] + \vec{\mathbf{s}}_h^k, \tag{3.28}$$

where we have defined the $(d \times N)$-matrices $\vec{\mathbf{u}}_h^k = (\vec{u}_{h,1}^k, \ldots, \vec{u}_{h,d}^k)^{\mathrm{T}}$ and $\vec{\mathbf{s}}_h^k = (\vec{s}_{h,1}^k, \ldots, \vec{s}_{h,d}^k)^{\mathrm{T}}$, and the $(d \times d \times N)$-matrices $\underline{\mathbf{f}}_h^k = (\vec{\mathbf{f}}_{h,1}^k, \ldots, \vec{\mathbf{f}}_{h,d}^k)$ and $\underline{\mathbf{f}}_h^* = (\vec{\mathbf{f}}_{h,1}^k, \ldots, \vec{\mathbf{f}}_{h,d}^k)$.

Note that the numerical flux – or more precisely, the normal projection of the numerical flux – still needs to be determined to complete our solution scheme. The simplest choice is to arithmetically average over the fluxes on both sides of the interface. This particular choice is known as the *central flux*. We will get to know a more elaborate flux scheme in the following section 3.2.

[4] How the DGTD method is applied to three-dimensional systems might become clearer when we use the scheme to solve Maxwell's equations (1.7) to (1.10). We comment briefly on this matter in section 3.3.

3.2 The Numerical flux

As mentioned in section 3.1, one of the key ideas of the DGTD method is to split the computational domain into non-overlapping elements, where the shape of these elements is arbitrary. The problem posed by the conservation law (3.21) is then solved locally on each of these elements. However, the splitting of the computational domain and, consequently, the splitting of the overall solution causes a problem: The local solutions at the interface of two neighboring elements are multiply defined. As a result the global solution becomes discontinuous if assembled directly from the local solutions. In order to fix this problem the numerical flux is introduced. It tells us how to combine the multiple solutions at each interface and by this it eliminates the discontinuities. Hence, the numerical flux leads to a convergent scheme and is, thus, a central element of the discontinuous Galerkin scheme. On a side note, we can use the numerical flux to enforce physical boundary conditions (cf. section 3.4) in addition.

Nevertheless, the choice of the numerical flux is not unique. There are several ways to combine the local solutions at the interface of two neighboring elements. Fortunately, the concept of the numerical flux itself is not new as it is commonly used in finite volume methods [15]. A comprehensive discussion on how to construct numerical fluxes can be found in [15, 61]. The simplest numerical flux choice is given by the *central flux*, which is the mean value of the fluxes at the interface of two elements. For a one-dimensional scalar problem (cf. (3.1)) of two neighboring elements denoted by $(-)$ and $(+)$, respectively, the central flux reads

$$f^*_{\text{central}} = \frac{1}{2}(f_- + f_+), \tag{3.29}$$

where $f_- = f(u_-)$ is the flux from the $(-)$-element and $f_+ = f(u_+)$ is the flux from the $(+)$-element taken at the interface. Unfortunately, the central flux does not always lead to a stable scheme [15]. Additionally, it might not be the appropriate choice for every problem at hand. To arrive at an accurate numerical scheme the choice of a particular numerical flux should depend on the underlying dynamics of the problem [14]. For example, for the one-dimensional scalar advection equation

$$\partial_t\, u(x,t) + c\,\partial_x\, u(x,t) = 0, \tag{3.30}$$

information only travels from one element to the next with constant speed c [15]. Therefore, a one-sided or *upwind-flux scheme*, where the information is only transported in one direction, is proven to be useful [14]. In the following we show how to derive a stable numerical upwind-flux scheme for *linear hyperbolic problems*. For this we introduce the so-called *Riemann problem* in section 3.2.1 to determine the behavior of the discontinuities in time and space. More specifically, we learn how to calculate the speeds at which the discontinuities propagate in time. We use these to construct the so-called *Rankine-Hugoniot jump conditions* in section 3.2.2, which will provide us with a method to calculate the desired upwind flux. We will see that the upwind flux can be seen as a weighted average over the fluxes from each pair of neighboring elements, which in addition smooths out the solution at the interface of these elements. Thereby, the weights are determined by the material properties in the respective elements and the speed of the discontinuities. By incroporating the upwind flux into the DGTD scheme these disconti-

nuities are eliminated. We will see later in section 3.3 that the upwind flux can be seen as an extension to the central flux in some specific cases.

3.2.1 The Riemann problem

According to the earlier discussion the DGTD scheme introduces discontinuities into the global solution, which need to be fixed. This situation is captured by the so-called *Riemann problem* [61, 62], which is an initial value problem for partial differential equations with a jump discontinuity in the initial conditions. If we want to fix the problem of the discontinuities within the DGTD scheme, it is helpful to engage in the Riemann problem first. In particular, we will see how the initial discontinuity behaves in time and space. In the following we illustrate the fundamental ideas on how to solve the one-dimensional scalar Riemann problem before proceeding to the three-dimensional case.

One-dimensional (quasi-)linear hyperbolic problems

We are, first, interested in the Riemann problem posed by the one-dimensional scalar conservation law

$$\partial_t\, u(x,t) + \partial_x\, f(u(x,t)) = 0, \tag{3.31}$$

without any additional sources (cf. (3.1)), and the piece-wise constant initial condition

$$u(x,0) = \begin{cases} u_- & x < \xi \\ u_+ & x > \xi \end{cases} \tag{3.32}$$

with a single jump discontinuity located at $x = \xi$ (see fig. 3.2a). Using the *method of characteristics* one can solve the Riemann problem [61, 62]: By taking the derivative of the flux function we express the conservation law (3.31) by

$$\partial_t\, u + f'(u(x,t))\, \partial_x\, u = 0. \tag{3.33}$$

If the flux derivative $f'(u)$ does not depend on the conserved quantity u, (3.33) is said to be linear. Otherwise the system is said to be nonlinear and (3.33) is referred to as the quasi-linear form of the conservation law (3.31). We shall consider mostly linear problems, where the solution $u(x,t)$ is smooth, and discuss nonlinear problems briefly in section 3.5. From (3.33) it follows that the total time derivative of u is given by

$$\frac{\mathrm{d}u}{\mathrm{d}t} = \frac{\partial u}{\partial t} + x'(t)\, \frac{\partial u}{\partial x} = 0, \tag{3.34}$$

along any curve that satisfies the ordinary differential equation

$$x'(t) = f'(u(x,t)). \tag{3.35}$$

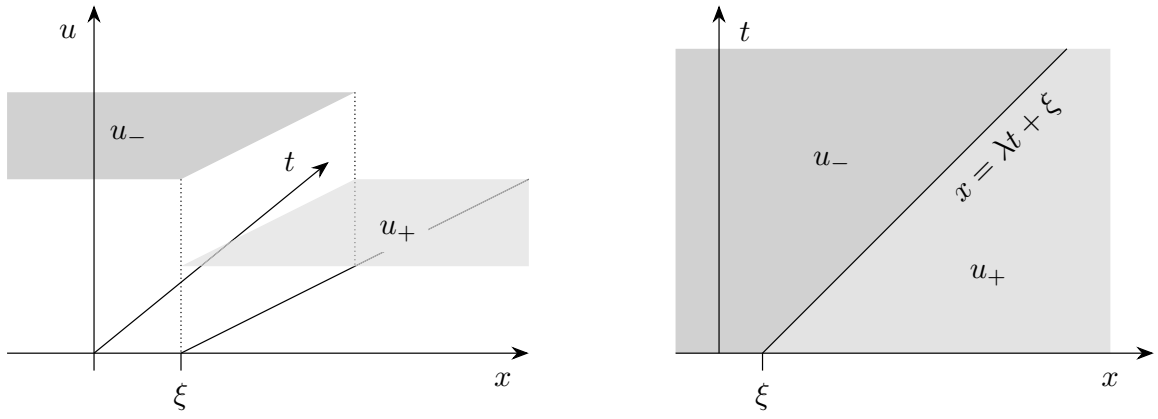

Figure 3.2: (a) (u,x,t)-diagram of the solution of the Riemann problem along characteristic curve $x = \lambda t + \xi$ (b) (x,t)-diagram for the characteristic curve $x = \lambda t + \xi$

(3.34) and (3.35) are referred to as *characteristic equations*. Furthermore, the curve $x(t)$ is called characteristic curve or simply *characteristic*, whereas $x'(t)$ is known as the *characteristic speed* of the solution, i.e. the speed at which the discontinuity is translated along the characteristic curve. Because the solution $u(x,t)$ is constant along the characteristic curve $x(t)$, the characteristic speed $x'(t)$ must be constant in time. Hence, the solution translates uniformly with a constant characteristic speed. If we denote this speed by $\lambda \equiv x'(t)$ the solution is expressed by the piece-wise constant function

$$u(x,t) = u(\xi,0) = \begin{cases} u_- & x - \lambda t < 0 \\ u_+ & x - \lambda t > 0 \end{cases} . \tag{3.36}$$

along the characteristic curve

$$x = \lambda t + \xi, \tag{3.37}$$

which is represented by a straight line, where ξ denotes a specific initial value of x. In fact, because our problem is linear every characteristic can be represented by a straight line with the same slope λ for any given initial data. The solution (3.36) is illustrated in fig. 3.2. We see that the solution is piece-wise constant and shows a jump along the characteristic curve represented by a solid line through the initial x-value ξ in the (x,t)-plane in fig. 3.2a. The projection of the solution onto the (x,t)-plane is displayed in fig. 3.2b showing that the solution space is split into two domains along the characteristic line. Note that the structure of the characteristics purely depends on the initial values $u(x,0)$.

Three-dimensional (quasi-)linear hyperbolic problems

We now apply the solution method of the one-dimensional Riemann problem (3.31) and (3.32) to three-dimensional problems (3.21). Suppose we have two neighboring elements of arbitrary shape. We denote these two elements by $(-)$ and $(+)$, respectively. The goal is now to formulate the three-dimensional problem (3.21) with some corresponding initial conditions as an effective one-dimensional Riemann problem. In order to do so we have to assume that the solution at the interface of those elements varies barely along the interface tangential. Hence, as an approximation the solution shall merely depend on the face normal component of the position $\breve{\mathbf{n}} \cdot \mathbf{r} \equiv x^{(\mathrm{n})}$, i.e. $\mathbf{u}(\mathbf{r}, t) \approx \mathbf{u}(x^{(\mathrm{n})}, t)$. Then the initial values shall be given by a piece-wise constant function along the face normal $\breve{\mathbf{n}}$, yielding

$$\mathbf{u}(x^{(\mathrm{n})}, t) = \begin{cases} \mathbf{u}_- & x^{(\mathrm{n})} < 0 \\ \mathbf{u}_+ & x^{(\mathrm{n})} > 0 \end{cases} . \tag{3.38}$$

If we denote the flux in normal direction by $\mathbf{f}^{(\mathrm{n})} \equiv \breve{\mathbf{n}} \cdot \underline{\mathbf{f}} = \sum_i (\breve{\mathbf{n}} \cdot \breve{\mathbf{e}}_i)\, \mathbf{f}^{(i)}$ and the spatial derivative in normal direction by $(\breve{\mathbf{n}} \cdot \nabla) = \frac{\partial}{\partial \breve{n}}$, the conservation law along the face normal reads

$$\frac{\partial \mathbf{u}(x^{(\mathrm{n})}, t)}{\partial t} + \underline{\mathbf{Q}}(\mathbf{u}, \mathbf{r}, t) \cdot \frac{\partial \mathbf{f}^{(\mathrm{n})}(\mathbf{u})}{\partial \breve{n}} = \mathbf{0}, \tag{3.39}$$

where $\underline{\mathbf{Q}}$ is a diagonalizable matrix. The initial value problem (3.38) and (3.39) can be seen as an effective Riemann problem (cf. (3.31) and (3.32)). By using the key ideas of the one-dimensional scalar Riemann problem we solve the system of equations (3.38) and (3.39) in the following. We can reformulate (3.39) by

$$\frac{\partial \mathbf{u}}{\partial t} + \underline{\mathbf{Q}} \cdot \sum_{k=1}^{3} \frac{\partial \mathbf{f}^{(\mathrm{n})}}{\partial u_k} \frac{\partial u_k}{\partial \breve{n}} = \mathbf{0} \tag{3.40}$$

and then define the matrix $\underline{\mathbf{A}}^{(\mathrm{n})}$ as the transposed Jacobian of the flux in normal direction $\mathbf{f}^{(\mathrm{n})}$, where we require

$$\frac{\partial \mathbf{f}^{(\mathrm{n})}}{\partial u_k} = \sum_{i,j=1}^{3} \left(\breve{\mathbf{n}} \cdot \breve{\mathbf{e}}_i \right) \left(\frac{\partial f_j^{(i)}}{\partial u_k} \breve{\mathbf{e}}_j \right) \equiv \sum_{j=1}^{3} A_{jk}^{(\mathrm{n})}\, \breve{\mathbf{e}}_j \tag{3.41}$$

for the matrix elements $A_{jk}^{(\mathrm{n})}$. In addition, we introduce the matrix $\underline{\mathbf{B}}$, where its elements are defined by

$$B_{ik} = \sum_{j=1}^{3} Q_{ij}\, A_{jk}^{(\mathrm{n})}. \tag{3.42}$$

Using (3.41) and (3.42) we can transform (3.40) into

$$\frac{\partial \mathbf{u}}{\partial t} + \underline{\mathbf{B}} \cdot \frac{\partial \mathbf{u}}{\partial \breve{n}} = \mathbf{0}, \tag{3.43}$$

Under the assumption that $\underline{\mathbf{B}}$ is diagonalizable with m eigenvalues $\lambda_1, \ldots, \lambda_m$ we expand the solution $\mathbf{u}$ in terms of the eigenvectors $\mathbf{v}_a$ of the matrix $\underline{\mathbf{B}}$

$$\mathbf{u}(x^{(\mathrm{n})}, t) = \sum_{a=1}^{m} \tilde{u}_a(x^{(\mathrm{n})}, t)\, \mathbf{v}_a, \tag{3.44}$$

where the expansion coefficients are denoted by $\tilde{u}_a(x^{(\mathrm{n})}, t)$. The according initial conditions for the expansion coefficients shall then be given by the piece-wise constant function

$$\tilde{u}_a(x^{(\mathrm{n})}, 0) = \begin{cases} \tilde{u}_{a,-} & x^{(\mathrm{n})} < 0 \\ \tilde{u}_{a,+} & x^{(\mathrm{n})} > 0 \end{cases} \tag{3.45}$$

with the jump discontinuity located at $x^{(\mathrm{n})} = 0$. By inserting the expansion (3.44) into (3.43) and applying the eigenvalue equation

$$\underline{\mathbf{B}} \cdot \mathbf{v}_a = \lambda_a \mathbf{v}_a \tag{3.46}$$

we obtain

$$\sum_a \mathbf{v}_a \left[\frac{\partial \tilde{u}_a}{\partial t} + \lambda_a \frac{\partial \tilde{u}_a}{\partial \breve{n}} \right] = 0 \tag{3.47}$$

or

$$\frac{\partial \tilde{u}_a}{\partial t} + \lambda_a \frac{\partial \tilde{u}_a}{\partial \breve{n}} = 0 \tag{3.48}$$

for every $a \in [1, m]$, if $v_{a,\mathrm{n}} \neq 0$. The system of equations (3.47) is said to be hyperbolic at $(\mathbf{r}, t)$ if the eigenvalues $\lambda_1, \ldots, \lambda_m$ are real. The system is said to be strictly hyperbolic if the eigenvalues $\lambda_1, \ldots, \lambda_m$ are distinct, meaning that they can be ordered, for example, by $\lambda_1 < \lambda_2 < \cdots < \lambda_m$.

The solution of (3.48) is given according to (3.36) but this time along the characteristic curve $x^{(\mathrm{n})} = \lambda_a\, t + \xi_{\mathrm{n}}$, where ξ_n denotes the normal projection of a specific initial spatial value $\mathbf{r}(0) = \boldsymbol{\xi}$. Using the solution (3.36) and the expansion (3.44) the solution of the effective Riemann problem along a face normal (3.38) and (3.39) is given by

$$\mathbf{u}(x^{(\mathrm{n})}, t) = \mathbf{u}(\xi_{\mathrm{n}}, 0) = \sum_{a=1}^{m} \mathbf{v}_a \begin{cases} \tilde{u}_{a,-} & x^{(\mathrm{n})} - \lambda_a\, t < 0 \\ \tilde{u}_{a,+} & x^{(\mathrm{n})} - \lambda_a\, t > 0 \end{cases} . \tag{3.49}$$

If we compare the solution to the effective Riemann problem along a face normal with the solution to the one-dimensional Riemann problem, we find that the solution has m jumps

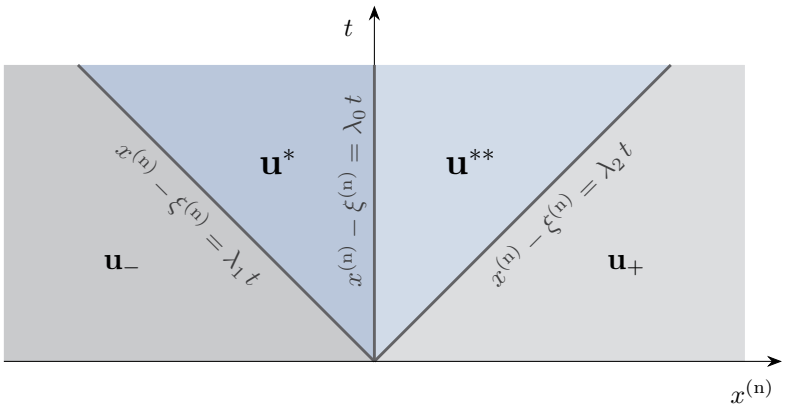

Figure 3.3: $(x^{(\mathrm{n})},t)$-plane projection of the solutions to Riemann problem with three different characteristic speeds $\lambda_0 = 0$, $\lambda_1 < 0$ and $\lambda_2 > 0$.

instead of a single one according to the number of characteristics to the problem. Each of the jump discontinuities are translated with the characteristic speeds $\lambda_1, \ldots, \lambda_m$, respectively, along the corresponding characteristic curves. Therefore, the solution is split into $m+1$ piece-wise constant regions. This behavior is illustrated by fig. 3.3 for a system with three characteristics with characteristic speeds $\lambda_0 = 0$, $\lambda_1 < 0$ and $\lambda_2 > 0$, respectively. Hence, the solution space is split into four piece-wise constant regions denoted by $\mathbf{u}_-$, $\mathbf{u}^*$, $\mathbf{u}^{**}$ and $\mathbf{u}_+$ with jump discontinuities along each of the characteristics. From fig. 3.3 we understand that taking the average mean over the fluxes from each element as done in the central flux (cf. (3.29)) represents this situation insufficiently as only one temporally constant discontinuity is taken into account. Thus, a more elaborate numerical flux is necessary.

We will use the information on the characteristic speeds to construct the so-called Rankine-Hugoniot jump conditions in the following section 3.2.2. These will provide us with a formula for the normal projection of the numerical upwind flux.

3.2.2 The Rankine-Hugoniot condition

In section 3.2.1 we have found the approximate solution to the three-dimensional conservation law along the interface normal between two regions with a piece-wise constant, discontinuous initial condition (3.38). We have seen that the discontinuity in the initial condition leads to additional discontinuities propagating with different (characteristic) speeds, where the solution space is split into several regions along the so-called characteristic curves (see fig. 3.3). Within this section we show how to eliminate these discontinuities from the DGTD scheme (3.20). For this we use the information on the characteristic speeds, which can be obtained according to section 3.2.1. Suppose that we have an initial value problem with three characteristic speeds $\lambda_1 < 0$, $\lambda_0 = 0$ and $\lambda_2 > 0$. This situation is illustrated in fig. 3.3. In this case the solution space is split into four regions by the three characteristics $s_0 = \xi^{(\mathrm{n})}$, $s_1(t) = \lambda_1 t + \xi^{(\mathrm{n})}$ and $s_2(t) = \lambda_2 t + \xi^{(\mathrm{n})}$ so that we encounter a jump discontinuity along each of these characteristics. Note that $x_0^{(\mathrm{n})}$ is constant in time as the corresponding characteristic speed is zero. In the following we construct the jump conditions of the solution going from one region to another. Let us first take a look at the jump discontinuity occurring at the transition from the region marked by $\mathbf{u}_-$ in fig. 3.3 to the region marked by $\mathbf{u}^*$. We, thus, integrate (3.39) over an

infinitesimally small region $[x_-^{(\mathrm{n})}, x_+^{(\mathrm{n})}]$ surrounding the jump discontinuity at $s_1(t)$

$\mathbf{u}_- \to \mathbf{u}^*$:

$$
\begin{aligned}
-\int_{x_-^{(\mathrm{n})}}^{x_+^{(\mathrm{n})}} \mathrm{d}\breve{n}\ \underline{\mathbf{Q}} \cdot \frac{\partial \mathbf{f}^{(\mathrm{n})}(\mathbf{u})}{\partial \breve{n}} &= \underline{\mathbf{Q}}_- \cdot \left[\mathbf{f}^{(\mathrm{n})}(\mathbf{u}_-) - \mathbf{f}^{(\mathrm{n})}(\mathbf{u}^*)\right] \\
&= \int_{x_-^{(\mathrm{n})}}^{x_+^{(\mathrm{n})}} \mathrm{d}\breve{n}\ \frac{\partial \mathbf{u}}{\partial t} = \frac{\mathrm{d}}{\mathrm{d}t} \int_{x_-^{(\mathrm{n})}}^{x_+^{(\mathrm{n})}} \mathrm{d}\breve{n}\ \mathbf{u} \\
&= \lim_{\epsilon \to 0} \frac{\mathrm{d}}{\mathrm{d}t} \left[\int_{x_-^{(\mathrm{n})}}^{s_1(t)-\epsilon} \mathrm{d}\breve{n}\ \mathbf{u} + \int_{s_1(t)+\epsilon}^{x_+^{(\mathrm{n})}} \mathrm{d}\breve{n}\ \mathbf{u} \right] = \\
&= \lim_{\epsilon \to 0} \left[\int_{x_-^{(\mathrm{n})}}^{s_1(t)-\epsilon} \mathrm{d}\breve{n}\ \frac{\partial \mathbf{u}}{\partial t} + \int_{s_1(t)+\epsilon}^{x_+^{(\mathrm{n})}} \mathrm{d}\breve{n}\ \frac{\partial \mathbf{u}}{\partial t} + \right. \\
&\qquad \left. + \frac{\mathrm{d}s_1}{\mathrm{d}t}\ \mathbf{u}(s_1(t)-\epsilon, t) - \frac{\mathrm{d}s_1}{\mathrm{d}t}\ \mathbf{u}(s_1(t)+\epsilon, t) \right],
\end{aligned}
\tag{3.50}
$$

where ϵ is a positive infinitesimally small integer. Note that in the first line of (3.50) we have assumed that $\underline{\mathbf{Q}}$ has the constant value $\underline{\mathbf{Q}}_-$ across the integration region. Since the derivative $\partial_t \mathbf{u}$ is bounded the integral in the last line of (3.50) vanishes identically as the left and right boundary, x_- and x_+ respectively, approach the characteristic[5] $s_1(t)$. Since the speed of the discontinuity is given by $\frac{\mathrm{d}s_1}{\mathrm{d}t} = \lambda_1$, we have $\lim_{\epsilon \to 0} \mathbf{u}(s_1(t) - \epsilon, t) = \mathbf{u}_-$ and $\lim_{\epsilon \to 0} \mathbf{u}(s_1(t) + \epsilon, t) = \mathbf{u}^*$ (cf. fig. 3.3). This results in the following jump condition

$\mathbf{u}_- \to \mathbf{u}^*$:

$$
\underline{\mathbf{Q}}_- \cdot \left[\mathbf{f}^{(\mathrm{n})}(\mathbf{u}_-) - \mathbf{f}^{(\mathrm{n})}(\mathbf{u}^*)\right] = \lambda_1(\mathbf{u}_- - \mathbf{u}^*) = -|\lambda_1|(\mathbf{u}_- - \mathbf{u}^*). \tag{3.51}
$$

We can apply the same kind of considerations to the two remaining jump discontinuities at the characteristics s_0 and $s_2(t)$, yielding

$\mathbf{u}^* \to \mathbf{u}^{**}$:

$$
\mathbf{f}^{(\mathrm{n})}(\mathbf{u}^*) - \mathbf{f}^{(\mathrm{n})}(\mathbf{u}^{**}) = \mathbf{0} \tag{3.52}
$$

[5] In the same manner any term resulting from an additional source term that is bounded would vanish identically. We, thus, do not need to include any source terms in deriving the numerical flux.

and

$\mathbf{u}^{**} \to \mathbf{u}_+$:

$$\underline{\mathbf{Q}}_+ \cdot \left[\mathbf{f}^{(\mathrm{n})}(\mathbf{u}^{**}) - \mathbf{f}^{(\mathrm{n})}(\mathbf{u}_+)\right] = \lambda_2(\mathbf{u}^{**} - \mathbf{u}_+), \tag{3.53}$$

where we have used $\lim_{\epsilon\to 0} \mathbf{u}(s_2(t) - \epsilon) = \mathbf{u}^{**}$ and $\lim_{\epsilon\to 0} \mathbf{u}(s_2(t) + \epsilon) = \mathbf{u}_+$. Each of the equations (3.51) and (3.53) are known as *Rankine-Hugoniot (jump) conditions* [14, 61]. From these conditions we can now calculate the normal projection of the numerical flux $\mathbf{f}^{(\mathrm{n})}(\mathbf{u}^*)$. For this we add (3.51) multiplied by $|\lambda_2|$ to (3.53) multiplied by $|\lambda_1|$ and insert condition (3.52). After some rearrangement we get

$$\begin{aligned}\mathbf{f}^{(\mathrm{n})}(\mathbf{u}^*) = (|\lambda_2|\,\underline{\mathbf{Q}}_- + |\lambda_1|\,\underline{\mathbf{Q}}_+)^{-1}\Big[&- |\lambda_1||\lambda_2|\,(\mathbf{u}_+ - \mathbf{u}_-) - |\lambda_1||\lambda_2|\,(\mathbf{u}^* - \mathbf{u}^{**}) + \\ &+ |\lambda_2|\,\underline{\mathbf{Q}}_- \cdot \mathbf{f}^{(\mathrm{n})}(\mathbf{u}_-) + |\lambda_1|\,\underline{\mathbf{Q}}_+ \cdot \mathbf{f}^{(\mathrm{n})}(\mathbf{u}_+)\Big],\end{aligned} \tag{3.54}$$

which is referred to as the normal projection of the upwind flux. From the last two terms we understand that the upwind flux contains a weighted average of the fluxes from two neighboring elements, where the characteristic speeds and the material properties within these elements are taken into account. By the first two terms the solution at the interface between two neighboring elements is smoothed out. Hence, the discontinuities are eliminated by inserting the numerical flux into the DGTD scheme (3.54). With the expression (3.54) for the normal projection of the numerical flux the numerical scheme (3.28) is now complete. Note, however, that the expression (3.54) still depends on the intermediate values $\mathbf{u}^*$ and $\mathbf{u}^{**}$. We will show that the numerical flux, in fact, only depends on the information from the $(-)$-region and the $(+)$-region, i.e. $\mathbf{u}_-$ and $\mathbf{u}_+$, in the concrete case. We derive the numerical flux for Maxwell's equations in section 3.3 and for the *hydrodynamic material* equations in section 4.3.

3.3 Application of the DGTD method to Maxwell's equations

Our overall goal is to solve Maxwell's equations (1.7) to (1.10) alongside with the according (possibly nonlinear) material equations numerically by using the DGTD method. In order to apply the DGTD scheme (3.28) to Maxwell's equations and also to the material equations the total system of equations needs to be represented by a conservation law (3.21). Therefore, we focus on the Maxwell equations, where the material information is solely contained in the charge and current density[6], (1.7) to (1.10). By taking the divergence of Maxwell's curl equation for the electric field (1.9)

$$\nabla \cdot [\nabla \times \mathbf{E}(\mathbf{r}, t)] \overset{(1.9)}{=} -\partial_t [\nabla \cdot \mathbf{B}(\mathbf{r}, t)] = 0, \tag{3.55}$$

[6] For the numerical flux derivation, where the material information is contained in the permittivity and the permeability see [63]. One can show that the expression of the numerical flux that is derived within this section is equivalent to the expression shown in [13, 63] in vacuum.

which must vanish identically, we see that the divergence of the magnetic field is temporally conserved, i.e. $\nabla \cdot \mathbf{B}(\mathbf{r}, t_0) = \nabla \cdot \mathbf{B}(\mathbf{r}, t)$. Therefore, if we ensure that the divergence equation of the magnetic field (1.8) is fulfilled at the beginning of our simulation, we do not need to include this particular equation in our DGTD scheme as it is temporally conserved. A similar consideration can be applied to the divergence of the electric field (1.7). By taking the divergence of Maxwell's curl equation for the magnetic field (1.10) we get

$$0 = \nabla \cdot [\nabla \times \mathbf{B}(\mathbf{r}, t)] \overset{(1.10)}{=} \mu_0 \, \nabla \cdot \mathbf{J}(\mathbf{r}, t) + \mu_0 \, \varepsilon_0 \, \partial_t \, \nabla \cdot \mathbf{E}(\mathbf{r}, t). \tag{3.56}$$

By inserting the continuity equation (1.11) into (3.56)

$$\mu_0 \, \varepsilon_0 \, \partial_t \, [\, -\varrho(\mathbf{r}, t) + \nabla \cdot \mathbf{E}(\mathbf{r}, t) \,] = 0 \tag{3.57}$$

we see that the divergence equation of the electric field is also conserved, i.e. $[\nabla \cdot \mathbf{E}(\mathbf{r}, t_0) - \varrho(\mathbf{r}, t_0)] = [\nabla \cdot \mathbf{E}(\mathbf{r}, t) - \varrho(\mathbf{r}, t)]$, but only if the continuity equation (1.11) is fulfilled simultaneously. Therefore, the continuity equation in some way needs to be included in the material equations. Consequently, we only need to incorporate Maxwell's curl equations (1.9) and (1.10) into the DGTD scheme. We, thus, define the global solution by the six component row vector

$$\mathbf{u}(\mathbf{r}, t) \equiv \begin{pmatrix} \mathbf{E}(\mathbf{r}, t) \\ \mathbf{B}(\mathbf{r}, t) \end{pmatrix}. \tag{3.58}$$

Furthermore, each component of the flux tensor $\underline{\mathbf{f}} = (\mathbf{f}^{(1)}, \mathbf{f}^{(2)}, \mathbf{f}^{(3)})$ shall be given by

$$\mathbf{f}^{(i)}(\mathbf{u}) \equiv \begin{pmatrix} -\tilde{\mathbf{e}}_i \times \mathbf{B}(\mathbf{r}, t) \\ \tilde{\mathbf{e}}_i \times \mathbf{E}(\mathbf{r}, t) \end{pmatrix} \tag{3.59}$$

and the source vector shall read

$$\mathbf{s}(\mathbf{r}, t) = \begin{pmatrix} -\frac{1}{\varepsilon_0} \mathbf{J}(\mathbf{r}, t) \\ \mathbf{0} \end{pmatrix} \tag{3.60}$$

so that we can retrieve the conservation law from Maxwell's curl equations by inserting (3.58) to (3.60) into (3.21)

$$\frac{\partial}{\partial t} \begin{pmatrix} \mathbf{E} \\ \mathbf{B} \end{pmatrix} + \begin{pmatrix} \frac{1}{\mu_0 \varepsilon_0} \mathbb{1}_3 & 0_{3,3} \\ 0_{3,3} & \mathbb{1}_3 \end{pmatrix} \sum_i \frac{\partial}{\partial x_i} \begin{pmatrix} -\breve{\mathbf{e}}_i \times \mathbf{B} \\ \breve{\mathbf{e}}_i \times \mathbf{E} \end{pmatrix} = \begin{pmatrix} -\frac{1}{\varepsilon_0} \mathbf{J} \\ \mathbf{0} \end{pmatrix}. \tag{3.61}$$

We can now readily incorporate the conservation law (3.61) into our DGTD scheme (3.28). But because the scheme introduces discontinuities at the interface of each neighboring elements, we need to eliminate these discontinuities. This is done by the numerical flux. Yet, we have to find an expression for the numerical flux – or rather its normal projection to the interface between neighboring elements (cf. (3.28)) – to complete the numerical scheme. As mentioned in section 3.2, the simplest numerical flux is given by the central flux (cf. (3.29)). For two

neighboring elements, where the solution of one element is denoted by $\mathbf{u}_- = (\mathbf{E}_-, \mathbf{B}_-)^{\mathrm{T}}$, whereas the solution of the other element is denoted by $\mathbf{u}_+ = (\mathbf{E}_+, \mathbf{B}_+)^{\mathrm{T}}$, the normal projection of the central flux to their interface is given by the mean value

$$\breve{\mathbf{n}} \cdot \mathbf{f}^*_{\text{central}} = \frac{1}{2}\,\breve{\mathbf{n}} \cdot \left[\mathbf{f}(\mathbf{u}_+) + \mathbf{f}(\mathbf{u}_-)\right] \overset{(3.59)}{=} \frac{1}{2} \begin{pmatrix} -\breve{\mathbf{n}} \times (\mathbf{B}_+ + \mathbf{B}_-) \\ \breve{\mathbf{n}} \times (\mathbf{E}_+ + \mathbf{E}_-) \end{pmatrix}. \tag{3.62}$$

Unfortunately, the central flux does not always lead to a stable numerical scheme [15] as pointed out in section 3.2. Instead, we use the more stable upwind flux, which has already been derived in general in section 3.2. Following the recipe from section 3.2 we formulate the problem of the conservation law (3.61) with jump discontinuity as an effective Riemann problem. Hence, we first need to define a set of initial conditions. To that end, we have to assume that the electromagnetic field at the interface between two neighboring elements barely depends on the tangential position. An appropriate set of initial conditions is given by

$$(\mathbf{E}, \mathbf{B})^{\mathrm{T}} = \begin{cases} (\mathbf{E}_-, \mathbf{B}_-)^{\mathrm{T}} & \breve{\mathbf{n}} \cdot \mathbf{r}_{\text{face}} < 0 \\ (\mathbf{E}_+, \mathbf{B}_+)^{\mathrm{T}} & \breve{\mathbf{n}} \cdot \mathbf{r}_{\text{face}} > 0 \end{cases}, \tag{3.63}$$

where a jump discontinuity is located at the interface position $\mathbf{r}_{\text{face}}$ and $\breve{\mathbf{n}}$ denotes the interface normal. We then establish the conservation law along the interface normal (cf. (3.39))

$$\frac{\partial}{\partial t} \begin{pmatrix} \mathbf{E} \\ \mathbf{B} \end{pmatrix} + \begin{pmatrix} \frac{1}{\mu_0 \varepsilon_0} \mathbb{1}_3 & 0_{3,3} \\ 0_{3,3} & \mathbb{1}_3 \end{pmatrix} \frac{\partial}{\partial \breve{n}} \begin{pmatrix} -\breve{\mathbf{n}} \times \mathbf{B} \\ \breve{\mathbf{n}} \times \mathbf{E} \end{pmatrix} = \begin{pmatrix} -\frac{1}{\varepsilon_0}\mathbf{J} \\ \mathbf{0} \end{pmatrix}. \tag{3.64}$$

If we express the spatial derivatives by

$$\begin{aligned} \frac{\partial(\breve{\mathbf{n}} \times \mathbf{B})}{\partial \breve{n}} &= \sum_{i=1}^{6} \frac{\partial(\breve{\mathbf{n}} \times \mathbf{B})}{\partial u_k} \left(\frac{\partial u_k}{\partial \breve{n}}\right) = \sum_{i=1}^{3} \frac{\partial(\breve{\mathbf{n}} \times \mathbf{B})}{\partial B_k} \left(\frac{\partial B_k}{\partial \breve{n}}\right) = \\ &= \underbrace{\begin{pmatrix} 0 & -n_z & n_y \\ n_z & 0 & -n_x \\ -n_y & n_x & 0 \end{pmatrix}}_{\equiv \underline{\mathbf{N}}} \cdot \frac{\partial \mathbf{B}}{\partial \breve{n}} \end{aligned} \tag{3.65}$$

and

$$\frac{\partial(\breve{\mathbf{n}} \times \mathbf{E})}{\partial \breve{n}} = \sum_{i=1}^{3} \frac{\partial(\breve{\mathbf{n}} \times \mathbf{E})}{\partial E_k} \left(\frac{\partial E_k}{\partial \breve{n}}\right) = \underline{\mathbf{N}} \cdot \frac{\partial \mathbf{E}}{\partial \breve{n}}, \tag{3.66}$$

(3.64) can be written in the form of

$$\frac{\partial}{\partial t} \begin{pmatrix} \mathbf{E} \\ \mathbf{B} \end{pmatrix} + \underline{\mathbf{A}}^{(\mathrm{n})} \frac{\partial}{\partial \breve{n}} \begin{pmatrix} \mathbf{E} \\ \mathbf{B} \end{pmatrix} = \begin{pmatrix} -\frac{1}{\varepsilon_0}\mathbf{J} \\ \mathbf{0} \end{pmatrix}, \tag{3.67}$$

where $\underline{\mathbf{A}}^{(\mathrm{n})}$ is the transposed Jacobian of the flux in normal direction according to (3.41). More specifically, $\underline{\mathbf{A}}^{(\mathrm{n})}$ is given by

$$\begin{aligned}\underline{\mathbf{A}}^{(\mathrm{n})} &= \begin{pmatrix} \frac{1}{\mu_0\varepsilon_0}\mathbb{1}_3 & 0_{3,3} \\ 0_{3,3} & \mathbb{1}_3 \end{pmatrix} \begin{pmatrix} \underline{\mathbf{N}} & 0_{3,3} \\ 0_{3,3} & \underline{\mathbf{N}} \end{pmatrix} \begin{pmatrix} 0_{3,3} & -\mathbb{1}_3 \\ \mathbb{1}_3 & 0_{3,3} \end{pmatrix} = \\ &= \begin{pmatrix} 0 & 0 & 0 & 0 & \frac{n_z}{\mu_0\varepsilon_0} & -\frac{n_y}{\mu_0\varepsilon_0} \\ 0 & 0 & 0 & -\frac{n_z}{\mu_0\varepsilon_0} & 0 & \frac{n_x}{\mu_0\varepsilon_0} \\ 0 & 0 & 0 & \frac{n_y}{\mu_0\varepsilon_0} & -\frac{n_x}{\mu_0\varepsilon_0} & 0 \\ 0 & -n_z & n_y & 0 & 0 & 0 \\ n_z & 0 & -n_x & 0 & 0 & 0 \\ -n_y & n_x & 0 & 0 & 0 & 0 \end{pmatrix}. \end{aligned} \tag{3.68}$$

The eigenvalues of $\underline{\mathbf{A}}^{(\mathrm{n})}$ give the speeds with which the initial jump discontinuity (cf. (3.63)) propagates. As a result one finds the doubly degenerate eigenvalues[7] $\lambda_0 = 0$, $\lambda_1 = -\frac{1}{\sqrt{\mu_0\varepsilon_0}}$ and $\lambda_2 = \frac{1}{\sqrt{\mu_0\varepsilon_0}}$. Hence, we have the same situation as depicted in fig. 3.3, where the solution space is split into four regions denoted by $(\mathbf{E}_-, \mathbf{B}_-)^{\mathrm{T}}$, $(\mathbf{E}^*, \mathbf{B}^*)^{\mathrm{T}}$, $(\mathbf{E}^{**}, \mathbf{B}^{**})^{\mathrm{T}}$ and $(\mathbf{E}_+, \mathbf{B}_+)^{\mathrm{T}}$. We now use these speeds to eliminate the discontinuities from the problem. Therefore, we formulate the Rankine-Hugoniot jump conditions (cf. (3.51) to (3.53)). For Maxwell's curl equations they read

$$\frac{1}{\sqrt{\mu_0\varepsilon_0}} \begin{pmatrix} \mathbf{E}_- - \mathbf{E}^* \\ \mathbf{B}_- - \mathbf{B}^* \end{pmatrix} + \begin{pmatrix} \frac{1}{\mu_0\varepsilon_0}\mathbb{1}_3 & 0_{3,3} \\ 0_{3,3} & \mathbb{1}_3 \end{pmatrix} \cdot \begin{pmatrix} -\breve{\mathbf{n}} \times (\mathbf{B}_- - \mathbf{B}^*) \\ \breve{\mathbf{n}} \times (\mathbf{E}_- - \mathbf{E}^*) \end{pmatrix} = \mathbf{0}, \tag{3.69}$$

$$\begin{pmatrix} -\breve{\mathbf{n}} \times (\mathbf{B}^* - \mathbf{B}^{**}) \\ \breve{\mathbf{n}} \times (\mathbf{E}^* - \mathbf{E}^{**}) \end{pmatrix} = \mathbf{0}, \tag{3.70}$$

$$-\frac{1}{\sqrt{\mu_0\varepsilon_0}} \begin{pmatrix} \mathbf{E}^{**} - \mathbf{E}_+ \\ \mathbf{B}^{**} - \mathbf{B}_+ \end{pmatrix} + \begin{pmatrix} \frac{1}{\mu_0\varepsilon_0}\mathbb{1}_3 & 0_{3,3} \\ 0_{3,3} & \mathbb{1}_3 \end{pmatrix} \cdot \begin{pmatrix} -\breve{\mathbf{n}} \times (\mathbf{B}^{**} - \mathbf{B}_+) \\ \breve{\mathbf{n}} \times (\mathbf{E}^{**} - \mathbf{E}_+) \end{pmatrix} = \mathbf{0}. \tag{3.71}$$

From these conditions (3.69) to (3.71) one could again construct the numerical flux for Maxwell's curl equations. As we have already derived the general expression for the numerical flux (3.54) from the general Rankine-Hugoniot conditions (3.51) to (3.53) in section 3.2.2 we just need to insert the corresponding solutions (3.58) and fluxes (3.59) of Maxwell's curl equations into

[7] The two-fold degeneracy is a consequence of how we introduce the material models into Maxwell's equations. As the material equations are incorporated via the current density and the charge density instead of the permittivity and the permeability we find constant eigenvalues of the directional flux Jacobian throughout the whole computational domain (cf. [63]). Note, that the maximal characteristic speed is given by the speed of light in vacuum in this case.

(3.54) instead, yielding

$$\begin{pmatrix} -\check{\mathbf{n}} \times \mathbf{B}^* \\ \check{\mathbf{n}} \times \mathbf{E}^* \end{pmatrix} = \frac{1}{2} \begin{pmatrix} -\check{\mathbf{n}} \times (\mathbf{B}_+ + \mathbf{B}_-) \\ \check{\mathbf{n}} \times (\mathbf{E}_+ + \mathbf{E}_-) \end{pmatrix} - \frac{1}{2\sqrt{\mu_0 \varepsilon_0}} \begin{pmatrix} \mathbf{E}_+ - \mathbf{E}_- \\ \mathbf{B}_+ - \mathbf{B}_- \end{pmatrix} + \frac{1}{2\sqrt{\mu_0 \varepsilon_0}} \begin{pmatrix} \mathbf{E}^{**} - \mathbf{E}^* \\ \mathbf{B}^{**} - \mathbf{B}^* \end{pmatrix}. \tag{3.72}$$

One can now replace the second term on the r.h.s. of (3.72) by an expression that merely contains the electromagnetic field information of the $(-)$- and $(+)$-region. For this we express $(\mathbf{E}^{**} - \mathbf{E}^*, \mathbf{B}^{**} - \mathbf{B}^*)^{\mathrm{T}}$ in terms of its normal and tangential component

$$\begin{pmatrix} \mathbf{E}^{**} - \mathbf{E}^* \\ \mathbf{B}^{**} - \mathbf{B}^* \end{pmatrix} = \begin{pmatrix} \check{\mathbf{n}} \left[\check{\mathbf{n}} \cdot (\mathbf{E}^{**} - \mathbf{E}^*) \right] \\ \check{\mathbf{n}} \left[\check{\mathbf{n}} \cdot (\mathbf{B}^{**} - \mathbf{B}^*) \right] \end{pmatrix} - \underbrace{\begin{pmatrix} \check{\mathbf{n}} \times \left[\check{\mathbf{n}} \times (\mathbf{E}^{**} - \mathbf{E}^*) \right] \\ \check{\mathbf{n}} \times \left[\check{\mathbf{n}} \times (\mathbf{B}^{**} - \mathbf{B}^*) \right] \end{pmatrix}}_{\overset{(3.70)}{=} \mathbf{0}}. \tag{3.73}$$

Because of condition (3.70) the tangential component in (3.73) vanishes. Since the projection of (3.72) onto the face normal $\check{\mathbf{n}}$ leads to

$$\begin{pmatrix} \check{\mathbf{n}} \cdot (\mathbf{E}^{**} - \mathbf{E}^*) \\ \check{\mathbf{n}} \cdot (\mathbf{B}^{**} - \mathbf{B}^*) \end{pmatrix} = \begin{pmatrix} \check{\mathbf{n}} \cdot (\mathbf{E}_+ - \mathbf{E}_-) \\ \check{\mathbf{n}} \cdot (\mathbf{B}_+ - \mathbf{B}_-) \end{pmatrix} \tag{3.74}$$

we can replace the normal component on the r.h.s. of (3.73) by (3.74). Thus, the upwind flux for Maxwell's curl equations (3.72) is given by[8]

$$\begin{aligned} \check{\mathbf{n}} \cdot \mathbf{f}^*_{\text{upwind}} &\equiv \begin{pmatrix} -\check{\mathbf{n}} \times \mathbf{B}^* \\ \check{\mathbf{n}} \times \mathbf{E}^* \end{pmatrix} = \\ &= \frac{1}{2} \begin{pmatrix} -\check{\mathbf{n}} \times (\mathbf{B}_+ + \mathbf{B}_-) \\ \check{\mathbf{n}} \times (\mathbf{E}_+ + \mathbf{E}_-) \end{pmatrix} + \frac{1}{2\sqrt{\mu_0 \varepsilon_0}} \begin{pmatrix} \check{\mathbf{n}} \left[\check{\mathbf{n}} \cdot (\mathbf{E}_+ - \mathbf{E}_-) \right] - (\mathbf{E}_+ - \mathbf{E}_-) \\ \check{\mathbf{n}} \left[\check{\mathbf{n}} \cdot (\mathbf{B}_+ - \mathbf{B}_-) \right] - (\mathbf{B}_+ - \mathbf{B}_-) \end{pmatrix}. \end{aligned} \tag{3.75}$$

The equations (3.61) and (3.75) form a complete set of equations for the DGTD scheme (3.28). One can show that the upwind flux (3.75) will lead to a stable scheme [14]. Unfortunately, it is not energy-conserving, which might lead to a less accurate scheme as compared to an energy conserving scheme [14, 63]. As a comparison, the central flux (3.62) is energy-conserving but not necessarily stable [15]. Thus, it is sometimes useful to introduce the so-called upwind parameter $\alpha \in [0, 1]$ into (3.75)

$$\check{\mathbf{n}} \cdot \mathbf{f}^*_\alpha = \begin{pmatrix} -\check{\mathbf{n}} \times \mathbf{B}^* \\ \check{\mathbf{n}} \times \mathbf{E}^* \end{pmatrix} = \frac{1}{2} \begin{pmatrix} -\check{\mathbf{n}} \times (\mathbf{B}_+ + \mathbf{B}_-) \\ \check{\mathbf{n}} \times (\mathbf{E}_+ + \mathbf{E}_-) \end{pmatrix} + \frac{\alpha}{2\sqrt{\mu_0 \varepsilon_0}} \begin{pmatrix} \check{\mathbf{n}} \left[\check{\mathbf{n}} \cdot (\mathbf{E}_+ - \mathbf{E}_-) \right] - (\mathbf{E}_+ - \mathbf{E}_-) \\ \check{\mathbf{n}} \left[\check{\mathbf{n}} \cdot (\mathbf{B}_+ - \mathbf{B}_-) \right] - (\mathbf{B}_+ - \mathbf{B}_-) \end{pmatrix} \tag{3.76}$$

[8] This expression only holds if the material information is completely contained in the source terms. For an expression with different constant permeabilities and permittivities at neighbouring elements see [13, 64].

to compromise between the two flux schemes: For $\alpha = 0$ we recover the central flux (3.62), whereas for $\alpha = 1$ we have the pure upwind flux (3.75). Any value $0 < \alpha < 1$ will result in a mixture of those fluxes. Thus, the amount of artificially introduced dissipation but also the stability of the overall scheme is controlled by the upwind parameter α. In the calculations within this thesis we only use pure upwind flux ($\alpha = 1$) to allow for a maximal flux stabilization. For an analysis of the stability and convergence behavior of the DGTD upwind scheme for Maxwell's curl equations with respect to the upwind parameter α see [14, 24].

One can now readily incorporate Maxwell's equations in conservation law form (3.61) and the numerical flux (3.75) into the DGTD scheme (3.28).

3.4 Physical boundary conditions and field sources

As pointed out in section 3.1 the numerical flux is used to recover the global solution of the DGTD scheme from the local solutions at each element. Additionally, one can utilize the numerical flux to impose physical boundary conditions as well as to inject electromagnetic fields at the interface between two neighboring elements [63].

Let us consider a 2D sample mesh consisting of a single circular scatterer embedded in a contrasting non-dispersive homogeneous material (cf. fig. 3.4). The scatterer shall be surrounded by a contour, the so-called *total-field/scattered-field (TfSf) contour* (marked by a red line in fig. 3.4), which divides the computational domain in two regions. The area enclosed by the TfSf contour contains the total electromagnetic field $(\mathbf{E}_{\text{tot}}, \mathbf{B}_{\text{tot}})$, which is the sum of the incident electromagnetic field $(\mathbf{E}_{\text{inc}}, \mathbf{B}_{\text{inc}})$ and the electromagnetic field scattered by the scatterer $(\mathbf{E}_{\text{scat}}, \mathbf{B}_{\text{scat}})$, i.e.

$$\mathbf{E}_{\text{tot}}(\mathbf{r}, t) = \mathbf{E}_{\text{inc}}(\mathbf{r}, t) + \mathbf{E}_{\text{scat}}(\mathbf{r}, t) \tag{3.77}$$

$$\mathbf{B}_{\text{tot}}(\mathbf{r}, t) = \mathbf{B}_{\text{inc}}(\mathbf{r}, t) + \mathbf{B}_{\text{scat}}(\mathbf{r}, t). \tag{3.78}$$

We refer to this area as the total field region. The incident field $(\mathbf{E}_{\text{inc}}, \mathbf{B}_{\text{inc}})$ is given by a predetermined analytical expression depending on what kind of external excitation is required, e.g. a plane wave with a Gaussian envelope. In contrast, only the scattered field $(\mathbf{E}_{\text{scat}}, \mathbf{B}_{\text{scat}})$ is contained in the area surrounding the total field region (outside of the TfSf contour). We refer to this outside region as the scattered field region. We now focus on two neighboring elements at the TfSf contour, one in the scattered field region denoted by $(+)$ and one in the total field region denoted by $(-)$ (cf. zoom on the l.h.s. of fig. 3.4). The incident field is now introduced into the DGTD scheme by an additional source (see (3.28)) in the form of a numerical upwind flux (3.75). For the element $(-)$ in the total field area this means that a source

$$\mathbf{s}_- \equiv \begin{pmatrix} \mathbf{E}_{\text{source}} \\ \mathbf{B}_{\text{source}} \end{pmatrix} = \frac{1}{2} \begin{pmatrix} -\breve{\mathbf{n}} \times \mathbf{B}_{\text{inc}} \\ \breve{\mathbf{n}} \times \mathbf{E}_{\text{inc}} \end{pmatrix} + \frac{\alpha}{2\sqrt{\mu_0 \varepsilon_0}} \begin{pmatrix} \breve{\mathbf{n}} \, (\breve{\mathbf{n}} \cdot \mathbf{E}_{\text{inc}}) - \mathbf{E}_{\text{inc}} \\ \breve{\mathbf{n}} \, (\breve{\mathbf{n}} \cdot \mathbf{B}_{\text{inc}}) - \mathbf{B}_{\text{inc}} \end{pmatrix} \tag{3.79}$$

is introduced at every node that is lying on the TfSf contour (see fig. 3.5). In contrast, at every node lying on the TfSf contour, which then belongs to the $(+)$-element, a source with

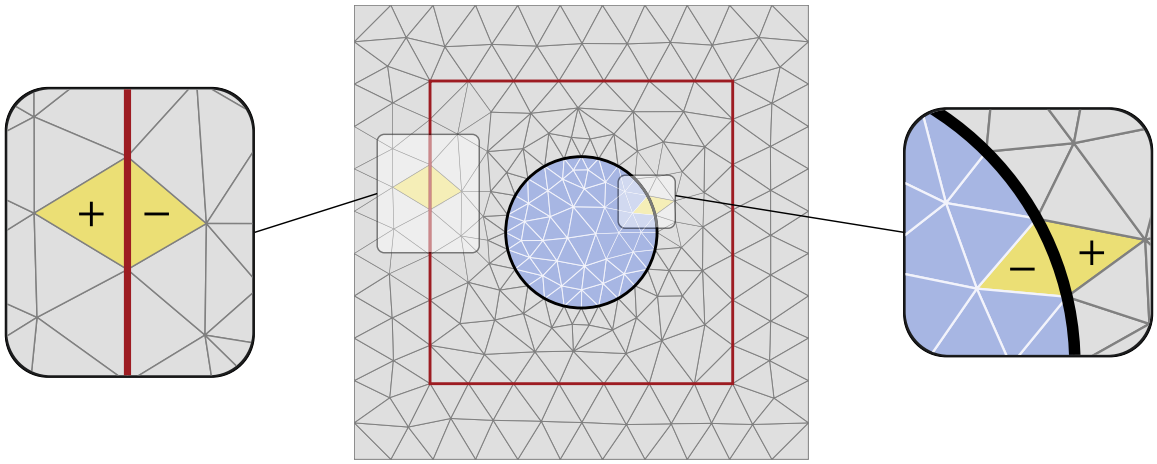

Figure 3.4: Sample mesh: scatterer (blue) surrounded by a deviant material (gray). The scatterer is enclosed by the TfSf contour. On the left we see a zoom onto a part of the TfSf contour, whereas on the right we see a zoom onto the interface between scatterer and surrounding material.

the opposite sign compared to (3.79) (see fig. 3.5) is introduced, i.e.

$$\mathbf{s}_+ = -\mathbf{s}_- = \begin{pmatrix} -\mathbf{E}_{\text{source}} \\ -\mathbf{B}_{\text{source}} \end{pmatrix}. \tag{3.80}$$

To inject a field throughout the whole TfSf contour the addition of sources according to (3.79) and (3.80) is executed not only for one but for every pair of elements along the TfSf contour.

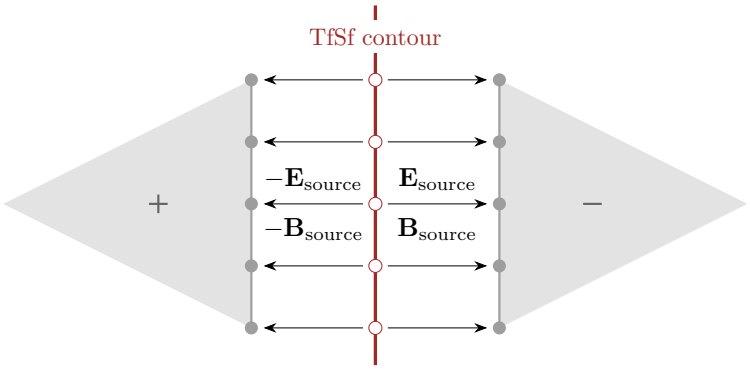

Figure 3.5: Addition of field sources for two neighboring elements at the nodes along the TfSf contour. The element in the total field region is denoted by (−) whereas the element in the scattered field region is denoted by (+) (cf. fig. 3.4).

In a similar manner, boundary conditions can be imposed by adding the appropriate numerical fluxes. Let us take, for example, two neighboring elements at the boundary of a scatterer, where the element within the scatterer is now denoted by (−) and the element outside the scatterer is denoted by (+) (see fig. 3.4). To apply a boundary condition, one simply has to insert the desired values for the electric and magnetic field of the (−) and (+) element into the

expression for the numerical flux, e.g. (3.75). For an element lying on the edge of the whole computational domain the imposition of boundary conditions is a bit more complicated as there is no corresponding neighboring element at the edge. In this case one has to construct a virtual or *ghost state* to mimic a neighboring element with virtual field values at the boundary. These virtual field values are again inserted into the numerical flux as neighboring element values. For instance, one can impose an approximation to the Silver-Müller radiation conditions [65] for finite distances to the scatterer to simulate out-going radiation. In this case one chooses the ghost states to have the electromagnetic field values $(\mathbf{E}_+, \mathbf{B}_+) = (-\mathbf{E}_-, -\mathbf{B}_-)$. For more information on how to derive these values see [57]. Note that in every scattering simulation within this thesis we use this approximation to the Silver-Müller radiation conditions at the outermost boundary of the computational domain. However, in most applications the approximation is not sufficient and reflections emerge from the boundary where the Silver-Müller radiation conditions are applied. We, therefore, employ the so-called (uniaxial) perfectly matched layers (PML) in addition [66, 67]. The idea is to attenuate the electromagnetic waves by an artificial absorbing material, which is non-reflecting due to 'perfect' impedance matching between itself and the adjacent physical material. For a elaborate study on the Silver-Müller boundary conditions and PMLs within the DGTD scheme see [57, 63].

The construction of ghost states is crucial to the imposition of the hard-wall boundary conditions in the hydrodynamic model. Therefore, see section 4.4 for further information.

3.5 Nonlinear problems and scheme stabilization

So far, we have only discussed linear hyperbolic problems. Unfortunately, there are certain issues emerging when dealing with nonlinear problems. As pointed out in section 3.2, if the conservation law (3.31) is linear, every characteristic is represented by a straight line with the same slope independent of the initial data. Hence, one can illustrate a set of parallel straight lines for different initial values (see fig. 3.6a). As a result, the solution translates uniformly with the characteristic speed [15, 62]. This no longer holds if the flux depends nonlinearly on the solution. Let us, for instance, again consider the one-dimensional quasi-linear form of the conservation law

$$\partial_t u + f'(u(x,t))\,\partial_x u = 0 \tag{3.33}$$

and a smooth initial value, e.g. a Gaussian profile

$$u(x,0) = \exp\left[-\frac{1}{2}\left(\frac{x-x_0}{\sigma}\right)^2\right]. \tag{3.81}$$

Then (independent of whether the problem is linear or not) the solution u is constant along the characteristic curve $x(t)$ as long as $f'(u) = x'(t)$. Hence, the characteristics can be represented by straight lines $x(t) = f'(u)\,t + \xi$ with characteristic speed $f'(u)$ (cf. section 3.2). However, in the nonlinear case $f'(u)$ depends on the initial data and, thus, for different initial values the characteristics are not necessarily parallel. The simplest type of nonlinear equations is the inviscid Burger equation [15], where the flux is given by $f(u) = \frac{1}{2}u^2$. For this case we have

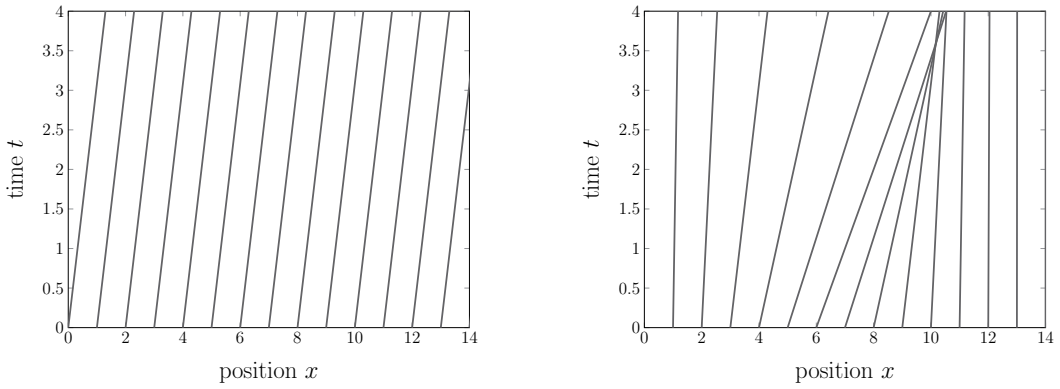

Figure 3.6: Characteristics at different initial values for (a) a linear hyperbolic problem (b) a nonlinear hyperbolic problem.

plotted the characteristics $x(t) = u\,t + \xi$ using the Gaussian initial value profile (3.81) centered around $x_0 = 6$ with a width of $\sigma = 4$ in fig. 3.6b. Because the characteristic speed varies for different initial values, some parts of the Gaussian profile move faster than others. This leads to a gradual distortion of the wave as the solution evolves in time fig. 3.7. Eventually, at some point in time the characteristics cross. In the present example, three of the characteristics cross at $t = 3.5$ (see fig. 3.6b). Therefore, the solution becomes discontinuous, as it is triple valued. At this point the solution becomes unphysical and the conservation law (3.33) breaks down[9]. The discontinuity itself is referred to as a shock, which moves with the speed given by the Rankine-Hugoniot condition

$$c_{\text{shock}} = \frac{f(u_{\text{R}}) - f(u_{\text{L}})}{u_{\text{R}} - u_{\text{L}}}, \tag{3.82}$$

where u_{L} is the solution on the left and u_{R} is the solution on the right of the shock. With that being said, most realistic physical systems are modeled by (3.33) only insufficiently. For example, in gas dynamics an additional viscosity term needs to be included to the internal friction between the gas particles, yielding

$$\partial_t\, u + f'(u(x,t))\;\partial_x\, u = \epsilon\,\partial_x^2\, u \tag{3.83}$$

for $\epsilon > 0$. One can show that (3.83) has a unique solution for all times $t > 0$ and any set of initial conditions. For $\epsilon = 0$ the original solution of (3.33) is recovered from the solution of (3.83). Mathematically speaking, one can always stabilize a nonlinear numerical scheme by introducing a small ($\epsilon \to 0$) viscosity term as in (3.83), which results in energy dissipation. This is referred to as the *vanishing-viscosity* approach [15]. In our numerical implementation we stabilize

[9] Nevertheless, the integral form, i.e. the weak form (cf. (3.9)) is still valid. This also holds for the strong form (cf. (3.10)), which includes the numerical flux. One could, hence, eliminate the shock by introducing an appropriate flux. Instead, we will see a different approach to stabilize the numerical scheme in the following.

the numerical scheme by using so-called exponential filters [14], which introduce the desired dissipation. In nonlinear problems instabilities usually stem from fast spatial oscillations, which are related to higher-order polynomials in the field expansions. The idea is then to damp these higher-order polynomials exponentially. For a detailed description on how these filters are introduced into the numerical scheme see [21].

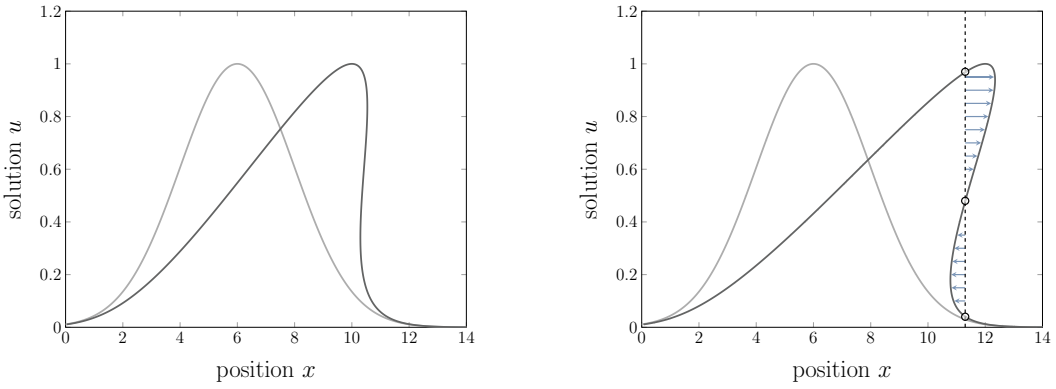

Figure 3.7: Solution of a nonlinear problem at different times. The initial wave profile is plotted in light gray. (a) Wave distortion is clearly visible at $t = 2$. (b) At a later time $t = 6$ the wave distortion has progressed and the solution is tripled-valued.

CHAPTER 4

Nonlinear metallic nano-structures

The field of nonlinear optics has emerged due to the discovery of SHG on crystalline glass by Franken et al. [8]. It has gained special interest in the plasmonic community after it has been observed by Brown et al. that SHG cannot only be found in dielectric crystals but also in silver films [10]. Since then it has been a quest on how to describe the nonlinear response of metallic structures theoretically. A well-known model for the description of metals is the Drude model [28, 68]. As this model is quite simple in nature, it is no longer sufficient for small plasmonic structures in the nanometer regime. In this case the hydrodynamic material model has been proven to be more successful [16–19] as it not only features nonlinear but also nonlocal material properties.

The following chapter is dedicated to the hydrodynamic model for the description of conduction electrons in metals. We, therefore, discuss in section 4.1 under which circumstances this material model is applicable. Though the hydrodynamic model has already been studied extensively in some previous works within our research group [20, 21], our advance within this thesis lies in the perturbative approach to the model, which is introduced in section 4.2. We will demonstrate later in section 4.5 how this approach yields additional information, which is not accessible otherwise. Using the hydrodynamic model we have to make some adjustments to incorporate it into the DGTD framework, especially, when applying the perturbative approach. These adjustments can be found in section 4.3. Furthermore, as we do not consider infinitely extended materials but rather focus on nanoparticles, we need to choose boundary conditions, which we discuss in section 4.4 in the context of the DGTD method. At last we show the results of the perturbative approach to the hydrodynamic model section 4.5, where we take a look at the second-order response of nanoantennas. In particular, we perform a special kind of frequency tuned wave-mixing on these structures. Note, that we have published the findings in section 4.5 previously in [H1].

4.1 The hydrodynamic material model

A simple way to describe metals is by imagining the material as a compound of two separate systems: a system of positive ions, which is approximated by a uniform positive background, and a system of free conduction electrons moving in the constant potential of this background. The conduction electrons are then modeled by a Fermionic gas of non-interacting particles, as suggested by the Sommerfeld theory of the free electron gas [43, 69]. Although this is an overly simplified model for metals, many properties like a linear specific heat capacity [70] and temperature-independent magnetic susceptibility at temperatures well below the Fermi temperature [71] are reproduced by the Sommerfeld model. This is quite remarkable given that the conduction electrons in a metal are not free but, in fact, interact with each other via the Coulomb interaction. Typically, the Coulomb energy in metals is comparable to the electron kinetic energy [72] and, thus, cannot be viewed as a small perturbation. Furthermore, the Coulomb interaction is long-ranged. Hence, each electron does not only interact with the electrons in its vicinity but with a very large number of electrons. This poses a fairly challenging many-body problem. Such a system of interacting electrons is referred to as a *charged Fermi liquid* or *quantum plasma* [73].

Instead of solving the whole many-body problem one can take a phenomenological course. One approach that justifies the free particle picture for metals to some extent is given by the *Landau-Silin theory of charged Fermi liquids* [72, 73], which was first developed by Landau in the 1950s for uncharged interacting Fermions [74] and extended by Silin to charged Fermions interacting via Coulomb interaction [25]. Within this theory one does not consider the bare conduction electrons but rather so-called *dressed electrons* which interact with each other via a short-ranged effective interaction, while moving in the potential of the positive ionic background: As a conduction electron moves through the material, it repels other conduction electrons due to the Coulomb interaction. This results in a region surrounding the electron where the probability to find another electron is very small. Hence the electron is effectively surrounded by a positive charge distribution due to the ionic background and is, thus, referred to as a *screening hole*. The bare conduction electron and its screening hole form a *quasi-particle* that is referred to as a dressed electron. Because the screening hole compensates the electron's negative charge, the electron's electric field is screened at large distances. Hence, the effective interaction between the dressed electrons is short-ranged. Note, that the quasi-particles still have the same quantum numbers as the free particles, e.g. spin, momentum and charge. However, its dynamic properties such as mass and magnetic moment are fundamentally different from the ones of the bare electron. These quantities need to be accessed externally, i.e. by experimental data. Thus, the Landau-Silin theory is a phenomenological one.

One fundamental assumption of the Landau-Silin theory is that, if the interaction between the originally non-interacting valence electrons is turned on adiabatically, the system will evolve from a given free-particle eigenstate into the ground-state of the interacting Fermi liquid. If this is the case, this system of interacting quasi-particles is called a *normal* Fermi liquid. There is a one-to-one correspondence between the free-particle state and the interacting quasi-particle state: the quasi-particles are still Fermionic with a sharp Fermi surface at zero temperature. The difference is now that the quasi-particles no longer move independently from each other but instead interact with each other self-consistently. As a consequence, the quasi-particle energies

$\epsilon_{\mathbf{p}\sigma}$ vary with the distribution function $n_{\mathbf{p}\sigma}$ for a given momentum $\mathbf{p}$ and spin state σ. This distribution function is given by[1]

$$n_{\mathbf{p}\sigma} = \frac{1}{\exp\left(\frac{\epsilon_{\mathbf{p}\sigma}[n_{\mathbf{p}\sigma}]-\mu}{k_\mathrm{B}T}\right)+1}, \tag{4.1}$$

where k_B is the Boltzmann constant, T is the temperature and μ denotes the chemical potential. At $T=0$ the distribution function is given by a step function $\Theta(\epsilon_\mathrm{F}-\epsilon_{\mathbf{p}\sigma})$ around the chemical potential at zero temperature, i.e. the Fermi energy ϵ_F. Though (4.1) holds some resemblance with the free-particle distribution function [76], we would like to point out that its functional form is much more complicated due to the functional dependence of the quasi-particle energy on the distribution function itself. Note, that not only the quasi-particle energies but also the system's total energy density is a functional of the distribution function (4.1).

Let us assume that the interacting system is in its ground state. In this case the Fermi liquid is homogeneous and in equilibrium. The equilibrium distribution function shall be given by $n^0_{\mathbf{p}\sigma}$, which depends on the equilibrium quasi-particle energy $\epsilon^0_{\mathbf{p}\sigma} = \epsilon_{\mathbf{p}\sigma}[n^0_{\mathbf{p}\sigma}]$ according to (4.1). We then perturb the system by applying an external macroscopic potential $U(\mathbf{r},t)$, which varies in space and time. As a result of this perturbation, the fluid is no longer homogeneous and the ground state distribution $n^0_{\mathbf{p}\sigma}$ is altered by a small amount $\delta n_{\mathbf{p}\sigma}$, i.e.

$$n_{\mathbf{p}\sigma}(\mathbf{r},t) = n^{(0)}_{\mathbf{p}\sigma} + \delta n_{\mathbf{p}\sigma}(\mathbf{r},t). \tag{4.2}$$

In principle, the notion of the distribution function $n_{\mathbf{p}\sigma}$ as a function of time and space would violate the uncertainty principle, since the quasi-particle's position $\mathbf{r}$ and momentum $\mathbf{p}$ cannot be known simultaneously. The same is true for the quasi-particle energy $\epsilon_{\mathbf{p}\sigma}$ and the time t. This conflict is solved by the claim that the perturbation is macroscopic. The perturbation's variation in time and space shall be such that they are much larger than any corresponding atomic parameter. For example, if the perturbation and, consequently, the variation of the distribution function vary over a characteristic length λ, the particles become localized in space within λ. At the same time the momentum of the quasi-particles vary over a characteristic momentum $\Delta p = \frac{k_\mathrm{B}T}{v_\mathrm{F}}$ at a temperature T, where v_F is the Fermi velocity, i.e. the velocity of the quasi-particle at the Fermi surface in equilibrium. Then due to the uncertainty principle the relation

$$\lambda \gg \frac{\hbar}{\Delta p} = \frac{\hbar v_\mathrm{F}}{k_\mathrm{B}T} \tag{4.3}$$

must be fulfilled [73, 75].

Landau claimed that for uncharged particles the total energy density can be expressed by a Taylor expansion [74]. Accordingly, the system's kinetic energy density as a functional of the

[1] For a proof that (4.1) is indeed the quasi-particle distribution see [75]. Note, that though at first glance (4.1) might resemble the Fermi distribution, it is, in fact, a more complicated function due to the dependence of the quasi-particle energy $\epsilon_{\mathbf{p}\sigma}$ on the distribution function $n_{\mathbf{p}\sigma}$.

distribution function can be written as

$$\mathcal{E}[n_{\mathbf{p}\sigma}] = \mathcal{E}_0 + \sum_{\sigma} \int \frac{\mathrm{d}^3 p}{(2\pi\hbar)^3}\, \epsilon^0_{\mathbf{p}\sigma}\, \delta n_{\mathbf{p}\sigma} + \frac{1}{2} \sum_{\sigma,\sigma'} \int \frac{\mathrm{d}^3 p}{(2\pi\hbar)^3} \int \frac{\mathrm{d}^3 p'}{(2\pi\hbar)^3}\, f_{\mathbf{p}\sigma,\mathbf{p}'\sigma'}\, \delta n_{\mathbf{p}'\sigma'}\, \delta n_{\mathbf{p}\sigma} + \dots \tag{4.4}$$

as long as the deviation from the equilibrium distribution $\delta n_{\mathbf{p}\sigma}$ is small. Thereby, $\mathcal{E}_0 = \mathcal{E}[n^0_{\mathbf{p}\sigma}]$ denotes the system's ground state energy. The quasi-particle ground-state energy is given by the first variational derivative of the kinetic energy density

$$\epsilon^0_{\mathbf{p}\sigma} = \left.\frac{\delta E}{\delta n_{\mathbf{p}\sigma}}\right|_{n^0_{\mathbf{p}\sigma}} \tag{4.5}$$

in (4.4). Moreover, the two-quasi-particle interaction is contained in the interaction energy $f_{\mathbf{p}\sigma,\mathbf{p}'\sigma'}$, which is given by the second variational derivative of the kinetic energy density

$$f_{\mathbf{p}\sigma,\mathbf{p}'\sigma'} = \left.\frac{\delta^2 E}{\delta n_{\mathbf{p}\sigma} \delta n_{\mathbf{p}'\sigma'}}\right|_{n^0_{\mathbf{p}\sigma}}. \tag{4.6}$$

For (4.4) to be valid, the interaction energy (4.6) must be short-ranged, meaning that the interaction length between the quasi-particles are required to be much smaller than the characteristic length λ of the perturbation. Silin has shown that expression (4.4) still holds for charged Fermi liquids, where formally the bare particles interact via the long-ranged Coulomb interaction [25]. Using the Thomas-Fermi screening theory one can show that the effective interaction between the quasi-particles is, in fact, short-ranged [73]. For a more comprehensive microscopic derivation of (4.4) from first principles we refer to the textbook of Pines and Nozières [73, chapter 5]. It is usually convenient to define the departure from the ground-state kinetic energy density by

$$\delta\mathcal{E} = \sum_{\sigma} \int \frac{\mathrm{d}^3 p}{(2\pi\hbar)^3}\, \epsilon_{\mathbf{p}\sigma}\, \delta n_{\mathbf{p}\sigma}, \tag{4.7}$$

where we have the quasi-particle energy

$$\epsilon_{\mathbf{p}\sigma} = \epsilon^0_{\mathbf{p}\sigma} + \frac{1}{2} \sum_{\sigma'} \int \frac{\mathrm{d}^3 p'}{(2\pi\hbar)^3}\, f_{\mathbf{p}\sigma,\mathbf{p}'\sigma'}\, \delta n_{\mathbf{p}'\sigma'} + \dots\ . \tag{4.8}$$

Then we have $\mathcal{E} = \mathcal{E}_0 + \delta\mathcal{E}$ for the total kinetic energy density. From the quasi-particle Hamiltonian (4.8) one can construct a transport equation by regarding the flow through a small element in phase space $\mathrm{d}^3 p\, \mathrm{d}^3 r$. In doing so we arrive at Liouville's equation [77] for quasi-particles

$$\frac{\partial n_{\mathbf{p}\sigma}}{\partial t} + \frac{\mathrm{d}\mathbf{r}}{\mathrm{d}t} \cdot \nabla n_{\mathbf{p}\sigma} + \frac{\mathrm{d}\mathbf{p}}{\mathrm{d}t} \cdot \nabla_{\mathbf{p}} n_{\mathbf{p}\sigma} = 0. \tag{4.9}$$

The last two terms on the l.h.s. of (4.9) describe the changes in the distribution function resulting from continuous changes in position and momentum. Yet, the transport equation (4.9) does not account for sudden changes in momenta due to quasi-particle collisions. Usually, these are considered by replacing the r.h.s. of (4.9) by the so-called collision integral $I[n_{\mathbf{p}\sigma}]$ [73, 75]. After including the collision integral, the transport equation (4.9) can be rewritten by

$$\frac{\partial n_{\mathbf{p}\sigma}}{\partial t} + (\nabla_{\mathbf{p}}\epsilon_{\mathbf{p}\sigma}) \cdot (\nabla n_{\mathbf{p}\sigma}) - (\nabla U + \nabla\epsilon_{\mathbf{p}\sigma}) \cdot (\nabla_{\mathbf{p}} n_{\mathbf{p}\sigma}) = I[n_{\mathbf{p}\sigma}], \tag{4.10}$$

where we have identified the group velocity of the quasi-particle wave-packet by

$$\frac{\mathrm{d}\mathbf{r}}{\mathrm{d}t} = \nabla_{\mathbf{p}}\epsilon_{\mathbf{p}\sigma}(\mathbf{r}, t) \tag{4.11}$$

and the force density acting on each quasi-particle

$$\frac{\mathrm{d}\mathbf{p}}{\mathrm{d}t} = -\nabla U - \nabla\epsilon_{\mathbf{p}\sigma} \tag{4.12}$$

[75]. The first term on the r.h.s. of (4.12) is the force due to the external potential, whereas the second term represents the force acting on each quasi-particle due to the interaction with the surrounding quasi-particles.

One can now derive the conservation laws of the quasi-particles by calculating the moments of the transport equation (4.10). The first moment is obtained by integrating (4.10) over momentum and spin space, i.e. $\sum_\sigma \int \frac{\mathrm{d}^3 p}{(2\pi\hbar)^3} \ldots$. If we define the quasi-particle density

$$n(\mathbf{r}, t) = \sum_\sigma \int \frac{\mathrm{d}^3 p}{(2\pi\hbar)^3}\; n_{\mathbf{p}\sigma}(\mathbf{r}, t) \tag{4.13}$$

and the flux of quasi-particles

$$\mathbf{i}(\mathbf{r}, t) = \sum_\sigma \int \frac{\mathrm{d}^3 p}{(2\pi\hbar)^3}\; [\nabla_{\mathbf{p}}\epsilon_{\mathbf{p}\sigma}(\mathbf{r}, t)]\, n_{\mathbf{p}\sigma}(\mathbf{r}, t), \tag{4.14}$$

the first moment yields the quasi-particle density conservation law[2]

$$\partial_t\, n(\mathbf{r}, t) + \nabla \cdot \mathbf{i}(\mathbf{r}, t) = 0. \tag{4.15}$$

Thereby, the average over the collision integral vanishes as the number of particles shall be conserved in collisions. If we introduce the charge density $\varrho_\mathrm{e} = q_\mathrm{e}\, n$ and the current density $\mathbf{J} = q_\mathrm{e}\, \mathbf{i}$, we obtain the continuity equation

$$\partial_t\, \varrho_\mathrm{e}(\mathbf{r}, t) + \nabla \cdot \mathbf{J}(\mathbf{r}, t) = 0 \tag{4.16}$$

[2] See appendix D.1 for more information on the deviation of (4.15).

from (4.15).

We now calculate the second moment of (4.10) by first multiplying the equation by the momentum $\mathbf{p}$ and then taking the average. If we define the momentum density

$$\mathbf{g}(\mathbf{r},t) = \sum_\sigma \int \frac{\mathrm{d}^3 p}{(2\pi\hbar)^3}\ \mathbf{p}\, n_{\mathbf{p}\sigma} \tag{4.17}$$

the convection tensor

$$\underline{\mathbf{t}} = \sum_\sigma \int \frac{\mathrm{d}^3 p}{(2\pi\hbar)^3}\ \mathbf{p} \otimes (\nabla_{\mathbf{p}} \epsilon_{\mathbf{p}\sigma})\, n_{\mathbf{p}\sigma} \tag{4.18}$$

and the pressure

$$\mathcal{P} = \sum_\sigma \int \frac{\mathrm{d}^3 p}{(2\pi\hbar)^3}\ \epsilon_{\mathbf{p}\sigma}\, n_{\mathbf{p}\sigma} - \mathcal{E}, \tag{4.19}$$

we obtain the momentum conservation law for quasi-particles

$$\partial_t\, \mathbf{g} + \nabla \cdot \underline{\mathbf{t}} + \nabla \mathcal{P} + n\, \nabla U = 0. \tag{4.20}$$

Note that, in arriving at (4.20) we have used that the second moment of the collision integral vanishes identically as the momentum shall be conserved in particle collisions. For more information on how to derive (4.20) in detail see appendix D.1. Similar to the considerations on the first moment we need to make further adjustments to (4.20) if we want to express the conservation law in terms of the current and charge density. To this end, we analyze the tensor (4.18): Under the premise that the interaction energy (4.6) is short-ranged, the expansion of the energy density (4.4) resembles the Hartree-Fock energy density [75, 76]. Hence, it is plausible to apply the Hartree-Fock approximation, also known as mean field approximation (MFA), to (4.18). Within this approximation the inter-particle interaction is expressed by an effective mean field [76], where the fluctuation of each observable around its thermodynamic value are neglected[3]. In the concrete case of (4.18) this means

$$\underline{\mathbf{t}}(\mathbf{r},t) \approx \frac{1}{n}\, \mathbf{g}(\mathbf{r},t) \otimes \mathbf{i}(\mathbf{r},t), \tag{4.21}$$

where we have used the expressions (4.17) and (4.14). The normalization by the particle density in (4.21) is due to our choice of the momentum space integration. One can show that within a Galilean invariant system the flux $\mathbf{i}$ can be expressed by the momentum density $\mathbf{g}$ [75]

$$\mathbf{i}(\mathbf{r},t) = \frac{1}{m_0}\, \mathbf{g}(\mathbf{r},t), \tag{4.22}$$

[3]For example, if we have two operators $\hat{A}$ and $\hat{B}$, we can express their product by $\hat{A}\hat{B} = (A - \langle\hat{A}\rangle)(B - \langle\hat{B}\rangle) + \hat{A}\langle\hat{B}\rangle + \langle\hat{A}\rangle\hat{B} - \langle\hat{A}\rangle\langle\hat{B}\rangle$ in general. Within the MFA the fluctuations $(A - \langle\hat{A}\rangle)$ and $(B - \langle\hat{B}\rangle)$ are neglected [77], yielding $\hat{A}\hat{B} \approx +\hat{A}\langle\hat{B}\rangle + \langle\hat{A}\rangle\hat{B} - \langle\hat{A}\rangle\langle\hat{B}\rangle$ and consequently $\langle\hat{A}\hat{B}\rangle \approx \langle\hat{A}\rangle\langle\hat{B}\rangle$ for the overall expectation value.

where m_0 is the bare electron mass. Thus, (4.20) reads

$$\partial_t \mathbf{g} + \nabla \cdot \left(\frac{1}{n\, m_0} \mathbf{g} \otimes \mathbf{g} \right) + \nabla \mathcal{P} + n\, \nabla U = 0 \tag{4.23}$$

By multiplying (4.23) by $\frac{q_\mathrm{e}}{m_\mathrm{e}}$, where q_e denotes the electron charge, we obtain the Euler equation [78]

$$\partial_t \mathbf{J} + \nabla \cdot \left(\frac{1}{\varrho_\mathrm{e}} \mathbf{J} \otimes \mathbf{J} \right) + \frac{q_\mathrm{e}}{m_0} \nabla \mathcal{P} + \frac{q_\mathrm{e}}{m_0} n\, \nabla U = 0, \tag{4.24}$$

where the second term on the l.h.s. of (4.24) describes convection within the Fermi liquid. One can take isotropic dissipation into account by replacing the r.h.s. of (4.24) by $(-\gamma\, \mathbf{J})$, where γ is a phenomenological damping parameter. In this case the damping is a product of the quasi-particle collisions, which result in a finite lifetime of the quasi-particles. Hence, the damping parameter is equivalent to the collision frequency. Note, that the Fermi liquid theory only makes sense if the lifetime of the quasi-particles exceeds the time of the adiabatic switching process. This can only be achieved if quasi-particles have momenta near the Fermi surface: due to the exclusion principle the phase-space in this region is small and, hence, quasi-particle decay is less likely to happen [72]. Thus, all of our considerations shall hold near equilibrium for which $\delta n_{\mathbf{p}\sigma}$ is small, i.e. at low temperatures.
The external potential gradient in (4.24) is given by the negative Lorentz force

$$\mathbf{F}_\mathrm{Lorentz} = q_\mathrm{e}(\mathbf{E} + \mathbf{v} \times \mathbf{B}) = -\nabla U \tag{4.25}$$

since the system shall be perturbed by electromagnetic waves. Note, that the mean particle velocity $\mathbf{v}$ is related to the current density by $\mathbf{J} = \varrho_\mathrm{e} \mathbf{v}$. Then the Euler equation can be written as

$$\begin{aligned} &\partial_t \mathbf{J}(\mathbf{r},t) + \nabla \cdot \left[\frac{1}{\varrho_\mathrm{e}(\mathbf{r},t)} \mathbf{J}(\mathbf{r},t) \otimes \mathbf{J}(\mathbf{r},t) \right] = \\ &\quad = -\gamma\, \mathbf{J}(\mathbf{r},t) + \frac{q_\mathrm{e}}{m_0} \left[\varrho_\mathrm{e}(\mathbf{r},t)\, \mathbf{E}(\mathbf{r},t) + \mathbf{J}(\mathbf{r},t) \times \mathbf{B}(\mathbf{r},t) \right] - \frac{q_\mathrm{e}}{m_0} \nabla \mathcal{P}(\mathbf{r},t). \end{aligned} \tag{4.26}$$

It describes the damped, convective motion of quasi-particles which move under the influence of an external Lorentz force, where the quasi-particles are under a certain pressure, which contains the quasi-particle interaction. The motion is not only nonlinear, but due to the convection and the pressure gradient in (4.26) also nonlocal [79].

From (4.26) we understand why the free electron model is so successful. The same form of transport equation could have been attained by using an effective free particle model, i.e. the Sommerfeld model [76], at $T \approx 0$, where the quasi-particle interaction and the influence of the ionic lattice is absorbed in a renormalized effective mass m_e[4]. The effective free particle

[4]This definition of the effective mass differs from the usual definition in condensed matter theory, where only the influence of the positive ionic lattice is taken into account [72, 76]. Furthermore, the effective mass of Landau's Fermi liquid theory is only clearly defined for materials with an isotropic distribution function such as

Hamiltonian of this model is given by [76]

$$\hat{H}_{\mathrm{S}} = \frac{\hat{p}^2}{2\,m_{\mathrm{e}}}\,\Theta\left(p_{\mathrm{F}} - p\right). \tag{4.27}$$

Thus, within this model the ionic lattice is described by a constant homogeneous positive background denoted by a constant positive charge distribution $\varrho_{\mathrm{n}} = \text{const.}$. For an overall neutral material with a total charge

$$\varrho(\mathbf{r}, t) = \varrho_{\mathrm{n}} + \varrho_{\mathrm{e}}(\mathbf{r}, t) \tag{4.28}$$

the positive charge of the ionic background ϱ_{n} balances the time-dependent charge of the Fermi liquid $\varrho_{\mathrm{e}}(\mathbf{r}, t)$.

Using (4.27) one then calculates the equation of motion for the free particle Wigner function [80]. In the classical limit ($\hbar \to 0$) the second moment of the equation of motion has the same form as (4.33) [81]. Hence, the quasi-particles move as if they were free particles with a renormalized mass under a certain pressure and with some phenomenological damping[5]. Effectively, one can take the particle interaction into account by replacing the bare electron mass by an effective mass m_{e} and calculating the pressure for the effective Hamiltonian (4.27). From the internal energy, i.e. the expectation value of the Hamiltonian (4.27),

$$\langle \hat{H}_{\mathrm{S}} \rangle = V \sum_{\sigma} \int \frac{\mathrm{d}^3 p}{(2\pi\hbar)^3}\,\frac{p^2}{2\,m_{\mathrm{e}}}\,\Theta\left(p_{\mathrm{F}} - p\right), \tag{4.29}$$

we obtain the pressure according to thermodynamics [86] by

$$\mathcal{P} = -\left(\frac{\partial \langle \hat{H}_{\mathrm{s}} \rangle}{\partial V}\right)_{T,N} = \zeta\,(\varrho_{\mathrm{e}}^{0})^{5/3}(\mathbf{r}, t) \tag{4.30}$$

at constant temperature and particle number N, where V is the system's volume and "0" denotes the equilibrium charge density. In arriving at (4.30) we have defined the constant

$$\zeta = \frac{(3\pi^2)^{2/3}\,\hbar^2}{5\,m_{\mathrm{e}}\,q_{\mathrm{e}}^{5/3}} \tag{4.31}$$

The expression (4.30) is known as degeneracy pressure. It emerges from the Pauli exclusion principle, which forbids the Fermions to occupy the same quantum state. However, it has been argued in literature [87] that for excitation frequencies ω much higher than the collision frequency of the particles γ one might use

$$\tilde{\mathcal{P}} \propto \left(\varrho_{\mathrm{e}}^{0}\right)^3 \tag{4.32}$$

alkali metals. For other materials the notion of an effective mass is somewhat artificial [73].

[5] On that note, one can also derive the hydrodynamic material equations by using a classical approach, where the hydrodynamic equations follow from the Bogoliubov–Born–Green–Kirkwood–Yvon (BBGKY) hierarchy [82–85]. However, as this approach is purely classical it lacks information on the particle interaction.

instead of (4.19). This regime, where $\omega \gg \gamma$, is known as the collisionless regime, as particle collisions play no role within this regime. The other end of the spectrum, where $\omega \ll \gamma$, is referred to as the hydrodynamic regime. Whether the assessment to use (4.32) for metals is correct, is still under debate [81, 87–89]. One might consider analyzing the full expression (4.19) in more detail to end the discourse about the pressure. At this point we will not discuss the pressure any further, but instead assume that we are in the hydrodynamic regime, for which we apply the degeneracy pressure (4.30).

Note that the hydrodynamic model does not take any interband transitions into account. We would like to point out that the inclusion of interband transitions is not straightforward. One way to include interband transitions in the case of the linearized hydrodynamic model equations was proposed by Toscano et al. [90] who modified the response function by an effective interband permittivity according to the approach by Liebsch [91]. However, it is not clear how to adapt the full nonlinear hydrodynamic model equations. In this case a look into the microscopic calculation of the Fermi liquid response function according to [73] might give us more insight. We do not touch further upon this matter as it exceeds the scope of this thesis.

We summarize the constitutive equations of the hydrodynamic material model, that we have found in this section, below

Hydrodynamic Equations

$$\partial_t \varrho_\mathrm{e}(\mathbf{r},t) + \nabla \cdot \mathbf{J}(\mathbf{r},t) = 0 \tag{4.16}$$

$$\begin{aligned} &\partial_t \mathbf{J}(\mathbf{r},t) + \nabla \cdot \left[\frac{1}{\varrho_\mathrm{e}(\mathbf{r},t)} \mathbf{J}(\mathbf{r},t) \otimes \mathbf{J}(\mathbf{r},t) \right] = \\ &\quad = -\gamma \mathbf{J}(\mathbf{r},t) + \frac{q_\mathrm{e}}{m_\mathrm{e}} \left[\varrho_\mathrm{e}(\mathbf{r},t)\, \mathbf{E}(\mathbf{r},t) + \mathbf{J}(\mathbf{r},t) \times \mathbf{B}(\mathbf{r},t) \right] - \frac{q_\mathrm{e}}{m_\mathrm{e}} \nabla \mathcal{P}(\mathbf{r},t) \end{aligned} \tag{4.33}$$

One could now solve the hydrodynamic material equations (4.16) and (4.33) alongside with Maxwell's equations (1.7) to (1.10). This has already been done within our research group by C. Prohm [21] and M. Moeferdt [20]. Within this thesis, however, the goal is to solve the hydrodynamic equations by using a perturbative approach (cf. section 4.2). We will see later in section 4.5 that it will provide additional information, which is not accessible by the non-perturbative approach.

4.2 Perturbative approach to the hydrodynamic model

As pointed out in section 2.1 one can represent the nonlinear polarization by a power series of the electric field (2.14) as long as the perturbative light-matter interaction energy is much smaller than the kinetic energy of the quasi-particles. Accordingly, one can also express the current density as well as the charge density of the material, which result from the electric polarization of charges, by a series

$$\varrho_\mathrm{e}(\mathbf{r},t) = \varrho_\mathrm{e}^{(0)}(\mathbf{r}) + \varrho_\mathrm{e}^{(1)}(\mathbf{r},t) + \varrho_\mathrm{e}^{(2)}(\mathbf{r},t) + \dots \tag{4.34}$$

$$\mathbf{J}(\mathbf{r},t) = \mathbf{J}^{(1)}(\mathbf{r},t) + \mathbf{J}^{(2)}(\mathbf{r},t) + \dots \ . \tag{4.35}$$

Note, that in (4.35) we have assumed that there is no static current density ($\mathbf{J}^{(0)} = \mathbf{0}$) prior to the perturbation. Furthermore, the initial static charge density shall be identical to the equilibrium quasi-particle charge density, i.e. $\varrho_{\mathrm{e}}^{(0)} = \varrho_{\mathrm{e}}^{0}$. In the same manner, one can expand the electric and magnetic field which result from the light-matter interaction by

$$\mathbf{E}(\mathbf{r},t) = \mathbf{E}^{(0)}(\mathbf{r}) + \mathbf{E}^{(1)}(\mathbf{r},t) + \mathbf{E}^{(2)}(\mathbf{r},t) + \dots \tag{4.36}$$

$$\mathbf{B}(\mathbf{r},t) = \mathbf{B}^{(1)}(\mathbf{r},t) + \mathbf{B}^{(2)}(\mathbf{r},t) + \dots \ . \tag{4.37}$$

In accordance with the lack of a static current density there is no static magnetic field ($\mathbf{B}^{(0)} = \mathbf{0}$). As the degeneracy pressure (4.19) is a functional of the charge density, we can use (4.34) to expand the pressure in a Taylor series around the equilibrium charge density $\varrho_{\mathrm{e}}^{(0)}$

$$\begin{aligned}
\mathcal{P}[\,\varrho_{\mathrm{e}}(\mathbf{r},t)\,] &= \mathcal{P}^{(0)} + \mathcal{P}^{(1)} + \mathcal{P}^{(2)} + \dots \\
&= \mathcal{P}\Big[\varrho_{\mathrm{e}}^{(0)}(\mathbf{r}) + \varrho_{\mathrm{e}}^{(1)}(\mathbf{r},t) + \varrho_{\mathrm{e}}^{(2)}(\mathbf{r},t) + \dots\Big] = \\
&= \sum_{i=0}^{\infty} \frac{1}{i!} \left(\frac{\partial^i \mathcal{P}}{\partial \varrho_{\mathrm{e}}}\right)\bigg|_{\varrho_{\mathrm{e}}=\varrho_{\mathrm{e}}^{(0)}} \left(\varrho_{\mathrm{e}} - \varrho_{\mathrm{e}}^{(0)}\right)^i
\end{aligned} \tag{4.38}$$

where we require $\sum_{i=1}^{\infty} \varrho_{\mathrm{e}}^{(i)} \ll \varrho_{\mathrm{e}}^{(0)}$. By inserting the expression (4.19) for the degeneracy pressure into (4.38) we calculate each of the orders of the nonlinear pressure

$$\mathcal{P}^{(0)} = \zeta \left(\varrho_{\mathrm{e}}^{(0)}\right)^{5/3} \tag{4.39}$$

$$\mathcal{P}^{(1)} = \frac{5}{3}\,\zeta \left(\varrho_{\mathrm{e}}^{(0)}\right)^{2/3} \varrho_{\mathrm{e}}^{(1)} \tag{4.40}$$

$$\mathcal{P}^{(2)} = \frac{5}{3}\,\zeta \left(\varrho_{\mathrm{e}}^{(0)}\right)^{2/3} \varrho_{\mathrm{e}}^{(2)} + \frac{5}{9}\,\zeta \left(\varrho_{\mathrm{e}}^{(0)}\right)^{-1/3} \left(\varrho_{\mathrm{e}}^{(1)}\right)^2 \tag{4.41}$$

$$\dots \ .$$

We can now proceed to reformulate the set of equations consisting of Maxwell's equations (1.7) to (1.10) and the hydrodynamic material equations (4.16) and (4.33) in terms of nonlinear orders by using the expansions (4.34) to (4.38). Equivalent results are found with the perturbative approach by Sipe et al. [92], where the material properties are expressed in terms of the nonlinear polarization and charge density.

Zeroth order:

From Maxwell's divergence equation for the electric field (1.7) it follows that

$$\nabla \cdot \mathbf{E}^{(0)}(\mathbf{r}) = \frac{1}{\varepsilon_0}\varrho(\mathbf{r},t) \overset{(4.28)}{=} \frac{1}{\varepsilon_0}\Big(\varrho_{\mathrm{e}}^{(0)}(\mathbf{r}) + \varrho_{\mathrm{n}}\Big). \tag{4.42}$$

Euler's equation (4.33) yields

$$\mathbf{E}^{(0)}(\mathbf{r}) = \frac{\zeta}{m_\mathrm{e}} \left(\varrho_\mathrm{e}^{(0)}(\mathbf{r})\right)^{-1/3} \nabla \varrho_\mathrm{e}^{(0)}(\mathbf{r}) \tag{4.43}$$

for the first order fields. The set of equations (4.42) and (4.43) constitute the *Thomas-Fermi model* [76].

First order:

From Maxwell's equations (1.7) to (1.10) we obtain the according set of partial differential equations for the first order fields

$$\nabla \cdot \mathbf{E}^{(1)}(\mathbf{r},t) = \frac{1}{\varepsilon_0}\, \varrho_\mathrm{e}^{(1)}(\mathbf{r},t) \tag{4.44}$$

$$\nabla \cdot \mathbf{B}^{(1)}(\mathbf{r},t) = 0 \tag{4.45}$$

$$\nabla \times \mathbf{E}^{(1)}(\mathbf{r},t) = -\partial_t\, \mathbf{B}^{(1)}(\mathbf{r},t) \tag{4.46}$$

$$\nabla \times \mathbf{B}^{(1)}(\mathbf{r},t) = \mu_0\, \mathbf{J}^{(1)}(\mathbf{r},t) + \mu_0\, \varepsilon_0\, \partial_t\, \mathbf{E}^{(1)}(\mathbf{r},t). \tag{4.47}$$

The first order continuity equation is given by

$$\partial_t\, \varrho_\mathrm{e}^{(1)}(\mathbf{r},t) + \nabla \cdot \mathbf{J}^{(1)}(\mathbf{r},t) = 0, \tag{4.48}$$

whereas the first order Euler equation reads

$$\partial_t\, \mathbf{J}^{(1)}(\mathbf{r},t) + \gamma\, \mathbf{J}^{(1)}(\mathbf{r},t) = \frac{q_\mathrm{e}}{m_\mathrm{e}} \left(\varrho_\mathrm{e}^{(0)}(\mathbf{r})\, \mathbf{E}^{(1)}(\mathbf{r},t) + \varrho_\mathrm{e}^{(1)}(\mathbf{r},t)\, \mathbf{E}^{(0)}(\mathbf{r})\right) - \frac{q_\mathrm{e}}{m_\mathrm{e}}\, \nabla \mathcal{P}^{(1)}\left[\varrho_\mathrm{e}^{(0)}, \varrho_\mathrm{e}^{(1)}\right]. \tag{4.49}$$

Second order:

Accordingly, we obtain the second order set of equations. The corresponding Maxwell's equations are given as

$$\nabla \cdot \mathbf{E}^{(2)}(\mathbf{r},t) = \frac{1}{\varepsilon_0}\, \varrho_\mathrm{e}^{(2)}(\mathbf{r},t) \tag{4.50}$$

$$\nabla \cdot \mathbf{B}^{(2)}(\mathbf{r},t) = 0 \tag{4.51}$$

$$\nabla \times \mathbf{E}^{(2)}(\mathbf{r},t) = -\partial_t\, \mathbf{B}^{(2)}(\mathbf{r},t) \tag{4.52}$$

$$\nabla \times \mathbf{B}^{(2)}(\mathbf{r},t) = \mu_0\, \mathbf{J}^{(2)}(\mathbf{r},t) + \mu_0\, \varepsilon_0\, \partial_t\, \mathbf{E}^{(2)}(\mathbf{r},t), \tag{4.53}$$

whereas the hydrodynamic second-order material equations read

$$\partial_t\, \varrho_\mathrm{e}^{(2)}(\mathbf{r},t) + \nabla \cdot \mathbf{J}^{(2)}(\mathbf{r},t) = 0. \tag{4.54}$$

and

$$\partial_t \mathbf{J}^{(2)}(\mathbf{r},t) + \gamma\, \mathbf{J}^{(2)}(\mathbf{r},t) = \frac{q_\mathrm{e}}{m_\mathrm{e}} \Big(\varrho_\mathrm{e}^{(0)}(\mathbf{r})\, \mathbf{E}^{(2)}(\mathbf{r},t) + \varrho_\mathrm{e}^{(1)}(\mathbf{r},t)\, \mathbf{E}^{(1)}(\mathbf{r},t) + \varrho_\mathrm{e}^{(2)}(\mathbf{r},t)\, \mathbf{E}^{(0)}(\mathbf{r}) \Big) - \\ - \frac{q_\mathrm{e}}{m_\mathrm{e}} \nabla \mathcal{P}^{(2)} \Big[\varrho_\mathrm{e}^{(0)}, \varrho_\mathrm{e}^{(1)}, \varrho_\mathrm{e}^{(2)} \Big]. \tag{4.55}$$

Euler's equations for each of the orders (4.43), (4.49) and (4.55) is simplified vastly if we require the initial equilibrium quasi-particle charge density to have a step profile (cf. fig. 4.1). In this case meaning the charge density has some constant value within the particle and drops abruptly to zero at the particle's boundary (see section 4.4 for further information). We, thus, demand $\nabla \varrho_\mathrm{e}^{(0)} = \mathbf{0}$ within the particle. As a consequence, we can solve the zeroth order set of equations immediately. From (4.43) we see that in this case the static electric field vanishes identically ($\mathbf{E}^{(0)} = \mathbf{0}$). Thus, the static quasi-particle charge density has to balance the charge density of the constant homogeneous ionic background, i.e. $\varrho_\mathrm{e}^{(0)} = -\varrho_\mathrm{n}$. Now, to ensure the overall charge neutrality of the material the higher-order charge densities need to be either zero or oscillate around the equilibrium value $\varrho_\mathrm{e}^{(0)}$. Using the hard-wall boundary conditions, the nonlinear orders of the pressure gradient become

$$\Big(\nabla \mathcal{P} \Big)^{(0)} = 0 \tag{4.56}$$

$$\Big(\nabla \mathcal{P} \Big)^{(1)} = \frac{5}{3}\, \zeta \left(\varrho_\mathrm{e}^{(0)} \right)^{2/3} \nabla \varrho_\mathrm{e}^{(1)} \tag{4.57}$$

$$\Big(\nabla \mathcal{P} \Big)^{(2)} = \frac{10}{9}\, \zeta \left(\varrho_\mathrm{e}^{(0)} \right)^{-1/3} \nabla \varrho_\mathrm{e}^{(2)} + \frac{5}{3}\, \zeta \Big(\varrho_\mathrm{e}^{(0)} \Big)^{2/3} \nabla \Big(\varrho_\mathrm{e}^{(1)} \Big)^2 \tag{4.58}$$

$$\dots\ .$$

These can then be inserted into the Euler equation for each nonlinear order. As a result one can summarize the full set of differential equations (4.44) to (4.55) for each nonlinear order $\alpha \in \mathbb{N}$ by

α-th order:

Maxwell's equations

$$\nabla \cdot \mathbf{E}^{(\alpha)}(\mathbf{r},t) = \frac{1}{\varepsilon_0}\, \varrho_\mathrm{e}^{(\alpha)}(\mathbf{r},t) \tag{4.59}$$

$$\nabla \cdot \mathbf{B}^{(\alpha)}(\mathbf{r},t) = \mathbf{0} \tag{4.60}$$

$$\nabla \times \mathbf{E}^{(\alpha)}(\mathbf{r},t) = \partial_t\, \mathbf{B}^{(\alpha)}(\mathbf{r},t) \tag{4.61}$$

$$\nabla \times \mathbf{B}^{(\alpha)}(\mathbf{r},t) = \mu_0\, \mathbf{J}^{(\alpha)}(\mathbf{r},t) + \mu_0\, \varepsilon_0\, \partial_t\, \mathbf{E}^{(\alpha)}(\mathbf{r},t), \tag{4.62}$$

the continuity equation

$$\partial_t\, \varrho_\mathrm{e}^{(\alpha)}(\mathbf{r},t) + \nabla \cdot \mathbf{J}^{(\alpha)}(\mathbf{r},t) = 0 \tag{4.63}$$

and the Euler equation

$$\partial_t \mathbf{J}^{(\alpha)}(\mathbf{r},t) + \gamma\, \mathbf{J}^{(\alpha)}(\mathbf{r},t) = \left(\frac{q_\mathrm{e}}{m_\mathrm{e}}\right) \varrho_\mathrm{e}^{(0)}(\mathbf{r})\, \mathbf{E}^{(\alpha)}(\mathbf{r},t) - \frac{5\, q_\mathrm{e}}{3\, m_\mathrm{e}}\, \zeta \left(\varrho_\mathrm{e}^{(0)}(\mathbf{r})\right)^{2/3} \nabla\, \mathcal{P}^{(\alpha)} + \mathbf{Q}_\mathrm{J}^{(\alpha)}(\mathbf{r},t). \tag{4.64}$$

In arriving at (4.64) we have defined the nonlinear source field $\mathbf{Q}_\mathrm{J}^{(\alpha)}$, which couples the lower-order non-static fields (order $< \alpha$) to the current density. In particular, by construction we have

$$\mathbf{Q}_J^{(1)} = \mathbf{0} \tag{4.65}$$

for the first order and

$$\mathbf{Q}_J^{(2)} = \underbrace{-\nabla \cdot \left(\frac{1}{\varrho_\mathrm{e}^{(0)}}\, \mathbf{J}^{(1)} \otimes \mathbf{J}^{(1)}\right)}_{\mathbf{Q}_\mathrm{conv}} + \underbrace{\frac{q_\mathrm{e}}{m_\mathrm{e}}\, \varrho_\mathrm{e}^{(1)}\, \mathbf{E}^{(1)}}_{\mathbf{Q}_\mathrm{el}} + \underbrace{\frac{q_\mathrm{e}}{m_\mathrm{e}}\, \mathbf{J}^{(1)} \times \mathbf{B}^{(1)}}_{\mathbf{Q}_\mathrm{mag}} \underbrace{- \frac{5\, q_\mathrm{e}\, \zeta}{9\, m_\mathrm{e}} \left(\varrho_\mathrm{e}^{(0)}\right)^{-1/3} \nabla \left(\varrho_\mathrm{e}^{(1)}\right)^2}_{\mathbf{Q}_\mathrm{press}} \tag{4.66}$$

for the second order, where (except for the damping term) each of the contributions in (4.66) is related to one of the contributions in the Euler equation: The nonlinear convection source term $\mathbf{Q}_\mathrm{conv}$ originates from the convection term in (4.33), the nonlinear electric force source term $\mathbf{Q}_\mathrm{el}$ stems from the electric part of the Lorentz force density in (4.33) and, accordingly, the nonlinear magnetic force source term $\mathbf{Q}_\mathrm{mag}$ emerges from the magnetic part of the Lorentz force density in (4.33). Lastly, the nonlinear pressure gradient source term $\mathbf{Q}_\mathrm{press}$ originates from the pressure gradient in (4.33). We will see in section 4.5 that by switching each of the nonlinear source terms of (4.66) off and on individually we can analyze the contribution of these terms to the second-order signal.

In this section we have found the partial differential equations, which we can solve by using the DGTD method (cf. chapter 3). To complete the numerical DGTD scheme (3.28) we, yet, need to apply a numerical flux. We show how to calculate an appropriate approximate numerical flux for the hydrodynamic material model in the following.

4.3 The numerical flux for the hydrodynamic equations

While Maxwell's equation for the respective nonlinear fields (4.59) to (4.62) can be solved by using an upwind-flux DGTD scheme (cf. section 3.3), we still need to find an appropriate numerical flux for the hydrodynamic material equations. In the following we derive an approximate numerical flux, namely the *Lax-Friedrichs-flux* [14], for the continuity equation (4.16) and the Euler equation (4.33). The construction of the Lax-Friedrichs-flux is very similar to the calculation of the upwind flux shown in section 3.2. Hence, we also need to formulate the problem in face normal direction (cf. (3.39))

$$\frac{\partial \varrho_\mathrm{e}}{\partial t} + \breve{\mathbf{n}} \cdot \frac{\partial \mathbf{J}}{\partial \breve{n}} = 0 \tag{4.67}$$

$$\frac{\partial \mathbf{J}}{\partial t} + \frac{\partial}{\partial \breve{n}} \breve{\mathbf{n}} \cdot \left(\frac{1}{\varrho_\mathrm{e}} \mathbf{J} \otimes \mathbf{J} \right) + \breve{\mathbf{n}} \left(\frac{q_\mathrm{e}}{m_\mathrm{e}} \right) \frac{\partial \mathcal{P}}{\partial \breve{n}} = \mathbf{s} \tag{4.68}$$

where we have defined the source

$$\mathbf{s} = \frac{q_\mathrm{e}}{m_\mathrm{e}} (\varrho_\mathrm{e} \mathbf{E} + \mathbf{J} \times \mathbf{B}) - \gamma \mathbf{J}. \tag{4.69}$$

The spatial derivatives in (4.68) can be expressed by

$$\frac{\partial}{\partial \breve{n}} \breve{\mathbf{n}} \cdot \left(\frac{1}{\varrho_\mathrm{e}} \mathbf{J} \otimes \mathbf{J} \right) = \frac{\partial}{\partial \varrho_\mathrm{e}} \left(\frac{1}{\varrho_\mathrm{e}} \breve{\mathbf{n}} \cdot \mathbf{J} \right) \frac{\partial \varrho_\mathrm{e}}{\partial \breve{n}} + \sum_{i=1}^{3} \frac{\partial}{\partial J_i} \left(\frac{1}{\varrho_\mathrm{e}} \breve{\mathbf{n}} \cdot \mathbf{J} \right) \frac{\partial J_i}{\partial \breve{n}} \tag{4.70}$$

and

$$\breve{\mathbf{n}} \frac{\partial \mathcal{P}}{\partial \breve{n}} = \breve{\mathbf{n}} \, \zeta \, \varrho_\mathrm{e}^{2/3} \frac{\partial \varrho_\mathrm{e}}{\partial \breve{n}} \, . \tag{4.71}$$

Therefore, (4.67) and (4.68) can be combined in

$$\frac{\partial}{\partial t} \begin{pmatrix} \varrho_\mathrm{e} \\ J_1 \\ J_2 \\ J_3 \end{pmatrix} + \underbrace{\begin{pmatrix} 0 & \breve{n}_1 & \breve{n}_2 & \breve{n}_3 \\ \breve{n}_1 \frac{q_\mathrm{e}}{m_\mathrm{e}} \zeta \varrho_\mathrm{e}^{2/3} - \frac{\breve{\mathbf{n}} \cdot \mathbf{J}}{\varrho_\mathrm{e}^2} J_1 & \frac{1}{\varrho_\mathrm{e}} (\breve{n}_1 J_1 + \breve{\mathbf{n}} \cdot \mathbf{J}) & \frac{1}{\varrho_\mathrm{e}} \breve{n}_2 J_1 & \frac{1}{\varrho_\mathrm{e}} \breve{n}_3 J_1 \\ \breve{n}_2 \frac{q_\mathrm{e}}{m_\mathrm{e}} \zeta \varrho_\mathrm{e}^{2/3} - \frac{\breve{\mathbf{n}} \cdot \mathbf{J}}{\varrho_\mathrm{e}^2} J_2 & \frac{1}{\varrho_\mathrm{e}} \breve{n}_1 J_2 & \frac{1}{\varrho_\mathrm{e}} (\breve{n}_2 J_2 + \breve{\mathbf{n}} \cdot \mathbf{J}) & \frac{1}{\varrho_\mathrm{e}} \breve{n}_3 J_2 \\ \breve{n}_3 \frac{q_\mathrm{e}}{m_\mathrm{e}} \zeta \varrho_\mathrm{e}^{2/3} - \frac{\breve{\mathbf{n}} \cdot \mathbf{J}}{\varrho_\mathrm{e}^2} J_3 & \frac{1}{\varrho_\mathrm{e}} \breve{n}_1 J_3 & \frac{1}{\varrho_\mathrm{e}} \breve{n}_2 J_3 & \frac{1}{\varrho_\mathrm{e}} (\breve{n}_3 J_3 + \breve{\mathbf{n}} \cdot \mathbf{J}) \end{pmatrix}}_{\equiv \underline{\mathbf{A}}} \frac{\partial}{\partial \breve{n}} \begin{pmatrix} \varrho_\mathrm{e} \\ J_1 \\ J_2 \\ J_3 \end{pmatrix} = \begin{pmatrix} 0 \\ s_1 \\ s_2 \\ s_3 \end{pmatrix}, \tag{4.72}$$

where $\underline{\mathbf{A}}$ is the transposed normal-directional flux Jacobian according to (3.41). Its eigenvalues, i.e. the characteristics speeds, are given by

$$\{\lambda\} = \left\{ \frac{1}{\varrho_\mathrm{e}} \breve{\mathbf{n}} \cdot \mathbf{J} \, , \; \frac{1}{\varrho_\mathrm{e}} \breve{\mathbf{n}} \cdot \mathbf{J} - \sqrt{\left| \frac{q_\mathrm{e}}{m_\mathrm{e}} \left(\frac{\partial \mathcal{P}}{\partial \varrho_\mathrm{e}} \right) \right|} \, , \; \frac{1}{\varrho_\mathrm{e}} \breve{\mathbf{n}} \cdot \mathbf{J} + \sqrt{\left| \frac{q_\mathrm{e}}{m_\mathrm{e}} \left(\frac{\partial \mathcal{P}}{\partial \varrho_\mathrm{e}} \right) \right|} \right\}. \tag{4.73}$$

One could now proceed to formulate the Rankine-Hugoniot conditions using the eigenvalues (4.73) and construct the numerical upwind flux from these conditions as was done in (3.54). Unfortunately, the resulting system of equations is more complicated than the one seen in section 3.3. Hence, instead of calculating the upwind flux we give an approximate flux, the Lax-Friedrichs flux

$$\begin{aligned} \breve{\mathbf{n}} \cdot \mathbf{f}^*_\mathrm{LF} = & \frac{1}{2} \left[\begin{pmatrix} \breve{\mathbf{n}} \cdot \mathbf{J}_\mathrm{R} \\ \frac{1}{\varrho_\mathrm{e,R}} \breve{\mathbf{n}} \cdot (\mathbf{J}_\mathrm{R} \otimes \mathbf{J}_\mathrm{R}) + \breve{\mathbf{n}} \frac{q_\mathrm{e}}{m_\mathrm{e}} \mathcal{P}_\mathrm{R} \end{pmatrix} + \begin{pmatrix} \breve{\mathbf{n}} \cdot \mathbf{J}_\mathrm{L} \\ \frac{1}{\varrho_\mathrm{e,L}} \breve{\mathbf{n}} \cdot (\mathbf{J}_\mathrm{L} \otimes \mathbf{J}_\mathrm{L}) + \breve{\mathbf{n}} \frac{q_\mathrm{e}}{m_\mathrm{e}} \mathcal{P}_\mathrm{L} \end{pmatrix} \right] + \\ & + \frac{C}{2} \begin{pmatrix} \varrho_\mathrm{e,L} - \varrho_\mathrm{e,R} \\ \mathbf{J}_\mathrm{L} - \mathbf{J}_\mathrm{R} \end{pmatrix}, \end{aligned} \tag{4.74}$$

based on the maximal eigenvalue of $\underline{\mathbf{A}}$, i.e. the maximal characteristic speed,

$$C = \max_{(\varrho_\mathrm{e},\mathbf{J})^\mathrm{T}} |\{\lambda\}| = \frac{1}{\varrho_\mathrm{e}} |\breve{\mathbf{n}} \cdot \mathbf{J}| + \sqrt{\left| \frac{q_\mathrm{e}}{m_\mathrm{e}} \left(\frac{\partial \mathcal{P}}{\partial \varrho_\mathrm{e}} \right) \right|}. \tag{4.75}$$

Note, however, that the expression (4.75) still allows for some interpretation in the context of the overall DGTD scheme. One can either calculate C for each element individually, which results in the so-called *local Lax-Friedrichs flux* scheme, or determine the maximal characteristic speed of all elements, which results in the so-called *global Lax-Friedrichs flux* scheme. In general the global Lax-Friedrichs flux scheme is more dissipative than the local one [14], which leads to a less accurate DGTD scheme. Within this thesis we only implement the local scheme. Whether one chooses a local or a global scheme, one needs to be careful in the choice of the temporal discretization length. If the smallest element in our spatial discretization denoted by k has a maximal specific length h_k, the time step of the Runge-Kutta scheme must be chosen so that

$$\Delta t \leq \frac{h_k}{C_k}, \tag{4.76}$$

where C_k is the maximal characteristic speed in that element. Otherwise the overall scheme will become unstable. The condition (4.76) is known as Courant-Friedrichs-Lewy (CFL) critereon [14].

Finally, because of $|\breve{\mathbf{n}} \cdot \mathbf{J}| \leq |\breve{\mathbf{n}}| \cdot |\mathbf{J}| = |\mathbf{J}|$ we can find an upper bound for the maximal characteristic speed

$$C_{k,\mathrm{upper}} = \frac{1}{\varrho_\mathrm{e}} |\mathbf{J}_k| + \sqrt{\left| \frac{q_\mathrm{e}}{m_\mathrm{e}} \left(\frac{\partial \mathcal{P}_k}{\partial \varrho_{\mathrm{e},k}} \right) \right|} \tag{4.77}$$

with which we approximate the Lax-Friedrichs flux in each element k, i.e. $C_k \approx C_{k,\mathrm{upper}}$.

To adjust the Lax-Friedrichs flux to the perturbative scheme of section 4.2, one needs to insert the expansions (4.34), (4.35) and (4.38) into (4.74) and (4.77) and then sort out the different nonlinear orders subsequently. For example, if we take the linear order $\alpha = 1$, the first order fields $\varrho_\mathrm{e}^{(1)}$ and $\mathbf{J}^{(1)}$ appear in the expression for the Lax-Friedrichs flux (4.74). Hence, the maximal characteristic speed is given by the constant value

$$C^{(1)} = \sqrt{\left| \frac{2\, q_\mathrm{e}}{3\, m_\mathrm{e}} \zeta \left(\varrho_\mathrm{e}^{(0)} \right)^{2/3} \right|}.$$

With the Lax-Friedrichs flux for the hydrodynamic equations (4.16) and (4.33) the numerical DGTD scheme (3.28) is now complete. However, to pose a complete mathematical problem we still need to specify initial values and boundary conditions for the charge and current density. We reserve the following section for this topic.

4.4 Initial values and the hard-wall boundary conditions

For a finite hydrodynamic material, e.g. a nano-particle, boundary conditions for the charge and current density need to be imposed on the material's surface ∂V_{HD} in addition to the conventional electromagnetic boundary conditions for the electric and magnetic field (cf. section 1.1.2). In real metals, which we mimic by using the hydrodynamic model, the electronic charge density decreases at the vicinity of the material's surface and vanishes smoothly outside of the material allowing for some electron spill-out (cf. fig. 4.1, [90, 93]). However, this kind of density profile is associated with some numerical complications: As can be shown by density-functional-theory calculations for metal half spaces, the charge density drops to zero within only a few Ångström [93]. At the same time the gradient of the charge density and, thus, the pressure (4.19) displays very large values. This leads to instabilities in the numerical scheme as described by Prohm [21]. Furthermore, the fast spatial decrease of the charge density requires a very fine discretization at the material's boundary [21, 94]. As the CFL criterion (4.76) must be fulfilled, the time-steps have to be chosen fairly small making the numerical calculations very expensive. We circumvent this problem by approximating the smooth initial electronic charge density[6] of the real material by a piecewise constant electronic charge density in a our hydrodynamic model (see fig. 4.1)

$$\varrho_{\mathrm{e}}^{(0)}(\mathbf{r},0) = \begin{cases} = \text{const.} & \text{within the material} \\ \neq 0 & \text{outside of the material} \end{cases}, \tag{4.78}$$

which are known as *hard-wall* boundary conditions[7]. Consequently, the boundary conditions for the overall charge density are given by

$$\varrho_{\mathrm{e}}(\mathbf{r},t) = \begin{cases} \neq 0 & \text{within the material} \\ = 0 & \text{outside of the material} \end{cases}. \tag{4.79}$$

In order to apply the boundary (4.79) conditions within the DGTD method we need to construct an artificial ghost state for any of the hydrodynamic material's boundary elements (cf. section 3.4). For every electronic charge density value at a boundary node $\varrho_{\mathrm{e}}^{(-)}$ a ghost state value $\varrho_{\mathrm{e}}^{(+)}$ is set so that the desired boundary value of 0 is acquired by the sum of the boundary and ghost state value at every node. Therefore, we demand $\varrho_{\mathrm{e}}^{(+)} = -\varrho_{\mathrm{e}}^{(-)}$.

Furthermore, we need to set boundary conditions for the current density. In fluid dynamics there are two common choices, the no-slip and the slip boundary conditions. For the no-slip boundary condition one assumes that the electron fluid's current density is zero at the material's surface, yielding

$$\mathbf{J}|_{\partial V_{\mathrm{HD}}} = \mathbf{0}. \tag{4.80}$$

[6] As stated in section 3.1 the initial electric and magnetic field as well as the initial current density are zero.

[7] The hard-wall boundary condition is equivalent to the boundary condition named ABC in [95]. They do not allow for an accumulation of electronic charges at the material's boundary forcing the normal component of the electric field to be continuous (cf. (1.28)).

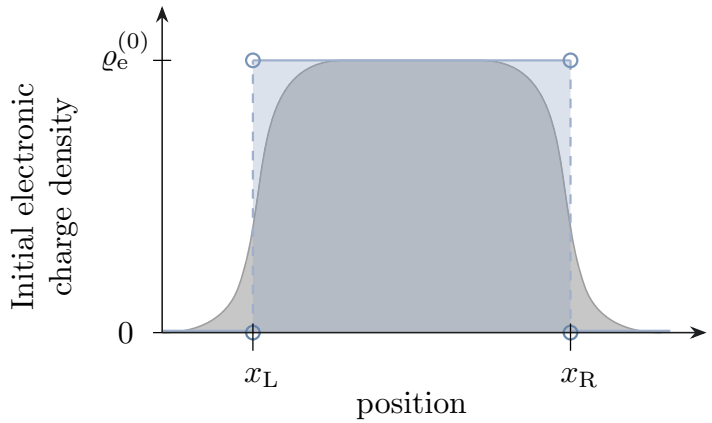

Figure 4.1: Sketch of a particle's smooth initial (equilibrium) density profile of a particle depicted by the gray area, where the particle's left and right boundary are marked by x_L and x_R. This smooth density profile is approximated by a piecewise constant density profile depicted by the blue box.

Similar to introduction of the boundary condition for the charge density (4.79) into the DGTD method a ghost state current density $\mathbf{J}_+$ needs to be chosen when implementing the boundary condition (4.80) so that it compensates the current density $\mathbf{J}_-$, i.e. $\mathbf{J}_+ = -\mathbf{J}_-$, at every surface nodal point.

In contrast to the no-slip boundary conditions, in the slip boundary conditions only the normal component of the current is assumed to vanish

$$\breve{\mathbf{n}} \cdot \mathbf{J}|_{\partial V_{\mathrm{HD}}} = 0 \tag{4.81}$$

whereas the tangential component $(-\breve{\mathbf{n}} \times \mathbf{J})$ needs to be continuous. We, hence, require $\breve{\mathbf{n}} \cdot \mathbf{J}_+ = -\breve{\mathbf{n}} \cdot \mathbf{J}_-$ for the normal component and $-\breve{\mathbf{n}} \times \mathbf{J}_+ = -\breve{\mathbf{n}} \times \mathbf{J}_-$ for the tangential component of the ghost state current density. Therefore, we demand $\mathbf{J}_+ = \mathbf{J}_- - 2\,\breve{\mathbf{n}}\,(\breve{\mathbf{n}} \cdot \mathbf{J}_-)$ for the total ghost state current density.

More vividly, one can imagine the two boundary conditions as follows: In the case of the no-slip boundary conditions a small layer of particles gets stuck to the material's boundary. They have no relative speed compared to remaining particle flow. In contrast the particles literally slip away from the material's surface in the case of the slip-boundary conditions. In both cases the particles cannot leave the material. The no-slip boundary conditions were proposed by Navier in 1823 [96] as an assumption. The validity of this assumption is still under debate after almost two centuries [97–100]. Some research suggests that slip boundary conditions are preferable for nano-scale transport [100, 101]. However, we will not join the debate within this thesis. Instead, we simply apply the slip boundary conditions within this thesis, which have been used in the previous works of Hille [102] and Moeferdt [20], to ensure a better comparability. On a side note it has been shown by Prohm [21] that in DGTD calculations the slip boundary condition produce a more pronounced blue shift in scattering spectrum than the no-slip boundary conditions, if one compares these computations to analytical Mie calculations. Nevertheless, to this point we do not have any information on which boundary condition describes the physical reality more accurately.

4.5 SHG and SFG in hydrodynamic materials

With the information of sections 4.2 to 4.4 we have posed a complete problem, that can be solved numerically by using the DGTD scheme. In the following we focus on second-order nonlinear phenomena such as SHG and SFG (cf. section 2.3.1) in the framework of the perturbative approach to the hydrodynamic model (cf. section 4.2). To this end, we first employ a 2D scattering setup consisting of an infinitely stretched (effective 2D) cylindrical silver nanowire with a radius of $a = 10\,\mathrm{nm}$, which is surrounded by air[8]. As material parameters, we use an effective mass of $m_\mathrm{e} = 0.96\,m_0 = 8.75 \cdot 10^{-31}\,\mathrm{kg}$ [70] as well as a plasma frequency of $\omega_\mathrm{p} = 1.39 \cdot 10^{16}\,\frac{\mathrm{rad}}{\mathrm{s}}$ and a damping coefficient of $\gamma = 3.23 \cdot 10^{13}\,\mathrm{Hz}$[9]. The last two parameters have been obtained by a fit of the simple Drude model [28, 68] to the experimental Johnson and Christie data [104]. Hence, within the Drude model the static charge density is given by[28]

$$\varrho_\mathrm{e}^{(0)} = \frac{\epsilon_0\, m_\mathrm{e}\, \omega_\mathrm{p}^2}{|q_\mathrm{e}|}, \tag{4.82}$$

which yields $\varrho_\mathrm{e}^{(0)} = 9.34 \cdot 10^{-15}\,\mathrm{C/nm^3}$ for the above silver parameters. The entire computational domain has a dimension of $520 \times 520\,\mathrm{nm}$, where the silver nanowire is located in the center surrounded by a $24 \times 24\,\mathrm{nm}$ TfSf contour (see fig. 4.2). Furthermore, we apply perfectly matched layers (PMLs) of 80 nm width and Silver–Müller boundary conditions beyond the PMLs (cf. section 3.4). The computational domain is discretized in space by a triangular mesh (see fig. 4.2), where the maximal element edge length at the nanowire's surface is chosen to be $h_\mathrm{max} = 0.54\,\mathrm{nm}$. This parameter follows from a convergence study by Moeferdt [20] for the exact same setup, where the linear scattering spectrum obtained by the DGTD code with a non-perturbative hydrodynamic approach (cf. section 4.1) was tested against analytical Mie calculations [105]. For most calculations this discretization turns out to be sufficient [19, 20].

To get a first impression of the perturbative approach to the hydrodynamic model (cf. section 4.2) we first draw a comparison to the non-perturbative approach previously used by Moeferdt [20]. To this end, we excite the nanowire with a single TE polarized ($E_z = 0$, $B_x = B_y = 0$)[10] Gaussian pulse. The results are presented in terms of the SHG scattering cross section (cf. section 1.1.3). In the case of the non-perturbative approach the total electromagnetic fields $\mathbf{E} = \mathbf{E}^{(1)} + \mathbf{E}^{(2)} + \dots$ and $\mathbf{B} = \mathbf{B}^{(1)} + \mathbf{B}^{(2)} + \dots$ are calculated by the DGTD method, where we have no clean distinction between the linear fields, $\mathbf{E}^{(1)}$ and $\mathbf{B}^{(1)}$, and the

[8] A three dimensional version can be found in the Bachelor thesis of M. Plock [103], which was created under my supervision.

[9] Given these material parameters one should elaborate on whether the application of the degeneracy pressure (4.30) can still be a good approximation.

[10] Note that there is no TM polarization for the hydrodynamic model equations (4.16) and (4.33).

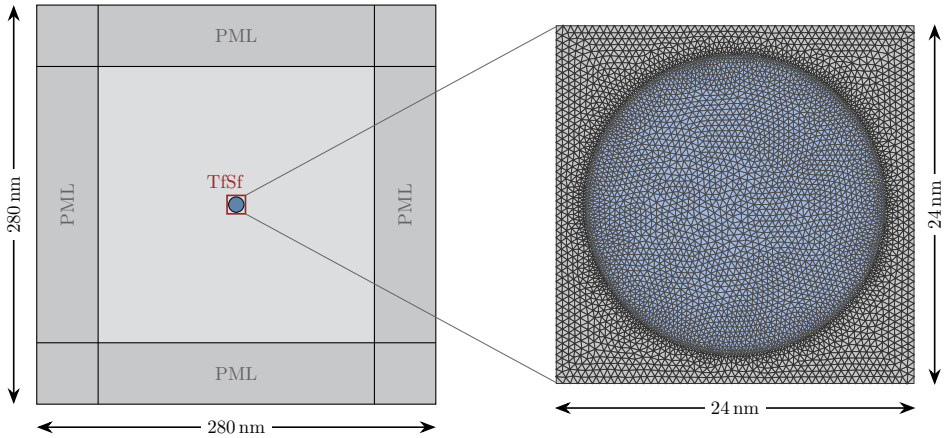

Figure 4.2: 2D scattering setup with circular scatterer of radius 10 nm. The zoom into the TfSf area shows the triangular mesh of this area produced with NETGEN-4.9.12 [106], where the maximal edge length of the discretization is $h_{\max} = 0.54\,\mathrm{nm}$.

nonlinear fields, $\mathbf{E}^{(2)}$ and $\mathbf{B}^{(2)}$. The scattering cross section is therefore given by[11]

$$C_{\mathrm{scat}}(\omega) = \frac{1}{2\,\mu_0\,\max|\boldsymbol{\sigma}_{\mathrm{inc}}|} \int\limits_{\substack{\mathrm{TfSf}\\ \mathrm{contour}}} \mathrm{d}r\; \breve{\mathbf{n}}(\mathbf{r}) \cdot \mathrm{Re}\left[\tilde{\mathbf{E}}_0(\mathbf{r},\omega) \times \tilde{\mathbf{B}}_0^*(\mathbf{r},\omega)\right], \tag{4.83}$$

where $\tilde{\mathbf{E}}_0^{(2)}(\mathbf{r},\omega)$ and $\tilde{\mathbf{B}}_0^{(2)}(\mathbf{r},\omega)$ denote the monochromatic field amplitudes of the respective total fields $\mathbf{E}$ and $\mathbf{B}$ (cf. (1.64)). Both are obtained by an on-the-fly Fourier transform [13]. Because there is no clean distinction between the linear and the nonlinear spectrum, special care has to be taken when choosing a pulse excitation, as the linear and nonlinear signal are very different in their orders of magnitudes. For instance, if we choose a pulse with an amplitude of $E_0 = 10^6\,\mathrm{V/m}$, the linear response is of the order 1 according to the linear polarization (2.16). In contrast, the second-order response is of the order of $E_0^{-1} = 10^{-6}\,\mathrm{m/V}$ according to the second-order polarization formula (2.18). Hence, the bandwidth of the pulse has to be chosen sufficiently small to prevent a superposition of the linear and nonlinear signal in the scattering cross section spectrum. Otherwise the nonlinear signal will be lost. We found a bandwidth of $\omega_{\mathrm{FWHM}} = 0.034\,\omega_{\mathrm{p}}$ to be sufficient, which corresponds to an pulse duration of $t_{\mathrm{pulse}} = 13.3 \cdot 10^{-15}\,\mathrm{s}$. To get a convergent result[13] we need an overall simulation duration of $T = 39.0 \cdot 10^{-14}\,\mathrm{s}$, where the time step is given by $\Delta t = 3.9 \cdot 10^{-19}\,\mathrm{s}$. These calculations are relatively expensive. For example, the third-order polynomial calculation will take a little more than three days using eight cores on an INTEL(R) XEON(R) E5-1650 processor. In contrast, we do not have the same requirements to the pulse duration in the perturbative approach,

[11] In (1.67) the cross section was normalized by $\boldsymbol{\sigma}_{\mathrm{inc}}(\omega)$ at each frequency ω. Because we are interested in the second-order signal at frequencies far from the incoming pulse frequencies, the value of incoming spectrum σ_{inc} goes to zero and, consequently, the cross section goes to infinity. Hence, in (4.83) we avoid this problem by normalizing by the maximum of the incoming spectrum instead.

which can be seen as a big advantage over the non-perturbative approach. In fact, the overall simulation time can be reduced by about 50% compared to the non-perturbative approach. This is a result of the clean distinction of the linear fields, $\mathbf{E}^{(1)}$ and $\mathbf{B}^{(1)}$, and the second-order fields, $\mathbf{E}^{(2)}$ and $\mathbf{B}^{(2)}$. Accordingly, we can calculate the isolated second-order scattering cross section by

$$C_{\text{scat}}^{(2)}(\omega) = \frac{1}{2\,\mu_0\,\max|\boldsymbol{\sigma}_{\text{inc}}|} \int\limits_{\substack{\text{TfSf}\\ \text{contour}}} \mathrm{d}r\ \breve{\mathbf{n}}(\mathbf{r}) \cdot \mathrm{Re}\left[\tilde{\mathbf{E}}_0^{(2)}(\mathbf{r},\omega) \times \tilde{\mathbf{B}}_0^{(2)*}(\mathbf{r},\omega)\right], \tag{4.84}$$

where $\tilde{\mathbf{E}}_0^{(2)}(\mathbf{r},\omega)$ and $\tilde{\mathbf{B}}_0^{(2)}(\mathbf{r},\omega)$ denote the monochromatic field amplitudes of the respective second-order fields. Note, however, that the clean separation of the linear and nonlinear order comes at the great cost of twice as many degrees of freedoms, which need to be calculated. For very fine meshes the non-perturbative approach can be quite expensive.

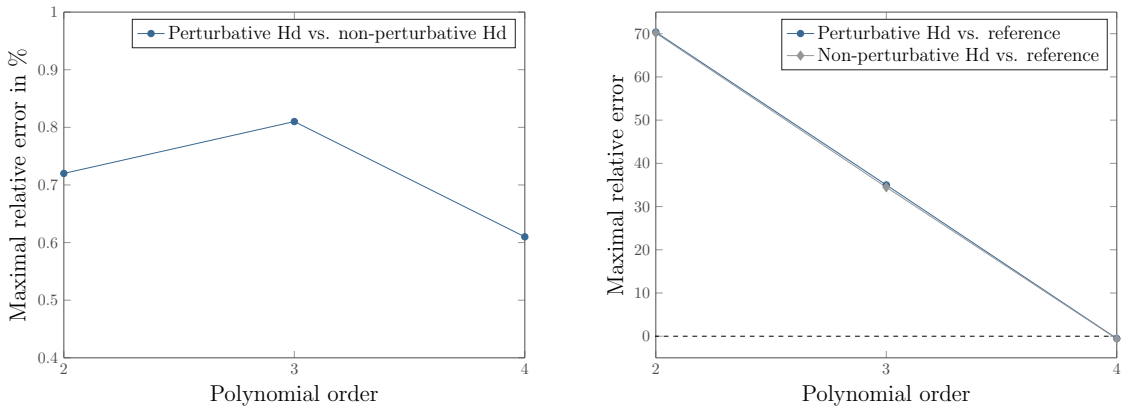

(a) (b)

Figure 4.3: Comparison of (a) the perturbative to the non-perturbative hydrodynamic approach (b) the non-perturbative and perturbative approach to a reference calculation.

Even though in general we are not restricted to narrow-band pulse excitations in the perturbative approach, we choose the same narrow-band excitation to get a fair comparison between the perturbative and non-perturbative approach. In both cases, we launch a pulse from the surrounding TfSf contour with an amplitude of $E_0 = 10^6\,\frac{\text{V}}{\text{m}}$, a duration of $t_{\text{pulse}} = 13.3 \cdot 10^{-15}\,\text{s}$ (corresponding to a bandwidth of $0.034\,\omega_{\text{p}}$) and a center frequency of $\omega_0 = 0.34\,\omega_{\text{p}}$, for which we expect a SHG signal at about $0.68\,\omega_{\text{p}}$. For both approaches we apply an exponential filter according to [21, section 2.5.1] to ensure the stability of the nonlinear numerical scheme (cf. section 3.5). As a result we get the scattering cross sections of the SHG signal as displayed in fig. 4.5, where the perturbative approach is marked by a solid black line and the non-perturbative approach is marked by dashed black line. Both of these calculations were carried out for a polynomial order of 4. In this case the relative difference between the two approaches is about 0.7%. A more detailed analysis is displayed in fig. 4.3. In fig. 4.3a we

see the maximal relative deviation of the perturbative approach from the non-perturbative, which was calculated from the respective scattering cross section data at different polynomial orders ranging form 2 to 4. For the current setup we see the smallest deviation at a polynomial order of 4. Furthermore, in fig. 4.3b we conclude that both approaches show the same convergence behaviour. For this we compare each of the approaches to a reference calculation by courtesy of Moeferdt [20]. Thereby, we use a maximal edge length of $h_{\max} = 0.54$ nm at the nanowire's surface as spatial discretization. In contrast, the reference calculation is obtained by a non-perturbative DGTD calculation for a notably finer mesh with a maximal element edge length of $h_{\max} = 0.16$ nm at a polynomial order of 4. Again the smallest error is found at a polynomial order of 4, where the perturbative approach displays an error of -0.5% and the non-perturbative approach shows an error of -0.6%. Both approaches slightly overshoot the reference calculation. Though there are great similarities between both approaches, the perturbative approach turns out to be about 59% to 62% slower than the non-perturbative approach due to the greater amount of degrees of freedoms. Nevertheless, one might be willing to accept the higher cost, as the perturbative approach is able to provide information, which cannot be obtained by the non-perturbative approach.

The separation between linear and nonlinear fields allows us to visualize these fields individually in the time domain. As an example, we present the field distribution of the fundamental $E_y^{(1)}$-field in fig. 4.4a and the corresponding second-harmonic $E_y^{(2)}$-field in fig. 4.4b. We see that the fundamental signal in fig. 4.4a is scattered symmetrically by the nano-antenna. However, it is more interesting to study the nonlinear field distribution in fig. 4.4b. There the SHG signal is most pronounced at the nanowire's surface but also extends into the core of the nanowire. This would be untypical for a centrosymmetric crystal, where the centrosymmetry is broken only at the material's surface. Hence, in that case the SHG signal would strongly suppressed in the bulk of a centrosymmetric crystal [50] (see section 2.2). Instead in fig. 4.4b we observe an entirely different behavior for the fluid (see also [51]): Without any external excitation the Fermi liquid is homogeneous and, hence, centrosymmetric in the bulk. Again the centrosymmetry is broken at the surface. If the perturbation is now turned on, the liquid can no longer be viewed as homogeneous as it is strongly influenced by the external excitation [73]. Even more, so if we consider the nonlocal nature of the fluid. As a consequence, whether the SHG signal is suppressed or not, strongly depends on the symmetry of the external excitation. We will discuss this behavior further in the following.

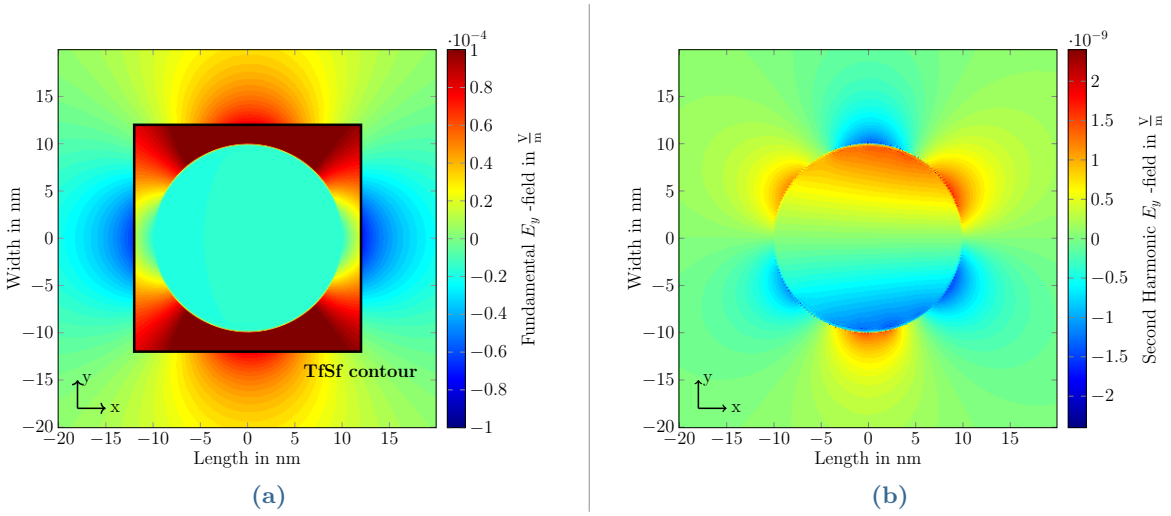

Figure 4.4: 2D E_y-field distribution of **(a)** and **(b)** the corresponding SHG signal. The structure was excited by a 13.3 fs Gaussian pulse with a center frequency of $0.34\,\omega_p$ and a field strength of $10^6\,\mathrm{V/m}$. The field distributions are displayed at the time, where the external excitation reaches its maximum.

As pointed out in section 4.2 the perturbative approach allows us to study the sources of the SHG. Accordingly, one can calculate the scattering cross section (4.84), where each of the nonlinear source terms in (4.66), namely $\mathbf{Q}_{\mathrm{el}}$, $\mathbf{Q}_{\mathrm{mag}}$, $\mathbf{Q}_{\mathrm{press}}$ and $\mathbf{Q}_{\mathrm{conv}}$, are switched on individually. The results are presented in fig. 4.5. We see that the largest contributions to the overall SHG signal (marked by the solid black line) stem form the magnetic and electric part of the Lorentz force (marked by the red solid and the blue dashed line, respectively). Thereby, the magnetic contribution is about 0.5% larger than the electric one. The pressure gradient and the convection contribution (marked in orange and green, respectively) are much smaller in comparison. Note, that both of these contributions are slightly blue shifted. This can be interpreted as a trait of their nonlocal nature [19]. We can analyze the relation of the magnetic contribution to the other contributions a little further: Except for the magnetic contribution, the surface nonlinearity of all other contributions delivers a signal, which exhibits an even symmetry with respect to the incident direction of the external field so that they do not contribute to a dipole moment in the quasi-static limit [20]. Instead, their contributions show up only at the quadrupole (and higher) moment. Thus, in this case a (small) dipole moment can be generated only through retardation effects. This is in contrast to the magnetic contribution, which delivers a finite dipole moment along the incident field direction, independent of the relative phase between current and magnetic fields. However, as the magnetic field is significantly smaller than the electric field, the magnetic contribution ends up to be of about the same magnitude as the electric contribution, which applies specifically to the present system. For other systems, notably for more complex geometries and further away from the quasi-static limit, the situation may be entirely different [H1] and would have to be analyzed in each individual case separately. Clearly, the possibility to carry out such a detailed discussion of the relative

contributions to the second-order signal is one of the advantages of the perturbative approach.

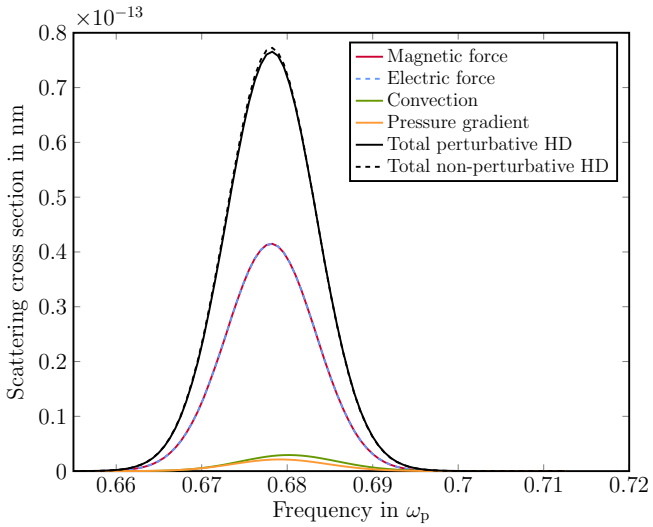

Figure 4.5: Source term contributions to the overall SHG signal seen in fig. 4.4b.

We now proceed to the study of SFG processes. To this end, we first excite the circular nanowire with a single spectrally broad laser pulse with a duration of $1.3 \cdot 10^{15}$ s (corresponding to a bandwidth of $\omega_{\mathrm{FWHM}} = 0.34\,\omega_{\mathrm{p}}$), a center frequency of $\omega_0 = 1.36\,\omega_{\mathrm{p}}$ and an electric field strength of $10^6\,\frac{\mathrm{V}}{\mathrm{m}}$ to obtain the linear absorption and scattering spectra (see fig. 4.6). From these spectra we determine the nanowire's resonances: At $\omega_{\mathrm{dip}} = 0.68\,\omega_{\mathrm{p}}$ we find a dipole resonance, where we show the real mode distribution $\mathrm{Re}[\tilde{E}_{0y}(\mathbf{r}, \omega_{\mathrm{dip}})]$ at this particular frequency in the left inset of fig. 4.6. At $\omega_{\mathrm{quad}} = 0.71\,\omega_{\mathrm{p}}$ we identify a quadrupole resonance, where we display the real mode distributions $\mathrm{Re}[\tilde{E}_{0y}(\mathbf{r}, \omega_{\mathrm{quad}})]$ in the right inset of fig. 4.6. We then use the information on the resonance frequencies to produce efficient second-order signals by wave-mixing (cf. section 2.3.1).

To this end we excite the nanowire by two spectrally narrow pulses with a duration of $t_{\mathrm{pulse}} = 13.3 \cdot 10^{-15}$ s (corresponding to a bandwidth of $\omega_{\mathrm{FWHM}} = 0.034\,\omega_{\mathrm{p}}$) and a field amplitude of $E_0 = 10^6\,\frac{\mathrm{V}}{\mathrm{m}}$ from opposite sides. Then with respect to the above discussion regarding the dipole and quadrupole moment, we choose the center frequencies of the incoming pulses, ω_1 and ω_2, such that either the second harmonic of one of the pulses ($2\omega_1$,$2\omega_2$) or their sum coincides ($\omega_1 + \omega_2$) with either the dipole resonance ω_{dip} or the quadrupole resonance ω_{quad}. Thereby we only vary one of the center frequencies, i.e. either ω_1 or ω_2, while keeping a separation length of $\Delta\omega = |\omega_1 - \omega_2| = 0.03\,\omega_{\mathrm{p}}$ from one center frequency to the other. This relatively large separation ensures that the resulting SHG and SFG signals are well distinguishable in the nonlinear spectra. The results can be viewed in fig. 4.7 and fig. 4.8, respectively. Note, that because the fundamental signals themselves do not lie on any of the nanowire's resonances, their values are notably smaller in comparison to the values found in the broadband spectra fig. 4.6. From fig. 4.7 we learn that the frequency tuning onto the dipole resonance, i.e. $2\,\omega_1 = 2\omega_{\mathrm{dip}}$, $\omega_1 + \omega_2 = \omega_{\mathrm{dip}}$ and $2\,\omega_2 = \omega_{\mathrm{dip}}$, does not always yield the most efficient signal in the second-order spectrum. In fig. 4.7 (I) and (II) we see that the off-resonant second-order signals near the quadrupole resonance are notably stronger than the resonant second-order signals at the

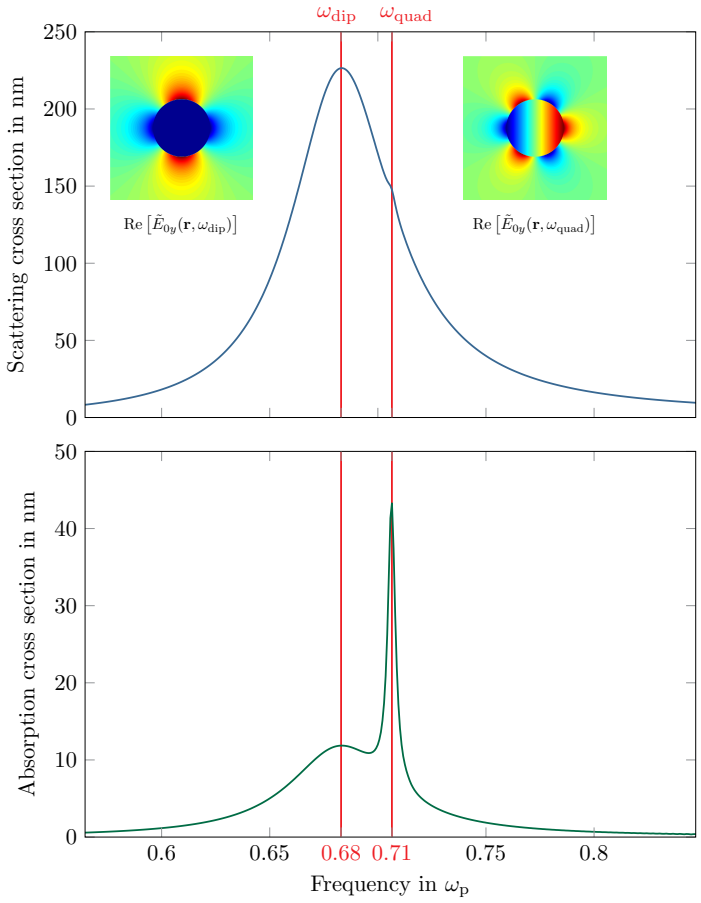

Figure 4.6: Linear scattering and absorption cross section for a cylindrical nanowire (cf. fig. 4.2). The nanowire was excited by a single broadband pulse with a duration of 1.3 fs (bandwidth of $\omega_{\mathrm{FWHM}} = 0.34\,\omega_{\mathrm{p}}$), a center frequency of $\omega_0 = 1.36\,\omega_{\mathrm{p}}$, and a field strength of $E_0 = 10^6\,\mathrm{V/m}$. The vertical red lines mark the position of the dipole (ω_{dip}) and quadrupole (ω_{quad}) resonance.

dipole resonance. Only in fig. 4.7 (III), where there is little spectral overlap of the second-order signals with the quadrupole resonance, the dominant contribution originates form the dipole resonance, where we have $2\,\omega_2 = \omega_{\mathrm{dip}}$. Nevertheless, we would like to point out that in this case the signals are still much weaker than those of fig. 4.7 (I) and (II), as can be seen by the one-order-of-magnitude difference of the second-order responses. In fact, the behaviour seen in fig. 4.7 is in accordance with our discussion about the second-order field distribution: The even symmetry of the incident field suppresses the dipole contributions to the second-order signals. Thus, we conclude that the quadrupole resonance, which also dominates the absorption cross section (see fig. 4.6), in fact generates a much stronger second-order signal than the dipole resonance as long as there is appreciable spectral overlap.

In fig. 4.8, we repeat the above exercise but now with the second-harmonic or the sum-frequency tuned in a way that they coincide with the quadrupole resonance. In agreement with our above findings, the second-order signals tuned onto the quadrupole resonance are considerably stronger: The SHG signals at the quadrupole resonance in fig. 4.8 (I) and (III) are much larger than the SHG signals at the dipole resonance in fig. 4.7 (I) and (III). The same goes for the SFG signal at the quadrupole resonance in fig. 4.8 (II) when comparing it to the SFG signal in fig. 4.7 (II). It is noteworthy that, while the SHG signals in fig. 4.8 (I) and (III),

which lie on the quadrupole resonance, have approximately the same magnitude compared to the maximal off-resonant signals in fig. 4.7 (I) and (II), the SFG signal at the quadrupole resonance in fig. 4.8 is almost three times larger than the SFG signal at the dipole resonance in fig. 4.7. Hence, we conclude that in order to obtain the most efficient second-order signal from a cylindrical nanowire, we need to tune the incoming pulses in a way that their sum-frequency coincides with the quadrupole frequency. These kinds of discussion are not restricted to cylindrical nanowires and can also be extended to any arbitrary nanoantenna structure.

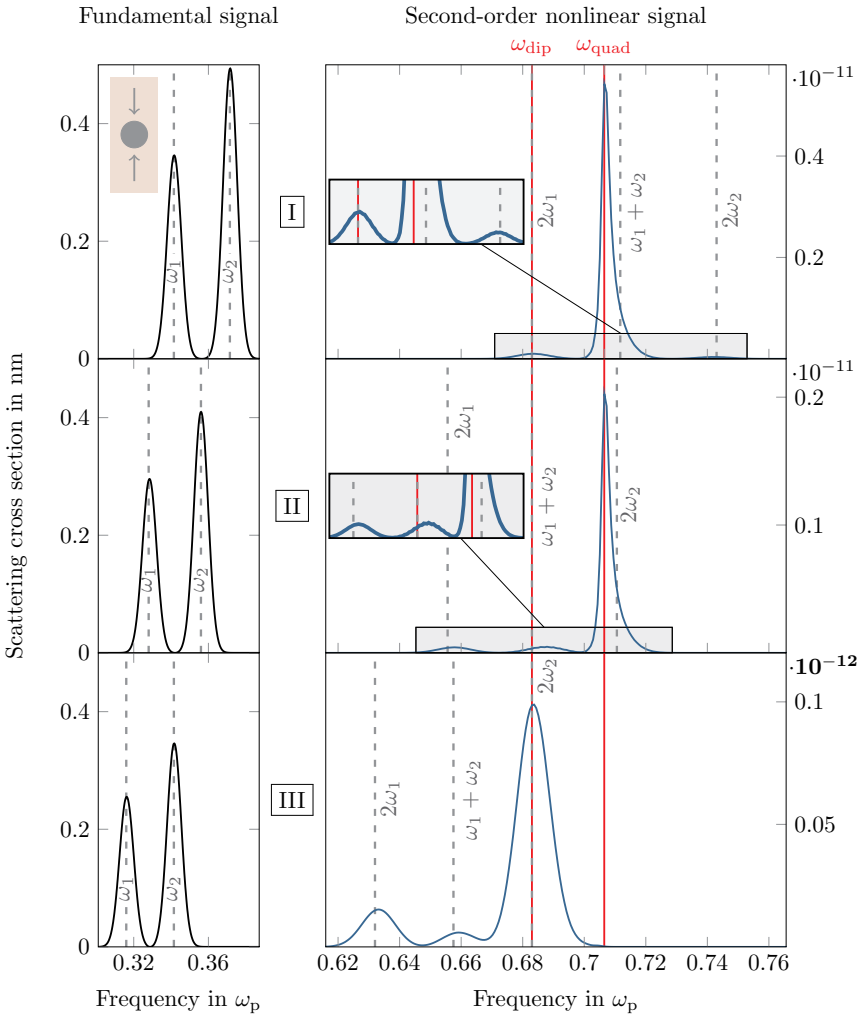

Figure 4.7: Scattering cross section for the second-order response of a circular nanowire (see fig. 4.2) for two excitation pulses injected from opposite sides with different central frequencies ω_1 and ω_2. In all cases, the two pulses are separated by $0.03\,\omega_p$ and the incident electric field has an amplitude of $E_0 = 10^6$ V/m. The incident pulses are chosen so that **(I)** $2\,\omega_1 = \omega_{dip}$, **(II)** $\omega_1 + \omega_2 = \omega_{dip}$, **(III)** $2\,\omega_2 = \omega_{dip}$.

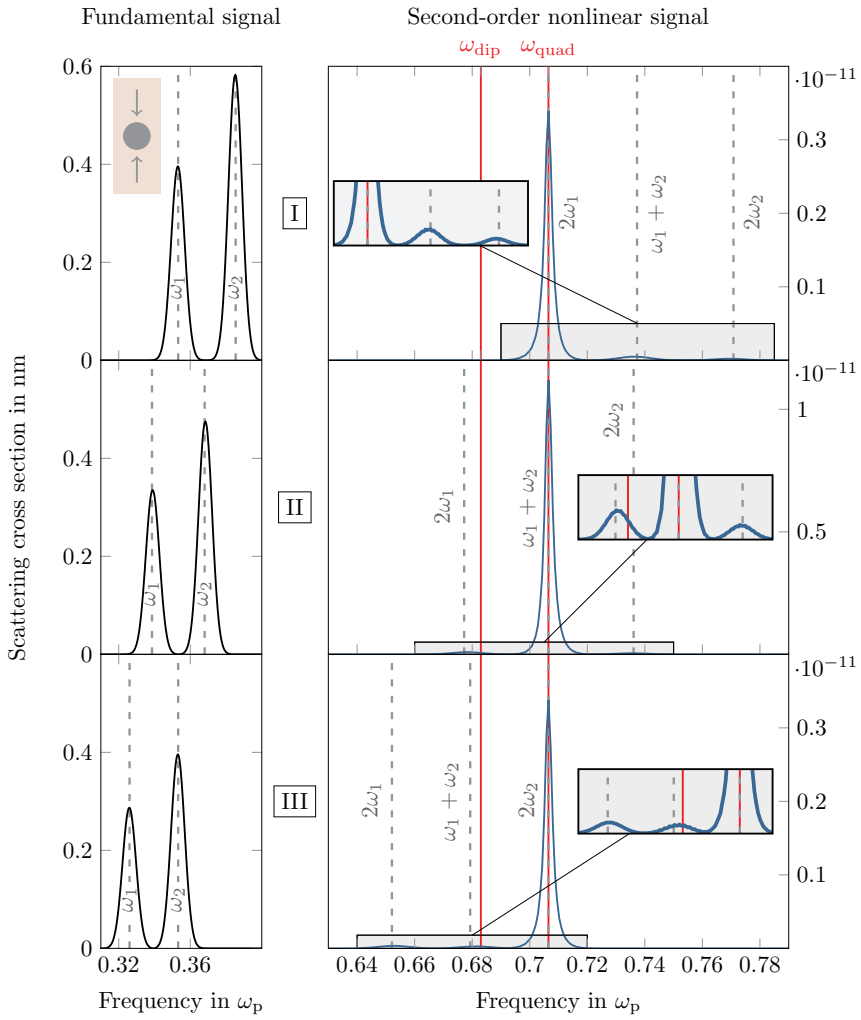

Figure 4.8: Scattering cross section for the second-order response of a circular nanowire (see fig. 4.2) for two excitation pulses injected from opposite sides with different central frequencies ω_1 and ω_2. In all cases, the two pulses are separated by $0.03\,\omega_{\mathrm{p}}$ and the incident electric field has an amplitude of $E_0 = 10^6\ \mathrm{V/m}$. The incident pulses are chosen so that **(I)** $2\,\omega_1 = \omega_{\mathrm{quad}}$, **(II)** $\omega_1 + \omega_2 = \omega_{\mathrm{quad}}$, **(III)** $2\,\omega_2 = \omega_{\mathrm{quad}}$.

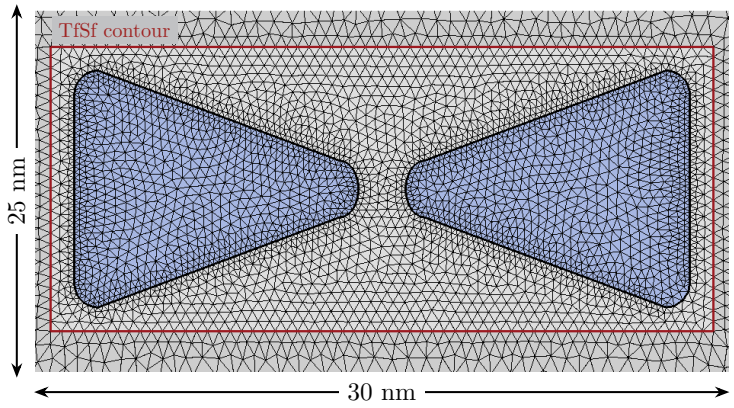

Figure 4.9: Mesh of a nanowire setup with a bowtie cross section. The maximal element edge length $h_{\max} = 1.3\,\mathrm{nm}$. The mesh was generated with NETGEN-4.9.12 [106].

As a second, more complicated structure, we investigate a nanowire dimer with a bowtie-shaped cross section as depicted in fig. 4.9. For this system, we expect a stronger second-order response in comparison to the case with single circular nanowire due to the field enhancement in the gap of the bowtie structure [107]. The bowtie antenna consists of two identical isosceles triangles with rounded corners, a base of 25 nm length, and a height of 30 nm, which are separated by a 5-nm gap. For the spatial discretization we choose maximal element edge size is $h_{\max} = 1.3\,\mathrm{nm}$ at bowtie's surfaces. While we employ the same material as for the cylinder, the nanoantenna is now not surrounded by air but embedded in a background medium with a constant permittivity ($\varepsilon = 2.25$). In fig. 4.10 we display the linear broadband scattering and absorption spectra under illumination from one side as indicated by the inset of fig. 4.10. The incoming pulse has a duration of $t_{\mathrm{pulse}} = 1.3 \cdot 10^{-15}\,\mathrm{s}$ (corresponding to a center frequency of $\omega_{\mathrm{FWHM}} = 0.34\,\omega_{\mathrm{p}}$), a center frequency of $\omega_0 = 0.68\,\omega_{\mathrm{p}}$ and an electric field amplitude of $E_0 = 10^6\,\mathrm{V/m}$. For the calculations we use the same filter properties, polynomial order and simulation time as for the cylindrical nanowire. The linear broadband spectrum fig. 4.6 reveals the four energetically lowest resonances, namely the dipole resonance ($\omega_{\mathrm{dip}} = 0.30\,\omega_{\mathrm{p}}$), the quadrupole resonance ($\omega_{\mathrm{quad}} = 0.47\,\omega_{\mathrm{p}}$), the hexapole resonance ($\omega_{\mathrm{hex}} = 0.53\,\omega_{\mathrm{p}}$), and the octopole resonance ($\omega_{\mathrm{oct}} = 0.56\,\omega_{\mathrm{p}}$), which are marked by the vertical red lines in fig. 4.10. The structure also features a multitude of resonances in the vicinity of $0.6\,\omega_{\mathrm{p}}$, which is purely typical for dimer structures and originates from the nonlocal nature of the hydrodynamic model [20].

Using the resonance frequencies we again perform a frequency tuning with two incoming pulses similar to the case of the cylindrical nanowire. Therefore, we excite the structure with two beams from opposite sides as indicated by the inset in fig. 4.11. In order to be able to quantitatively compare the second-order spectra of the bowtie system with the second-order spectra of the circular nanowire, we use the same temporal profiles and the same electric field amplitude as in the case of the circular nanowire. Because the bowtie antenna exhibits very rich linear spectra (cf. fig. 4.10), we have a multitude of possibilities to tune our incident pulses to on-resonance conditions. As before, we can choose our incident pulses such that a SHG signal or the SFG signal coincides with one of the resonances. In addition, we can tune one of the fundamental signals to coincide with the energetically lowest-lying resonance ($\omega_{\mathrm{dip}} = 0.30\,\omega_{\mathrm{p}}$), thus achieving a double-resonant scenario. Without attempting to be exhaustive, we study in the remainder some exemplary single- and double-resonant cases: In fig. 4.11 (I), we tune one

of the excitation pulses to be on the dipole resonance ($\omega_2 = \omega_{\mathrm{dip}}$) and the other one in a way that the SFG signal coincides with the octopole resonance ($\omega_1 + \omega_2 = \omega_{\mathrm{oct}}$). This generates a rather large SFG signal; it is about 5000 times larger than the strongest signal of the circular nanowire (cf fig. 4.8 (II)). We also observe an enhancement of the SHG signals compared to the case of the cylindrical nanowire. However, this enhancement is less pronounced as compared to the SFG. In fig. 4.11 (II) we depict the situation where one pulse frequency remains on the dipole resonance, i.e. $\omega_2 = \omega_{\mathrm{dip}}$, and the other pulse is tuned so that its second-harmonic lies on the quadrupole resonance, i.e. $2\,\omega_1 = \omega_{\mathrm{quad}}$. Even with the SHG signal lying on the quadrupole resonance this signal is still weak compared to the SFG signal which only lies in the vicinity of another resonance. Thus, fig. 4.11 (I) and (II) serve to substantiate our above findings: SFG signals are generally stronger than SHG signals. In fig. 4.11 (III) we show the second-order spectra for a case where neither of the incident pulses is on-resonance but both second-harmonic frequencies lie on a resonance, i.e. $2\omega_1 = \omega_{\mathrm{quad}}$ and $2\omega_2 = \omega_{\mathrm{hex}}$. The SHG signal at $2\omega_2$ is relatively strong compared the other SHG signal at $2\omega_1$ and the SFG signal at $\omega_1 + \omega_2$. Hence, the hexapole resonance at appears to be particularly well suited for an efficient SHG. Note, that the same resonance is also responsible for the large SFG signal in fig. 4.11 (II). Finally, in fig. 4.11 (IV) we display another case where neither of the incident pulses themselves lies on a resonance, i.e. $\omega_1 = 0.22\,\omega_{\mathrm{p}}$ and $\omega_2 = 0.26\,\omega_{\mathrm{p}}$. Here, we see a relatively strong SFG signal in the proximity of the quadrupole resonance. In comparison the SHG signal, which lies even closer to the quadrupole resonance, seems relatively modest.

We come to the overall conclusion that by judiciously tuning the incident pulses and choosing an intelligent plasmonic nanostructure design we can optimize the second-order response.

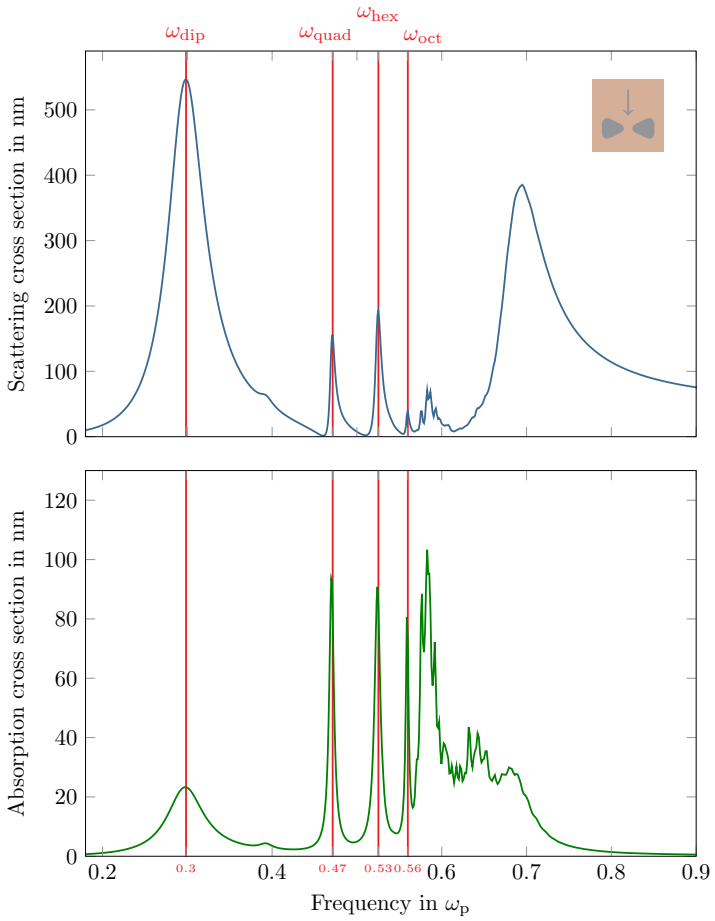

Figure 4.10: Linear scattering and absorption spectra for a bowtie-shaped nanowire (cf. fig. 4.9). The nanowire was excited with a single excitation pulse with a duration of $t_{\mathrm{pulse}} = 1.3\,\mathrm{fs}$, a band width of $\omega_0 = 0.34\,\omega_{\mathrm{p}}$ and an amplitude of $E_0 = 10^6\,\mathrm{V/m}$. The vertical red lines mark the positions of the dipole ($\omega_{\mathrm{dip}} = 0.30\,\omega_{\mathrm{p}}$) and quadrupole ($\omega_{\mathrm{quad}} = 0.47\,\omega_{\mathrm{p}}$), hexapole ($\omega_{\mathrm{hex}} = 0.53\,\omega_{\mathrm{p}}$) and octopole ($\omega_{\mathrm{oct}} = 0.56\,\omega_{\mathrm{p}}$) resonance.

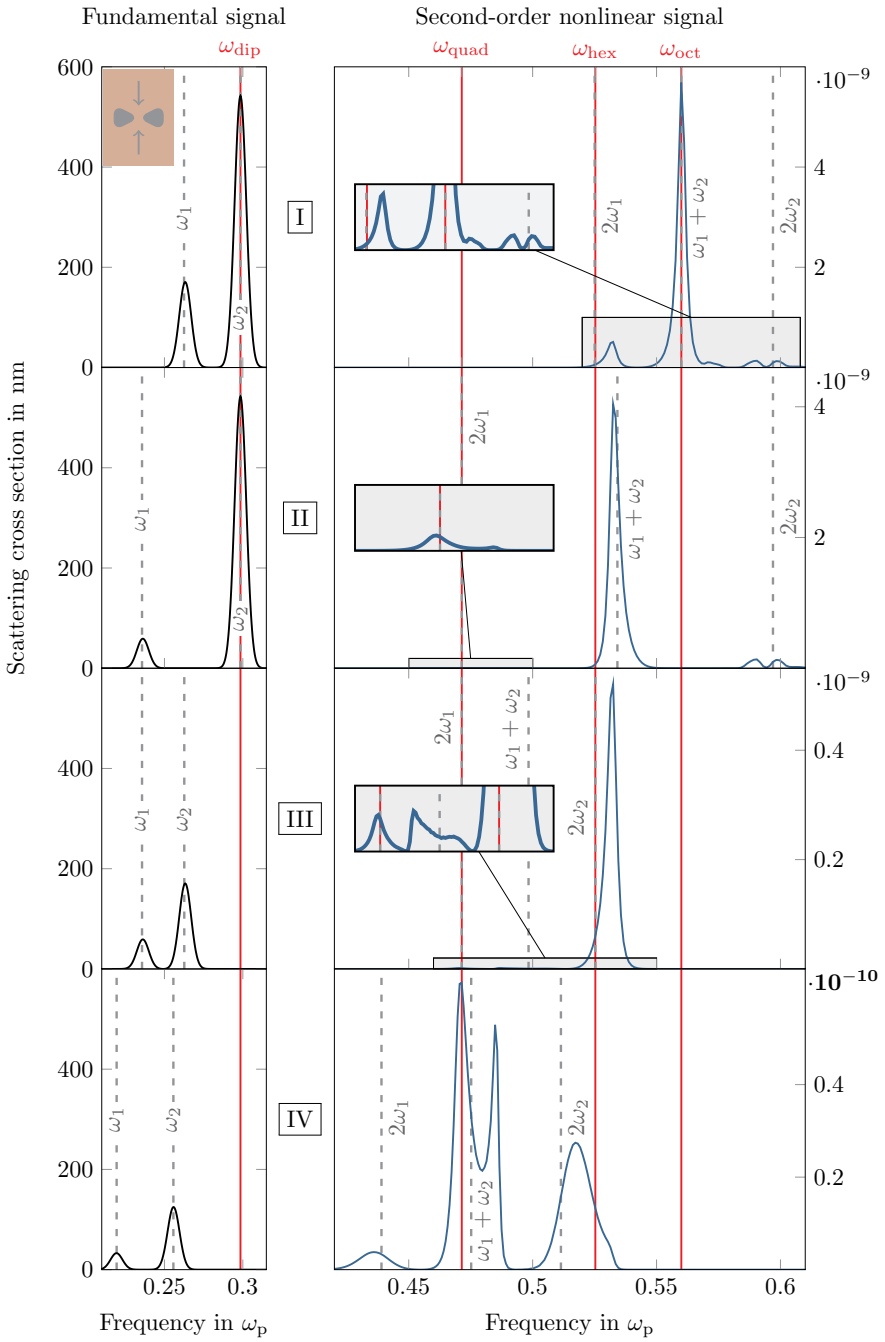

Figure 4.11: Scattering cross section for the second-order response of a bowtie-shaped nanowire (cf. fig. 4.9) for two excitation pulses with different central frequencies ω_1 and ω_2, which are injected from opposite sides. The central frequencies are tuned so that **(I)** $\omega_2 = \omega_{dip}$ and $\omega_1 + \omega_2 = \omega_{oct}$, **(II)** $\omega_2 = \omega_{dip}$ and $2\omega_1 = \omega_{quad}$, **(III)** $2\omega_1 = \omega_{quad}$, $2\omega_2 = \omega_{hex}$, **(IV)** $\omega_1 = 0.22\,\omega_p$, $\omega_2 = 0.26\,\omega_p$

CHAPTER 5

Raman-active dielectric materials

A common nonlinear phenomenon in dielectric materials is the effect of Raman scattering. Unlike the wave-mixing processes seen in the previous chapter 4, Raman scattering is an indirect resonant effect. In particular, stimulated Raman scattering is a dissipative process best described by a third-order polarization.

In the following section 5.1 we illustrate how to model Raman-active dielectric materials in terms of the third-order polarization. To this end, we first present in section 5.1.1 the fundamental assumptions, which are applied to the model. Proceeding from these, we construct the third-order polarization at optical frequencies in section 5.1.2 and section 5.1.3. Most of the considerations made in section 5.1 can also be found in the work of Hellwarth [26].

New, however, is our attempt to incorporate the three-dimensional material model into the DGTD framework. Though the in the previous work by Taflove and Goorjian [108] and more recently in the paper of Varin et al. [22] attempts have been made to solve the model equations along with Maxwell's equations in FDTD, it is not entirely clear how this needs to be done for a DGTD scheme – especially in three dimensions. We, therefore, dedicate section 5.2 to the construction of an appropriate set of equations, which are suitable for the DGTD method. Subsequently in section 5.2.2, we present the results obtained by the corresponding DGTD calculations.

5.1 Third-order polarization in Born-Oppenheimer approximation

Stimulated Raman scattering (SRS) is a third-order nonlinear process [49]. To substantiate this claim, one needs to analyze the third-order nonlinear polarization in detail. In the following we are going to calculate the nonlinear polarization of a non-magnetic material in electric-dipole approximation (cf. section 1.2). For this, we follow the argumentation line of Hellwarth [26], where we apply the Born-Oppenheimer approximation (BOA).

5.1.1 Fundamental assumptions

Let us consider a non-magnetic dielectric with volume $\mathcal{V}$, which consists of N_n atomic nuclei and N_e electrons[1]. The Schrödinger equation of the total system shall be given by

$$\hat{H}\left|\psi(\mathbf{r}^{(\mathrm{e})},\mathbf{r}^{(\mathrm{n})},\mathbf{E})\right\rangle = \mathcal{E}\left|\psi(\mathbf{r}^{(\mathrm{e})},\mathbf{r}^{(\mathrm{n})},\mathbf{E})\right\rangle, \tag{5.1}$$

where $\hat{H}$ denotes the total Hamiltonian, $\left|\psi(\mathbf{r}^{(\mathrm{e})},\mathbf{r}^{(\mathrm{n})},\mathbf{E})\right\rangle$ denotes an eigenstate of the system and $\mathcal{E}$ is the corresponding eigen energy. The total Hamiltonian is given by several different contributions

$$\hat{H} = \hat{T}_\mathrm{e} + \hat{T}_\mathrm{n} + \hat{V}_\mathrm{ee} + \hat{V}_\mathrm{nn} + \hat{V}_\mathrm{ne} + \hat{V}_\mathrm{eE} + \hat{V}_\mathrm{nE}, \tag{5.2}$$

where the kinetic energy of the electrons is given by

$$\hat{T}_\mathrm{e} = \sum_{\alpha=1}^{N_\mathrm{e}} \left(\frac{\hat{\mathbf{p}}_\alpha^2}{2m_\mathrm{e}}\right), \tag{5.3}$$

whereas the kinetic energy of the nuclei is given by

$$\hat{T}_\mathrm{n} = \sum_{\beta=1}^{N_\mathrm{n}} \left(\frac{\hat{\mathbf{P}}_\beta^2}{2M_\beta}\right). \tag{5.4}$$

Thereby, $\hat{\mathbf{p}}_\alpha$ denotes the momentum of the α-th electron, whereas $\hat{\mathbf{P}}_\beta$ denotes the momentum and M_β the mass of the β-th nucleus. Furthermore, the electrons interact with themselves by $\hat{V}_\mathrm{ee}$, whereas the inter-nuclear interaction is represented by $\hat{V}_\mathrm{nn}$. In the presence of an external electromagnetic field the electrons and nuclei couple to this field by $\hat{V}_\mathrm{eE}$ and $\hat{V}_\mathrm{nE}$, respectively.

We can now simplify the problem (5.1) by making the following assumptions:

- We consider the applied electric field $\mathbf{E}(\mathbf{r},t)$ to be macroscopic. Therefore, it varies over a characteristic length that is much larger than any atomic distance. As a result, the

[1] The following discussion can be carried out in the same way if we describe the material by the means of outer shell electrons and ions.

electric field can be regarded as uniform over the material[2]. In this case the electric-dipole approximation applies and the field-electron interaction as well as the field-nuclei interaction can be described by the according electric-dipole interaction for the non-magnetic material (1.89).

- The external electric field is sufficiently weak, so that we can treat the problem by using perturbation theory (cf section 2.1).
- The BOA applies: due to the large differences in mass, the electronic motion happens on a much smaller time-scale compared to the nuclear motion. Hence, the nuclear kinetic energy in (5.2) can be treated perturbatively as the difference in magnitudes of the nuclear and the electronic kinetic energy is about 10^4 to 10^5. Consequently, one can separate the electronic degrees of freedom from the nuclear ones as a first approximation [76]. Thus, the electrons experience the presence of the atomic cores by an effective potential. They follow the fields of the fluctuating nuclei adiabatically and remain in their ground-state for any given nuclear configuration at a given macroscopic point in time.
- The material is transparent and non-conducting. For such media, the electronic gap-frequency is much higher than any optical frequency[26]. Hence, for optical excitations the electronic motion follows the electric field nearly adiabatically. In this case we can treat the electronic-light interaction by the time-independent Rayleigh-Schrödinger theory [46].

With the assumptions above we can now proceed to calculate the polarization in electric-dipole approximation (cf. section 1.2)

$$P_i = -\frac{1}{\mathcal{V}} \left(\frac{\partial \left\langle \hat{V}_{\mathrm{eE}} + \hat{V}_{\mathrm{nE}} \right\rangle}{\partial E_i} \right). \tag{5.5}$$

5.1.2 Effective light-matter interaction operator

In the following we show how to calculate the expectation value of the light matter interaction

$$\left\langle \hat{V}_{\mathrm{eE}} + \hat{V}_{\mathrm{nE}} \right\rangle = \left\langle \psi(\mathbf{r}^{(\mathrm{e})}, \mathbf{r}^{(\mathrm{n})}, \mathbf{E}) \right| \left(\hat{V}_{\mathrm{nE}} + \hat{V}_{\mathrm{eE}} \right) \left| \psi(\mathbf{r}^{(\mathrm{e})}, \mathbf{r}^{(\mathrm{n})}, \mathbf{E}) \right\rangle. \tag{5.6}$$

In electric-dipole approximation the electron-field interaction is given by

$$\hat{V}_{\mathrm{eE}} = -q_{\mathrm{e}} \sum_{\alpha=1}^{N_{\mathrm{e}}} \hat{\mathbf{r}}_{\alpha}^{(\mathrm{e})} \cdot \mathbf{E}(\mathbf{r}, t) \tag{5.7}$$

[2] Note, that this assumption is in stark contrast to those assumptions that can be made for metalls (cf. chapter 4).

and the nucleus-field interaction is given by

$$\hat{V}_{\mathrm{nE}} = -\sum_{\beta=1}^{N_{\mathrm{n}}} Q_\beta \, \mathbf{r}_\beta^{(\mathrm{n})} \cdot \mathbf{E}(\mathbf{r}, t), \tag{5.8}$$

where Q_β denotes the charge of the β-th nucleus. As pointed out in section 5.1.1 we can separate the electronic from the nuclear problem in BOA, which yields the separation ansatz

$$\left|\psi(\mathbf{r}^{(\mathrm{e})}, \mathbf{r}^{(\mathrm{n})}, \mathbf{E})\right\rangle = \left|\psi^{(\mathrm{n})}(\mathbf{r}^{(\mathrm{n})}, \mathbf{E})\right\rangle \left|\psi^{(\mathrm{e})}(\mathbf{r}^{(\mathrm{e})}; \mathbf{r}^{(\mathrm{n})}, \mathbf{E})\right\rangle, \tag{5.9}$$

where we have introduced the nuclear states $|\psi^{(\mathrm{n})}(\mathbf{r}^{(\mathrm{n})}, \mathbf{E})\rangle$ and the electronic states $|\psi^{(\mathrm{e})}(\mathbf{r}^{(\mathrm{e})}; \mathbf{r}^{(\mathrm{n})}, \mathbf{E})\rangle$. Note, that while the electronic state depends on the electronic positions $\mathbf{r}^{(\mathrm{e})} = (\mathbf{r}_1^{(\mathrm{e})}, \ldots, \mathbf{r}_{N_e}^{(\mathrm{e})})$ explicitly, it depends on the nuclear configuration $\mathbf{r}^{(\mathrm{n})} = (\mathbf{r}_1^{(\mathrm{n})}, \ldots, \mathbf{r}_{N_n}^{(\mathrm{n})})$ as well as the electric field $\mathbf{E}$ only parametrically. Because the electrons are in their ground-state for any given nuclear configuration and electric field, we can replace the general state $|\psi^{(\mathrm{e})}(\mathbf{r}^{(\mathrm{e})}; \mathbf{r}^{(\mathrm{n})}, \mathbf{E})\rangle$ by the ground-state $|\psi_0^{(\mathrm{e})}(\mathbf{r}^{(\mathrm{e})}; \mathbf{r}^{(\mathrm{n})}, \mathbf{E})\rangle$. We can then calculate the expectation value (5.6) by

$$\begin{aligned} &\left\langle \psi(\mathbf{r}^{(\mathrm{e})}, \mathbf{r}^{(\mathrm{n})}, \mathbf{E})\right| \left(\hat{V}_{\mathrm{nE}} + \hat{V}_{\mathrm{eE}} \right) \left|\psi(\mathbf{r}^{(\mathrm{e})}, \mathbf{r}^{(\mathrm{n})}, \mathbf{E})\right\rangle = \\ &\quad = \left\langle \psi^{(\mathrm{n})}(\mathbf{r}^{(\mathrm{n})}, \mathbf{E})\right| \left(\hat{V}_{\mathrm{nE}} + \hat{V}_{\mathrm{eE}}^{\mathrm{eff}} \right) \left|\psi^{(\mathrm{n})}(\mathbf{r}^{(\mathrm{n})}, \mathbf{E})\right\rangle, \end{aligned} \tag{5.10}$$

where the electronic degrees of freedom are absorbed in the effective light-matter interaction operator

$$\hat{V}_{\mathrm{eE}}^{\mathrm{eff}} = \left\langle \psi_0^{(\mathrm{e})}(\mathbf{r}^{(\mathrm{e})}; \mathbf{r}^{(\mathrm{n})}, \mathbf{E})\right| \hat{V}_{\mathrm{eE}} \left|\psi_0^{(\mathrm{e})}(\mathbf{r}^{(\mathrm{e})}; \mathbf{r}^{(\mathrm{n})}, \mathbf{E})\right\rangle. \tag{5.11}$$

Since we consider the electrons to follow the external electric field adiabtically, the electronic problem can be treated in the static limit. Hence, we calculate the expectation value (5.11) by using (time-independent) Rayleigh-Schrödinger perturbation theory [37, 47]. As a result we can express (5.11) in ascending powers of the electric field[3]

$$\hat{V}_{\mathrm{eE}}^{\mathrm{eff}} = -\sum_i \hat{\mu}_i E_i - \frac{1}{2}\sum_{i,j} \hat{\alpha}_{ij} E_i E_j - \frac{1}{3}\sum_{i,j,k} \hat{\beta}_{ijk} E_i E_j E_k - \frac{1}{4}\sum_{i,j,k,l} \hat{\gamma}_{ijkl} E_i E_j E_k E_l - \ldots \, . \tag{5.12}$$

Note, that the coefficients in (5.12) still implicitly depend on the nuclear configuration $\mathbf{r}^{(\mathrm{n})}$. Furthermore, the coefficients are real and totally symmetric under interchange of their space indices $i, j, k, l, \ldots$, which is commonly referred to as Kleinman's symmetry (cf. section 2.2).

We can now use the effective operator (5.12) to evaluate the expectation value (5.6) further. This will lead us to the nonlinear polarization (5.5).

[3] For a detailed derivation of (5.12) see appendix C.1.

5.1.3 Nonlinear total polarization

We now proceed to calculate the polarization (5.5) using (5.11) and (5.12). The nonlinear polarization can then be expressed in ascending powers of the electric field

$$P_i = \frac{1}{\mathcal{V}}\left(\left\langle \hat{m}_i \right\rangle_{\mathrm{n}} + \sum_j \left\langle \hat{\alpha}_{ij} \right\rangle_{\mathrm{n}} E_j + \sum_{j,k} \left\langle \hat{\beta}_{ijk} \right\rangle_{\mathrm{n}} E_j E_k + \sum_{j,k,l} \left\langle \hat{\gamma}_{ijkl} \right\rangle_{\mathrm{n}} E_j E_k E_l + \dots \right) \tag{5.13}$$

where we employ the expectation values $\langle \dots \rangle_{\mathrm{n}}$ with respect to the nuclear states $|\psi^{(\mathrm{n})}(\mathbf{r}^{(n)}, \mathbf{E})\rangle$. Note, that in arriving at (5.13) we have introduced the abbreviation

$$\hat{m}_i \equiv -e \sum_\alpha \hat{x}^{(\mathrm{e})}_{i,\alpha} + \sum_\beta Q_\beta \, \hat{x}^{(\mathrm{n})}_{i,\beta}. \tag{5.14}$$

We would like to point out that the operators in (5.13) depend on the nuclear configuration. In contrast to the electrostatic calculation of (5.12), we can no longer calculate the expectation values in terms of the Rayleigh-Schrödinger perturbation theory as the nuclear states cannot be viewed as static at macroscopic time-scales. Instead, we apply the nonlinear response-theory formalism of section 2.1, where we use (5.12) as interaction operator to calculate the expectation values in (5.13) from the corresponding Dyson series. In doing so, we determine the linear polarization by

$$\begin{aligned} P_i^{(1)}(\mathbf{r},t) =& \frac{1}{\mathcal{V}} \sum_j \mathrm{Tr}\left\{\hat{\alpha}_{ij}\,\hat{\varrho}_0\right\} E_j(\mathbf{r},t) - \\ &- \frac{1}{\mathrm{i}\hbar\mathcal{V}} \sum_j \int \mathrm{d}t' \; \mathrm{Tr}\left\{ \left[\hat{m}_i{}^{(\mathrm{D})}(t), \hat{m}_j{}^{(\mathrm{D})}(t')\right]_- \hat{\varrho}_0 \right\} E_j(\mathbf{r},t')\,\Theta(t-t'). \end{aligned} \tag{5.15}$$

Then the second-order polarization can be expressed by

$$\begin{aligned} P_i^{(2)}(\mathbf{r},t) =& \frac{1}{\mathcal{V}} \sum_{j,k} \mathrm{Tr}\left\{\hat{\beta}_{ijk}\,\hat{\varrho}_0\right\} E_j(\mathbf{r},t)\, E_k(\mathbf{r},t) - \\ &- \frac{1}{\mathrm{i}\hbar\mathcal{V}} \sum_{j,k} \int \mathrm{d}t' \left(\mathrm{Tr}\left\{ \left[\hat{\alpha}_{ij}{}^{(\mathrm{D})}(t), \hat{m}_k{}^{(\mathrm{D})}(t')\right]_- \hat{\varrho}_0 \right\} E_j(\mathbf{r},t)\, E_k(\mathbf{r},t') + \right. \\ &\left. + \mathrm{Tr}\left\{ \left[\hat{m}_i{}^{(\mathrm{D})}(t), \frac{1}{2}\,\hat{\alpha}_{jk}{}^{(\mathrm{D})}(t')\right]_- \hat{\varrho}_0 \right\} E_j(\mathbf{r},t')\, E_k(\mathbf{r},t') \right) \Theta(t-t') - \\ &- \frac{1}{\hbar^2\mathcal{V}} \sum_{j,k,l} \int \mathrm{d}t' \int \mathrm{d}t'' \; \mathrm{Tr}\left\{ \left[\left[\hat{m}_i{}^{(\mathrm{D})}(t), \hat{m}_j{}^{(\mathrm{D})}(t')\right]_-, \hat{m}_k{}^{(\mathrm{D})}(t'')\right]_- \hat{\varrho}_0 \right\} \cdot \\ &\cdot E_j(\mathbf{r},t')\, E_k(\mathbf{r},t'')\,\Theta(t-t')\,\Theta(t'-t''). \end{aligned} \tag{5.16}$$

However, if we assume that the material is centrosymmetric, the bulk dielectric (local) material will not display any second-order of nonlinear polarization (cf. section 2.2)[4]. Therefore, the leading nonlinear order is assumed to be of third-order with respect to the electric field. The third-order polarization in BOA consists in total of eight different contributions, which can be divided into one instantaneous contribution

$$P_i^{(3.1)}(\mathbf{r},t) = \frac{1}{\mathcal{V}} \sum_{j,k,l} \mathrm{Tr}\left\{ \hat{\gamma}_{ijkl}\, \hat{\varrho}_0 \right\} E_j(\mathbf{r},t)\, E_k(\mathbf{r},t)\, E_l(\mathbf{r},t), \tag{5.17}$$

and seven contributions with retardation

$$P_i^{(3.2)}(\mathbf{r},t) = -\frac{1}{\mathrm{i}\hbar\mathcal{V}} \sum_{j,k,l} \int \mathrm{d}t'\ \mathrm{Tr}\left\{ \left[\hat{\beta}_{ijk}{}^{(\mathrm{D})}(t), \hat{m}_l{}^{(\mathrm{D})}(t') \right]_- \hat{\varrho}_0 \right\} \cdot \\ \cdot E_j(\mathbf{r},t)\, E_k(\mathbf{r},t)\, E_l(\mathbf{r},t')\, \Theta(t-t'), \tag{5.18}$$

$$P_i^{(3.3)}(\mathbf{r},t) = -\frac{1}{\mathrm{i}\hbar\mathcal{V}} \sum_{j,k,l} \int \mathrm{d}t'\ \mathrm{Tr}\left\{ \left[\hat{m}_i{}^{(\mathrm{D})}(t), \frac{1}{3}\, \hat{\beta}_{jkl}{}^{(\mathrm{D})}(t') \right]_- \hat{\varrho}_0 \right\} \cdot \\ \cdot E_j(\mathbf{r},t')\, E_k(\mathbf{r},t')\, E_l(\mathbf{r},t')\, \Theta(t-t'), \tag{5.19}$$

$$P_i^{(3.4)}(\mathbf{r},t) = -\frac{1}{\mathrm{i}\hbar\mathcal{V}} \sum_{j,k,l} \int \mathrm{d}t'\ \mathrm{Tr}\left\{ \left[\hat{\alpha}_{ij}{}^{(\mathrm{D})}(t), \frac{1}{2}\, \hat{\alpha}_{kl}{}^{(\mathrm{D})}(t') \right]_- \hat{\varrho}_0 \right\} \cdot \\ \cdot E_j(\mathbf{r},t)\, E_k(\mathbf{r},t')\, E_l(\mathbf{r},t')\, \Theta(t-t'), \tag{5.20}$$

$$P_i^{(3.5)}(\mathbf{r},t) = -\frac{1}{\hbar^2\mathcal{V}} \sum_{j,k,l} \int \mathrm{d}t' \int \mathrm{d}t''\ \mathrm{Tr}\left\{ \left[\left[\hat{m}_i{}^{(\mathrm{D})}(t), \hat{m}_j{}^{(\mathrm{D})}(t') \right]_-, \frac{1}{2}\, \hat{\alpha}_{kl}{}^{(\mathrm{D})}(t'') \right]_- \hat{\varrho}_0 \right\} \cdot \\ \cdot E_j(\mathbf{r},t')\, E_k(\mathbf{r},t'')\, E_l(\mathbf{r},t'')\, \Theta(t-t')\, \Theta(t'-t''), \tag{5.21}$$

$$P_i^{(3.6)}(\mathbf{r},t) = -\frac{1}{\hbar^2\mathcal{V}} \sum_{j,k,l} \int \mathrm{d}t' \int \mathrm{d}t''\ \mathrm{Tr}\left\{ \left[\left[\hat{m}_i{}^{(\mathrm{D})}(t), \frac{1}{2}\hat{\alpha}_{jk}{}^{(\mathrm{D})}(t') \right]_-, \hat{m}_l{}^{(\mathrm{D})}(t'') \right]_- \hat{\varrho}_0 \right\} \cdot \\ \cdot E_j(\mathbf{r},t')\, E_k(\mathbf{r},t')\, E_l(\mathbf{r},t'')\, \Theta(t-t')\, \Theta(t'-t''), \tag{5.22}$$

[4] That being said, one might not be able to neglect the second-order contribution to the polarization if one considers a material with a certain geometry, i.e. a material with a surface, as the inversion symmetry is broken at the surface (cf. section 2.2). Further investigation are needed in this case (cf. [51]).

$$P_i^{(3.7)}(\mathbf{r},t) = -\frac{1}{\hbar^2\mathcal{V}}\sum_{j,k,l}\int \mathrm{d}t' \int \mathrm{d}t''\ \mathrm{Tr}\left\{\left[\left[\hat{\alpha}_{ij}{}^{(\mathrm{D})}(t), \hat{m}_k{}^{(\mathrm{D})}(t')\right]_-, \hat{m}_l{}^{(\mathrm{D})}(t'')\right]_- \hat{\varrho}_0\right\}\cdot \\ \cdot E_j(\mathbf{r},t)\, E_k(\mathbf{r},t')\, E_l(\mathbf{r},t'')\, \Theta(t-t')\, \Theta(t'-t''), \tag{5.23}$$

and

$$P_i^{(3.8)}(\mathbf{r},t) = -\frac{1}{\mathrm{i}\hbar^3\mathcal{V}}\sum_{j,k,l}\int \mathrm{d}t' \int \mathrm{d}t'' \int \mathrm{d}t'''\ \mathrm{Tr}\left\{\left[\left[\left[\hat{m}_i{}^{(\mathrm{D})}(t), \hat{m}_j{}^{(\mathrm{D})}(t')\right]_-, \hat{m}_k{}^{(\mathrm{D})}(t'')\right]_-, \hat{m}_l{}^{(\mathrm{D})}(t''')\right]_- \hat{\varrho}_0\right\}\cdot \\ \cdot E_j(\mathbf{r},t')\, E_k(\mathbf{r},t'')\, E_l(\mathbf{r},t''')\, \Theta(t-t')\, \Theta(t'-t'')\, \Theta(t''-t'''), \tag{5.24}$$

which are summed up to form the total third-order polarization $P_i^{(3)} = \sum_{s=1}^{8} P_i^{(3.s)}$. If we assume the electromagnetic excitation to be at optical frequencies, the expression for the third-order polarization can be reduced significantly. We will see that not all non-instantaneous terms (5.18) to (5.24) will contribute to the overall polarization. In order to do so we examine the corresponding susceptibility tensors at optical frequencies.

5.1.4 Nonlinear frequency-dependent susceptibilities in the limit of optical excitations

Let us return to the linear polarization (5.15). More specifically, we are interested in the non-instantaneous part of (5.15), i.e. the second term of (5.15). We can express this term by

$$P_i^{(1.2)} = \varepsilon_0 \sum_j \int \mathrm{d}t'\ \mathcal{R}_{ij}^{(1.2)}(t-t')\, E_j(\mathbf{r},t'), \tag{5.25}$$

where we have defined the response kernel

$$\mathcal{R}_{ij}^{(1.2)}(t-t') = -\frac{1}{\mathrm{i}\hbar\varepsilon_0\mathcal{V}}\ \mathrm{Tr}\left\{\left[\hat{m}_i^{(D)}(t), \hat{m}_j^{(D)}(t')\right]_- \hat{\varrho}_0\right\}\Theta(t-t'). \tag{5.26}$$

We evaluate the trace in (5.26) further by studying the nuclear problem without the electric field perturbation

$$\hat{H}_{0\mathrm{n}}|a\rangle = \hbar\omega_a|a\rangle, \tag{5.27}$$

where we have defined the Hamiltonian $\hat{H}_{0\mathrm{n}} = \hat{T}_{\mathrm{n}} + \hat{V}_{\mathrm{nn}}$, the eigenstates $|a\rangle$ and the eigen frequencies ω_a. Thereby, the states $|a\rangle$ form a complete orthonormal set of eigen functions of the Hamiltonian $\hat{H}_{0\mathrm{n}}$. Using $\hat{H}_{0\mathrm{n}}$ we construct the time-evolution operator

$$\hat{U}_0(t) = \exp\left[-\frac{\mathrm{i}}{\hbar}\hat{H}_{0\mathrm{n}}\, t\right] \tag{5.28}$$

for the unperturbed nuclear system and the according steady-state density operator

$$\hat{\varrho}_0 = \frac{\mathrm{e}^{-\beta \hat{H}_{0\mathrm{n}}}}{\mathrm{Tr}\left\{\mathrm{e}^{-\beta \hat{H}_{0\mathrm{n}}}\right\}}. \tag{5.29}$$

We then apply (5.27) to (5.29) to the non-instantaneous linear polarization (5.26) yielding

$$\mathcal{R}_{ij}^{(1.2)}(t-t') = -\frac{1}{\mathrm{i}\hbar\varepsilon_0 \mathcal{V}} \sum_{a,b} \frac{\mathrm{e}^{-\beta\hbar\omega_a}}{\sum_c \mathrm{e}^{-\beta\hbar\omega_c}} \left(\left\langle a \right| \hat{m}_i \left| b \right\rangle \left\langle b \right| \hat{m}_j \left| a \right\rangle \mathrm{e}^{i\omega_{ab}(t-t')} - \mathrm{c.c.} \right) \Theta(t-t'), \tag{5.30}$$

where we have introduced the phonon frequency $\omega_{ab} = \omega_a - \omega_b$. Note that, in arriving at (5.30) we have assumed that the occurring transition matrix elements are real, which can be done w.l.o.g.. So far, we have not accounted for any kind of damping within our system. A simple way to incorporate damping is by inserting an exponential damping factor $\mathrm{e}^{-\gamma_{ab}(t-t')}$ for every vibrational transition into (5.30)[5]. Thereby, γ_{ab} denotes the phenomenological relaxation rate or dephasing parameter, which gives the spectral line width for the transition between the two vibrational modes $|a\rangle$ and $|b\rangle$ [49]. We, furthermore, assume that $\gamma_{ab} = \gamma_{ba}$. Moreover, if we require

$$\int \mathrm{d}\tau \; \mathcal{R}_{ij}^{(1.2)}(\tau) = \sum_{a,b} \; \chi^{(1)}_{0,ij,ab} = \text{const.}$$

where each constant value $\chi^{(1)}_{0,ij,ab}$ represents the *anisotropic oscillator strength* [41]

$$\chi^{(1)}_{0,ij,ab} = \left(\frac{2}{\hbar\varepsilon_0\mathcal{V}}\right) \left(\frac{\omega_{ab}}{\omega_{ab}^2 + \gamma_{ab}^2}\right) \left(\frac{\mathrm{e}^{-\beta\hbar\omega_a}}{\sum_c \mathrm{e}^{-\beta\hbar\omega_c}}\right) \left\langle a \right| \hat{m}_i \left| b \right\rangle \left\langle b \right| \hat{m}_j \left| a \right\rangle, \tag{5.31}$$

the response tensor including phenomenological damping can be expressed by the causal damped sine function

$$\mathcal{R}_{ij}^{(1.2)}(t-t') = \sum_{a,b} \chi^{(1)}_{0,ab,ij} \left(\frac{\omega_{ab}^2 + \gamma_{ab}^2}{\omega_{ab}}\right) \sin[\omega_{ab}(t-t')] \; \mathrm{e}^{-\gamma_{ab}(t-t')} \, \Theta(t-t'). \tag{5.32}$$

Using the representation

$$\Theta(t-t') = \frac{\mathrm{i}}{2\pi} \int \mathrm{d}\omega \; \frac{\mathrm{e}^{-\mathrm{i}\omega(t-t')}}{\omega + \mathrm{i}\epsilon}, \qquad \text{where} \quad \epsilon \downarrow 0 \tag{5.33}$$

[5] For more information on how the phenomenological damping factor is formally incorporated into the time-dependent perturbation theory and in consequence into the nonlinear polarization see appendix C.2.

of the Heaviside step function [43] we perform a Fourier transform of the response kernel (5.32), which yields the linear susceptibility

$$\chi_{ij}^{(1.2)}(-\omega;\omega) = \sum_{a,b} \frac{\chi_{0,ab,ij}^{(1)}\ \bar{\omega}_{ab}^2}{\bar{\omega}_{ab}^2 - 2\,\mathrm{i}\,\gamma_{ab}\,\omega - \omega^2}. \tag{5.34}$$

In arriving at (5.34) we have defined the quadratic frequency $\bar{\omega}_{ab}^2 = \omega_{ab}^2 + \gamma_{ab}^2$. From (5.34) we realize that the linear response function acts as a sum of narrow band filters around each vibrational frequency ω_{ab} [26, 41]. Therefore, in order to evoke a strong linear material response, any excitation needs to be chosen in a way that a phonon is created. Hence, in the presence of an external field that is at purely optical frequencies ($\sim 10^{15}\,\mathrm{Hz}$) the linear signal might be small but not negligible in comparison to a nonlinear response signal. Note, that for an isotropic material we have $\chi_{0,ab,ij}^{(1)} \to \chi_{0,ab}^{(1)}\delta_{ij}$. In this case the susceptibility (5.34) resembles the classical Lorentz oscillator model [28].

For reasons given in section 5.1.3 we do not consider the second-order polarization and its susceptibility. Instead we assume the third-order to be the leading order. As pointed out in section 5.1.3, the expression for the third-order polarization consisting of the contributions (5.17) to (5.24) can be vastly simplified if we assume the excitations to be at optical frequencies since most of the non-instantaneous terms can be neglected. The discussion is similar to the one for the linear response at optical frequencies. We, first, study the third-order polarization contribution (5.19)

$$P_i^{(3.3)}(\mathbf{r},t) = \varepsilon_0 \sum_{j,k,l} \int \mathrm{d}t'\ \mathcal{R}_{ijkl}^{(3.3)}(t-t')\,E_j(\mathbf{r},t')\,E_k(\mathbf{r},t')\,E_l(\mathbf{r},t')$$

and its corresponding response function

$$\mathcal{R}_{ijkl}^{(3.3)}(t-t') = -\frac{1}{3\mathrm{i}\hbar\varepsilon_0\mathcal{V}} \sum_{a,b} \frac{\mathrm{e}^{-\beta\hbar\omega_a}}{\sum_c \mathrm{e}^{-\beta\hbar\omega_c}} \Big(\Big\langle a \Big| \hat{m}_i \Big| b \Big\rangle \Big\langle b \Big| \hat{\beta}_{ijkl} \Big| a \Big\rangle \mathrm{e}^{\mathrm{i}\omega_{ab}(t-t')} - \mathrm{c.c.} \Big)\, \mathrm{e}^{-\gamma_{ab}(t-t')}\,\Theta(t-t'), \tag{5.35}$$

where we have applied (5.27) to (5.29) to the expression (5.19) and already inserted the phenomenological damping factor for each vibrational transition. Then the polarization amplitude can be expressed by

$$\begin{aligned} \tilde{P}_i^{(3.3)}(\mathbf{r},\omega) = \varepsilon_0 \left(\frac{1}{2\pi}\right)^2 \sum_{j,k,l} \int \mathrm{d}\omega_1 \int \mathrm{d}\omega_2 \int \mathrm{d}\omega_3\ \chi_{ijkl}^{(3.3)}(-\omega;\omega_1,\omega_2,\omega_3)\cdot \\ \cdot \tilde{E}_j(\mathbf{r},\omega_1)\,\tilde{E}_k(\mathbf{r},\omega_2)\,\tilde{E}_l(\mathbf{r},\omega_3)\,\delta(\omega-\omega_1-\omega_2-\omega_3) \end{aligned} \tag{5.36}$$

where the susceptibility is calculated from the Fourier transform of (5.35) by using the representation of the Heaviside step function (5.33)

$$\chi_{ijkl}^{(3.3)}(-\omega;\omega_1,\omega_2,\omega_3) = \frac{1}{3\hbar\varepsilon_0\mathcal{V}} \sum_{a,b} \frac{\mathrm{e}^{-\beta\hbar\omega_a}}{\sum_c \mathrm{e}^{-\beta\hbar\omega_c}} \Big\langle a \Big| \hat{m}_i \Big| b \Big\rangle \Big\langle b \Big| \hat{\beta}_{jkl} \Big| a \Big\rangle \left(\frac{2\omega_{ab}}{\omega_{ab}^2 - (\omega_1+\omega_2+\omega_3+\mathrm{i}\gamma_{ab})^2} \right), \tag{5.37}$$

where we again assume the occurring matrix elements to be real and require $\omega = \omega_1 + \omega_2 + \omega_3$. One realizes that similar to the linear susceptibility (5.34), the third-order susceptibility (5.37) acts as a narrow band filter around the vibrational mode frequencies ω_{ab}. Hence, for a purely optical pulse excitation, where the pulses are spectrally sufficiently sharp so that none of the material's vibrational modes are excited by the external fields directly, we can now decide on whether (5.37) contributes or not. As the vibrational mode frequencies ω_{ab} are much smaller than the optical pulse frequencies ω_1, ω_2 and ω_3 the optical waves have to mix in a way that these three optical frequencies form a frequency in the order of magnitude of the vibrational mode frequency to bypass the filtering action of the susceptibility (see section 2.3.1 for information on wave-mixing phenomena). However, there is no linear combination of three optical frequencies that would fulfill this condition when (four-)wave-mixing is taking place. Hence, the susceptibility (5.37) vanishes

$$\chi^{(3.4)}_{ijkl}(-\omega;\omega_1,\omega_2,\omega_3) \propto \frac{2\omega_{ab}}{\omega_{ab}^2 - (\omega_1+\omega_2+\omega_3+\mathrm{i}\gamma_{ab})^2} \xrightarrow{\omega_{ab} \ll \omega_1+\omega_2+\omega_3} 0,$$

at optical frequency excitations. In the same way all contributions containing a retarded response function have a corresponding susceptibility that acts as a narrow band filter around the material's vibrational mode frequencies. Thus, nearly all non-instantaneous contributions to the total polarization, i.e. (5.18), (5.19) and (5.21) to (5.24), can be neglected for optical frequency excitations with the exception of (5.20). To proof this fact we again express the polarization (5.20) by the convolution over the response function and the electric fields

$$P_i^{(3.4)}(\mathbf{r},t) = \varepsilon_0 \sum_{j,k,l} E_j(\mathbf{r},t) \int \mathrm{d}t'\ \mathcal{R}^{(3.4)}_{ijkl}(t-t')\, E_k(\mathbf{r},t')\, E_l(\mathbf{r},t'),$$

where the corresponding response function is given by

$$\mathcal{R}^{(3.4)}_{ijkl}(t-t') = -\frac{1}{2\hbar\varepsilon_0\mathcal{V}} \sum_{a,b} \frac{\mathrm{e}^{-\beta\hbar\omega_a}}{\sum_c \mathrm{e}^{-\beta\hbar\omega_c}} \Big(\Big\langle a \Big| \hat{\alpha}_{ij} \Big| b \Big\rangle \Big\langle b \Big| \hat{\alpha}_{kl} \Big| a \Big\rangle \mathrm{e}^{-\mathrm{i}\omega_{ab}(t-t')} - \text{c.c.} \Big)\, \mathrm{e}^{-\gamma_{ab}(t-t')}\, \Theta(t-t'). \quad (5.38)$$

Then the polarization amplitude can be expressed by

$$\begin{aligned} \tilde{P}_i^{(3.4)}(\mathbf{r},\omega) = \varepsilon_0 \left(\frac{1}{2\pi}\right)^2 \sum_{j,k,l} \int \mathrm{d}\omega_1 \int \mathrm{d}\omega_2 \int \mathrm{d}\omega_3\ \chi^{(3.4)}_{ijkl}(-\omega;\omega_1,\omega_2,\omega_3) \cdot \\ \cdot \tilde{E}_j(\mathbf{r},\omega_1)\, \tilde{E}_k(\mathbf{r},\omega_2)\, \tilde{E}_l(\mathbf{r},\omega_3)\, \delta(\omega-\omega_1-\omega_2-\omega_3) \end{aligned} \quad (5.39)$$

where the according susceptibility actually only depends on the frequencies ω_2 and ω_3. Explicitly, the susceptibility is given by

$$\chi^{(3.4)}_{ijkl}(-\omega;\omega_1,\omega_2,\omega_3) = \frac{1}{2\hbar\varepsilon_0\mathcal{V}} \sum_{a,b} \frac{\mathrm{e}^{-\beta\hbar\omega_a}}{\sum_c \mathrm{e}^{-\beta\hbar\omega_c}} \Big\langle a \Big| \hat{\alpha}_{ij} \Big| b \Big\rangle \Big\langle b \Big| \hat{\alpha}_{kl} \Big| a \Big\rangle \frac{2\omega_{ab}}{\omega_{ab}^2 - (\omega_2+\omega_3+\mathrm{i}\gamma_{ab})^2}, \quad (5.40)$$

where we have assumed the matrix element $\langle a|\hat{\alpha}_{ij}|b\rangle$ to be real and again require $\omega = \omega_1 + \omega_2 + \omega_3$. With respect to (5.40) one can find a wave-mixing process where the two occurring optical frequencies $\omega_2 + \omega_3$ are combined in a way that the resulting wave has a frequency, which is on the same order of magnitude as the vibrational mode frequencies of the material. Namely, we have the DFG process, where the resulting wave has the frequency $|\omega_2 - \omega_3|$ for which the susceptibility (5.40) does not vanish. Therefore, the corresponding contribution to the polarization (5.20) cannot be neglected. Hence, (5.20) is the only retarded contribution to the overall nonlinear polarization at optical frequencies. Due to the missing filtering action of the instantaneous term (5.17) the total third-order polarization is then expressed by

$$\begin{aligned} P_i^{(3)}(\mathbf{r},t) &= P_i^{(3.1)}(\mathbf{r},t) + P_i^{(3.4)}(\mathbf{r},t) = \\ &= \varepsilon_0 \sum_{j,k,l} \left[\sigma_{ijkl}\, E_j(\mathbf{r},t) E_k(\mathbf{r},t) E_l(\mathbf{r},t) + E_j(\mathbf{r},t) \int \mathrm{d}t'\; \mathcal{R}_{ijkl}^{(3.4)}(t-t')\, E_k(\mathbf{r},t') E_l(\mathbf{r},t') \right] \end{aligned} \tag{5.41}$$

$$\text{where} \quad \sigma_{ijkl} = \mathrm{Tr}\left\{ \hat{\gamma}_{ijkl}\, \hat{\varrho}_0 \right\} \tag{5.42}$$

in the limit of non-resonant optical frequency excitations. Depending on whether one wants to describe instantaneous or retarded nonlinear optical effects (wave-mixing, optical Kerr effect, Raman scattering, etc.) one can model the corresponding polarization either by the means of the first or second term of (5.41).

5.2 A simple model for stimulated Raman scattering

A special case of third-order nonlinear optical processes is the process of SRS (c.f. section 2.3.2). In stimulated Raman scattering two optical pulses are introduced into the system, one pump pulse at center frequency ω_p and one pulse operating at the Stokes or Anti-Stokes shifted center frequency ω_s relative to the pump pulse's center frequency. For our purposes we assume that the excitations have their center frequencies at optical frequencies ($\sim 10^{15}\,\mathrm{Hz}$), where we require their spectral widths to be sufficiently sharp so that the pulses are not able to excite a phonon directly. In this case the difference frequency of the incoming pulses needs to match a low frequency phonon mode ($\sim 10^{13}\,\mathrm{Hz}$) in order for SRS to take place. This condition is known as *Raman (resonance) condition* [49]. As we have explained earlier in section 2.3.2, Raman scattering is a dispersive process, since the nuclear response is not fast enough to follow the external field instantly. Thus, according to the discussion in section 5.1 SRS can only be described by the non-instantaneous and, therefore, dispersive part of the third-order polarization[6] (5.41)

$$P_{i,\mathrm{Raman}}^{(3)}(\mathbf{r},t) = \varepsilon_0 \sum_{j,k,l} E_j^{(1)}(\mathbf{r},t) \int \mathrm{d}t'\; \mathcal{R}_{ijkl}^{(3.3)}(t-t')\, E_k^{(1)}(\mathbf{r},t')\, E_l^{(1)}(\mathbf{r},t'). \tag{5.43}$$

[6] We have introduced the index (1) in (5.43) to emphasize on the linear nature of the external electric field. In contrast, the material's nonlinear response can be expressed in terms of the nonlinear electric field according to the expansion (4.36).

Only for this polarization the Raman condition can be fulfilled. If we introduce the anisotropic nonlinear oscillator strength

$$\chi^{(3)}_{0,ij,ab} = \left(\frac{1}{\hbar\mathcal{V}}\right)\left(\frac{\omega_{ab}}{\bar{\omega}^2_{ab}}\right)\left(\frac{\mathrm{e}^{-\beta\hbar\omega_a}}{\sum_c \mathrm{e}^{-\beta\hbar\omega_c}}\right)\Big\langle a\Big|\,\hat{\alpha}_{ij}\,\Big|b\Big\rangle\Big\langle b\Big|\,\hat{\alpha}_{kl}\,\Big|a\Big\rangle \tag{5.44}$$

we can express the response function (5.38) by the damped sine function

$$\mathcal{R}^{(3.4)}_{ijkl}(t-t') = \sum_{a,b}\ \chi^{(3)}_{0,ijkl,ab}\left(\frac{\bar{\omega}^2_{ab}}{\omega_{ab}}\right)\,\sin[\,\omega_{ab}(t-t')\,]\,\mathrm{e}^{-\gamma_{ab}(t-t')}\,\Theta(t-t') \tag{5.45}$$

under the assumption that the matrix element $\langle a|\hat{\alpha}_{ij}|b\rangle$ is real. The expression (5.45) is reduced vastly if we only consider a single phonon mode of the material. In this case, it makes sense to introduce the phonon mode frequency ω_{ph} and the spectral line width γ_{Raman} for the corresponding vibrational transition. Furthermore, we define the Raman frequency ω_{Raman}, where its square shall be given by $\omega^2_{\mathrm{Raman}} = \omega^2_{\mathrm{ph}} + \gamma^2_{\mathrm{Raman}}$, and the single oscillator strength $\chi^{(3)}_{0,ijkl,ab} \to \chi^{(3)}_{0,ijkl}$. The response function can be simplified further if we assume the material to be isotropic. According to [26] the nuclear response kernel can in this case be expressed by two separate terms

$$\mathcal{R}^{(3.3)}_{ijkl}(t-t') = a(t-t')\,\delta_{ij}\delta_{kl} + b(t-t')\,\delta_{ik}\delta_{jl}, \tag{5.46}$$

where $a(t-t')+b(t-t')$ is related to the coupling between parallel polarizations in the excitation and the scattered light. In contrast, $b(t-t')$ by itself conducts the coupling between orthogonal polarizations in the excitation and the scattered light. For most frequency shifts the coupling between orthogonal polarizations is weak [26, 41]. Thus, one can approximate $b(t-t') \approx 0$ yielding

$$\mathbf{P}^{(3)}_{\mathrm{Raman}}(\mathbf{r},t) = \mathbf{E}^{(1)}(\mathbf{r},t)\,S^{(2)}(\mathbf{r},t) \tag{5.47}$$

for the third-order polarization, where we have defined the auxiliary field

$$S^{(2)}(\mathbf{r},t) = \varepsilon_0 \int \mathrm{d}t'\ a(t-t')\,\left(\mathbf{E}^{(1)}\right)^2(\mathbf{r},t'). \tag{5.48}$$

Thus, the nuclear response kernel for isotropic materials is given by a single damped sine function

$$a(t-t') = \chi^{(3)}_{0,\mathrm{Raman}}\left(\frac{\omega^2_{\mathrm{Raman}}}{\omega_{\mathrm{ph}}}\right)\,\sin[\omega_{\mathrm{ph}}(t-t')]\,\mathrm{e}^{-\gamma_{\mathrm{Raman}}(t-t')}\,\Theta(t-t') \tag{5.49}$$

(cf. fig. 5.1a). Thereby, $\chi^{(3)}_{0,\mathrm{Raman}}$ denotes the oscillator strength for a single phonon mode in an isotropic material. This oscillator strength is chosen in a way that $\chi^{(3)}_{0,\mathrm{Raman}} = \int \mathrm{d}t'\ a(t-t')$.

Hence, the polarization amplitude of (5.43) can be expressed by

$$\begin{aligned}\tilde{\mathbf{P}}^{(3)}_{\text{Raman}}(\mathbf{r},t) = \varepsilon_0 \int \mathrm{d}\omega_1 \int \mathrm{d}\omega_2 \int \mathrm{d}\omega_3 \; \chi^{(3)}_{\text{Raman}}(-\omega;\omega_1,\omega_2,\omega_3)\cdot \\ \cdot \tilde{\mathbf{E}}^{(1)}(\mathbf{r},\omega_1)\Big[\tilde{\mathbf{E}}^{(1)}(\mathbf{r},\omega_2)\cdot\tilde{\mathbf{E}}^{(1)}(\mathbf{r},\omega_3)\Big]\delta(\omega-\omega_1-\omega_2-\omega_3)\end{aligned} \tag{5.50}$$

for isotropic materials with a single phonon mode. The corresponding susceptibility in (5.50) is given by a single Lorentzian (cf. fig. 5.1b)

$$\begin{aligned}\chi^{(3)}_{\text{Raman}}(-\omega;\omega_1,\omega_2,\omega_3) &\equiv \int \mathrm{d}(t-t')\; a(t-t')\,\mathrm{e}^{\mathrm{i}\omega(t-t')} \\ &= \frac{\chi^{(3)}_{0,\text{Raman}}\,\omega^2_{\text{Raman}}}{\omega^2_{\text{Raman}} - 2\,\mathrm{i}\,\gamma_{\text{Raman}}\,(\omega_2+\omega_3) - (\omega_2+\omega_3)^2}.\end{aligned} \tag{5.51}$$

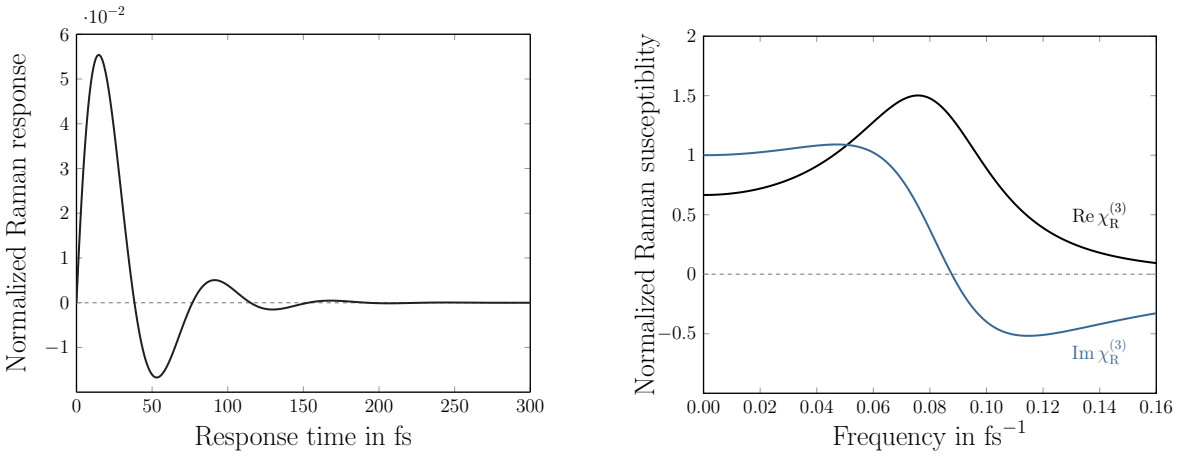

(a) (b)

Figure 5.1: (a) Raman response according to (5.49) and (b) Raman susceptibility according to (5.51) for single phonon mode of silica glass ($\gamma_{\text{Raman}} = (32\,\text{fs})^{-1}$, $\omega_{\text{ph}} = 51.50 \cdot 10^{13}\ \text{rad/s}$) normalized by the oscillator strength. (The plots were produced with MATLAB R2017a [109].)

Note, that for two monochromatic wave excitations at the pump frequency ω_p and the shifted stimulating frequency ω_s, respectively, the third-order susceptibility is given by

$$\chi^{(3)}_{\text{Raman}}(-\omega_\text{s};\omega_\text{s},-\omega_\text{p},\omega_\text{s}) = \frac{\chi^{(3)}_{0,\text{Raman}}\,\omega^2_{\text{Raman}}}{\omega^2_{\text{Raman}} - 2\,\mathrm{i}\,\gamma_{\text{Raman}}\,(-\omega_\text{p}+\omega_\text{s}) - (-\omega_\text{p}+\omega_\text{s})^2}, \tag{5.52}$$

where the Raman condition is fulfilled exactly. Though the susceptibility (5.51) only models a single vibrational mode, one can mimic a full material response by adding an appropriate number of Lorentzians to the system of equations. For example, Walrafen et al. [110] found

that thirteen oscillators are required for an adequate fit to the Raman gain spectrum of fused silica. Note that the model equations (5.49) and (5.51) are identical to the model equations for SRS proposed by Blow and Wood [111] in 1989.

5.2.1 Constitutive equations for isotropic Raman-active materials

Our goal is now to incorporate the nonlinear response of Raman-active materials into the DGTD scheme (3.28). According to section 3.1 we can accomplish this task by introducing a current density to Maxwell's equations as a source. Using (1.16) we obtain the current density for isotropic Raman-active materials by calculating the partial time derivative of the polarization (5.47), yielding

$$\partial_t \mathbf{P}^{(3)}_{\text{Raman}}(\mathbf{r},t) = \mathbf{J}^{(3)}_{\text{Raman}}(\mathbf{r},t) \tag{5.53}$$

Yet, the DGTD scheme requires an expression for the time evolution of the current density (5.53). By taking the time derivative of (5.53) we get

$$\partial_t \mathbf{J}^{(3)}_{\text{Raman}}(\mathbf{r},t) = \left[\partial_t^2 \mathbf{E}^{(1)}(\mathbf{r},t)\right] S^{(2)}(\mathbf{r},t) + 2\left[\partial_t \mathbf{E}^{(1)}(\mathbf{r},t)\right]\left[\partial_t S^{(2)}(\mathbf{r},t)\right] + \mathbf{E}^{(1)}(\mathbf{r},t)\left[\partial_t^2 S^{(2)}(\mathbf{r},t)\right] \tag{B.1}$$

Within the DGTD framework we are not able to handle the time derivatives on the r.h.s. of (B.1) directly[7]. Instead we need an additional set of auxiliary differential equations (ADEs) to attain a scheme that is suitable for the DGTD method. We divide this set of equations into ADEs which are linear and ADEs which are nonlinear in the electric field.

Linear ADEs

We first consider the linear auxiliary field equations, i.e. those equations in (B.1) that are proportional to the electric field. The time-evolution of the electric field itself is, thereby, handled by Maxwell's curl equation for linear fields (cf. (1.9))

$$\partial_t \mathbf{E}^{(1)}(\mathbf{r},t) = \frac{1}{\mu_0}\nabla \times \mathbf{B}^{(1)}(\mathbf{r},t) - \mathbf{J}^{(1)}_{\text{Lorentz}}(\mathbf{r},t) \equiv \mathbf{Q}_{\text{E}}, \tag{5.54}$$

where $\mathbf{J}^{(1)}_{\text{Lorentz}}$ denotes the linear current density of the Lorentz oscillator model (cf. section 5.1.4). For convenience we denote the temporal derivative of the electric field by $\mathbf{Q}^{(1)}_{\text{E}}$. To incorporate the linear current density into the DGTD scheme (3.20), we need to determine its time evolution. In order to do so, we use the linear polarization (5.25) as an auxiliary field, which is related to the Lorentz current by

$$\partial_t \mathbf{P}^{(1)}(\mathbf{r},t) = \mathbf{J}^{(1)}_{\text{Lorentz}}(\mathbf{r},t). \tag{A.1}$$

[7] Note, that the handling of the r.h.s. of (B.1) is much simpler in an FDTD scheme. An example, for such a solution scheme to (B.1) can be found in [112].

Unfortunately, (A.1) does not give us the time-evolution of the Lorentz current density, yet. Luckily, we can perform a trick to deduce the desired time evolution. For this, we set up the polarization amplitude for isotropic materials

$$\tilde{\mathbf{P}}^{(1)}(\mathbf{r},\omega) = \varepsilon_0\, \chi^{(1)}_{\mathrm{Lorentz}}(\omega)\, \tilde{\mathbf{E}}^{(1)}(\mathbf{r},\omega), \tag{5.55}$$

which is obtained by a temporal Fourier transform of (5.25). Conveniently, we have already derived an expression for the Lorentz oscillator model susceptibility in section 5.1.4. For a single isotropic oscillator the susceptiblity is given by

$$\chi^{(1)}_{\mathrm{Lorentz}}(\omega) = \frac{\chi^{(1)}_{0,\mathrm{Lorentz}}\, \omega^2_{\mathrm{Lorentz}}}{\omega^2_{\mathrm{Lorentz}} - 2\,\mathrm{i}\,\gamma_{\mathrm{Lorentz}}\,\omega - \omega^2} \tag{5.56}$$

(cf. (5.34)), where $\chi_{0,\mathrm{Lorentz}}$ denotes the oscillator strength, $\omega_{\mathrm{Lorentz}}$ the resonance frequency and $\gamma_{\mathrm{Lorentz}}$ the phenomenological damping coefficient. Similar to the Raman susceptibility one can extend the model by adding an appropriate number of oscillators.

After inserting (5.56) into (5.55) and rearranging the result, we get

$$\left(\omega^2_{\mathrm{Lorentz}} - 2\,\mathrm{i}\,\gamma_{\mathrm{Lorentz}}\,\omega - \omega^2\right) \tilde{\mathbf{P}}^{(1)}(\mathbf{r},\omega) = \varepsilon_0\, \omega^2_{\mathrm{Lorentz}}\, \chi^{(1)}_{0,\mathrm{Lorentz}}\, \tilde{\mathbf{E}}^{(1)}(\mathbf{r},\omega). \tag{5.57}$$

We then perform a Fourier transform of (5.57) back into time-domain, which yields

$$\left(\omega^2_{\mathrm{Lorentz}} + 2\,\gamma_{\mathrm{Lorentz}}\,\partial_t + \partial_t^2\right) \mathbf{P}^{(1)}(\mathbf{r},t) = \varepsilon_0\, \omega^2_{\mathrm{Lorentz}}\, \chi^{(1)}_{0,\mathrm{Lorentz}}\, \mathbf{E}^{(1)}(\mathbf{r},t). \tag{5.58}$$

By inserting (A.1) into (5.58) and rearranging the resulting equation we obtain the ADE for the Lorentz current density

$$\partial_t\, \mathbf{J}^{(1)}_{\mathrm{Lorentz}}(\mathbf{r},t) = \omega^2_{\mathrm{Lorentz}} \left(\varepsilon_0\, \chi^{(1)}_{0,\mathrm{Lorentz}}\, \mathbf{E}^{(1)}(\mathbf{r},t) - \mathbf{P}^{(1)}(\mathbf{r},t)\right) - 2\,\gamma_{\mathrm{Lorentz}}\, \mathbf{J}^{(1)}_{\mathrm{Lorentz}}(\mathbf{r},t) \equiv \mathbf{Q}^{(1)}_{\mathrm{J}}. \tag{A.2}$$

For convenience, we denote the time evolution of the Lorentz current density by the auxiliary field $\mathbf{Q}^{(1)}_{\mathrm{J}}$. One can show that the set of ADEs for the Lorentz model (A.1) and (A.2) is equivalent to the set of equations derived for the same model by Busch et al. [13]. Nevertheless, unlike in [13] we abstain from introducing any artificial auxiliary fields for the Lorentz oscillator model itself.

From (B.1) it follows that we do not only need the time evolution of the electric field (5.54) but also the time evolution of its temporal derivative, i.e.

$$\partial_t^2\, \mathbf{E}^{(1)} = \partial_t\, \mathbf{Q}^{(1)}_{\mathrm{E}} \tag{5.59}$$

Combining (5.54) and Maxwell's curl equation for the magnetic field (1.10) yields

$$\partial_t^2\, \mathbf{E}^{(1)} = \partial_t\, \mathbf{Q}^{(1)}_{\mathrm{E}} = -\nabla \cdot \underline{\mathbf{F}}^{(1)}_{\mathrm{E}} - \mathbf{Q}^{(1)}_{\mathrm{J}}, \tag{A.3}$$

where we have used (1.9) and defined the flux

$$\underline{\mathbf{F}}_{\mathrm{E}}^{(1)} = \left(\mathbf{F}_{\mathrm{E},1}^{(1)}, \mathbf{F}_{\mathrm{E},2}^{(1)}, \mathbf{F}_{\mathrm{E},3}^{(1)}\right)^{\mathrm{T}}. \tag{5.60}$$

Each component of the flux is given by

$$\mathbf{F}_{\mathrm{E},i}^{(1)} = -\frac{1}{\mu_0}\left[\,\breve{\mathbf{e}}_i \times \left(\nabla \times \mathbf{E}^{(1)}\right)\right], \qquad i \in \{1,2,3\}. \tag{A.4}$$

Note, that the flux term in (A.3) requires the introduction of an additional numerical flux into the DGTD scheme (cf. (3.54)). It has been shown by Hesthaven and Warburton [14, theorem 7.2] that for equations like (A.3), which have the form of the heat equation, a simple central flux (3.29) is stable.

Furthermore, we define the auxiliary field

$$\partial_t \mathbf{Q}_{\mathrm{E}}^{(1)} = \mathbf{R}_{\mathrm{E}}^{(1)}, \tag{5.61}$$

which will be contained in the nonlinear ADEs. We summarize the linear set of ADEs by

Linear ADEs

$$\partial_t \mathbf{P}^{(1)} = \mathbf{J}_{\mathrm{Lorentz}}^{(1)} \tag{A.1}$$

$$\partial_t \mathbf{J}_{\mathrm{Lorentz}}^{(1)} = \omega_{\mathrm{Lorentz}}^2\left(\varepsilon_0\, \chi_{0,\mathrm{Lorentz}}^{(1)}\, \mathbf{E}^{(1)} - \mathbf{P}^{(1)}\right) - 2\,\gamma_{\mathrm{Lorentz}}\, \mathbf{J}_{\mathrm{Lorentz}}^{(1)} \equiv \mathbf{Q}_{\mathrm{J}}^{(1)} \tag{A.2}$$

$$\partial_t \mathbf{Q}_{\mathrm{E}}^{(1)} = -\left(\nabla \cdot \underline{\mathbf{F}}_{\mathrm{E}}^{(1)}\right) - \mathbf{Q}_{\mathrm{J}}^{(1)} \equiv \mathbf{R}_{\mathrm{E}}^{(1)} \tag{A.3}$$

where

$$\mathbf{F}_{\mathrm{E},i}^{(1)} = -\frac{1}{\mu_0}\left[\,\breve{\mathbf{e}}_i \times \left(\nabla \times \mathbf{E}^{(1)}\right)\right], \qquad i \in \{1,2,3\}. \tag{A.4}$$

Nonlinear ADEs

We now proceed to derive the nonlinear ADEs, i.e. those equations associated with the second-order auxiliary field $S^{(2)}(\mathbf{r},t)$. Because $S^{(2)}(\mathbf{r},t)$ contains a convolution in time (see (5.48)) the calculation of this field poses a special challenge to the DGTD scheme as it is not feasible to store the response kernel $a(t-t')$ for all times. In the following we show a method to bypass the convolution in (5.48), which is similar to the method presented by Goorjian and Taflove [108] for finite difference time-domain methods[8]. We first perform the temporal Fourier transform

[8] Note, however that the signs of the susceptibility in [108] and also in the adapted text book version [112] are not entirely correct. Moreover, the scheme was derived only for one-dimensional systems.

On another note, the ADEs in [112] have been used by Vani et al. [22] to model SRS in a three-dimensional FDTD framework. However, I find this three-dimensional extension somewhat questionable.

of (5.48) using (5.49)

$$\tilde{S}^{(2)}(\mathbf{r},\omega) = \tilde{a}(\omega)\,\frac{1}{2\pi}\int \mathrm{d}\omega'\;\tilde{\mathbf{E}}^{(1)}(\mathbf{r},\omega')\cdot\tilde{\mathbf{E}}^{(1)}(\mathbf{r},\omega-\omega'), \tag{5.62}$$

where the susceptibility $\tilde{a}(\omega)$ is given by (5.51). By inserting (5.51) and rearranging the result, we obtain

$$\begin{aligned}\left(\omega_{\mathrm{Raman}}^2 - 2\mathrm{i}\,\gamma_{\mathrm{Raman}}\,\omega - \omega^2\right)\tilde{S}^{(2)}(\mathbf{r},\omega) = \\ = \varepsilon_0\,\chi^{(3)}_{0,\mathrm{Raman}}\,\omega_{\mathrm{Raman}}^2\,\frac{1}{2\pi}\int \mathrm{d}\omega'\;\tilde{\mathbf{E}}^{(1)}(\mathbf{r},\omega')\cdot\tilde{\mathbf{E}}^{(1)}(\mathbf{r},\omega-\omega').\end{aligned} \tag{5.63}$$

We then define

$$\partial_t\, S^{(2)}(\mathbf{r},t) = Q_{\mathrm{S}}^{(2)}(\mathbf{r},t). \tag{B.2}$$

and revoke the Fourier transform in (5.63), which yields

$$\partial_t\, Q_{\mathrm{S}}^{(2)}(\mathbf{r},t) = \omega_{\mathrm{Raman}}^2\left[\varepsilon_0\,\chi^{(3)}_{0,\mathrm{Raman}}\left(\mathbf{E}^{(1)}\right)^2(\mathbf{r},t) - S^{(2)}(\mathbf{r},t)\right] - 2\,\gamma_{\mathrm{Raman}}\,Q_{\mathrm{S}}^{(2)}(\mathbf{r},t) \equiv R_{\mathrm{S}}^{(2)}(\mathbf{r},t) \tag{B.3}$$

in time domain, where we denote the time evolution of $Q_{\mathrm{S}}^{(2)}$ by the auxiliary field $R_{\mathrm{S}}^{(2)}$. We summarize the nonlinear ADEs by

Nonlinear ADEs

$$\partial_t\,\mathbf{J}^{(3)}_{\mathrm{Raman}} = \mathbf{R}_{\mathrm{E}}^{(1)}\,S^{(2)} + 2\,\mathbf{Q}_{\mathrm{E}}^{(1)}\,Q_{\mathrm{S}}^{(2)} + \mathbf{E}^{(1)}\,R_{\mathrm{S}}^{(2)} \tag{B.1}$$

$$\partial_t\, S^{(2)} = Q_{\mathrm{S}}^{(2)} \tag{B.2}$$

$$\partial_t\, Q_{\mathrm{S}}^{(2)} = \omega_{\mathrm{Raman}}^2\left[\varepsilon_0\,\chi^{(3)}_{0,\mathrm{Raman}}\left(\mathbf{E}^{(1)}\right)^2 - S^{(2)}\right] - 2\,\gamma_{\mathrm{Raman}}\,Q_{\mathrm{S}}^{(2)} \equiv R_{\mathrm{S}}^{(2)}. \tag{B.3}$$

In the following we show the SRS results of DGTD calculations with the integrated set of ADEs (A.1) to (A.4) and (B.1) to (B.3).

5.2.2 Raman scattering in fused silica

As a demonstration of the ADEs for Raman-active materials we employ the same scattering setup[9] as seen in fig. 4.2. We choose fused silica as the material of the scatterer, which is known to be Raman-active. In literature [111, 113, 114] we find a phonon life time of $t_{\mathrm{life}} = 32$ fs corresponding to a damping coefficient $\gamma_{\mathrm{Raman}} = 3.13\cdot 10^{13}\ \mathrm{s}^{-1}$ as well as a phonon frequency of $\omega_{\mathrm{Raman}} = 51.50\cdot 10^{13}\ \mathrm{rad/s}$. The nonlinear oscillator strength has a value of $\chi^{(3)}_{0,\mathrm{Raman}} = 10^{-22}\ \frac{\mathrm{m}^2}{\mathrm{V}^2}$.According to [115] the linear susceptibility of fused silica can be char-

[9] Though we use a relatively fast two dimensional test setup, the method in general does not cause any problems to the implementation in three dimensions as the ADEs are formulated for a three-dimensional scheme.

acterized by Sellmeier's equation for the frequency dependent refraction index

$$n(\omega) = 1 + \sum_{i=1}^{3} \frac{\chi^{(1)}_{0,\text{Lorentz}}\, \omega^2_{i,\text{Lorentz}}}{\omega^2_{i,\text{Lorentz}} - \omega^2}, \tag{5.64}$$

where the parameters are given by

i	$\chi^{(1)}_{0,\text{Lorentz}}$	$\omega_{i,\text{Lorentz}}$ in $10^{15}\ \frac{\text{rad}}{\text{s}}$
1	0.8975	1.9034
2	0.4079	162.0465
3	0.6961	275.3703

Table 5.1: Sellmeier parameters for bulk fused silica, data extracted from [115]

The Sellmeier equation (5.64) can be translated into the linear susceptibility (5.56) for a lossless material by

$$\chi^{(1)}_{\text{Lorentz}}(\omega) = \sum_{i=1}^{3} \chi^{(1)}_{i,\text{Lorentz}}(\omega) = n(\omega) - 1. \tag{5.65}$$

To get the full spectrum, we have to couple each of the terms in (5.65) to the nonlinear fields individually.

In order to evoke SRS in the material, the excitation must be chosen so that the Raman condition is fulfilled (cf. section 5.2). One can either introduce two monochromatic wave excitations, where their center frequencies have a separation in the order of the phonon frequency ω_{Raman}, or illuminate the material with a single pulse with a width larger than ω_{Raman}. As the phonon frequency is fairly small compared to optical frequencies we choose a single TE polarized excitation pulse with a center frequency of $\omega_0 = 9.43 \cdot 10^{15}\ \frac{\text{rad}}{\text{s}}$ and a width of $\omega_{\text{FWHM}} = 1.88 \cdot 10^{15}\ \frac{\text{rad}}{\text{s}}$ (corresponding to a pulse duration of $t_{\text{pulse}} = 3.33 \cdot 10^{-15}$ s). Like in section 4.5 we use a polynomial order of 4 and apply filters to stabilize the numerical scheme (cf. section 3.5). Furthermore, we choose a maximal element edge size of $h_{\max} = 1.2\,\text{nm}$ as spatial discretization within the scatterer. For this we find a time step of $\Delta t = 5.14 \cdot 10^{-19}$ s to be stable. The simulation duration is $T = 2.75 \cdot 10^{-14}$ s.

To get a good impression of the model, we calculate the linear and nonlinear scattering cross section according to (1.67) by inserting the corresponding linear and nonlinear fields, respectively. The result of these calculations are displayed in fig. 5.2. In fig. 5.2a we show the linear spectrum for two different excitation amplitudes, $E_0 = 10^{15}\ \frac{\text{V}}{\text{m}}$ and $E_0 = 10^{16}\ \frac{\text{V}}{\text{m}}$. The signal is centered around the excitation frequency ω_0. The associated Stokes-shifted nonlinear signals for the different excitation amplitudes are shown in fig. 5.2b. The nonlinear signals are centered around $\omega_{\text{s}} = 8.92 \cdot 10^{15}\ \frac{\text{rad}}{\text{s}}$, which fulfills the Raman condition $\omega_{\text{Raman}} = \omega_0 - \omega_{\text{s}}$. By comparing figs. 5.2a and 5.2b we can study the scaling behaviour of the Stokes-shifted signals: A difference of one order of magnitude in the linear signals translates to a three-order-of-magnitude difference in the nonlinear signals. This is the scaling behaviour one would expect from a third-order nonlinear process according to (5.43). Hence, we conclude that the ADE scheme, which we have

derived previously, can indeed be used to model SRS, as it fulfills the Raman condition and shows the correct scaling behaviour. Nevertheless, the method needs to be tested against a real physical setup to substantiate our claim. Note, that the calculated effect of Raman scattering is rather small ($C_{\text{scat}} \sim 10^{-17}$ nm, cf. fig. 5.2b). Thus, a surface enhanced Raman scattering system, i.e. a compound of a plasmonic and a dielectric material, would be interesting [116]. In these systems Raman scattering is much stronger due to the coupling to surface plasmons.

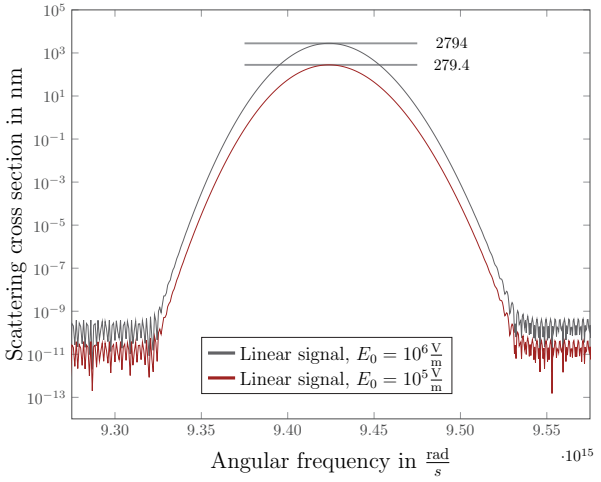

(a)

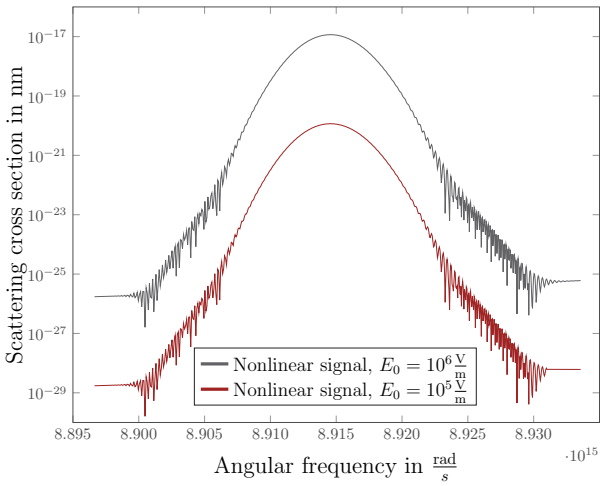

(b)

Figure 5.2: (a) Linear scattering cross section and **(b)** corresponding Stokes-shifted (nonlinear) signal for two different excitation amplitudes E_0.

An advantage due to the clean separation between linear and nonlinear fields is the possibility to visualize the electromagnetic field distributions in time-domain (cf. fig. 5.3). Because of the large difference in the order of magnitudes between linear and nonlinear signal, these are not accessible by experiments. In fig. 5.3 we see how the SRS is generated strongly within the particle (cf. fig. 5.3a) and scattered in a dipole-like fashion (cf. fig. 5.3b). Thereby, the magnetic field displays the smallest contribution (cf. fig. 5.3c).

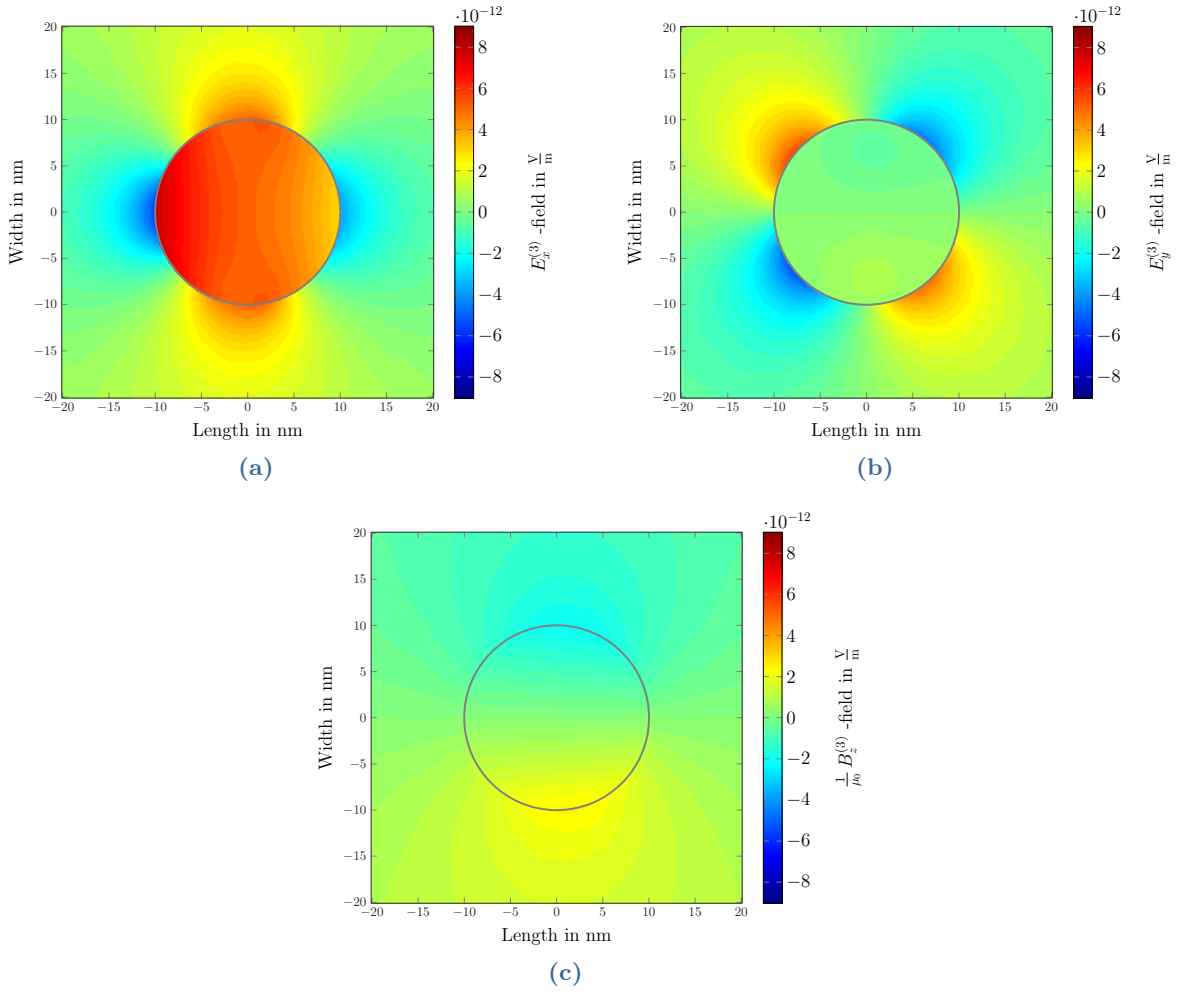

Figure 5.3: Field distribution of the third-order **(a)** $E_x^{(3)}$-, **(b)** $E_y^{(3)}$- and **(c)** $H_z^{(3)}$-field at the time with the maximal field strength.

CHAPTER 6

Conclusion

In this thesis I presented the theoretical description of nonlinear optical phenomena with respect to two different material models – the hydrodynamic model for plasmonic materials and the model for Raman-active dielectrics. In both cases, I implemented a perturbative approach, which allows a clean distinction between linear and nonlinear effects. This approach is especially well-suited for the DGTD method, as it opens up the possibility to observe the time-resolved nonlinear fields. Due to the commonly large difference in magnitudes between linear and nonlinear effects, these are usually not accessible.

More specifically, in chapter 4 I examined the second-order nonlinear response of plasmonic nanoantennas to an electromagnetic excitation, where I used a perturbative approach to the hydrodynamic model. The nonlinear field distributions of a cylindrical nanoantenna revealed that in plasmonic structures, which are described by the hydrodynamic model, the response is strongly influenced by the symmetry of the electromagnetic field. Considering the field distributions calculated in section 4.5 I claimed the following: As the electric field response exhibits an even symmetry with respect to the incident direction of the external excitation, the contribution to the electric dipole moment stemming from the electric field is highly suppressed. Hence, the electric field only evokes a strong second-harmonic signal at the surface of the nanoantenna, where the symmetry is broken. Because the magnetic field does not exhibit such symmetry, it contributes to the SHG also within the bulk. Accordingly, the field distribution of the cylindrical nanoantenna showed that, while most of the second-harmonic signal were generated at the surface, significant SHG was also found within the bulk. These claims were substantiated by the calculation of the individual contributions to the nonlinear response. Furthermore, I used the above information to develop a tuning scheme for two excitation pulses at different frequencies, for which I computed the wave-mixing signals of these pulses. This was done for a cylindrical as well as a bowtie-shaped nanoantenna. I showed that the most efficient second-order nonlinear response is produced, if the sum-frequency of the incident pulses coincides with a resonance of the system, which is of higher than the dipole resonance. In addition, an optimized design like the bowtie nanoantenna will also increase the nonlinear response. Thus, this tuning scheme is a powerful tool to predict the most efficient nonlinear response for a given nanoantenna design.

In chapter 5 I studied a very different material model – the model for Raman-active dielectrics.

In particular, I examined the third-order nonlinear process of SRS. To this end, I reviewed the material model by Hellwarth [26], where the third-order polarization was constructed using the BOA. This polarization had a variety of contributions, where only two were relevant at optical frequency excitations. One of these contributions was associated with SRS. Using this particular polarization contribution, I derived an ADE scheme to introduce the material model into the DGTD method, in which a set of linear ADEs was coupled to a set of nonlinear ADEs. Finally, I showed the results of the DGTD scheme with the Raman-active material model. Besides a Stokes shifted signal in the nonlinear spectrum, The linear and nonlinear spectra revealed the correct scaling behaviour associated with a third-order nonlinear optical nonlinearity.

Outlook

Though the hydrodynamic model for plasmonic systems already proofs to be fairly complex when incorporating it into a DGTD framework, more is to be desired. One issue are the hard-wall boundary conditions, which I imposed onto the material equation of the charge density. These were implemented due to their simplicity. Unfortunately, they model the physical reality of the charge density at the surface only insufficiently. Toscano et al. [90, 117] have shown that electronic spill-out will lead to a variety of effects such as tunneling and Benett resonances[118], where the hydrodynamic model needs to be extended in terms of quantum effects. One way of lifting the constraint to hard-wall boundaries within the DGTD method would be by introducing the particle-in-cell method [119, 120], where the individual fluid particles are tracked throughout the elements of the computational domain. Another short-coming of the applied hydrodynamic model is the inability to describe interband transitions, which might be of importance for noble metals. Though for the linearized model an extension was suggested by Liebsch [91] it is unclear how to modify the nonlinear equations. In addition, the notion of Landau damping [121] would be interesting.

In the case of the Raman-active material model, testing against an experimental setup is needed. As the effect of SRS is rather small, a surface enhanced Raman-spectroscopy[116, 122] setup could be one possibility, where the Raman scattering is enhanced due to the coupling to surface plasmons of metallic structures. This is particularly interesting, as we can combine the hydrodynamic model for plasmonic materials with the Raman-active model for dielectrics.

APPENDIX A

General remarks on light-matter interaction

A.1 Time-averaged Poynting vector

We want to show how to calculate the time-averaged Poynting vector for a non-monochromatic electromagnetic field. Our starting point is as follows

$$\left\langle \mathbf{S}(\mathbf{r},t)\right\rangle_t = \lim_{\tau\to\infty}\frac{1}{\tau}\int_0^\tau \mathrm{d}t\ \mathbf{S}(\mathbf{r},t) = \lim_{\tau\to\infty}\frac{1}{\tau}\int_0^\tau \mathrm{d}t\ \mathbf{E}(\mathbf{r},t)\times\mathbf{H}(\mathbf{r},t). \tag{A.1}$$

For non-monochromatic fields the discrete Fourier transforms of the electric field and the magnetic field strength are given as

$$\mathbf{E}(\mathbf{r},t) = \frac{1}{2}\int \mathrm{d}\omega\ \tilde{\mathbf{E}}(\mathbf{r},\omega)\,\mathrm{e}^{-\mathrm{i}\omega t} = \frac{1}{2}\int_0^\infty \mathrm{d}\omega\ \left(\tilde{\mathbf{E}}(\mathbf{r},\omega)\,\mathrm{e}^{-\mathrm{i}\omega t} + \mathrm{c.c.}\right) \tag{A.2}$$

$$\mathbf{H}(\mathbf{r},t) = \frac{1}{2}\int \mathrm{d}\omega\ \tilde{\mathbf{H}}(\mathbf{r},\omega)\,\mathrm{e}^{-\mathrm{i}\omega t} = \frac{1}{2}\int_0^\infty \mathrm{d}\omega\ \left(\tilde{\mathbf{H}}(\mathbf{r},\omega)\,\mathrm{e}^{-\mathrm{i}\omega t} + \mathrm{c.c.}\right). \tag{A.3}$$

By inserting these into (A.1) we obtain

$$\begin{aligned}\left\langle \mathbf{S}(\mathbf{r},t)\right\rangle_t &= \frac{1}{4}\int \mathrm{d}\omega \int \mathrm{d}\omega'\ \tilde{\mathbf{E}}(\mathbf{r},\omega)\times\tilde{\mathbf{H}}(\mathbf{r},\omega')\left[\lim_{\tau\to\infty}\frac{1}{\tau}\int_0^\tau \mathrm{d}t\ \mathrm{e}^{-\mathrm{i}(\omega+\omega')t}\right] = \\ &= \frac{1}{4}\int \mathrm{d}\omega \int \mathrm{d}\omega'\ \tilde{\mathbf{E}}(\mathbf{r},\omega)\times\tilde{\mathbf{H}}^*(\mathbf{r},\omega')\left[\lim_{\tau\to\infty}\frac{1}{\tau}\int_0^\tau \mathrm{d}t\ \mathrm{e}^{-\mathrm{i}(\omega-\omega')t}\right]\end{aligned} \tag{A.4}$$

where we have used that $\mathbf{H}(\mathbf{r},t)$ needs to be real in the second line, which leads to $\tilde{\mathbf{H}}(\mathbf{r},-\omega) = \tilde{\mathbf{H}}^*(\mathbf{r},\omega)$. We now want to calculate the time integral in (A.4)

$$\lim_{\tau\to\infty}\frac{1}{\tau}\int_0^\tau \mathrm{d}t\ \mathrm{e}^{-\mathrm{i}(\omega-\omega')t} = \lim_{\tau\to\infty}\frac{\mathrm{i}}{(\omega-\omega')\tau}\left[\mathrm{e}^{-\mathrm{i}(\omega-\omega')\tau}-1\right] \tag{A.5}$$

where we need to analyze the two cases

$\omega = \omega'$:

$$\lim_{\tau\to\infty}\lim_{\omega\to\omega'}\frac{\mathrm{i}}{(\omega-\omega')\tau}\left[\mathrm{e}^{-\mathrm{i}(\omega-\omega')\tau}-1\right] \overset{\text{L'Hôpital's rule}}{=} \lim_{\tau\to\infty}\lim_{\omega\to\omega'}\frac{-\mathrm{i}^2\,\tau}{\tau}\,\mathrm{e}^{-\mathrm{i}(\omega-\omega')\tau} = 1 \tag{A.6}$$

and

$\omega \neq \omega'$:

$$\lim_{\tau\to\infty}\frac{\mathrm{i}}{(\omega-\omega')\tau}\left[\mathrm{e}^{-\mathrm{i}(\omega-\omega')\tau}-1\right] = 0. \tag{A.7}$$

From (A.6) and (A.7) it follows for (A.4)

$$\begin{aligned}\Big\langle \mathbf{S}(\mathbf{r},t)\Big\rangle_t &= \frac{1}{4}\int \mathrm{d}\omega\ \tilde{\mathbf{E}}(\mathbf{r},\omega)\times\tilde{\mathbf{H}}^*(\mathbf{r},\omega) = \frac{1}{4}\int_0^\infty \mathrm{d}\omega\ \left[\tilde{\mathbf{E}}(\mathbf{r},\omega)\times\tilde{\mathbf{H}}^*(\mathbf{r},\omega)+\text{c.c.}\right] = \\ &= \frac{1}{2}\,\mathrm{Re}\left[\tilde{\mathbf{E}}(\mathbf{r},\omega)\times\tilde{\mathbf{H}}^*(\mathbf{r},\omega)\right].\end{aligned} \tag{A.8}$$

A.2 Coulomb and Lorenz gauge

Two very common choices of gauge transformations are the Coulomb and the Lorenz gauge, (1.75) and (1.76). One advantage of these gauge transformations is that they simplify the electromagnetic partial differential equations (1.71) and (1.72) signifcantly. In the following we discuss how the gauge potential needs to be chosen so that the Colomb and Lorenz gauge is fulfilled, respectively.

Coulomb gauge

We can now choose the gauge potential $\chi(\mathbf{r},t)$ in a way that

$$\nabla\cdot\mathbf{A}(\mathbf{r},t) = 0. \tag{1.75}$$

Every gauge that satisfies equation (1.75) is called Coulomb or transversal gauge[31]. We discuss the term *transversal gauge* in appendix A.3. One can show that (1.75) can always be fulfilled: Let us consider the gauge transformation of the vector potential (1.74). Now assume

that

$$\nabla \cdot \mathbf{A}(\mathbf{r},t) \overset{(1.74)}{=} \nabla \cdot \mathbf{A}'(\mathbf{r},t) - \Delta\,\chi(\mathbf{r},t) \equiv C(\mathbf{r},t) \neq 0 \tag{A.9}$$

where $C(\mathbf{r},t)$ is an arbitrary scalar field. One then poses the question if one can transform $\mathbf{a}$ into a vector field $\mathbf{A}'$ so that this field will fulfill the Coulomb gauge

$$\nabla \cdot \mathbf{A}'(\mathbf{r},t) = 0. \tag{A.10}$$

From (A.9) and (A.10) it follows that the gauge potential fulfills Poisson's equation

$$\nabla\,\chi(\mathbf{r},t) = -C(\mathbf{r},t), \tag{A.11}$$

which has the solution

$$\chi(\mathbf{r},t) = \frac{1}{4\pi\varepsilon_0}\int \mathrm{d}^3r'\;\frac{C(\mathbf{r}',t)}{|\mathbf{r}-\mathbf{r}'|}. \tag{A.12}$$

Because (A.11) has a solution, we can always transform the vector potential by a gauge potential, so that (1.75) will hold.

If we use the Coulomb gauge (1.75) the second-order partial differential equations (1.71) and (1.72) become Poisson's equation with respect to the scalar potential

$$\Delta\,\phi(\mathbf{r},t) = -\frac{1}{\varepsilon_0}\varrho(\mathbf{r},t), \tag{A.13}$$

with the solution

$$\phi(\mathbf{r},t) = \frac{1}{4\pi\varepsilon_0}\int \mathrm{d}^3r'\;\frac{\varrho(\mathbf{r}',t)}{|\mathbf{r}-\mathbf{r}'|} \tag{A.14}$$

and the wave equation with respect to the vector potential

$$\left[\Delta\; - \varepsilon_0\,\mu_0\,\partial_t^2\right]\mathbf{A}(\mathbf{r},t) = \partial_t\,\nabla\,\phi(\mathbf{r},t) - \mu_0\,\mathbf{J}(\mathbf{r},t). \tag{A.15}$$

Lorenz gauge

Another type of gauge fixing of the electromagnetic potentials is given by the Lorenz gauge

$$\nabla \cdot \mathbf{A}(\mathbf{r},t) + \varepsilon_0\,\mu_0\,\partial_t\,\Phi(\mathbf{r},t) = 0. \tag{1.76}$$

The Lorenz gauge is Lorentz invariant and, thus, also bears the name Lorentz condition. In a similar manner to the Coulomb gauge one can show that it can always be fulfilled. Suppose that

$$\nabla \cdot \mathbf{A}(\mathbf{r},t) + \varepsilon_0\,\mu_0\,\partial_t\,\Phi(\mathbf{r},t) = C(\mathbf{r},t) \neq 0 \tag{A.16}$$

where $C(\mathbf{r},t)$ is an arbitrary scalar field. From the gauge transformations (1.73) and (1.74) we obtain by inserting them into (A.16)

$$\nabla\cdot\mathbf{A}'(\mathbf{r},t)+\varepsilon_0\,\mu_0\,\partial_t\,\Phi'(\mathbf{r},t)-\left[\Delta\,-\varepsilon_0\,\mu_0\,\partial_t^2\right]\chi(\mathbf{r},t)=C(\mathbf{r},t). \tag{A.17}$$

Let us now assume that the gauge potential transforms the electromagnetic potentials in a way that the Lorenz gauge holds for the resulting transformed potentials

$$\nabla\cdot\mathbf{A}'(\mathbf{r},t)+\varepsilon_0\,\mu_0\,\partial_t\,\Phi'(\mathbf{r},t)=0 \tag{A.18}$$

then the gauge potential must fulfill the inhomogeneous wave equation

$$\left[\Delta\,-\varepsilon_0\,\mu_0\,\partial_t^2\right]\chi(\mathbf{r},t)=-C(\mathbf{r},t). \tag{A.19}$$

Note that there is no unique gauge potential χ that would fulfill (A.19) but rather a set of solutions to the wave equation. Hence, the Lorentz condition defines a gauge class. For every particulate solution one can add every solution χ_{hom} of the homogeneous wave equation

$$\left[\Delta\,-\varepsilon_0\,\mu_0\,\partial_t^2\right]\chi_{\mathrm{hom}}(\mathbf{r},t)=0. \tag{A.20}$$

Returning to the partial differential equations (1.71) and (1.72) one obtains

$$\left[\Delta\,-\varepsilon_0\,\mu_0\,\partial_t^2\right]\phi(\mathbf{r},t)=-\frac{1}{\varepsilon_0}\varrho(\mathbf{r},t) \tag{A.21}$$

$$\left[\Delta\,-\varepsilon_0\,\mu_0\,\partial_t^2\right]\mathbf{A}(\mathbf{r},t)=-\mu_0\,\mathbf{J}(\mathbf{r},t) \tag{A.22}$$

by imposing the Lorenz gauge. The differential equations of the electromagnetic potentials Φ and $\mathbf{A}$ are decoupled completely by the Lorenz gauge.

A.3 Transversal/Coulomb gauge

By inserting (A.14) into (A.15) one finds

$$\left(\Delta\,-\varepsilon_0\,\mu_0\,\partial_t^2\right)\mathbf{A}(\mathbf{r},t)=-\mu_0\,\mathbf{J}(\mathbf{r},t)-\frac{\mu_0}{4\pi}\nabla_{\mathbf{r}}\int\mathrm{d}^3r'\frac{\nabla_{\mathbf{r}'}\cdot\mathbf{J}(\mathbf{r}',t)}{\mathbf{r}-\mathbf{r}'} \tag{A.23}$$

One can split the microsopic current density into a longitudinal (curl free) and a transversal (divergence free) part

$$\mathbf{J}(\mathbf{r},t)=\mathbf{J}^{(\mathrm{l})}(\mathbf{r},t)+\mathbf{J}^{(\mathrm{t})}(\mathbf{r},t) \tag{A.24}$$

$$\nabla\times\mathbf{J}^{(\mathrm{l})}(\mathbf{r},t)=\mathbf{0} \tag{A.25}$$

$$\nabla\cdot\mathbf{J}^{(\mathrm{t})}(\mathbf{r},t)=0 \tag{A.26}$$

Due to (A.25) and (A.26) one can make the following ansatzes

$$\mathbf{J}^{(\mathrm{l})}(\mathbf{r},t) = \nabla\,\alpha(\mathbf{r},t) \tag{A.27}$$

$$\mathbf{J}^{(\mathrm{t})}(\mathbf{r},t) = \nabla\times\beta(\mathbf{r},t), \tag{A.28}$$

which leads to

$$\alpha(\mathbf{r},t) = -\frac{1}{4\pi}\int \mathrm{d}^3r'\frac{\nabla_{\mathbf{r}'}\cdot\mathbf{J}(\mathbf{r}',t)}{|\mathbf{r}-\mathbf{r}'|} \tag{A.29}$$

$$\beta(\mathbf{r},t) = \frac{1}{4\pi}\int \mathrm{d}^3r'\frac{\nabla_{\mathbf{r}'}\times\mathbf{J}(\mathbf{r}',t)}{|\mathbf{r}-\mathbf{r}'|} \tag{A.30}$$

See [31] for the proof of (A.29) and (A.30). From (A.27) to (A.30) we obtain

$$\mathbf{J}^{(\mathrm{l})}(\mathbf{r},t) = -\frac{1}{4\pi}\nabla_{\mathbf{r}}\cdot\int \mathrm{d}^3r'\frac{\nabla_{\mathbf{r}'}\cdot\mathbf{J}(\mathbf{r}',t)}{|\mathbf{r}-\mathbf{r}'|} \tag{A.31}$$

$$\mathbf{J}^{(\mathrm{t})}(\mathbf{r},t) = \frac{1}{4\pi}\nabla_{\mathbf{r}}\times\int \mathrm{d}^3r'\frac{\nabla_{\mathbf{r}'}\times\mathbf{J}(\mathbf{r}',t)}{|\mathbf{r}-\mathbf{r}'|} \tag{A.32}$$

After inserting (A.31) and (A.32) into (A.23) one arrives at

$$\left(\Delta - \varepsilon_0\,\mu_0\,\partial_t^2\right)\mathbf{A}(\mathbf{r},t) = -\mu_0\,\mathbf{J}^{(\mathrm{t})}(\mathbf{r},t). \tag{A.33}$$

Therefore, in Coulomb gauge is also called transversal gauge.

A.4 Charged particles in an electromagnetic field

Let us return to the Lorentz force (1.77). If we express the microscopic electric field and the microscopic magnetic field at each particle position $\mathbf{r}+\mathbf{r}_\alpha$ by the according electromagnetic potentials $\phi(\mathbf{r}+\mathbf{r}_\alpha,t)$ and $\mathbf{a}(\mathbf{r}+\mathbf{r}_\alpha,t)$

$$\mathbf{b}(\mathbf{r}+\mathbf{r}_\alpha,t) = \nabla_{\mathbf{r}_\alpha}\times\mathbf{a}(\mathbf{r}+\mathbf{r}_\alpha,t), \tag{A.34}$$

$$\mathbf{e}(\mathbf{r}+\mathbf{r}_\alpha,t) = -\nabla_{\mathbf{r}_\alpha}\phi(\mathbf{r}+\mathbf{r}_\alpha,t) - \partial_t\,\mathbf{a}(\mathbf{r}+\mathbf{r}_\alpha,t) \tag{A.35}$$

we find the Lorentz force on each particle

$$\mathbf{f}(\mathbf{r}+\mathbf{r}_\alpha,t) = q_\alpha\left\{-\nabla_{\mathbf{r}_\alpha}\phi(\mathbf{r}+\mathbf{r}_\alpha,t) + \dot{\mathbf{r}}_\alpha\left[\nabla_{\mathbf{r}_\alpha}\times\mathbf{a}(\mathbf{r}+\mathbf{r}_\alpha,t)\right]\right\} \tag{A.36}$$

acting on each of the N charged particles denoted by the index α. We then obtain

$$\dot{\mathbf{r}}_\alpha\left[\nabla_{\mathbf{r}_\alpha}\times\mathbf{a}\right] = \sum_{i,j,k}\epsilon_{ijk}\,\tilde{\mathbf{e}}_i\,\dot{x}_{j,\alpha}\,(\nabla_{\mathbf{r}_\alpha}\times\mathbf{a})_k = \sum_{i,j,k}\sum_{m,n}\epsilon_{ijk}\epsilon_{kmn}\,\tilde{\mathbf{e}}_i\,\dot{x}_{j,\alpha}\frac{\partial a_n}{\partial x_{m,\alpha}} =$$

$$
\begin{aligned}
&= \sum_{i,j,m,n} (\delta_{im}\delta_{jn} - \delta_{in}\delta_{jm})\, \tilde{\mathbf{e}}_i\, \dot{x}_{j,\alpha}\, \frac{\partial a_n}{\partial x_{m,\alpha}} = \sum_{i,j} \tilde{\mathbf{e}}_i\, \dot{x}_{j,\alpha} \left(\frac{\partial a_j}{\partial x_{i,\alpha}} - \frac{\partial a_i}{\partial x_{j,\alpha}} \right) = \\
&= \sum_{i,j} \tilde{\mathbf{e}}_i\, \frac{\partial}{\partial x_{i,\alpha}} (\dot{x}_{j,\alpha} a_j) - \mathrm{d}_t \sum_i a_i\, \tilde{\mathbf{e}}_i - \partial_t \sum_i a_i\, \tilde{\mathbf{e}}_i = \\
&= \nabla_{\mathbf{r}_\alpha} (\dot{\mathbf{r}}_\alpha \cdot \mathbf{a}) - \mathrm{d}_t\, \mathbf{a} - \partial_t\, \mathbf{a},
\end{aligned} \tag{A.37}
$$

which is inserted into (A.36) and leads to

$$
\mathbf{f}(\mathbf{r} + \mathbf{r}_\alpha, t) = q_\alpha \left\{ -\nabla_{\mathbf{r}_\alpha} [\phi(\mathbf{r} + \mathbf{r}_\alpha, t) - \dot{\mathbf{r}}_\alpha \cdot \mathbf{a}(\mathbf{r} + \mathbf{r}_\alpha, t)] - \mathrm{d}_t\, \mathbf{a}(\mathbf{r} + \mathbf{r}_\alpha, t) \right\}. \tag{A.38}
$$

We use

$$
\mathrm{d}_t\, \mathbf{a}(\mathbf{r} + \mathbf{r}_\alpha, t) = \mathrm{d}_t\, \nabla_{\dot{\mathbf{r}}_\alpha} [\dot{\mathbf{r}}_\alpha \cdot \mathbf{a}(\mathbf{r} + \mathbf{r}_\alpha, t)] \tag{A.39}
$$

$$
\mathrm{d}_t\, \nabla_{\mathbf{r}_\alpha} \phi(\mathbf{r} + \mathbf{r}_\alpha, t) = \mathbf{0} \tag{A.40}
$$

to arrive at

$$
\begin{aligned}
\mathbf{f}(\mathbf{r} + \mathbf{r}_\alpha, t) =& q_\alpha \Big\{ \mathrm{d}_t\, \nabla_{\dot{\mathbf{r}}_\alpha} [\phi(\mathbf{r} + \mathbf{r}_\alpha, t) - \dot{\mathbf{r}}_\alpha \cdot \mathbf{a}(\mathbf{r} + \mathbf{r}_\alpha, t)] - \\
&- \nabla_{\mathbf{r}_\alpha} [\phi(\mathbf{r} + \mathbf{r}_\alpha, t) - \dot{\mathbf{r}}_\alpha \cdot \mathbf{a}(\mathbf{r} + \mathbf{r}_\alpha, t)] \Big\} = \\
&= \mathrm{d}_t\, \nabla_{\dot{\mathbf{r}}_\alpha} \sum_\beta\, q_\beta\, [\phi(\mathbf{r} + \mathbf{r}_\beta, t) - \dot{\mathbf{r}}_\beta \cdot \mathbf{a}(\mathbf{r} + \mathbf{r}_\beta, t)] - \\
&- \nabla_{\mathbf{r}_\alpha} \sum_\beta\, q_\beta [\phi(\mathbf{r} + \mathbf{r}_\beta, t) - \dot{\mathbf{r}}_\beta \cdot \mathbf{a}(\mathbf{r} + \mathbf{r}_\beta, t)]
\end{aligned} \tag{A.41}
$$

Hence, the total Lorentz force is given as

$$
\mathbf{F}(\mathbf{r}, t) = \sum_\alpha \mathbf{f}(\mathbf{r} + \mathbf{r}_\alpha, t) = \mathrm{d}_t \sum_\alpha [\nabla_{\dot{\mathbf{r}}_\alpha} U(\mathbf{r}_1, \mathbf{r}_2, \ldots, \mathbf{r}_N) - \nabla_{\mathbf{r}_\alpha} U(\mathbf{r}_1, \mathbf{r}_2, \ldots, \mathbf{r}_N)] \tag{A.42}
$$

where $U(\mathbf{r}_1, \mathbf{r}_2, \ldots, \mathbf{r}_N)$ is the potential of the force

$$
U(\mathbf{r}_1, \mathbf{r}_2, \ldots, \mathbf{r}_N) = \sum_\alpha q_\alpha [\phi(\mathbf{r} + \mathbf{r}_\alpha, t) - \dot{\mathbf{r}}_\alpha \cdot \mathbf{a}(\mathbf{r} + \mathbf{r}_\alpha, t)] \tag{A.43}
$$

From this and the kinetic energy $T = \sum_\alpha \frac{1}{2}\, m_\alpha\, \dot{\mathbf{r}}_\alpha^2$ we obtain the Lagrangian

$$
L = T - U = \sum_\alpha \left[\frac{1}{2}\, m_\alpha\, \dot{\mathbf{r}}_\alpha^2 - q_\alpha\, \phi(\mathbf{r} + \mathbf{r}_\alpha, t) + q_\alpha\, \dot{\mathbf{r}}_\alpha \cdot \mathbf{a}(\mathbf{r} + \mathbf{r}_\alpha, t) \right]. \tag{A.44}
$$

The generalized momentum is given by $\mathbf{p}_\alpha = m_\alpha\, \dot{\mathbf{r}}_\alpha + q_\alpha\, \mathbf{a}(\mathbf{r} + \mathbf{r}_\alpha, t)$ where the mechanical momentum is $\mathbf{p}_{\mathrm{mech},\alpha} = m_\alpha\, \dot{\mathbf{r}}_\alpha$. From this and the Lagrangian (A.44) we construct the Hamil-

tonian

$$\begin{aligned} H &= \sum_\alpha \mathbf{p}_\alpha \cdot \dot{\mathbf{r}}_\alpha - L = \sum_\alpha \left[\frac{1}{2}\, m_\alpha\, \dot{\mathbf{r}}_\alpha^2 + q_\alpha\, \phi(\mathbf{r}+\mathbf{r}_\alpha, t) \right] = \\ &= \sum_\alpha \left\{ \frac{1}{2m_\alpha} [\mathbf{p}_\alpha - q_\alpha\, \mathbf{a}(\mathbf{r}+\mathbf{r}_\alpha, t)] + q_\alpha\, \phi(\mathbf{r}+\mathbf{r}_\alpha, t) \right\}. \end{aligned} \tag{A.45}$$

For

$$\begin{aligned} \mathbf{p}_\alpha &\to \hat{\mathbf{p}}_\alpha \\ \mathbf{r}_\alpha &\to \hat{\mathbf{r}}_\alpha \\ \phi(\mathbf{r}+\mathbf{r}_\alpha, t) &\to \hat{\phi}(\mathbf{r}+\hat{\mathbf{r}}_\alpha, t) \\ \mathbf{a}(\mathbf{r}+\mathbf{r}_\alpha, t) &\to \hat{\mathbf{a}}(\mathbf{r}+\hat{\mathbf{r}}_\alpha, t) \end{aligned}$$

we obtain the quantum mechanical Hamiltonian

$$\hat{H} = \sum_\alpha \left\{ \frac{1}{2m_\alpha} \left[\hat{\mathbf{p}}_\alpha - q_\alpha\, \hat{\mathbf{a}}(\mathbf{r}+\mathbf{r}_\alpha, t) \right]^2 + q_\alpha\, \hat{\phi}(\mathbf{r}+\mathbf{r}_\alpha, t) \right\}. \tag{A.46}$$

APPENDIX B

Nonlinear optics

B.1 Commutator identity

Let us proof the identity

$$\mathrm{Tr}\left\{A\left[B_m, C\right]_-^{(m)}\right\} \stackrel{!}{=} \mathrm{Tr}\left\{\left[A, B_m\right]_-^{(m)} C\right\} \tag{B.1}$$

where we have defined

$$\left[B_m, C\right]_-^{(m)} = \Big[B_m, \Big[B_{m-1}, \ldots \left[B_1, C\right]_- \ldots\Big]_-\Big]_- \tag{B.2}$$

and

$$\left[A, B_m\right]_-^{(m)} = \Big[\ldots\Big[\left[A, B_m\right]_-, B_{m-1}\Big]_-, \ldots, B_1\Big]_- . \tag{B.3}$$

By induction we can show

Base ($m = 1$) :

$$\begin{aligned}\mathrm{Tr}\left\{A\left[B, C\right]_-\right\} &= \mathrm{Tr}\left\{ABC\right\} - \mathrm{Tr}\left\{ACB\right\} = \\ &= \mathrm{Tr}\left\{ABC\right\} - \mathrm{Tr}\left\{BAC\right\} = \\ &= \mathrm{Tr}\left\{\left[A, B\right]_- C\right\}\end{aligned}$$

Induction step ($m \to m+1$) :

$$\begin{aligned}
\mathrm{Tr}\left\{A\left[B_{m+1},C\right]_{-}^{(m+1)}\right\} =& \mathrm{Tr}\left\{AB_{m+1}\left[B_m,C\right]_{-}^{(m)}\right\} - \mathrm{Tr}\left\{A\left[B_m,C\right]_{-}^{(m)}B_{m+1}\right\} = \\
=& \mathrm{Tr}\left\{AB_{m+1}\left[B_m,C\right]_{-}^{(m)}\right\} - \mathrm{Tr}\left\{B_{m+1}A\left[B_m,C\right]_{-}^{(m)}\right\} = \\
\overset{(B.1)}{=}& \mathrm{Tr}\left\{\left[AB_{m+1},B_m\right]_{-}^{(m)}C\right\} - \mathrm{Tr}\left\{\left[B_{m+1}A,B_m\right]_{-}^{(m)}C\right\} = \\
=& \mathrm{Tr}\left\{\left[\left[A,B_{m+1}\right]_{-},B_m\right]_{-}^{(m+1)}C\right\}.
\end{aligned}$$

APPENDIX C

Raman-active dielectric materials

C.1 Electronic ground state energy in BOA

We will demonstrate how to calculate the coefficients in (5.12) with regards to time-independent non-degenerate (Rayleigh-Schrödinger) perturbation theory [76, 123]. Note, that the following derivations need to be extended if the states are degenerate. The reader is referred to standard textbooks at this point [47, 123].

$$\hat{H}_{\mathrm{e}} = \hat{H}_{0\mathrm{e}} + \hat{V}_{\mathrm{eE}} \tag{C.1}$$

where $\hat{H}_{0\mathrm{e}} = \hat{T}_{\mathrm{e}} + \hat{V}_{\mathrm{ee}} + \hat{V}_{\mathrm{ne}}$ is the Hamiltonian of the unperturbed system and the interaction operator is given by

$$\hat{V}_{\mathrm{eE}} = -\hat{\mathbf{d}} \cdot \mathbf{E}(\mathbf{r}, t) \tag{C.2}$$

for a fixed point in time t and the dipole operator is given by

$$\hat{\mathbf{d}} = \sum_{\alpha} q_{\alpha} \hat{\mathbf{r}}_{\alpha}, \tag{C.3}$$

where the charge $q_{\alpha} = -e \quad \forall\, \alpha$ for an electronic system. From time-independent non-degenerate perturbation theory we know that

$$\mathcal{E}_0^{(0)} = \sum_{\alpha} q_{\alpha} \Phi(\mathbf{r}, t) \tag{C.4}$$

$$\mathcal{E}_n^{(p)} = \left\langle \mathcal{E}_n^{(0)} \middle| \hat{V}_{\mathrm{eE}} \middle| \mathcal{E}_n^{(p-1)} \right\rangle \tag{C.5}$$

$$\left|\mathcal{E}_n^{(p)}\right\rangle = \sum\!\!\!\!\!\!\int_{\substack{m \\ m\neq n}} \left|\mathcal{E}_m^{(0)}\right\rangle \frac{\left\langle \mathcal{E}^{(0)}\right| \hat{V}_{\mathrm{eE}} \left|\mathcal{E}_n^{(p-1)}\right\rangle}{\mathcal{E}_n^{(0)} - \mathcal{E}_m^{(0)}} - \sum_{j=1}^{p} \mathcal{E}_n^{(j)} \sum\!\!\!\!\!\!\int_{\substack{m \\ m\neq n}} \left|\mathcal{E}^{(0)}\right\rangle \frac{\left\langle \mathcal{E}_m^{(0)}\right| \mathcal{E}_n^{(p-j)}\rangle}{\mathcal{E}_n^{(0)} - \mathcal{E}_m^{(0)}}, \tag{C.6}$$

where each electronic state is given as a state

$$\left|\mathcal{E}_n^{(p)}\right\rangle \equiv \left|\mathcal{E}_n^{(p)},\, \{\mathbf{R}_\beta,\, \mathbf{E}(\mathbf{r},t)\}\right\rangle \tag{C.7}$$

for a fixed nuclear configuration with a given electric Field $\{\mathbf{R}_\beta, \mathbf{E}(\mathbf{r},t)\}$ at time t.

$p = 1$:

$$\mathcal{E}_n^{(1)} = -\sum_i \mu_i^{(n)} E_i \tag{C.8}$$

$$\mu_i^{(n)} \equiv \left\langle \mathcal{E}_n^{(0)}\right| \hat{d}_i \left|\mathcal{E}_n^{(0)}\right\rangle \tag{C.9}$$

$$\left|\mathcal{E}_n^{(1)}\right\rangle = -\sum_i \sum\!\!\!\!\!\!\int_{\substack{m \\ m\neq n}} \left|\mathcal{E}_m^{(0)}\right\rangle \frac{\left\langle \mathcal{E}_m^{(0)}\right| \hat{d}_i \left|\mathcal{E}_n^{(0)}\right\rangle}{\mathcal{E}_n^{(0)} - \mathcal{E}_m^{(0)}} E_i \tag{C.10}$$

$p = 2$:

$$\mathcal{E}_n^{(2)} = -\frac{1}{2} \sum_{i,j} \alpha_{ij}^{(n)} E_i E_j \tag{C.11}$$

$$\alpha_{ij}^{(n)} \equiv -2 \sum\!\!\!\!\!\!\int_{\substack{m \\ m\neq n}} \frac{\left\langle \mathcal{E}_n^{(0)}\right| \hat{d}_i \left|\mathcal{E}_m^{(0)}\right\rangle \left\langle \mathcal{E}_m^{(0)}\right| \hat{d}_j \left|\mathcal{E}_n^{(0)}\right\rangle}{\mathcal{E}_n^{(0)} - \mathcal{E}_m^{(0)}} \tag{C.12}$$

$$\left|\mathcal{E}_n^{(2)}\right\rangle = \sum_{i,j} \sum\!\!\!\!\!\!\int_{\substack{m \\ m\neq n}} \left|\mathcal{E}_m^{(0)}\right\rangle \left[\sum\!\!\!\!\!\!\int_{\substack{o \\ o\neq n}} \frac{\left\langle \mathcal{E}_m^{(0)}\right| \hat{d}_i \left|\mathcal{E}_o^{(0)}\right\rangle \left\langle \mathcal{E}_o^{(0)}\right| \hat{d}_j \left|\mathcal{E}_n^{(0)}\right\rangle}{\left(\mathcal{E}_n^{(0)} - \mathcal{E}_m^{(0)}\right)\left(\mathcal{E}_n^{(0)} - \mathcal{E}_o^{(0)}\right)} - \mu_i^{(n)} \frac{\left\langle \mathcal{E}_m^{(0)}\right| \hat{d}_j \left|\mathcal{E}_n^{(0)}\right\rangle}{\left(\mathcal{E}_n^{(0)} - \mathcal{E}_m^{(0)}\right)^2} \right] E_i E_j \tag{C.13}$$

$p = 3$:

$$\mathcal{E}_n^{(3)} = -\frac{1}{3} \sum_{i,j,k} \beta_{ijk}^{(n)} E_i E_j E_k \tag{C.14}$$

$$\beta_{ijk}^{(n)} = 3 \sum\!\!\!\!\!\!\int_{\substack{m \\ m\neq n}} \left[\sum\!\!\!\!\!\!\int_{\substack{o \\ o\neq n}} \frac{\left\langle \mathcal{E}_n^{(0)} \right| \hat{d}_i \left| \mathcal{E}_m^{(0)} \right\rangle \left\langle \mathcal{E}_m^{(0)} \right| \hat{d}_j \left| \mathcal{E}_o^{(0)} \right\rangle \left\langle \mathcal{E}_o^{(0)} \right| \hat{d}_k \left| \mathcal{E}_n^{(0)} \right\rangle}{\left(\mathcal{E}_n^{(0)} - \mathcal{E}_m^{(0)} \right) \left(\mathcal{E}_n^{(0)} - \mathcal{E}_o^{(0)} \right)} - \right.$$
$$\left. - \mu_i^{(n)} \frac{\left\langle \mathcal{E}_n^{(0)} \right| \hat{d}_j \left| \mathcal{E}_m^{(0)} \right\rangle \left\langle \mathcal{E}_m^{(0)} \right| \hat{d}_k \left| \mathcal{E}_n^{(0)} \right\rangle}{\left(\mathcal{E}_n^{(0)} - \mathcal{E}_m^{(0)} \right)^2} \right] \tag{C.15}$$

$$\left| \mathcal{E}_n^{(3)} \right\rangle = - \sum_{i,j,k} \sum\!\!\!\!\!\!\int_{\substack{m \\ m\neq n}} \left| \mathcal{E}_m^{(0)} \right\rangle \left\{ \sum\!\!\!\!\!\!\int_{\substack{o \\ o\neq n}} \left[\sum\!\!\!\!\!\!\int_{\substack{q \\ q\neq n}} \frac{\left\langle \mathcal{E}_m^{(0)} \right| \hat{d}_i \left| \mathcal{E}_o^{(0)} \right\rangle \left\langle \mathcal{E}_o^{(0)} \right| \hat{d}_j \left| \mathcal{E}_q^{(0)} \right\rangle \left\langle \mathcal{E}_q^{(0)} \right| \hat{d}_k \left| \mathcal{E}_n^{(0)} \right\rangle}{\left(\mathcal{E}_n^{(0)} - \mathcal{E}_m^{(0)} \right) \left(\mathcal{E}_n^{(0)} - \mathcal{E}_o^{(0)} \right) \left(\mathcal{E}_n^{(0)} - \mathcal{E}_q^{(0)} \right)} \right.\right.$$
$$- \mu_i^{(n)} \frac{\left\langle \mathcal{E}_m^{(0)} \right| \hat{d}_j \left| \mathcal{E}_o^{(0)} \right\rangle \left\langle \mathcal{E}_o^{(0)} \right| \hat{d}_k \left| \mathcal{E}_n^{(0)} \right\rangle}{\left(\mathcal{E}_n^{(0)} - \mathcal{E}_m^{(0)} \right) \left(\mathcal{E}_n^{(0)} - \mathcal{E}_o^{(0)} \right)} \left(\frac{1}{\mathcal{E}_n^{(0)} - \mathcal{E}_m^{(0)}} + \frac{1}{\mathcal{E}_n^{(0)} - \mathcal{E}_o^{(0)}} \right) + \tag{C.16}$$
$$\left. \left. + \mu_i^{(n)} \mu_j^{(n)} \frac{\left\langle \mathcal{E}_o^{(0)} \right| \hat{d}_k \left| \mathcal{E}_n^{(0)} \right\rangle}{\left(\mathcal{E}_n^{(0)} - \mathcal{E}_m^{(0)} \right) \left(\mathcal{E}_n^{(0)} - \mathcal{E}_o^{(0)} \right)^2} \right] + \frac{1}{2} \alpha_{ij}^{(n)} \frac{\left\langle \mathcal{E}_m^{(0)} \right| \hat{d}_k \left| \mathcal{E}_n^{(0)} \right\rangle}{\left(\mathcal{E}_n^{(0)} - \mathcal{E}_m^{(0)} \right)^2} \right\} E_i E_j E_k$$

$p = 4$:

$$\mathcal{E}_n^{(4)} = - \frac{1}{4} \sum_{i,j,k,l} \gamma_{ijkl}^{(n)} E_i E_j E_k E_l \tag{C.17}$$

$$\gamma_{ijkl}^{(n)} = -4 \sum\!\!\!\!\!\!\int_{\substack{m \\ m\neq n}} \left\langle \mathcal{E}_n^{(0)} \right| \hat{d}_i \left| \mathcal{E}_m^{(0)} \right\rangle \left\{ \sum\!\!\!\!\!\!\int_{\substack{o \\ o\neq n}} \left[\sum\!\!\!\!\!\!\int_{\substack{q \\ q\neq n}} \frac{\left\langle \mathcal{E}_m^{(0)} \right| \hat{d}_j \left| \mathcal{E}_o^{(0)} \right\rangle \left\langle \mathcal{E}_o^{(0)} \right| \hat{d}_k \left| \mathcal{E}_q^{(0)} \right\rangle \left\langle \mathcal{E}_q^{(0)} \right| \hat{d}_l \left| \mathcal{E}_n^{(0)} \right\rangle}{\left(\mathcal{E}_n^{(0)} - \mathcal{E}_m^{(0)}\right)\left(\mathcal{E}_n^{(0)} - \mathcal{E}_o^{(0)}\right)\left(\mathcal{E}_n^{(0)} - \mathcal{E}_q^{(0)}\right)} - \right.\right.$$
$$- \mu_j^{(n)} \frac{\left\langle \mathcal{E}_m^{(0)} \right| \hat{d}_k \left| \mathcal{E}_o^{(0)} \right\rangle \left\langle \mathcal{E}_o^{(0)} \right| \hat{d}_l \left| \mathcal{E}_n^{(0)} \right\rangle}{\left(\mathcal{E}_n^{(0)} - \mathcal{E}_m^{(0)}\right)\left(\mathcal{E}_n^{(0)} - \mathcal{E}_o^{(0)}\right)} \left(\frac{1}{\mathcal{E}_n^{(0)} - \mathcal{E}_m^{(0)}} + \frac{1}{\mathcal{E}_n^{(0)} - \mathcal{E}_o^{(0)}} \right) +$$
$$\left. + \mu_j^{(n)} \mu_k^{(n)} \frac{\left\langle \mathcal{E}_o^{(0)} \right| \hat{d}_l \left| \mathcal{E}_n^{(0)} \right\rangle}{\left(\mathcal{E}_n^{(0)} - \mathcal{E}_m^{(0)}\right)\left(\mathcal{E}_n^{(0)} - \mathcal{E}_o^{(0)}\right)^2} \right] + \frac{1}{2} \alpha_{jk}^{(n)} \frac{\left\langle \mathcal{E}_m^{(0)} \right| \hat{d}_l \left| \mathcal{E}_n^{(0)} \right\rangle}{\left(\mathcal{E}_n^{(0)} - \mathcal{E}_m^{(0)}\right)^2} \Bigg\} \tag{C.18}$$

If we regard $\left|\mathcal{E}_n^{(0)}\right\rangle = \left|\mathcal{E}_0^{(0)}\right\rangle$ we obtain the electronic ground state energy

$$\mathcal{E}_0 = \mathcal{E}_0^{(0)} - \sum_i \mu_i E_i - \frac{1}{2} \sum_{i,j} \alpha_{ij} E_i E_j - \frac{1}{3} \sum_{i,j,k} \beta_{ijk} E_i E_j E_k - \frac{1}{4} \sum_{i,j,k,l} \gamma_{ijkl} E_i E_j E_k E_l - \ldots, \tag{C.19}$$

where $\mu_i = \mu_i^{(0)}$, $\alpha_{ij} = \alpha_{ij}^{(0)}$, $\beta_{ijk} = \beta_{ijk}^{(0)}$, and $\gamma_{ijkl} = \gamma_{ijkl}^{(0)}$.

C.2 Linear polarization in BOA with phenomenological damping

In the following we show how to incorporate the damping of the vibrational modes phenomenologically. The von-Neumann equation including phenomenological damping [50] shall be given by

$$\partial_t \hat{\varrho}(t) = \frac{1}{\mathrm{i}\hbar} \left[\hat{H}_0 + \hat{V}(\mathbf{r}, t), \hat{\varrho}(t) \right]_- - \hat{\gamma} \left(\hat{\varrho}(t) - \hat{\varrho}^{(\mathrm{eq})} \right) \tag{C.20}$$

We denote the complete eigen basis of the unperturbed Hamiltonian $\hat{H}_0$ by $\{\left|a\right\rangle\}$ yielding

$$\hat{H}_0 \left|a\right\rangle = \hbar\omega_a \left|a\right\rangle, \tag{C.21}$$

where the basis $\{\left|a\right\rangle\}$ shall be orthonormal in addition. In terms of the Dirac representation the equation of motion for each matrix element $\left\langle a\right|\hat{\varrho}\left|b\right\rangle \equiv \varrho_{ab}$ is given by

$$\partial_t\, \varrho_{ab}{}^{(\mathrm{D})}(t) = \frac{1}{\mathrm{i}\hbar}\left\langle a\right|\left[\hat{V}^{(\mathrm{D})}(\mathbf{r},t),\hat{\varrho}^{(\mathrm{D})}(t)\right]_-\left|b\right\rangle - \gamma_{ab}\left(\varrho_{ab}{}^{(\mathrm{D})}(t) - \varrho_{ab}^{(\mathrm{eq})}\right). \tag{C.22}$$

Therein, we have introduced the damping constant γ_{ab} for each transition with frequency ω_{ab}, which denotes the relaxation rate from ϱ_{ab} to the equilibrium value $\varrho_{ab}^{(\mathrm{eq})} = \text{const.}$. We require that $\gamma_{ab} = \gamma_{ba}$. From (C.22) it follows that

$$\partial_t\left(\varrho_{ab} - \varrho_{ab}^{(\mathrm{eq})}\right)\mathrm{e}^{\gamma_{ab}t} = \frac{1}{\mathrm{i}\hbar}\left\langle a\right|\left[\hat{V}^{(\mathrm{D})}(\mathbf{r},t),\hat{\varrho}^{(\mathrm{D})}(t)\right]_-\left|b\right\rangle\mathrm{e}^{\gamma_{ab}t}. \tag{C.23}$$

We then construct the Dyson series by integrating (C.23) in time

$$\begin{aligned}\varrho_{ab}(t) =& \varrho_{ab}^{(\mathrm{eq})} + \frac{1}{\mathrm{i}\hbar}\int_{-\infty}^{t}\mathrm{d}t'\left\langle a\right|\left[\hat{V}^{(\mathrm{D})}(\mathbf{r},t'),\hat{\varrho}^{(\mathrm{eq})}\right]_-\left|b\right\rangle\mathrm{e}^{-\gamma_{ab}(t-t')} + \\ &+\left(\frac{1}{\mathrm{i}\hbar}\right)^2\int_{-\infty}^{t}\mathrm{d}t'\left\langle a\right|\left[\hat{V}^{(\mathrm{D})}(\mathbf{r},t'),\left[\hat{V}^{(\mathrm{D})}(\mathbf{r},t''),\hat{\varrho}^{(\mathrm{eq})}\right]_-\right]_-\left|b\right\rangle\mathrm{e}^{-\gamma_{ab}(t-t')}\,\mathrm{e}^{-\gamma_{ab}(t-t'')} + \ldots\end{aligned} \tag{C.24}$$

To determine the equilibrium density matrix $\varrho^{(\mathrm{eq})}$ in (C.24) we first solve the steady-state problem of (C.20)

$$\left\langle a\right|\left[\hat{H}_0,\hat{\varrho}^{(0)}\right]_-\left|b\right\rangle = \mathrm{i}\hbar\,\gamma_{ab}\left(\varrho_{ab}^{(0)} - \varrho_{ab}^{(\mathrm{eq})}\right). \tag{C.25}$$

From the evaluation of the left hand side of (C.25)

$$\begin{aligned}\left\langle a\right|\left[\hat{H}_0,\hat{\varrho}^{(0)}\right]_-\left|b\right\rangle =& \sum_c\left(\left\langle a\right|\hat{H}_0\left|c\right\rangle\left\langle c\right|\hat{\varrho}^{(0)}\left|b\right\rangle - \left\langle a\right|\hat{\varrho}^{(0)}\left|c\right\rangle\left\langle c\right|\hat{H}_0\left|b\right\rangle\right) = \\ \overset{(\mathrm{C.21})}{=}& \sum_c\left(\hbar\omega_a\,\delta_{ac}\left\langle c\right|\hat{\varrho}_0\left|b\right\rangle - \left\langle a\right|\hat{\varrho}_0\left|c\right\rangle\hbar\omega_b\,\delta_{cb}\right) = \\ =& \left(\hbar\omega_a\,\varrho_{aa}^{(0)} - \hbar\omega_b\,\varrho_{bb}^{(0)}\right)\delta_{ab} = 0\end{aligned} \tag{C.26}$$

that the steady-state solution is identical with the equilibrium value $\varrho_{ab}^{(0)} = \varrho_{ab}^{(\mathrm{eq})}$ by construction. Note, that the steady state solution is given by (2.7) and, thus, is purely diagonal ($\varrho_{ab}^{(0)} = 0$, for $a \neq b$). We define $\varrho_{ab}(t) = \varrho_{ab}^{(0)} + \varrho_{ab}^{(1)} + \varrho_{ab}^{(2)} + \ldots$, where

$$\varrho_{ab}^{(0)} = \varrho_{ab}^{(\mathrm{eq})} \tag{C.27}$$

$$\varrho_{ab}^{(1)} = \frac{1}{\mathrm{i}\hbar}\int_{-\infty}^{t}\mathrm{d}t'\left\langle a\right|\left[\hat{V}^{(\mathrm{D})}(\mathbf{r},t'),\hat{\varrho}^{(\mathrm{eq})}\right]_-\left|b\right\rangle\mathrm{e}^{-\gamma_{ab}(t-t')} \tag{C.28}$$

$$\varrho_{ab}^{(2)} = \left(\frac{1}{\mathrm{i}\hbar}\right)^2 \int_{-\infty}^{t} \mathrm{d}t' \left\langle a\right| \left[\hat{V}^{(\mathrm{D})}(\mathbf{r},t'), \left[\hat{V}^{(\mathrm{D})}(\mathbf{r},t''), \hat{\varrho}^{(\mathrm{eq})}\right]_-\right]_- \left|b\right\rangle \mathrm{e}^{-\gamma_{ab}(t-t')}\,\mathrm{e}^{-\gamma_{ab}(t-t'')} \tag{C.29}$$

$\ldots$.

Let us define the interaction operator $\hat{V}(\mathbf{r},t) = -\sum_i \hat{m}\, E_i(\mathbf{r},t)$. Using (5.13) we calculate the non-instantaneous part of the linear polarization by

$$P_i^{(1.2)}(\mathbf{r},t) = \frac{1}{\mathcal{V}} \sum_{a,b} \left\langle a\right| \hat{m}_i{}^{(\mathrm{D})}(t) \left|b\right\rangle \varrho_{ba}^{(1)}, \tag{C.30}$$

which is in accordance with the non-instantaneous part of expression (5.15) but this time the phenomenological damping factor is already included in the density matrix.

APPENDIX D

Hydrodynamics

D.1 Calculation of the first and second moment of the transport equation for quasi-particles in a Fermi liquid

The transport for quasi-particles is given according to section 4.1 by

$$\frac{\partial n_{\mathbf{p}\sigma}}{\partial t} + (\nabla_{\mathbf{p}}\epsilon_{\mathbf{p}\sigma}) \cdot (\nabla n_{\mathbf{p}\sigma}) - (\nabla U + \nabla\epsilon_{\mathbf{p}\sigma}) \cdot (\nabla_{\mathbf{p}} n_{\mathbf{p}\sigma}) = I[n_{\mathbf{p}\sigma}] \tag{4.10}$$

We now calculate the moments of (4.10).

1st moment:

The first moment is obtained by taking the average of (4.10) by

$$\sum_{\sigma} \int \frac{\mathrm{d}^3 p}{(2\pi\hbar)^3} \left[\frac{\partial n_{\mathbf{p}\sigma}}{\partial t} + (\nabla_{\mathbf{p}}\epsilon_{\mathbf{p}\sigma}) \cdot (\nabla n_{\mathbf{p}\sigma}) - (\nabla U + \nabla\epsilon_{\mathbf{p}\sigma}) \cdot (\nabla_{\mathbf{p}} n_{\mathbf{p}\sigma}) \right] = \sum_{\sigma} \int \frac{\mathrm{d}^3 p}{(2\pi\hbar)^3}\, I[n_{\mathbf{p}\sigma}]. \tag{D.1}$$

The particle density shall then be given by

$$n(\mathbf{r}, t) = \sum_{\sigma} \int \frac{\mathrm{d}^3 p}{(2\pi\hbar)^3}\, n_{\mathbf{p}\sigma}(\mathbf{r}, t). \tag{4.13}$$

Because the particle number is conserved in collisions the average over the collision integral should vanish, i.e.

$$\sum_{\sigma} \int \frac{\mathrm{d}^3 p}{(2\pi\hbar)^3}\, I[n_{\mathbf{p}\sigma}(\mathbf{r}, t)] = 0. \tag{D.2}$$

We then calculate the last two terms on the l.h.s. of (D.1), which yields

$$\begin{aligned}\sum_\sigma \int \frac{\mathrm{d}^3p}{(2\pi\hbar)^3}\, &[(\nabla_{\mathbf{p}}\epsilon_{\mathbf{p}\sigma})\cdot(\nabla n_{\mathbf{p}\sigma}) - (\nabla U + \nabla\epsilon_{\mathbf{p}\sigma})\cdot(\nabla_{\mathbf{p}} n_{\mathbf{p}\sigma})] = \\ &= \nabla\cdot\left(\sum_\sigma \int \frac{\mathrm{d}^3p}{(2\pi\hbar)^3}\,(\nabla_{\mathbf{p}}\epsilon_{\mathbf{p}\sigma})\, n_{\mathbf{p}\sigma}\right) - \sum_\sigma \int \frac{\mathrm{d}^3p}{(2\pi\hbar)^3}\,[\nabla_{\mathbf{p}}\cdot(\nabla\epsilon_{\mathbf{p}\sigma})]\, n_{\mathbf{p}\sigma} - \\ &- (\nabla U)\cdot \underbrace{\left(\sum_\sigma \int \frac{\mathrm{d}^3p}{(2\pi\hbar)^3}\nabla_{\mathbf{p}} n_{\mathbf{p}\sigma}\right)}_{\to 0} - \sum_\sigma \int \frac{\mathrm{d}^3p}{(2\pi\hbar)^3}\,(\nabla\epsilon_{\mathbf{p}\sigma})\cdot(\nabla_{\mathbf{p}} n_{\mathbf{p}\sigma}),\end{aligned} \tag{D.3}$$

where in the second line we used that $(\nabla_{\mathbf{p}}\epsilon_{\mathbf{p}})\cdot(\nabla n_{\mathbf{p}\sigma}) = \nabla\cdot[(\nabla\epsilon_{\mathbf{p}\sigma})\, n_{\mathbf{p}\sigma}] - [\nabla_{\mathbf{p}}\cdot(\nabla\epsilon_{\mathbf{p}\sigma})]\, n_{\mathbf{p}\sigma}$. Furthermore, in the third line of (D.3) we assumed that the distribution function vanishes as the momentum goes to infinity. At last we calculate the second term on the r.h.s. of (D.3). Integration by parts yields

$$\sum_\sigma \int \frac{\mathrm{d}^3p}{(2\pi\hbar)^3}\,[\nabla_{\mathbf{p}}\cdot(\nabla\epsilon_{\mathbf{p}\sigma})] n_{\mathbf{p}\sigma} = -\sum_\sigma \int \frac{\mathrm{d}^3p}{(2\pi\hbar)^3}\,(\nabla\epsilon_{\mathbf{p}\sigma})\cdot(\nabla_{\mathbf{p}} n_{\mathbf{p}\sigma}). \tag{D.4}$$

If we then define the flux

$$\mathbf{i}(\mathbf{r},t) = \sum_\sigma \int \frac{\mathrm{d}^3p}{(2\pi\hbar)^3}\,[\nabla_{\mathbf{p}}\epsilon_{\mathbf{p}\sigma}(\mathbf{r},t)]\, n_{\mathbf{p}\sigma}(\mathbf{r},t), \tag{4.14}$$

we obtain the conservation law

$$\partial_t\, n(\mathbf{r},t) + \nabla\cdot\mathbf{i}(\mathbf{r},t) = 0 \tag{4.15}$$

from (D.1) by using (4.13) and (D.2) to (D.4).

2nd moment:

The second moment of the transport equation (4.10) is obtained by

$$\begin{aligned}\sum_\sigma \int \frac{\mathrm{d}^3p}{(2\pi\hbar)^3}\,\mathbf{p}\left[\frac{\partial n_{\mathbf{p}\sigma}}{\partial t} + (\nabla_{\mathbf{p}}\epsilon_{\mathbf{p}\sigma})\cdot(\nabla n_{\mathbf{p}\sigma}) - (\nabla U + \nabla\epsilon_{\mathbf{p}\sigma})\cdot(\nabla_{\mathbf{p}} n_{\mathbf{p}\sigma})\right] = \\ = \sum_\sigma \int \frac{\mathrm{d}^3p}{(2\pi\hbar)^3}\,\mathbf{p}\, I[n_{\mathbf{p}\sigma}].\end{aligned} \tag{D.5}$$

Because the momentum is conserved in particle collisions, the second moment of the collision integral shall vanish, i.e.

$$\sum_{\sigma} \int \frac{\mathrm{d}^3 p}{(2\pi\hbar)^3}\; I[n_{\mathbf{p}\sigma}(\mathbf{r},t)] = 0. \tag{D.6}$$

We calculate i-th component of the second term on the l.h.s. of (D.5) by

$$\begin{aligned} &\sum_{\sigma} \int \frac{\mathrm{d}^3 p}{(2\pi\hbar)^3}\; p_i (\nabla_{\mathbf{p}} \epsilon_{\mathbf{p}\sigma}) \cdot (\nabla n_{\mathbf{p}\sigma}) = \\ &\quad = \nabla \cdot \left[\sum_{\sigma} \int \frac{\mathrm{d}^3 p}{(2\pi\hbar)^3}\; p_i \, (\nabla_{\mathbf{p}} \epsilon_{\mathbf{p}\sigma}) \, n_{\mathbf{p}\sigma} \right] - \sum_{\sigma} \int \frac{\mathrm{d}^3 p}{(2\pi\hbar)^3}\; [\nabla_{\mathbf{p}} \cdot (\nabla \epsilon_{\mathbf{p}\sigma})] \, p_i \, n_{\mathbf{p}\sigma} \end{aligned} \tag{D.7}$$

Integration by parts of the second term on the r.h.s. of (D.7) yields

$$\sum_{\sigma} \int \frac{\mathrm{d}^3 p}{(2\pi\hbar)^3}\; [\nabla_{\mathbf{p}} \cdot (\nabla \epsilon_{\mathbf{p}\sigma})] \, p_i \, n_{\mathbf{p}\sigma} = - \sum_{\sigma} \int \frac{\mathrm{d}^3 p}{(2\pi\hbar)^3}\; (\nabla \epsilon_{\mathbf{p}\sigma}) \cdot [\, \breve{\mathbf{e}}_j \delta_{ij} n_{\mathbf{p}\sigma} + p_i \, (\nabla_{\mathbf{p}} n_{\mathbf{p}\sigma}) \,], \tag{D.8}$$

where again we have used that the distribution function vanishes sufficiently fast as the momentum goes to infinity. Using (D.7) and (D.8) we can express the i-th component of (D.5) by

$$\sum_{\sigma} \int \frac{\mathrm{d}^3 p}{(2\pi\hbar)^3} \left[p_i \frac{\partial n_{\mathbf{p}\sigma}}{\partial t} + \frac{\partial \epsilon_{\mathbf{p}\sigma}}{\partial x_i} \, n_{\mathbf{p}\sigma} - p_i \, (\nabla U) \cdot (\nabla_{\mathbf{p}} n_{\mathbf{p}\sigma}) \right] = 0. \tag{D.9}$$

We can analyze the second term on the l.h.s. of (D.9) further. To this end we reformulate this term by

$$\sum_{\sigma} \int \frac{\mathrm{d}^3 p}{(2\pi\hbar)^3}\; \frac{\partial \epsilon_{\mathbf{p}\sigma}}{\partial x_i} \, n_{\mathbf{p}\sigma} = \sum_{\sigma} \int \frac{\mathrm{d}^3 p}{(2\pi\hbar)^3}\; \epsilon_{\mathbf{p}\sigma} \, n_{\mathbf{p}\sigma} - \sum_{\sigma} \int \frac{\mathrm{d}^3 p}{(2\pi\hbar)^3}\; \epsilon_{\mathbf{p}\sigma} \frac{\partial n_{\mathbf{p}\sigma}}{\partial x_i} \tag{D.10}$$

Using the expression for the kinetic energy density

$$\mathcal{E} = \mathcal{E}_0 + \sum_{\sigma} \int \frac{\mathrm{d}^3 p}{(2\pi\hbar)^3}\; \epsilon_{\mathbf{p}\sigma} \, \delta n_{\mathbf{p}\sigma} \tag{D.11}$$

the last term in (D.10) can be replaced by

$$\sum_{\sigma} \int \frac{\mathrm{d}^3 p}{(2\pi\hbar)^3}\; \epsilon_{\mathbf{p}\sigma} \frac{\partial n_{\mathbf{p}\sigma}}{\partial x_i} = \frac{\partial \mathcal{E}}{\partial x_i}. \tag{D.12}$$

Furthermore, we calculate the third term in (D.10) by integrating it by parts

$$(\nabla U) \cdot \left[\sum_{\sigma} \int \frac{\mathrm{d}^3 p}{(2\pi\hbar)^3} \, p_i \, (\nabla_{\mathbf{p}} n_{\mathbf{p}\sigma}) \right] \overset{(4.13)}{=} -n \, \frac{\partial U}{\partial x_i} \tag{D.13}$$

If we define the momentum density

$$\mathbf{g}(\mathbf{r}, t) = \sum_{\sigma} \int \frac{\mathrm{d}^3 p}{(2\pi\hbar)^3} \, \mathbf{p} \, n_{\mathbf{p}\sigma}, \tag{4.17}$$

the convection tensor

$$\underline{\mathbf{t}} = \sum_{\sigma} \int \frac{\mathrm{d}^3 p}{(2\pi\hbar)^3} \, \mathbf{p} \otimes (\nabla_{\mathbf{p}} \epsilon_{\mathbf{p}\sigma}) \, n_{\mathbf{p}\sigma} \tag{4.18}$$

and the pressure

$$\mathcal{P} = \sum_{\sigma} \int \frac{\mathrm{d}^3 p}{(2\pi\hbar)^3} \, \epsilon_{\mathbf{p}\sigma} \, n_{\mathbf{p}\sigma} - \mathcal{E}, \tag{4.19}$$

we obtain the momentum conservation law

$$\frac{\partial g_i}{\partial t} + \sum_{k=1}^{3} \frac{\partial t_{ik}}{\partial x_k} + \frac{\partial \mathcal{P}}{\partial x_i} + n \, \frac{\partial U}{\partial x_i} = 0 \tag{4.20}$$

after inserting (D.10), (D.12) and (D.13) into (D.9).

D.2 Prefactors in the hydrodynamic kernels of SWG version 2.2

As we use our own implementation of a DGTD maxwell solver, the SWG version 2.2, there are certain things to consider when using the code. One of them is how to calculate the input parameters that are needed to run the code with a hydrodynamic material model. Let us, therefore, take a look at the Euler equation (see (4.33)) once again

$$\begin{aligned} &\partial_t \, \mathbf{J}(\mathbf{r}, t) + \nabla \cdot \left[\frac{1}{\varrho_{\mathrm{e}}(\mathbf{r}, t)} \, \mathbf{J}(\mathbf{r}, t) \otimes \mathbf{J}(\mathbf{r}, t) \right] + \gamma \, \mathbf{J}(\mathbf{r}, t) = \\ &= \frac{q_{\mathrm{e}}}{m_{\mathrm{e}}} \left[\varrho_{\mathrm{e}}(\mathbf{r}, t) \, \mathbf{E}(\mathbf{r}, t) + \mathbf{J}(\mathbf{r}, t) \cdot \mathbf{B}(\mathbf{r}, t) \right] - \frac{q_{\mathrm{e}}}{m_{\mathrm{e}}} \, \nabla p(\mathbf{r}, t) \end{aligned} \tag{D.14}$$

where we use the *quantum pressure*

$$p = \underbrace{\frac{(3\,\pi^2)^{2/3}\,\hbar^2}{5\,m_\mathrm{e}^*}\,|q_\mathrm{e}|^{-5/3}}_{\equiv\zeta}\,|\varrho_\mathrm{e}|^{5/3}. \tag{D.15}$$

Thereby, m_e denotes effective mass. For silver the effective mass is given by $m_\mathrm{e} = 0.96\,m_0$ [70].

In SWG version 2.2 there are three material kernels, which are based on the hydrodynamic material model. We show how to calculate the input parameters for each of these kernels. To do so we first give a conversion table to formulate the Euler equation in dimensionless units

time	t_0	$= \frac{l_0}{c}$
electric field	E_0	$= 10^9\,\frac{\mathrm{V}}{\mathrm{m}}$
magnetic field	B_0	$= \frac{1}{c}\,E_0$
charge density	ϱ_0	$= \frac{\varepsilon_0}{l_0}\,E_0$
current density	j_0	$= c\,\varrho_0 = c\,\frac{\varepsilon_0}{l_0}\,E_0$

Table D.1: Units for Maxwell's equations. Unless stated otherwise we choose the unit length l_0 as 1 nm.

which can be obtained via Maxwell's equations (1.7) to (1.10). Thereby, we choose a unit length of $l_0 = 1\,\mathrm{nm}$ and a unit electric field strength of $E_0 = 10^9\,\mathrm{V/m}$. Furthermore, from (D.15) we calculate the unit pressure

$$p_0 = \zeta\,\varrho_0^{5/3} = \frac{(3\,\pi^2)^{2/3}\,\hbar^2}{5\,m_\mathrm{e}\,l_0^5} \tag{D.16}$$

using table D.1. In the following we give a recipe on how to calculate the SWG version 2.2 specific input parameters for the three hydrodynamic kernels *IsoHdFermi*, *IsoHdLinear* and *IsoHdPerturbative*.

IsoHdFermi kernel (full hydrodynamic model)

The IsoHdFermi kernel contains the full hydrodynamic equations without any perturbative approach. There are three parameters one needs to consider when using this kernel, which relate to the three terms on the r.h.s. of (D.14).

pressureGradCoeff:

We first consider the term in (D.14) containing the pressure gradient.

$$\partial_t\,\mathbf{J} \to -\frac{q_\mathrm{e}}{m_\mathrm{e}}\nabla p. \tag{D.17}$$

In dimensionless units this term is exrpessed by

$$\partial_{\tilde{t}}\,\tilde{\mathbf{J}} \rightarrow \left(\frac{t_0}{j_0}\right)\left(-\frac{q_\mathrm{e}}{m_\mathrm{e}}\right)\left(\frac{p_0}{l_0}\right)\tilde{\nabla}\tilde{p} = \left(-\frac{q_\mathrm{e}}{m_\mathrm{e}\,c^2}\,\zeta\,\varrho_0^{2/3}\right)\tilde{\nabla}\tilde{p}. \tag{D.18}$$

Then we define the so-called "pressureGradCoeff" (cf. SWG version 2.2)

$$C_\mathrm{p} \equiv \frac{q_\mathrm{e}}{m_\mathrm{e}\,c^2}\,\zeta\,\varrho_0^{2/3}. \tag{D.19}$$

couplingToE:

Let us now consider the term in (D.14) related to the electric force

$$\partial_t\,\mathbf{J} \rightarrow \frac{q_\mathrm{e}}{m_\mathrm{e}}\,\varrho_\mathrm{e}\,\mathbf{E}. \tag{D.20}$$

In dimensionless units this yields

$$\partial_{\tilde{t}}\,\tilde{\mathbf{J}} \rightarrow \left(\frac{t_0}{j_0}\right)\left(\frac{q_\mathrm{e}}{m_\mathrm{e}}\right)\left(\varrho_0\,E_0\right)\,\tilde{\varrho}_\mathrm{e}\,\tilde{\mathbf{E}} = \left(\frac{q_\mathrm{e}^2\,\mu_0}{m_\mathrm{e}\,l_0}\right)\,\tilde{\varrho}_\mathrm{e}\,\tilde{\mathbf{E}}. \tag{D.21}$$

We then define the so-called "couplinToE" parameter (cf. SWG version 2.2)

$$C_\mathrm{E} = \frac{q_\mathrm{e}^2\,\mu_0}{m_\mathrm{e}\,l_0}. \tag{D.22}$$

couplingToH:

At last we consider the term in (D.14) related to the magnetic force

$$\partial_t\,\mathbf{J} = \frac{q_\mathrm{e}}{m_\mathrm{e}}\,\mathbf{J}\cdot\mathbf{B} = \frac{q_\mathrm{e}}{m_\mathrm{e}}\mu_0\,\mathbf{J}\cdot\mathbf{H}, \tag{D.23}$$

where we have a non-magnetic material. In dimensionless units this is expressed by

$$\partial_{\tilde{t}}\,\tilde{\mathbf{J}} \rightarrow \left(\frac{t_0}{j_0}\right)\left(\frac{q_\mathrm{e}}{m_\mathrm{e}}\right)\underbrace{\left(j_0\,B_0\right)}_{=\varrho_0\,E_0}\tilde{\mathbf{J}}\cdot\tilde{\mathbf{B}}, \tag{D.24}$$

which results in a prefactor "couplingToH"

$$C_\mathrm{H} \equiv C_\mathrm{E} \tag{D.25}$$

that is identical to the prefactor "couplingToE".

IsoHdLinear/IsoHdPerturbative (linearized/perturbative hydrodynamic model)

Instead of the "pressureGradCoeff" parameter both the IsoHdLinear and the IsoHdPerturbative use a parameter that is called "densityGradCoeff" instead. To determine this parameter we have a look at the linearized version of the pressure gradient term in (D.14)

$$\partial_t \mathbf{J} \to -\frac{q_\mathrm{e}}{m_\mathrm{e}} \nabla p^{(1)} \tag{D.26}$$

or in dimensionless units

$$\partial_{\tilde{t}} \tilde{\mathbf{J}} \to \left(\frac{t_0}{j_0}\right)\left(-\frac{q_\mathrm{e}}{m_\mathrm{e}}\right)\left(\frac{p_0}{l_0}\right) \tilde{\nabla}\tilde{p}^{(1)} = C_\mathrm{p}\, \tilde{\nabla}\tilde{p}^{(1)}. \tag{D.27}$$

As the linearized pressure gradient, where hard-wall boundaries are already applied ($\nabla \varrho_\mathrm{e}^{(0)} = 0$), is given by

$$\nabla p^{(1)} = \frac{5}{3}\zeta \left(\varrho_\mathrm{e}^{(0)}\right)^{2/3} \nabla \varrho_\mathrm{e}^{(1)} \tag{D.28}$$

(for more information section 4.2) or in dimensionless units by

$$\tilde{\nabla}\tilde{p}^{(1)} = \left(\frac{l_0}{p_0}\right)\left(\frac{5}{3}\right)\underbrace{\left(\zeta\, \varrho_0^{5/3}\right)}_{\overset{(\mathrm{D.16})}{=} p_0}\left(\frac{1}{l_0}\right)\left(\tilde{\varrho}_\mathrm{e}^{(0)}\right)^{2/3} \tilde{\nabla}\tilde{\varrho}_\mathrm{e}^{(1)} = \frac{5}{3}\left(\tilde{\varrho}_\mathrm{e}^{(0)}\right)^{2/3} \tilde{\nabla}\tilde{\varrho}_\mathrm{e}^{(1)} \tag{D.29}$$

Inserting (D.29) into (D.27) yields

$$\partial_{\tilde{t}} \tilde{\mathbf{J}} \to \frac{5}{3} C_\mathrm{p} \left(\tilde{\varrho}_\mathrm{e}^{(0)}\right)^{2/3} \tilde{\nabla}\tilde{\varrho}_\mathrm{e}^{(1)}. \tag{D.30}$$

We then define the "densityGradCoeff" as

$$C_\varrho = \frac{5}{3} C_\mathrm{p} \left(\tilde{\varrho}_\mathrm{e}^{(0)}\right)^{2/3}. \tag{D.31}$$

Bibliography

1. O. Darrigol, *A history of optics from Greek antiquity to the nineteenth century* (Oxford University Press, 2012).
2. J. Maxwell, “A Dynamical Theory of the Electromagnetic Field", Philosophical transactions of the Royal Society of London **155,** 459 (1864).
3. J. C. Maxwell, *A treatise on electricity and magnetism* (Clarendon press, 1881).
4. C. Raman and K. Krishnan, “A new type of secondary radiation", Nature **121,** 501 (1928).
5. C. V. Raman and K. S. Krishnan, “The optical analogue of the Compton effect", Nature **121,** 711 (1928).
6. C. V. Raman, *Nobel Lecture: The Molecular Scattering of Light* (Nobelprize.org. Nobel Media AB 2014. Web., 1939).
7. T. Maiman, “Stimulated optical radiation in ruby", SPIE milestone series, 61 (2002).
8. e. P. Franken, A. E. Hill, C. e. Peters and G Weinreich, “Generation of optical harmonics", Physical Review Letters **7,** 118 (1961).
9. T. Verbiest, K. Clays and V. Rodriguez, *Second-order Nonlinear Optical Characterization Techniques: An Introduction* (CRC Press, 2009).
10. F. Brown, R. E. Parks and A. M. Sleeper, “Nonlinear Optical Reflection from a Metallic Boundary", Phys. Rev. Lett. **14,** 1029 (1965).
11. H. Simon, D. Mitchell and J. Watson, “Optical second-harmonic generation with surface plasmons in silver films", Physical Review Letters **33,** 1531 (1974).
12. M. Kauranen and A. V. Zayats, “Nonlinear plasmonics", Nature Photonics **6,** 737 (2012).
13. K. Busch, M. König and J. Niegemann, “Discontinuous Galerkin methods in nanophotonics", Laser & Photonics Reviews **5,** 773 (2011).
14. J. Hesthaven and T. Warburton, *Nodal Discontinuous Galerkin Methods: Algorithms, Analysis, and Applications* (Springer New York, 2007).
15. R. LeVeque, *Finite Volume Methods for Hyperbolic Problems* (Cambridge University Press, 2002).

16. J. M. McMahon, S. K. Gray and G. C. Schatz, “Nonlocal optical response of metal nanostructures with arbitrary shape", Physical review letters **103,** 097403 (2009).
17. C. David and F. J. Garcia de Abajo, “Spatial nonlocality in the optical response of metal nanoparticles", The Journal of Physical Chemistry C **115,** 19470 (2011).
18. G. Toscano, S. Raza, A.-P. Jauho, N. A. Mortensen and M. Wubs, “Modified field enhancement and extinction by plasmonic nanowire dimers due to nonlocal response", Optics express **20,** 4176 (2012).
19. A. Hille *et al.,* “Second harmonic generation from metal nano-particle resonators: Numerical analysis on the basis of the hydrodynamic drude model", The Journal of Physical Chemistry C **120,** 1163 (2016).
20. M. Moeferdt, *Nonlocal and Nonlinear Properties of Plasmonic Nanostructures Within the Hydrodynamic Drude Model*, PhD thesis (Humboldt-Universität zu Berlin, Mathematisch-Naturwissenschaftliche Fakultät, 2017).
21. C. Prohm, *Modellierung der linearen und nichtlinearen optischen Eigenschaften metallischer Nanostrukturen mithilfe unstetiger Galerkin Verfahren*, MA thesis (Karlsruhe Institute of Technology, 2010).
22. C. Varin, R. Emms, G. Bart, T. Fennel and T. Brabec, “Explicit formulation of second and third order optical nonlinearity in the FDTD framework", Computer Physics Communications **222,** 70 (2018).
23. V. A. Bokil, Y. Cheng, Y. Jiang and F. Li, “Energy stable discontinuous Galerkin methods for Maxwell’s equations in nonlinear optical media", Journal of Computational Physics **350,** 420 (2017).
24. J. Hesthaven and T. Warburton, “Nodal High-Order Methods on Unstructured Grids", Journal of Computational Physics **181,** 186 (2002).
25. V. Silin, “Theory of a degenerate electron liquid", Soviet Physics Jetp-Ussr **6,** 387 (1957).
26. R. W. Hellwarth, “Third-order optical susceptibilities of liquids and solids", Progress in Quantum Electronics **5,** 1 (1977).
27. O. Heaviside, “A gravitational and electromagnetic Analogy", The Electrician **31,** 5125 (1893).
28. J. Jackson, *Klassische Elektrodynamik* (De Gruyter, 2014).
29. D. Griffiths, *Introduction to Electrodynamics* (Pearson Education, 2014).
30. L. Landau and E. Lifschitz, *Elektrodynamic der Kontinua* (Akademie Verlag, 1990).
31. W. Nolting, *Grundkurs Theoretische Physik 3:* (Springer, 2004).
32. B. Saleh and M. Teich, *Grundlagen der Photonik* (Wiley-VCH, 2008).
33. W. Cai and V. Shalaev, *Optical Metamaterials: Fundamentals and Applications* (Springer New York, 2009).
34. R. Nevels and C.-S. Shin, “Lorenz, Lorentz, and the gauge", IEEE Antennas and Propagation Magazine **43,** 70 (2001).

35. F. Scheck, *Theoretische Physik 3: Klassische Feldtheorie: Von Elektrodynamik, nicht-Abelschen Eichtheorien und Gravitation* (Springer Berlin Heidelberg, 2017).
36. L. Barron and C. Gray, "The multipole interaction Hamiltonian for time dependent fields", Journal of Physics A: Mathematical, Nuclear and General **6,** 59 (1973).
37. W. Nolting, *Grundkurs Theoretische Physik 3: Elektrodynamik* (Springer Berlin Heidelberg, 2013).
38. R. Raab and O. De Lange, *Multipole Theory in Electromagnetism: Classical, Quantum, and Symmetry Aspects, with Applications* (OUP Oxford, 2005).
39. R. Kubo, "Statistical-Mechanical Theory of Irreversible Processes. I. General Theory and Simple Applications to Magnetic and Conduction Problems", Journal of the Physical Society of Japan **12,** 570 (1957).
40. S. Jha, "Nonlinear response theory—I", English. Pramana **22,** 173 (1984).
41. K. Rottwitt and P. Tidemand-Lichtenberg, *Nonlinear Optics: Principles and Applications* (CRC Press, 2014).
42. D. Forster, *Hydrodynamic Fluctuations, Broken Symmetry, and Correlation Functions* (Avalon Publishing, 1995).
43. W. Nolting, *Grundkurs Theoretische Physik 7: Viel-Teilchen-Theorie* (Springer Berlin Heidelberg, 2014).
44. G. Mahan, *Many-Particle Physics* (Springer, 2000).
45. A. Altland and B. Simons, *Condensed Matter Field Theory* (Cambridge University Press, 2010).
46. W. Nolting, *Grundkurs Theoretische Physik 5/1: Quantenmechanik - Grundlagen* (Springer Berlin Heidelberg, 2013).
47. F. Schwabl, *Quantenmechanik (QM I): Eine Einführung* (Springer Berlin Heidelberg, 2013).
48. K. Huang, *Statistical Mechanics* , 2 (John Wiley & Sons, 1987).
49. P. Butcher and D. Cotter, *The Elements of Nonlinear Optics* (Cambridge University Press, 1991).
50. R. Boyd, *Nonlinear optics* (Academic press, 2003).
51. O. Keller, *Nonlinear Optics in Solids: Proceedings of the International Summer School, Aalborg, Denmark, July 31—August 4, 1989* (Springer Berlin Heidelberg, 2012).
52. J. Gieseler, *Discontinuous Galerkin Finite Element Time-Domain Methods for the Numerical Treatment of the Nonlinear Maxwell's Equations*, MA thesis (Universität (TH) Karlsruhe, 2008).
53. K. Yee, "Numerical solution of initial boundary value problems involving maxwell's equations in isotropic media", IEEE Transactions on Antennas and Propagation **14,** 302 (1966).

54. A. Akyurtlu, D. H. Werner, V. Veremey, D. J. Steich and K. Aydin, “Staircasing errors in FDTD at an air-dielectric interface", IEEE Microwave and Guided Wave Letters **9,** 444 (1999).

55. A. Ditkowski, K. Dridi and J. Hesthaven, “Convergent Cartesian Grid Methods for Maxwell’s Equations in Complex Geometries", Journal of Computational Physics **170,** 39 (2001).

56. X. Li and J. M. Jin, “A Comparative Study of Three Finite Element-Based Explicit Numerical Schemes for Solving Maxwell’s Equations", IEEE Transactions on Antennas and Propagation **60,** 1450 (2012).

57. J. Niegemann, *Higher-Order Methods for Solving Maxwell’s Equations in the Time-Domain*, PhD thesis (Universität (TH) Karlsruhe, 2009).

58. J. Niegemann, R. Diehl and K. Busch, “Efficient low-storage Runge–Kutta schemes with optimized stability regions", Journal of Computational Physics **231,** 364 (2012).

59. M. Dubiner, “Spectral methods on triangles and other domains", Journal of Scientific Computing **6,** 345 (1991).

60. T. Warburton, “An explicit construction of interpolation nodes on the simplex", Journal of Engineering Mathematics **56,** 247 (2006).

61. E. Toro, *Riemann Solvers and Numerical Methods for Fluid Dynamics: A Practical Introduction* (Springer Berlin Heidelberg, 2009).

62. L. Debnath, *Nonlinear Partial Differential Equations for Scientists and Engineers* (Birkhäuser Boston, 2013).

63. M. König, *Discontinuous Galerkin Metthods in Nanophotonics*, PhD thesis (Karlsruhe Institute of Technology, 2011).

64. J. Hesthaven and T. Warburton, “Discontinuous Galerkin methods for the time-domain Maxwell" s equations", ACES Newsletter **19,** 10 (2004).

65. P. Monk, *Finite Element Methods for Maxwell’s Equations* (Clarendon Press, 2003).

66. J.-P. Berenger, “A perfectly matched layer for the absorption of electromagnetic waves", Journal of Computational Physics **114,** 185 (1994).

67. T. Lu, P. Zhang and W. Cai, “Discontinuous Galerkin methods for dispersive and lossy Maxwell’s equations and PML boundary conditions", Journal of Computational Physics **200,** 549 (2004).

68. P. Drude, “Zur Elektronentheorie der Metalle", Annalen der Physik **306,** 566.

69. K. Kopitzki, P. Herzog and P. Herzog, *Einführung in die Festkörperphysik* (Springer, 1989).

70. C. Kittel, J. M. Gress and A. Lessard, *Einführung in die Festkörperphysik* (Oldenbourg München, 1969).

71. W. Nolting and A. Ramakanth, *Quantum theory of magnetism* (Springer Science & Business Media, 2009).

72. P. Coleman, *Introduction to Many-Body Physics* (Cambridge University Press, 2015).
73. D. Pines and P. Nozières, *Theory of Quantum Liquids: Normal fermi liquids* (Addison-Wesley Publishing Company, Advanced Book Program, 1989).
74. L. Landau, “The theory of a Fermi liquid", Soviet Physics Jetp-Ussr **3,** 920 (1957).
75. G. Baym and C. Pethick, *Landau Fermi-Liquid Theory: Concepts and Applications* (Wiley, 2008).
76. G. Czycholl, *Theoretische Festkörperphysik: Von den klassischen Modellen zu modernen Forschungsthemen* (Springer Berlin Heidelberg, 2013).
77. W. Nolting, *Grundkurs Theoretische Physik 6: Statistische Physik* (Springer Berlin Heidelberg, 2013).
78. L. Landau and E. Lifshitz, *Hydrodynamik* (Akademie Verlag, 1990).
79. K. Hiremath, L. Zschiedrich and F. Schmidt, “Numerical solution of nonlocal hydrodynamic Drude model for arbitrary shaped nano-plasmonic structures using Nédélec finite elements", Journal of Computational Physics **231,** 5890 (2012).
80. W. B. Case, “Wigner functions and Weyl transforms for pedestrians", American Journal of Physics **76,** 937 (2008).
81. F. Haas, “An introduction to quantum plasmas", ArXiv e-prints, arXiv:1206.1079 (2012).
82. J. Kirkwood, “The Statistical Mechanical Theory of Transport Processes I. General Theory", The Journal of Chemical Physics **14,** 180 (1946).
83. J. Kirkwood, “The Statistical Mechanical Theory of Transport Processes II. Transport in Gases", The Journal of Chemical Physics **15,** 72 (1947).
84. W. Klassmann, “Eine hydrodynamische Beschreibung des Plasmas im Rahmen der BBGKY-Hierarchie", German. Zeitschrift für Physik **204,** 83 (1967).
85. G. Kremer, *An Introduction to the Boltzmann Equation and Transport Processes in Gases* , 1 (Springer-Verlag Berlin Heidelberg, 2010).
86. W. Nolting, *Grundkurs Theoretische Physik 4/2: Thermodynamik* (Springer Berlin Heidelberg, 2016).
87. P. Halevi, “Hydrodynamic model for the degenerate free-electron gas: Generalization to arbitrary frequencies", Phys. Rev. B **51,** 7497 (1995).
88. J. Chihara, I. Fukumoto, M. Yamagiwa and H. Totsuji, “Pressure formulae for liquid metals and plasmas based on the density-functional theory", Journal of Physics: Condensed Matter **13,** 7183 (2001).
89. G. Manfredi and F. Haas, “Self-consistent fluid model for a quantum electron gas", Phys. Rev. B **64,** 075316 (2001).
90. G. Toscano *et al.,* “Resonance shifts and spill-out effects in self-consistent hydrodynamic nanoplasmonics", Nature communications **6,** 7132 (2015).
91. A Liebsch, “Surface-plasmon dispersion and size dependence of Mie resonance: silver versus simple metals", Physical Review B **48,** 11317 (1993).

92. J. Sipe, V. So, M. Fukui and G. Stegeman, “Analysis of second-harmonic generation at metal surfaces", Phys. Rev. B **21,** 4389 (1980).

93. N. Lang and W. Kohn, “Theory of Metal Surfaces: Charge Density and Surface Energy", Phys. Rev. B **1,** 4555 (1970).

94. T. Köllner, *Berechnung der Elektronendichteverteilung an metallischen Oberflächen*, MA thesis (Karlsruhe Institute of Technology, 2011).

95. M. del Castillo-Mussot and W. L. Mochán, “Effect of plasma waves on the optical properties of conducting superlattices", Phys. Rev. B **36,** 1779 (1987).

96. C. Navier, “Mémoire sur les lois du mouvement des fluides", Mémoires de l’Académie Royale des Sciences de l’Institut de France **6,** 389 (1823).

97. S Goldstein, “Note on the condition at the surface of contact of a fluid with a solid body", Modern Development in Fluid Mechanics **2** (1965).

98. E. Lauga, M. Brenner and H. Stone. *Springer Handbook of Experimental Fluid Mechanics* 1219 (Springer Berlin Heidelberg, Berlin, Heidelberg, 2007).

99. M. A. Day, “The no-slip condition of fluid dynamics", Erkenntnis **33,** 285 (1990).

100. J.-J. Shu, J. Bin Melvin Teo and W. Kong Chan, “Fluid Velocity Slip and Temperature Jump at a Solid Surface", Applied Mechanics Reviews **69,** 020801 (2017).

101. J.-J. Shu, J. B. M. Teo and W. K. Chan, “A new model for fluid velocity slip on a solid surface", Soft Matter **12,** 8388 (2016).

102. A. Hille, *Das unstetige Galerkin-Verfahren in der Nanooptik*, PhD thesis (Technische Universität Dresden, 2012).

103. M. Plock, “Störungstheoretische Betrachtung von Drei-Wellen-Mischen im Rahmen des hydrodynamischen Modells", 2017.

104. P. B. Johnson and R. W. Christy, “Optical Constants of the Noble Metals", Phys. Rev. B **6,** 4370 (1972).

105. C. Bohren and D. Huffman, *Absorption and Scattering of Light by Small Particles* (Wiley, 2008).

106. J. Schöberl, “NETGEN An advancing front 2D/3D-mesh generator based on abstract rules", Computing and Visualization in Science **1,** 41.

107. A. Sundaramurthy *et al.,* “Field enhancement and gap-dependent resonance in a system of two opposing tip-to-tip Au nanotriangles", Phys. Rev. B **72,** 165409 (2005).

108. P. Goorjian and A. Taflove, “Direct time integration of Maxwell’s equations in nonlinear dispersive media for propagation and scattering of femtosecond electromagnetic solitons", Opt. Lett. **17,** 180 (1992).

109. MATLAB, *Version 9.2 (R2017a)* (The MathWorks Inc., Natick, Massachussettes, 2017).

110. G. Walrafen and P. Krishnan, “Model analysis of the Raman spectrum from fused silica optical fibers", Appl. Opt. **21,** 359 (1982).

111. K. Blow and D. Wood, “Theoretical description of transient stimulated Raman scattering in optical fibers", IEEE Journal of Quantum Electronics **25,** 2665 (1989).

112. A. Taflove and S. Hagness, *Computational Electrodynamics: The Finite-difference Time-domain Method* (Artech House, 2005).

113. R. H. Stolen and C. Lin, “Self-phase-modulation in silica optical fibers", Phys. Rev. A **17,** 1448 (1978).

114. S. T. Davey, D. L. Williams, B. J. Ainslie, W. J. M. Rothwell and B. Wakefield, “Optical gain spectrum of GeO/sub 2/-SiO/sub 2/ Raman fibre amplifiers", IEE Proceedings J - Optoelectronics **136,** 301 (1989).

115. G. Agrawal, *Nonlinear Fiber Optics* (Academic Press, 2007).

116. G. Toscano *et al.,* “Surface-enhanced Raman spectroscopy: nonlocal limitations", Optics Letters **37,** 2538 (2012).

117. G. Toscano, A.-P. Jauho and M. Wubs, *Semiclassical theory of nonclocal plasmonic excitation in metallic nanostructures*, PhD thesis (2013).

118. A. J. Bennett, “Influence of the electron charge distribution on surface-plasmon dispersion", Physical Review B **1,** 203 (1970).

119. J. M. Dawson, “Particle simulation of plasmas", Rev. Mod. Phys. **55,** 403 (1983).

120. C. Peltz, C. Varin, T. Brabec and T. Fennel, “Fully microscopic analysis of laser-driven finite plasmas using the example of clusters", New Journal of Physics **14,** 065011 (2012).

121. G. Vignale, C. A. Ullrich and S. Conti, “Time-dependent density functional theory beyond the adiabatic local density approximation", Physical review letters **79,** 4878 (1997).

122. M. G. Albrecht and J. A. Creighton, “Anomalously intense Raman spectra of pyridine at a silver electrode", Journal of the american chemical society **99,** 5215 (1977).

123. W. Nolting, *Grundkurs Theoretische Physik: Klassische Mechanik* (Springer Berlin Heidelberg, 2013).

Publication List

H1. D.-N. Huynh, M. Moeferdt, C. Matyssek, C. Wolff and K. Busch, “Ultrafast three-wave-mixing in plasmonic nanostructures", Applied Physics B **122,** 139 (2016).

H2. P. Varytis, D.-N. Huynh, W. Hartmann, W. Pernice and K. Busch, “Design study of random spectrometers for applications at optical frequencies", ArXiv e-prints, arXiv:1802.02515 (2018, submitted for review).

H3. D.-N. Huynh, P. Varytis and K. Busch, “A slab waveguide source for discontinuous Galerkin time-domain methods", SPIE Conference Proceedings, Photonics Europe **10688-31** (2018, submitted for review).

H4. D.-N. Huynh and K. Busch, “Stimulated Raman Scattering of Fused Silica within the Discontinuous Galerkin Time-Domain Framework", (in preparation).

Acknowledgments

Ich möchte allen voran meinem Betreuer Prof. Dr. Kurt Busch danken. Er hat über die Dauer meiner Promotion viel Verständnis und Geduld gezeigt. Er war mir nicht nur fachlich sondern auch auf menschlicher Ebene immer eine große Unterstützung. Ohne ihn wäre diese Dissertation selbstredend nicht möglich gewesen. Für ihn kenne ich keine bessere Bezeichnung als bärenstark.

Mein Dank gilt ebenfalls Markus Krecik. Er war nicht nur dazu bereit weite Teile dieser Dissertation Korrektur zu lesen, sondern hat auch die Achterbahnfahrt meiner Doktorandenzeit mitgemacht. Er war mir in selbst in schwierigen Zeiten immer ein verständnisvoller und verlässlicher Partner.

Als nächstes möchte ich meinem Freund und Kollegen Matthias Moeferdt danken. Besonders der fachliche Austausch im Bereich Hydrodynamik, war wichtig für meine Arbeit.

Meinen Kollegen Kathrin Hermann und Philip Kristensen möchte ich für das Korrekturlesen einiger Teile meiner Arbeit danken. Beide schätze ich nur nicht für ihre starke fachliche Kompetenz, sondern auch für die gute Freundschaft. Des Weiteren gilt mein Dank Francesco Intravaia, Julia Werra, Torsten Wendav und Thomas Kiel für viele fachliche Diskussionen und persönliche Unterstützung während meiner Doktorandenzeit.

Ich danke außerdem unserer Sekretärin Frau Marion Goetsch. Als gute Seele unserer Arbeitsgruppe hält sie alle Dinge am laufen.

Meinen Kollegen Marty Oelschläger und Daniel Reichert danke ich für viel Freude und deren Freundschaft. Gerade das freitagliche "Feierabendbier" war wichtig, um die Moral untereinander hoch zu halten.

Christian Wolff danke ich für die treue Freundschaft. Es ist anerkennend zu erwähnen, dass allen Arbeiten mit der DGTD-Methode in der AG theoretische Optik & Photonik an der HU Berlin Christians Implementierung der Methode zu Grunde liegt. Sein Code hat meine Dissertation erst ermöglicht.

Zuletzt möchte ich allen Freunden und Kollegen danken, die ich hier nicht namentlich erwähnt habe.